Lecture Notes in Mechanical Engineering

Dilip Sharma
Somnath Roy *Editors*

Emerging Trends in Energy Conversion and Thermo-Fluid Systems

Select Proceedings of iCONECTS 2021

Springer

Lecture Notes in Mechanical Engineering

Lecture Notes in Mechanical Engineering (LNME) publishes the latest developments in Mechanical Engineering—quickly, informally and with high quality. Original research reported in proceedings and post-proceedings represents the core of LNME. Volumes published in LNME embrace all aspects, subfields and new challenges of mechanical engineering. Topics in the series include:

- Engineering Design
- Machinery and Machine Elements
- Mechanical Structures and Stress Analysis
- Automotive Engineering
- Engine Technology
- Aerospace Technology and Astronautics
- Nanotechnology and Microengineering
- Control, Robotics, Mechatronics
- MEMS
- Theoretical and Applied Mechanics
- Dynamical Systems, Control
- Fluid Mechanics
- Engineering Thermodynamics, Heat and Mass Transfer
- Manufacturing
- Precision Engineering, Instrumentation, Measurement
- Materials Engineering
- Tribology and Surface Technology

To submit a proposal or request further information, please contact the Springer Editor of your location:

China: Ms. Ella Zhang at ella.zhang@springer.com
India: Priya Vyas at priya.vyas@springer.com
Rest of Asia, Australia, New Zealand: Swati Meherishi
at swati.meherishi@springer.com
All other countries: Dr. Leontina Di Cecco at Leontina.dicecco@springer.com

To submit a proposal for a monograph, please check our Springer Tracts in Mechanical Engineering at https://link.springer.com/bookseries/11693 or contact Leontina.dicecco@springer.com

Indexed by SCOPUS. All books published in the series are submitted for consideration in Web of Science.

Dilip Sharma · Somnath Roy
Editors

Emerging Trends in Energy Conversion and Thermo-Fluid Systems

Select Proceedings of iCONECTS 2021

Springer

Editors
Dilip Sharma
Department of Mechanical Engineering
Malaviya National Institute of Technology
Jaipur, Rajasthan, India

Somnath Roy
Department of Mechanical Engineering
Indian Institute of Technology Kharagpur
Kharagpur, West Bengal, India

ISSN 2195-4356 ISSN 2195-4364 (electronic)
Lecture Notes in Mechanical Engineering
ISBN 978-981-19-3409-4 ISBN 978-981-19-3410-0 (eBook)
https://doi.org/10.1007/978-981-19-3410-0

This Springer imprint is published by the registered company Springer Nature Singapore Pte Ltd.
The registered company address is: 152 Beach Road, #21-01/04 Gateway East, Singapore 189721, Singapore

Preface

In the recent years, sustainability has gained a keen interest globally by both governmental and non-governmental organizations. Earlier, the words "environment" and "sustainability" were of concern only for a handful of agencies. Lately, people have realized the importance of sustainable living, and a consensus is bulding to act unanimously to protect the Mother Nature. As the citizens of this planet, we need to understand that neither we own nor we inherit Earth and all its resources. Rather, we are in debt of our future generations who have loaned it to us. It is our moral responsibility to hand over a liveable planet to future generations. So, this book has taken up an essential theme on energy conversion in this context. Energy conversion has an extensive scope ranging from energy generation, utilization, conversion, storage, transmission, conservation management, and sustainability. The term energy in itself is very broad, including every form of energy source, albeit being renewable or non-renewable energy. Therefore, innovative research is highly desirable to improve the existing technologies' sustainability and develop sustainable alternatives. For scalable use, priority must be given to the interdisciplinary research in the allied area of energy using all possible solution methodologies for numerical studies and empirical investigation.

This book attempts to introduce the field of energy, its importance and alternatives, and the way forward. Also, cutting-edge research like thermal management, additive manufacturing, green buildings, fluid–structure interaction, high-performance computing, numerical methods, aerodynamics, and micro- and nano-scale transport phenomena in the biological systems, along with the traditional research in power plants, internal combustion engines, refrigeration, and air-conditioning, is presented.

We believe that this book is unique and covers an extensive gamut of topics on energy conversion and efficiency, thermo-fluid systems, and interdisciplinary topics on the subject matter from a group of authors recognized in their respective fields. We hope that it will prove to be a great help for the graduate and undergraduate students, researchers, and managers in their quest to explore and understand the current state of the art of the said research interests.

Jaipur, India — Dilip Sharma
Kharagpur, India — Somnath Roy

Contents

About the Editors

Dr. Dilip Sharma is currently a professor in the Department of Mechanical Engineering, Malaviya National Institute of Technology Jaipur (MNIT Jaipur), Rajasthan. He received his masters' degree in Thermal Engineering from IIT Roorkee, and Ph.D. from MNIT Jaipur in 2005. He is a senior academician with over 30 years of experience, and has published over 150 research articles in the international journals and conferences. His research interests include internal combustion engines, alternate fuels and emissions, non-conventional sources of energy, hydrogen energy, engine combustion, cogeneration/trigeneration system, biofuels, combustion generated emission, solar thermal systems, etc.

Dr. Somnath Roy is currently Associate Professor at Indian Institute of Technology Kharagpur. He received his masters' degree in Mechanical Engineering from IIT Kanpur in 2004, and Ph.D. in Mechanical Engineering from Louisiana State University, USA, in 2010. Before joining IIT Kharagpur, he worked as research associate and visiting faculty at Louisiana State University, USA, followed by Assistant Professor at Indian Institute of Technology Patna. His research interest is turbulence, arterial flows, moving boundary flow simulation, high-performance computing using cluster and GPGPUs. His primary area of work is computational fluid dynamics (CFD). He has hosted two GIAN programs on computational methods and has also offered online course (NPTEL) on matrix solvers. His research group works on developing immersed boundary method (IBM)-based computationally efficient algorithms to solve moving boundary problems and on utilizing these implementations to predict flow and heat transfer in engineering and biological applications.

Power Generation Techniques

Energy Harvesting Through a Low-Cost Device Using Reverse Electrowetting on Dielectric (REWOD)

Diwakar Singh, Gaurav Bhutani, Satinder Sharma, and Rajeev Kumar

Nomenclature

ALD	Atomic layer deposition
EDL	Electric double-layer
EWOD	Electrowetting on dielectric
FOM	Figure of merit
ITO	Indium tin oxide
PTFE	Polytetrafluoroethylene
PVDF	Polyvinylidene fluoride
PZT	Lead zirconium titanate
REWOD	Reverse electrowetting on dielectric
SBT	Strontium bismuth tantalite
SEM	Scanning electron microscope
ZnO	Zinc oxide
d	Dielectric thickness (m)
f	Frequency of applied vibration (Hz)
i	Current (A)
k	Dielectric constant (F/m)
$q_{\min}$	Initial charges (C)
$q_{\max}$	Total charges (C)
A	Contact area (m^2)
A_{IJ}	Contact area between phases I and J (m^2)

D. Singh (✉) · G. Bhutani · R. Kumar
School of Engineering, IIT Mandi, Mandi, Himachal Pradesh 175005, India
e-mail: d19002@students.iitmandi.ac.in

S. Sharma
School of Computing and Electrical Engineering, IIT Mandi, Mandi, Himachal Pradesh 175005, India

D. Sharma and S. Roy (eds.), *Emerging Trends in Energy Conversion and Thermo-Fluid Systems*, Lecture Notes in Mechanical Engineering,
https://doi.org/10.1007/978-981-19-3410-0_1

C	Capacitance (F)
$C_{\min}$	Minimum capacitance (F)
$C_{\max}$	Maximum capacitance (F)
I_{C}	Current due to charging and discharging (A)
I_{R}	Constant leakage current (A)
I_{rms}	Root mean square current (A)
P	Power output (W)
P_{h}	Power converted from mechanical into electrical domain (W)
R_{L}	Load resistance (Ω)
U	Energy stored (J)
$U_{\min}$	Minimum potential energy (J)
$U_{\max}$	Maximum potential energy (J)
V	Electric potential (V)
W	Work done (J)
γ_{IJ}	Interfacial tension between phases I and J (N/m)
ε_0	Permittivity of free space (F/m)
ε_{r}	Relative dielectric constant
θ_{r}	Young's angle (rad)

1 Introduction

There has been continuous research in the field of sustainable micro/nano energy production. Conventionally, we have been producing electricity from hydroelectric, thermal, and nuclear power using the electromagnetic induction phenomenon. Since the rate of depletion of fossil fuels is higher in comparison to its replenishment rate, it is important to explore new methods of harvesting energy, which are clean and portable. Energy harvesting from freely available mechanical energy sources such as machines, vehicle vibrations, and passive human walking can be a useful source of input energy. This has motivated research in the field of mechanical energy harvesting techniques.

Common energy harvesting methods include Piezoelectric [1], Triboelectric [2], and Electric double-layer (EDL) harvesting. Energy harvesting through reverse electrowetting on dielectric (REWOD) is a novel approach to harvest freely available low-frequency vibration energy [3]. This method is getting popular over other energy harvesting methods due to its high power density, which is of the order of 10^3 W/m^2 [3]. External mechanical vibration causes the droplet to change its shape, which leads to the generation of electrical energy. Output current depends on the rate of change of effective contact area of the droplet with the dielectric surface.

Atomic layer deposition (ALD) and sputtering machines, which are used for the deposition of thin material layers, cost up to tens of crores INR. The expensive nature of these fabrication techniques has restricted their use at a mass scale. In contrast to these complex and expensive approaches, the present project has used a simple and cost-effective technique of spin coating to fabricate the REWOD device. The material required costs only a few thousand per 500 g. Only 1–2 g is required for one sample fabrication, which makes it cost-effective. Low material cost along with cost-effective fabrication methods makes this process a very novel and desirable choice for REWOD device fabrication at a small scale.

2 Literature Review and Objective

Only a few attempts have been executed in the field of energy harvesting through REWOD. The work of Krupenkin et al. [3] has shown the output power of 103 W/m^2 with the help of an array of conducting droplets. It is followed by the work of Moon et al. [4] which eliminates the bias voltage provided between the electrodes. The output power of 0.003 W/m^2 was obtained over an indium tin oxide (ITO)-coated glass slide (electrode) and a layer of PTFE acting both as a dielectric and hydrophobic layer. A new method of energy harvesting through REWOD with the help of bubble growth and collapse was introduced by Hsu et al. [5]. This method gives a lightweight device producing a high range of power output. The work of Yang et al. [6] has shown that the dielectric layer formed by ALD has a high dielectric constant, higher breakdown voltage, and low leakage current. The maximum power output was 110 W/m^2. The device works on the principle of movement of charges, which requires a conducting medium between the electrodes. Hence, the choice of conducting medium is important in making the process effective. The conducting droplet can be an ionic salt solution or a liquid metal droplet. In the REWOD device, researchers have used both ionic salt solution and metal liquid [6]. Liquid metals are a better alternative for conducting liquid as they have electrons which are better charge carriers than ions. For a product to be market-ready, a device must be cost-effective. Hence, it is important to select a low-cost fabrication method. There are various methods available for the microfabrication of dielectric film such as ALD, sputtering, and spin coating. The machines used for ALD and sputtering are way too expensive in comparison with a spin coater. The deposition rate of ALD and sputtering is generally low which is 1.2 Å/cycle and 50 nm/h, respectively [6]. At this deposition rate, it will take hours to obtain a dielectric film of a few μm thicknesses. As thickness is an important parameter to obtain a high breakdown voltage. On the other hand, spin coating is a simple technique of obtaining a dielectric layer of a few nm to μm thick within a few minutes. One other attractive option for a dielectric layer is nanowires, which are easy to fabricate. They can be fabricated by electrochemical and hydrothermal deposition techniques. The material required costs only a few thousand per 500 gm. Only 1–2 gm is required for one sample fabrication, which makes it cost-effective. ZnO nanowires have potential application in energy harvesting through REWOD due to their higher dielectric constant. There are many different methods to synthesize the one-dimensional non-aligned ZnO nanowires, but this literature review has covered only two of them, which are (1) Hydrothermal [7, 8] and (2) Electrochemical deposition [9]. In the present work, ZnO nanowires coated with polytetrafluoroethylene (PTFE) are used as a dielectric layer in REWOD device. The problem of Leakage current is prominent in the dielectric layer composed of nanowires because the leakage current travels through grain boundaries. It can be reduced by coating the dielectric layer with any fluoropolymer [6, 10]. The energy harvesting through REWOD is based on the principle of EWOD. In EWOD, the bias voltage is required to accumulate the charges in the form of an electric double layer between conducting droplet and dielectric surface. Accumulated charges apply an electrostatic force over the triple contact line of the droplet, causing the change in the shape of a droplet. Devices have been fabricated to reduce the required bias voltage by increasing the dielectric constant and decreasing dielectric thickness [11]. In REWOD device, output current depends on the rate of change of effective contact area of the droplet with the dielectric surface. This change in effective contact area will be maximum only when the droplet will regain the maximum possible percentage of its initial contact area.

In this work, energy harvesting through REWOD has been demonstrated on ZnO nanoarrays spin-coated with a layer of PTFE. Copper tape glued over a glass slide was used as an electrode in the present experiments, which makes it cost-effective in comparison with the sputtering and atomic layer deposition techniques used by previous researches for electrode deposition [3–6]. Coating of a 30 nm PTFE layer over the zinc oxide layer significantly reduced the leakage current density, which resulted in higher breakdown voltages. Mercury was used as the conducting droplet between the two plates since electrons are better charge carriers than ions. A conducting droplet having ions as charge carriers would have limited the power density due to the low mobility of ions. A variable capacitor was obtained when the two-plate and drop setup was actuated using a vibration generator; the periodic charging and discharging of this capacitor helped to harvest mechanical energy into electrical energy.

Reverse electrowetting on dielectric (REWOD) is based on the principle of electrowetting. Electrowetting on dielectric (EWOD) generally refers to the manipulation of surface energy by the application of external voltage—hydrophobic surface transformation to the hydrophilic surface when the voltage is applied. The phenomenon of EWOD can be easily understood from the electrowetting or Berge Lippmann Young equation that is given as [3]

$$\cos\theta = \cos\theta_{\mathrm{r}} + \frac{\varepsilon_0\varepsilon_{\mathrm{r}}}{2d\gamma_{\mathrm{LG}}}U^2, \tag{1}$$

$$C(t) \cong \frac{\varepsilon_0\varepsilon_{\mathrm{r}}}{d}A(t), \tag{2}$$

The total charge at the solid–liquid interface increases as the droplet is squeezed, and the opposite happens as the droplet is relaxed. Useful power can therefore be generated as excessive charges flow through the droplet, electrode, and the external electrical circuit, where an external load can be connected. Figure 1 shows the schematic diagram of the droplet for energy harvesting through REWOD. It can be observed from Fig. 1a that the variable capacitor has some charges, let us assume the number of charges is $q_{\min}$. After applying the mechanical vibration to the bottom plate, the droplet got squeezed; therefore, more amount of charge got stored in the variable capacitor [12]. The total number of charges stored is $q_{\max}$. Let us assume that there is no charge trapping in the dielectric material, hence when the droplet will again resume its relaxed position then this extra charge (q_0) which was stored during squeezing, will be released.

From Fig. 1, the potential difference (V) between the plates at that instant will be q/kC. If an extra increment of charge dq is then transferred the increment of work is [12],

$$\mathrm{d}W = V\mathrm{d}q, \tag{3}$$

The work required to bring the total capacitor charge up to a final value $q_{\min}$ is:

$$W = \int \mathrm{d}W = \frac{1}{\mathrm{KC}} \int\limits_0^{q_{\min}} q\mathrm{d}q, \tag{4}$$

As $q_{\min} = kC_{\min}V$ where V is the applied voltage. So, work stored as potential energy $U_{\min}$ in a capacitor is,

$$U_{\min} = \frac{q_{\min}^2}{2Ck} = \frac{kC_{\min}V^2}{2}. \tag{5}$$

Form Fig. 1b, charging of capacitor from $q_{\min}$ to $q_{\max}$ as the shape of the capacitor is changing; hence, the capacitance will be [12],

$$C_0 = C_{\max} - C_{\min}. \tag{6}$$

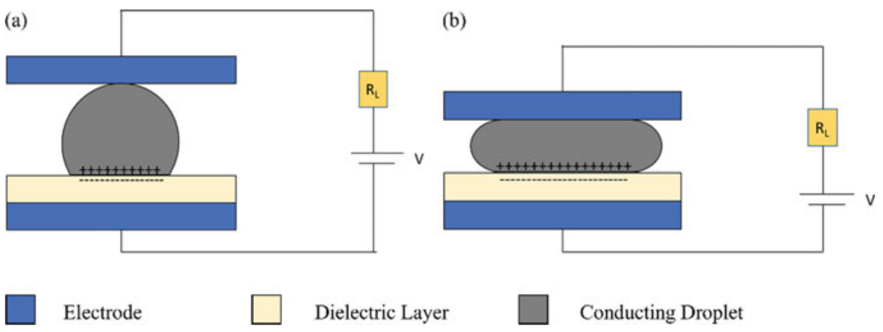

Fig. 1 **a** Schematic diagram of relaxed droplet, **b** schematic diagram of squeezed droplet

Let us assume that there is no charge trapping in the dielectric and this increased charge q_0 during charging (squeezing of the droplet) is completely released during discharging (relaxed droplet).

So, work required to bring the increased capacitor charge $q_0 = (q_{\max} - q_{\min})$ from $q_{\min}$ to final value $q_{\max}$ [12].

$$W_{\max} = \frac{1}{2kC} q_{\max}^2. \tag{7}$$

The amount of work stored in the capacitor in form of potential energy is,

$$U_{\max} = \frac{q_{\max}^2}{2kC_{\max}} = \frac{kC_{\max} V^2}{2}. \tag{8}$$

Potential energy which will be released during discharging is,

$$\nabla U = U_{\max} - U_{\min} = k\frac{V^2}{2}(C_{\max} - C_{\min}). \tag{9}$$

Using the thermodynamic approach of electrowetting, from Fig. 1a, b, the external work is equal to the difference of high surface energy associated with wetted surface and low surface energy associated with non-wetted surface.

$$\text{External work} = \text{high surface energy} - \text{ low surface energy} \tag{10}$$

$$\delta W_{\text{ext}} = \delta A_{\text{LG}} \gamma_{\text{LG}} + \delta A_{\text{SL}} \gamma_{\text{SL}} + \delta A_{\text{SG}} \gamma_{\text{SG}}. \tag{11}$$

Now, the change in Helmholtz free energy ($\tilde{F} = 0$) after squeezing of the droplet is equal to zero.

$$\delta W = K\frac{V^2}{2}(C_{\max} - C_{\min}) \delta A_{\text{SL}}. \tag{12}$$

The right-hand side of Eq. (12) represents the amount of energy stored. Therefore, when the W_{ext} is applied the contact angle changes from θ to θ_0 and the energy stored in a variable capacitor is $K\frac{V^2}{2}(C_{\max} - C_{\min})$. As

$$i = \frac{d}{\mathrm{d}t}(C_{\max} - C_{\min})V. \tag{13}$$

3 Materials and Methods

3.1 Electrochemical Deposition of ZnO Nanoarrays

The copper tape adhered over a glass slide of dimension 2 cm × 5 cm, followed by ultrasonic cleaning in acetone for 15 min for the removal of grease, oil, dirt, and rust. Further cleaning with isopropyl alcohol for 15 min was carried out to remove any remaining traces of oil. It was subsequently dried with a nitrogen gun. 0.1 M solution of zinc nitrate hexahydrate ($Zn(NO_3)_2.6H_2O$) (procured from *Sigma-Aldrich*, CAS number 10196–18-6, molecular weight 297.49) was prepared. The solution was used as an electrolyte for the chemical deposition of ZnO on copper tape. The beaker containing cathode (i.e., copper tape), anode (i.e., a platinum electrode), and the electrolyte was placed over a hot plate, which was maintained at a temperature of 75 °C. To ensure a stable open-circuit voltage between the cathode and anode, no external voltage was applied for 10 s. A 3 V DC voltage was applied across the cathode and anode for 75 min. After chemical deposition, the sample was left in open atmospheric air for 10 min.

The ZnO nanoarrays were analyzed using cross SEM to inspect the surface morphology, as shown in Fig. 2a. An arbitrarily connected flower petal-like structure can be seen in the image. The sample was uniformly covered with this array and pores, or any other defects were not observed. The deposited ZnO nanoarrays were 5–6 μm thick, as shown in a slightly less magnified surface in Fig. 2b. The thickness of ZnO nanoarrays layer can be reduced by lowering the electric potential applied during electrochemical deposition of ZnO. The surface obtained from the nanowires was rough enough to enhance the hydrophobic nature of the surface, which can be attributed to Wenzel's law.

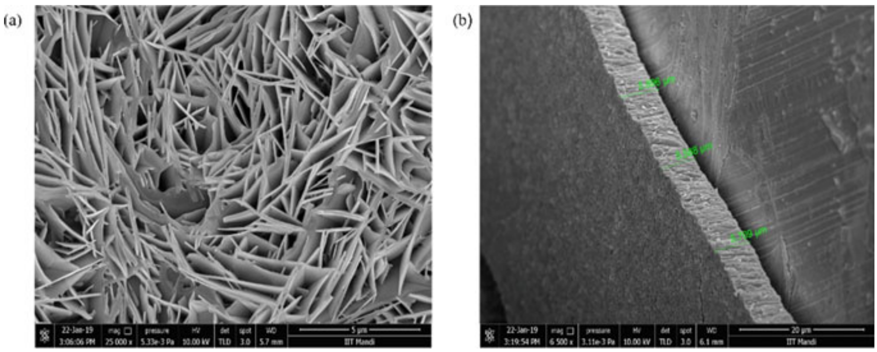

Fig. 2 **a** Surface morphology of the ZnO nanoarrays, **b** SEM image of ZnO nanowires coated on Cu tape; thickness of the ZnO layer can be seen

3.2 Spin Coating of PTFE

PTFE (445,096 Sigma-Aldrich) 60 wt.% dispersion in H_2O was diluted with deionized (DI) water in the ratio of 1:30 (volume: volume). The solution was homogenized for 15 min, post which it was spin-coated at 4000 rpm, acceleration time 10 s, dwell time 45 s. After spin coating, the sample was cured at 120 °C for 15 min.

3.3 Breakdown Voltage, Capacitance, and Contact Angle

The breakdown voltage of ZnO nanoarray dielectric layer coated with PTFE is ranging between 60 and 70 V, and its capacitance is 8.50×102 nF/cm^2. The breakdown voltage and capacitance were measured with SCS 4200 Keithley Instruments. The contact angle of mercury droplet over this dielectric surface was 144.788°. An experimental setup for the exploration of low-cost energy harvesting through reverse electrowetting on dielectric (REWOD) was designed and fabricated. The complete setup required to perform the REWOD experiment involved spring setup, fixture, vibration generator, power supply of vibration generator (SP, Sl. No. 2626/07/16, Spranktronics Bangalore-79), DC power supply (ST4077, Scientech Technologies Pvt. Ltd.), mixed-signal oscilloscope (VB8012, National Instruments), and PC as shown in Fig. 3a. The REWOD device was placed over the nob of the vibration generator, with the help of a fixture. The power oscillation provides the power and specific frequency of vibration to the vibration generator. DC power supply was used to provide the bias voltage in a resistor–capacitor circuit as shown in Fig. 3b. The voltage was measured across the load resistance RL with the help of a mixed-signal oscilloscope. A breadboard was used to realize the resistance capacitor circuit as shown in Fig. 3b. IR and IC refer to the constant leakage current and the current due to charging or discharging of the capacitor, respectively, as shown in Fig. 3b. The conducting liquid used was mercury Hg.

4 Results and Discussion

ZnO wires synthesized by the electrochemical deposition method have columnar grains resulting in the development of vertical grain boundaries [9]. Nano/micro-sized physical defects are usually embodied in this type of grain boundary, which enables the leakage of electrical charges even at a small electric field. Leakage current is one of the reasons for breakdown [13]. In the present study, ZnO nanoarrays were coated with PTFE which helped to increase the breakdown voltage range from 30–40 V to 60–70 V. This breakdown voltage was increased by the onset of reduction in leakage current due to the filling of voids by the PTFE, which in turn increased the film density. The increased film density helped to reduce the leakage of charges. The

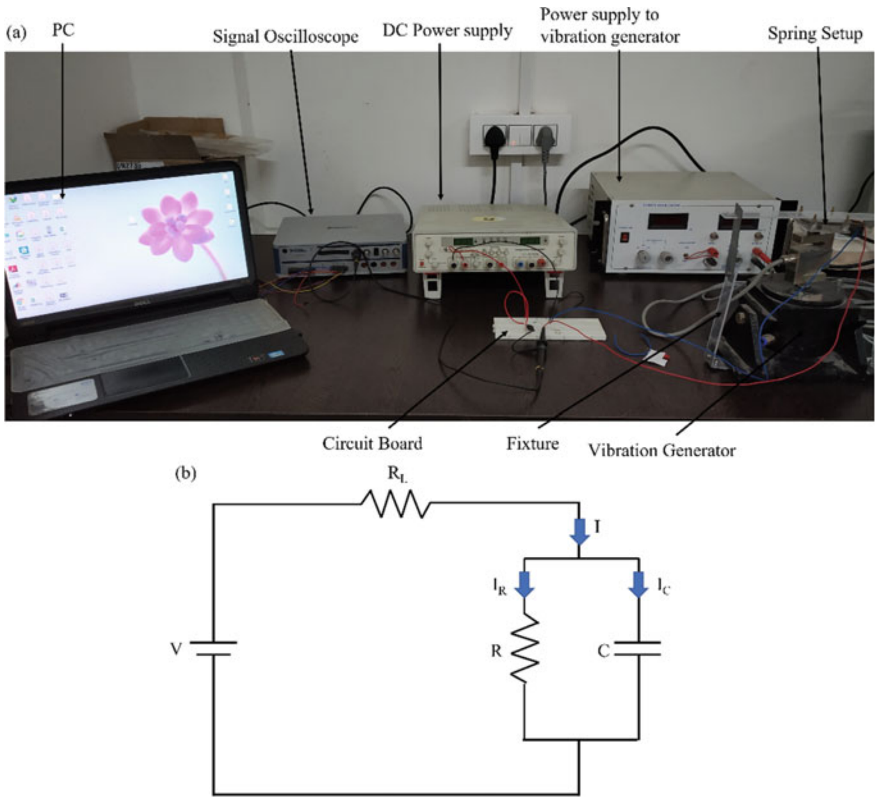

Fig. 3 **a** Photograph of the experimental setup, **b** resistor–capacitor circuit model

layer of PTFE not only helped in raising the breakdown voltage but also helped to enhance the surface hydrophobicity. The average contact angle of mercury droplet of volume 30 μL, elevated from 134° on ZnO nanoarrays to 144° on PTFE coated over ZnO nanoarrays. Surface hydrophobicity is desired in REWOD, as it will help the droplet to regain the maximum possible initial contact angle.

Table 1 lists the contact angle, breakdown voltage, and capacitance of ZnO nanoarrays and PTFE-coated ZnO nanoarrays. An extra layer of hydrophobic material (PTFE) helped to improve the breakdown voltage and contact angle but at the expense of capacitance. In a series of two dielectric layers, net capacitance sifts toward the lower capacitance. Hence, the capacitance of PTFE-coated ZnO nanoarrays is 8.50×10^2 nF/cm^2 while the capacitance of ZnO nanoarrays is 6.43×10^3 nF/cm^2.

To see the effect of PTFE-coated ZnO nanoarray on energy harvesting through reverse electrowetting on dielectrics (REWOD), the voltage was measured across a load resistance of 1 MΩ with the help of a mixed-signal oscilloscope. The current in the circuit was then calculated using Ohm's law across the load resistance, plots

Table 1 The measured contact angle of mercury droplet, breakdown voltage, and capacitance of ZnO nanoarrays and PTFE-coated ZnO nanoarrays

Dielectric layer	Contact angle	Breakdown voltage range (V)	Capacitance (nF/cm^2)
ZnO nanoarray	134°	30–40	6.43×10^3
PTFE-coated ZnO nanoarray	144°	60–70	8.50×10^2

The contact angle of mercury droplet was measured by drop shape analyzer, and breakdown voltage and capacitance were measured by I–V and C–V measurement.

for which are shown in Fig. 4. The experiments were conducted starting with a 2 V bias voltage, which was increased in steps of 2 V until breakdown occurred.

Figure 4a shows two peaks in a time window of 1 s, which agrees with the 2 Hz actuation frequency used in the experiments. When the voltage across load resistance was measured for each iteration, current data was recorded for six seconds, and twelve similar peaks were obtained. The plot, however, shows only two peaks out of the twelve for a time window of one second for clarity. The increase and decrease in the current as seen in each peak correspond to the discharging and charging of the REWOD device acting as a variable capacitor. It can be observed from Fig. 4a that the baseline of current plotted with time did not coincide with zero due to leakage current. Leakage current exists because of the conductivity of dielectric, only an ideal dielectric can have zero leakage current. It can be observed from Fig. 4b that generated current is almost constant for three hundred cycles. The breakdown of the dielectric layer occurred at 12 V DC bias voltage due to the erosion of the surface by the mercury droplet. In the present work, life cycle of the REWOD device is

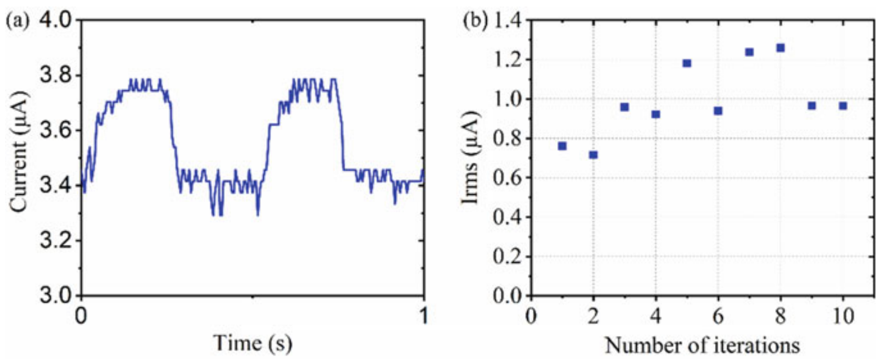

Fig. 4 **a** Current calculated across load resistance of 1 MΩ is plotted with time, **b** Irms with the number of iterations at the bias voltage 6 V and vibrational frequency 2 Hz on a layer of PTFE spin-coated over zinc oxide nanowires as a dielectric layer and every next graph is recorded at a time gap of 30 s

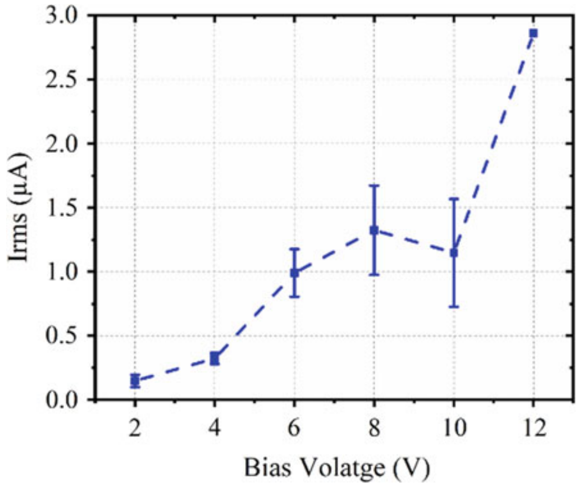

Fig. 5 Irms versus bias voltages for PTFE-coated zinc oxide nanowires at vibrational frequency 2 Hz

defined as the product of the number of iterations performed before a breakdown, time between two iterations, and the number of cycles in one second. The life cycle of spin-coated PTFE over ZnO nanoarrays was 3120 cycles. When the DC bias voltage was increasing, the root mean square current was also increasing because of the increase in bias voltage. The amount of charge in the Gaussian surface of the variable capacitor increases and now more charges were available to move across the circuit, which is shown in Fig. 5.

The higher breakdown voltage strength is desired to obtain the higher power density, as power density is directly proportional to the square of the current generated. Power density is defined as the power output ($P = \mathrm{Irms}^2 \times R_L$) per unit contact area of conducting droplet. It is an important characteristic as in any energy harvesting method. In energy harvesting through REWOD device, power density increases parabolically with bias voltage, until breakdown occurred at 12 V. The maximum power density at 12 V is 3.87 $\mathrm{mW/cm^2}$ as shown in Fig. 6a. The energy density per cycle was calculated by integrating the power density over one cycle to determine the applicability of any energy harvesting method, the energy density per cycle plays an important role because even if any method has high power density, then it does not mean the amount of energy which can be utilized is sufficient for practical applications. It can be observed from Fig. 6b that the maximum energy density per cycle was 204.5 $\mu\mathrm{J/cm^2}$ at a bias voltage of 12 V. Practical applications where REWOD has its potential cannot be incorporated with high bias voltage and these results reveal that PTFE-coated ZnO nanoarrays can be used as a dielectric layer for REWOD device.

To establish an adequate comparison of different vibrational energy harvesting methods. The figure of merit was first introduced by Baset et al. [14] which is defined as,

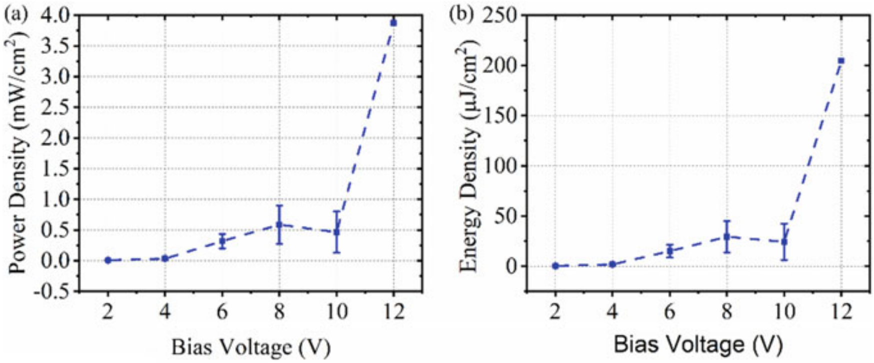

Fig. 6 **a** Power density vs bias voltage, **b** energy density per cycle vs bias voltage for PTFE layer spin-coated over zinc oxide nanowires as the dielectric layer

Table 2 Figure of merit of this work and previous works in the field of energy harvesting from mechanical vibrations

Reference	Basset et al. [14]	Yang et al. [6]	Current work
FOM (10^{-8} μW/mm^2 Hz V^2)	5.78	6,342,593	13,437,500

$$\mathrm{FOM} = \frac{P_\mathrm{h}}{V^2 f A} \tag{14}$$

where P_h refers to power converted to electrical domain from mechanical domain, V refers to a maximum applied bias voltage, f refers to the frequency of the applied vibration and A refers to the effective contact area. For this work, that is the energy harvesting through reverse electrowetting on dielectric with one mercury droplet on PTFE as a dielectric layer and copper tape as an electrode, the maximum average output power density obtained is 0.435 μW/mm^2 at 20 V of applied bias voltage.

The FOM for previous works reported in Table 2 was obtained from an array of droplets, and all of them have used expensive fabrication methods like atomic layer deposition, sputtering, and thermal deposition. In this work, the energy harvesting through REWOD was done with only one mercury droplet over a layer which was fabricated with a cheap fabrication technique spin coating. FOM for zinc oxide nanoarrays coated with PTFE is highest in comparison with all previous works.

5 Conclusions

In the present work, a low-frequency mechanical vibration energy harvesting device has been fabricated with the cost-effective technique of spin coating. In previous works, dielectric layers were fabricated by expensive techniques such as sputtering and thermal deposition. To eliminate the expense of sputtering, copper tape has been used as an electrode. For fabrication purposes, a spin-coated layer of PTFE and ZnO nanowires was used as a dielectric layer. ZnO nanoarrays were coated with a 30 nm thick layer of PTFE, which leads the leakage current to half of its initial value. The maximum power density and maximum energy density procured at 12 V were 3.87 mW/cm^2 and 204.5 μJ/cm^2, respectively. These results were achieved for only one mercury droplet of 30μL and mechanical energy of 2 Hz. FOM has been evaluated which indicates a significant improvement in energy harvesting over previous methods. An array of conducting droplets will boost up the harvesting of low-frequency mechanical vibrational energy.

References

1. Kumar A, Kiran R, Kumar S, Chauhan VS, Kumar R, Vaish R (2018) A comparative numerical study on piezoelectric energy harvester for self-powered pacemaker application. Glob Challenges 2:1700084
2. Kumar S, Singh D, Kumar R, Jain SC (2021) No-wear vibration energy harvester based on a triboelectric mechanism. J Electron Mater 1–14
3. Krupenkin T, Taylor JA (2011) Reverse electrowetting as a new approach to high-power energy harvesting. Nat Commun 2:1–8. https://doi.org/10.1038/ncomms1454
4. Moon JK, Jeong J, Lee D, Pak HK (2013) Electrical power generation by mechanically modulating electrical double layers. Nat Commun 4:1486–1487. https://doi.org/10.1038/ncomms2485
5. Hsu TH, Manakasettharn S, Taylor JA, Krupenkin T (2015) Bubbler: a novel ultra-high power density energy harvesting method based on reverse electrowetting. Sci Rep 5:1–13. https://doi.org/10.1038/srep16537
6. Yang H, Hong S, Koo B, Lee D, Kim YB (2017) High-performance reverse electrowetting energy harvesting using atomic-layer-deposited dielectric film. Nano Energy 31:450–455. https://doi.org/10.1016/j.nanoen.2016.11.006
7. Liu Z, EL, Ya J, Xin Y (2009) Growth of ZnO nanorods by aqueous solution method with electrodeposited ZnO seed layers. Appl Surf Sci 255:6415–6420. https://doi.org/10.1016/j.apsusc.2009.02.030
8. Bramantyo A, Poespawati NR, Kenji M (2016) Optimization of ZnO seed layer for growth of vertically aligned ZnO nanorods on glass surface. 4:011103. https://doi.org/10.7567/jjapcp.4.011103
9. Sharma SK, Rammohan A, Sharma A (2010) Templated one step electrodeposition of high aspect ratio n-type ZnO nanowire arrays. J Colloid Interface Sci 344:1–9. https://doi.org/10.1016/j.jcis.2009.12.026
10. Wu J, Xia J, Lei W, Wang BP (2010) Electrowetting on ZnO nanowires. Appl Phys A Mater Sci Process 99:931–934. https://doi.org/10.1007/s00339-010-5697-x
11. Moon H, Cho SK, Garrell RL, Kim CJ (2002) Low voltage electrowetting-on-dielectric. J Appl Phys 92:4080–4087. https://doi.org/10.1063/1.1504171
12. Florentino HR, Galayko D, Freire RCS, Luciano BA, Florentino C (2011) Energy harvesting circuit using variable capacitor with higher performance. J Integr Circ Syst 6:68–74

13. Bhattacharya P, Komeda T, Park KH, Nishioka Y (1993) Comparative study of amorphous and crystalline (Ba, Sr)Tio_3 thin films deposited by laser ablation. Jpn J Appl Phys 32:4103–4106. https://doi.org/10.1143/JJAP.32.4103
14. Basset P, Galayko D, Paracha AM, Marty F, Dudka A, Bourouina T (2009) A batch-fabricated and electret-free silicon electrostatic vibration energy harvester. J Micromech Microeng 19. https://doi.org/10.1088/0960-1317/19/11/115025

Biomass Steam Gasification for Bio-hydrogen Production via Co_2 Capture

Sunil L. Narnaware and N. L. Panwar

1 Introduction

Energy security and environmental protection have reignited interest in green and clean energy sources such as solar energy, wind energy, biomass energy and others. Among these renewable energy sources, biomass is the natural source of carbon that can substitute fossil fuel with its abundant availability [1]. All three forms of energy fuels are possible to derive from biomass and can be utilized for both heat and power generation [2]. Biomass is an environment-friendly renewable energy source as it contains less sulphur, has CO_2 neutral nature or lower CO_2 emissions and available in huge quantity and has great potential to produce bio-hydrogen [3, 4]. Hydrogen is the clean energy carrier with very less effect on the environment as it does not produce CO_2 emissions like other fossil fuels and makes an important fuel to be used in internal combustion (IC) engines and fuel cell technology. Combustion, pyrolysis and gasification are routes used for the thermal conversion of biomass. Among the thermal conversion technologies such as combustion, pyrolysis and gasification, gasification has the advantage to give higher thermal efficiency to produce gaseous fuel. Biomass gasification is an eco-friendly energy technology that has a lot of potential for sustainable energy development globally and can help to reduce our reliance on fossil fuels. Renewable hydrogen can be produced through biomass gasification process which has high thermal efficiency, high rate for carbon conversion and can adapt different variety of fuels [3, 5].

Biomass gasification is defined as a thermal conversion of biomass fuel into a low-energy product in gaseous form through a partial oxidation at high temperatures. The gaseous product, known as producer gas or syngas, is a mixture of combustible

S. L. Narnaware (✉) · N. L. Panwar
Department of Renewable Energy Engineering, College of Technology and Engineering, Maharana Pratap University of Agriculture and Technology, Udaipur 313001, India
e-mail: narnawaresunil@gmail.com

D. Sharma and S. Roy (eds.), *Emerging Trends in Energy Conversion and Thermo-Fluid Systems*, Lecture Notes in Mechanical Engineering,
https://doi.org/10.1007/978-981-19-3410-0_2

Table 1 Performance of gasification process for hydrogen production

Particulars	Gasification medium		
	Air	Oxygen	Steam
Syngas heating value, MJ/Nm^3	4–6	10–15	10–18
Reaction temp., °C	900–1100	1000–1400	700–1200
Gas compositions	CO: 20% H_2: 15% CH_4: 2% CO_2: 15% N_2: 48%	CO: 40% H_2: 40% CO_2: 20%	CO: 25% H_2: 40% CH_4: 8% CO_2: 25% N_2: 2%
H_2: CO	0.75	1	1
Cost	Cheap	Costly	Medium

gases such as carbon monoxide (CO), hydrogen (H_2) and methane (CH_4), as well as non-combustible gases such as carbon dioxide (CO_2) and nitrogen (N_2) [6, 7]. As a gasification agent, the air is mostly the preferred media for industrial application as it required lower investment and provides stable and simple operation. However, because of the significant dilution of nitrogen, using air produces syngas which has lower heating value (LHV) ranging within 4–6 MJ/Nm^3. Other gasification media such as oxygen or steam as depicted in Table 1, if used generates syngas of medium heating value between 10 and 18 MJ/Nm^3 but has the disadvantage of higher investment making the process more complex [8–10].

Biomass steam gasification using is regarded as a technically feasible and attractive process for producing H_2-rich syngas which provides the highest stoichiometric yield of hydrogen [11, 12]. The technology can satisfy the future need for large-scale hydrogen production without adverse impact on the environment [13, 14]. A fluidized bed gasifier (Fig. 1) is considered a promising reactor for hydrogen production through steam gasification as they provide several advantages such as wide fuel adaptability, good heat and mass transfer and high carbon conversion [15, 16].

2 Application of H_2 Enriched Syngas

Producer gas or syngas provides flexibility in the application for power generation or liquid fuel production through different intermediate conversion technologies. The use of syngas for power generation using an internal combustion (IC) engine or gas turbine is one of the popular applications [17, 18]. Fuel cell technology is another advanced application of syngas having higher hydrogen content. Syngas can be used for more advanced applications such as fuel cells for power generation after meeting the purity requirement. The fuel cells like solid oxide fuel cell (SOFC) and molten carbonate fuel cell (MCFC) have exhibited good performance for using syngas as fuel [19, 20]. Fischer–Tropsch synthesis can be used to derive the liquid fuel using

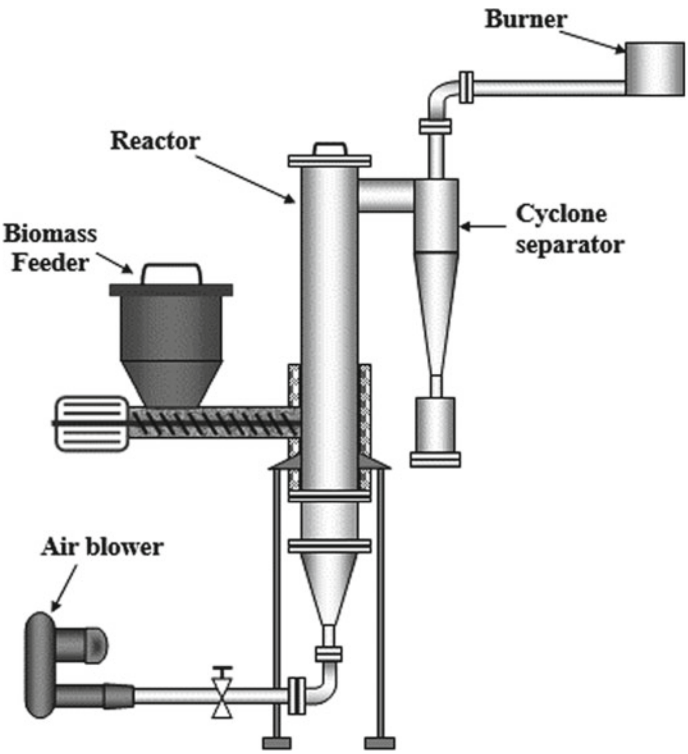

Fig. 1 Fluidized bed gasifier

syngas as a primary source [21, 22]. Methanol and dimethyl ether are also produced using syngas [23, 24].

3 Steam Gasification Mechanism

Biomass gasification uses steam as gasification agent, operates at the temperature between 600 and 800 °C and triggers the water gas shift (WGS) reaction (Eq. 1). WGS reaction is responsible for more hydrogen generation, and at the same time, steam promotes tar conversion through the cracking and reforming process (Eq. 2) which further enhances the concentration of hydrogen and carbon dioxide [25, 26]. However, the thermodynamic equilibrium in steam gasification put the restriction to the hydrogen content up to 50% on volumetric basis and contains major gases associated with carbon such as CO, CO_2 and CH_4 [27, 28]. Water–gas shift (WGS) reaction consumes part of CO decreasing its concentration [29]. The initial cracking of the C=O functional group, the WGS reaction and the reforming of pyrolytic volatiles by steam are the major cause for the increase in carbon dioxide concentration [28].

WGS reaction

$$CO + H_2O \leftrightarrow CO_2 + H_2 \qquad -36\frac{kJ}{mol} \tag{1}$$

Steam reforming of hydrocarbon

$$C_xH_y + xH_2O \leftrightarrow xCO + (x + 0.5y)H_2 \tag{2}$$

4 Calcium Oxide as CO_2 Sorbent

In-situ capture of carbon dioxide generated during the steam gasification of biomass can enhance the overall volumetric concentration of the hydrogen. The solid-based sorbent is best suited for the absorption of carbon dioxide because of high absorption efficiency at higher temperature [30]. Steam gasification enhanced with CO_2 absorption using calcium oxide (CaO) provides a single-step solution for hydrogen production as in-situ CO_2 removal shift the thermodynamic equilibrium of WGS reaction which benefits in higher H_2 concentration with high final gas purity (>99%) and lower traces of CO and CH_4 [5, 31–33]. CaO a metal oxide works effectively at higher temperature to capture CO_2 and provides better thermodynamic and kinetic efficiencies [34]. The experimental study by Li et al. revealed that at the lower temperature (550–650 °C), CaO shows a better affinity towards the absorption of CO_2 in order to increase the overall concentration of hydrogen and reduces the CO and CO_2 content. At the higher temperatures (700–800 °C), pyrolytic volatiles get effectively cracked and also support the volatile and char gasification along with WGS reaction to produce more H_2 [28]. The amount of CaO used, i.e. CaO-to-biomass ratio also affects the hydrogen generation. It was found that when ratio of CaO/biomass was increased to 2 from 0, the concentration of H_2 was enhanced from 23.29 to 54.54%, whereas the yield of H_2 was improved by 2.7 fold [32]. A similar observation was reported by Han et. al for the gasification of the sawdust when ratio of CaO/ biomass improved from 0 to 2, an increment in H_2 concentration was observed from initial concentration of 34.5% to final concentration of 59.1%, whereas the yield of H_2 was also increased from 41 to 59 g per unit kilogram of biomass [35]. Higher reaction pressure also has a beneficial influence on H_2 production, as reported by some studies [36, 37].

5 Calcium Looping

Calcium looping (Fig. 2) is a technique that uses a chemical process to capture CO_2 effectively. It is a single-stage process for reforming tar and CO_2 capture in in-situ mode using the catalytic bed. This method is called as sorption enhanced reforming (SER). The operation temperature during gasification (carbonation) varies between 600 and 700 °C while it is >800 °C in combustion reactor (calcination) [38, 39]. The process involves an exothermic reaction of carbonation (Eq. 3) between CaO and CO_2 to form the calcium carbonate ($CaCO_3$), and CaO is regenerated as $CaCO_3$ undergoes the endothermic calcination process (Eq. 4). [40–42]. Calcium looping helps to reduce the overall material requirement and supplies heat for the regeneration process of CaO released during exothermic combustion [27, 38, 43].

$$CaO + CO_2 \rightarrow CaCO_3 \quad \Delta H_R^{650} = -170\frac{kJ}{mol} \tag{3}$$

$$CaCO_3 \rightarrow CaO + CO_2 \quad \Delta H_R^{850} = -167\frac{kJ}{mol} \tag{4}$$

The performance CaO as a CO_2 absorbent for gasification of different biomass such as sawdust, corn stalk and rice straw as shown in Fig. 3 [28, 32, 44–46]. CaO can be used as a bed material or by maintaining a certain ratio of CaO to biomass during the gasification process. It can be seen that the hydrogen content was almost more than 50%vol. with a lesser concentration of $CO_{2.}$ CaO works as an effective absorbent for CO_2 which is formed during the steam gasification and maintains the high concentration of hydrogen in the syngas.

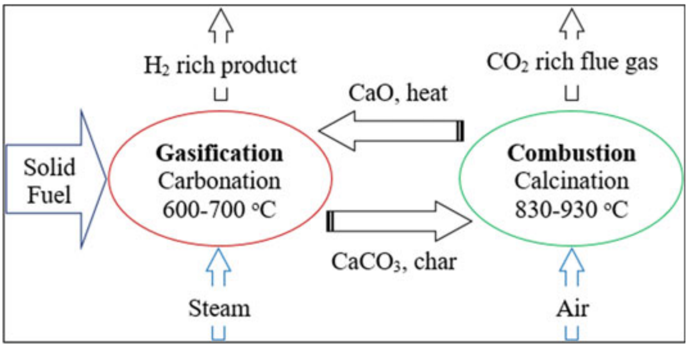

Fig. 2 Calcium looping process

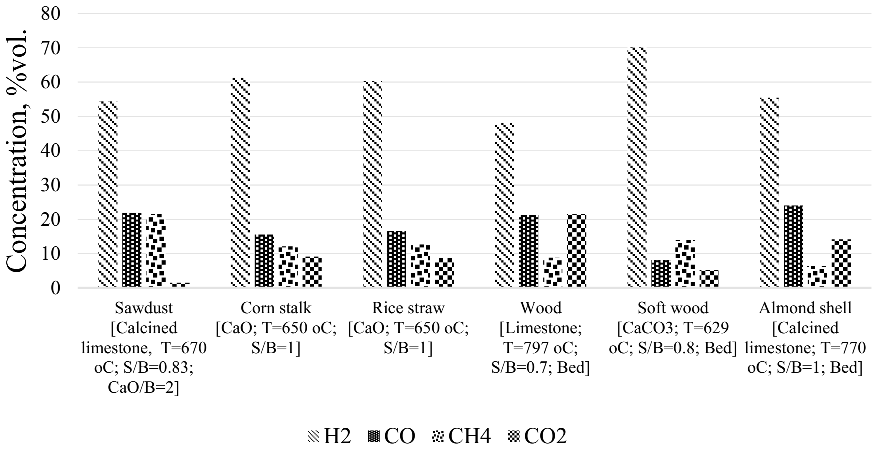

Fig. 3 Gas composition using calcium oxide (CaO)

6 Catalytic Activity of CaO

CaO has been reported to have catalytic properties when it comes into contact with the tar components, assisting in increasing the H_2 concentration by decomposing tar. The presence of some minerals such as dolomite and limestone in CaO possesses catalytic properties which help in tar cracking [47, 48]. A comparative study between sand and CaO showed that the concentration of tar was reduced to 26.71 g/Nm^3 from 81.28 g/Nm^3 when sand bed was replaced with CaO [49]. The tar species belonging to class 1 and class 4 were found to be reduced in concertation by 14% and 7%, respectively reducing the overall tar content by 67% [49]. This shows that apart from acting as CO_2 absorbent, CaO also works as a catalyst.

7 Conclusion

Hydrogen is regarded as a vital energy carrier for fulfilling future energy needs. Biomass steam gasification provides a promising alternative to producing hydrogen from biomass resources. However, the conventional steam gasification process is constrained by limited H_2 concentration and more CO_2 generation. Calcium oxide, used in steam gasification, can act efficiently as a CO_2 absorbent and also shows catalytic properties that help in the destruction of the pyrolytic volatiles and tar. Hydrogen-enriched syngas can be used in a variety of traditional technologies, such as IC engines or gas turbines, as well as in more advanced energy conversion technologies, such as power generation via fuel cells or Fischer–Tropsch synthesis for liquid fuel. It is also a suitable fuel to obtain some chemicals such as methanol and dimethyl ether (DME).

References

1. Balat M, Ayar G (2005) Biomass energy in the world, use of biomass and potential trends. Energy Sources 27:931–940. https://doi.org/10.1080/00908310490449045
2. Huber GW, Iborra S, Corma A (2006) Synthesis of transportation fuels from biomass: chemistry, catalysts, and engineering
3. Kalinci Y, Hepbasli A, Dincer I (2009) Biomass-based hydrogen production: a review and analysis
4. Tock L, Maréchal F (2012) Co-production of hydrogen and electricity from lignocellulosic biomass: Process design and thermo-economic optimization. Energy 45:339–349. https://doi.org/10.1016/j.energy.2012.01.056
5. Fermoso J, Rubiera F, Chen D (2012) Sorption enhanced catalytic steam gasification process: a direct route from lignocellulosic biomass to high purity hydrogen. Energy Environ Sci 5:6358–6367. https://doi.org/10.1039/c2ee02593k
6. Basu P (2010) Biomass gasification and pyrolysis. Elsevier Inc
7. Narnaware SL, Srivastava NSL, Vahora S (2017) Gasification: an alternative solution for energy recovery and utilization of vegetable market waste. Waste Manag Res. 35:276–284. https://doi.org/10.1177/0734242X16679257
8. Lv PM, Xiong ZH, Chang J, Wu CZ, Chen Y, Zhu JX (2004) An experimental study on biomass air-steam gasification in a fluidized bed. Bioresour Technol 95:95–101. https://doi.org/10.1016/j.biortech.2004.02.003
9. Fu Q, Huang Y, Niu M, Yang G, Shao Z (2014) Experimental and predicted approaches for biomass gasification with enriched air-steam in a fluidised bed. Waste Manag Res 32:988–996. https://doi.org/10.1177/0734242X14552555
10. Campoy M, Gómez-Barea A, Villanueva AL, Ollero P (2008) Air-steam gasification of biomass in a fluidized bed under simulated autothermal and adiabatic conditions. Ind Eng Chem Res 47:5957–5965. https://doi.org/10.1021/ie800220t
11. Parthasarathy P, Narayanan KS (2014) Hydrogen production from steam gasification of biomass: influence of process parameters on hydrogen yield—a review
12. Delgado J, Aznar MP, Corella J (1997) Biomass gasification with steam in fluidized bed: effectiveness of CaO, MgO, and CaO-MgO for hot raw gas cleaning. Ind Eng Chem Res 36:1535–1543. https://doi.org/10.1021/ie960273w
13. Nipattummakul N, Ahmed II, Gupta AK, Kerdsuwan S (2011) Hydrogen and syngas yield from residual branches of oil palm tree using steam gasification. Int J Hydrogen Energy 36:3835–3843. https://doi.org/10.1016/j.ijhydene.2010.04.102
14. Corella J, Toledo JM, Molina G (2008) Biomass gasification with pure steam in fluidised bed: 12 variables that affect the effectiveness of the biomass gasifier. Int J Oil Gas Coal Technol 1:194–207. https://doi.org/10.1504/IJOGCT.2008.016739
15. Dutta A, Acharya B, Basu P (2009) Chemical looping gasification of biomass for hydrogen enriched gas production with in-process carbon-dioxide capture. In: Proceedings of the 20th international conference on fluidized bed combustion
16. García L, Salvador ML, Arauzo J, Bilbao R (1999) Catalytic steam gasification of pine sawdust. Effect of catalyst weight/biomass flow rate and steam/biomass ratios on gas production and composition. Energy Fuels 13:851–859. https://doi.org/10.1021/ef980250p
17. Dasappa S, Sridhar HV (2013) Performance of a diesel engine in a dual fuel mode using producer gas for electricity power generation. Int J Sustain Energy 32:153–168. https://doi.org/10.1080/14786451.2011.605945
18. Rabou LPLM, Grift JM, Conradie RE, Fransen S (2008) Micro gas turbine operation with biomass producer gas and mixtures of biomass producer gas and natural gas. Energy Fuels 22:1944–1948. https://doi.org/10.1021/ef700630z
19. Hofmann P, Panopoulos KD, Fryda LE, Schweiger A, Ouweltjes JP, Karl J (2008) Integrating biomass gasification with solid oxide fuel cells: effect of real product gas tars, fluctuations and particulates on Ni-GDC anode. Int J Hydrogen Energy 33:2834–2844. https://doi.org/10.1016/j.ijhydene.2008.03.020

20. Iaquaniello G, Mangiapane A (2006) Integration of biomass gasification with MCFC. Int J Hydrogen Energy 31:399–404. https://doi.org/10.1016/j.ijhydene.2005.09.010
21. Riedel T, Claeys M, Schulz H, Schaub G, Nam SS, Jun KW, Choi MJ, Kishan G, Lee KW (1999) Comparative study of Fischer-Tropsch synthesis with H_2/CO and H_2/CO_2 syngas using Fe- and Co-based catalysts. Appl Catal A Gen 186:201–213. https://doi.org/10.1016/S0926-860X(99)00173-8
22. dos Santos RG, Alencar AC (2020) Biomass-derived syngas production via gasification process and its catalytic conversion into fuels by Fischer Tropsch synthesis: a review. Int J Hydrogen Energy 45:18114–18132. https://doi.org/10.1016/j.ijhydene.2019.07.133
23. Giuliano A, Freda C, Catizzone E (2020) Techno-economic assessment of bio-syngas production for methanol synthesis: a focus on the water–gas shift and carbon capture sections. Bioengineering 7:1–19. https://doi.org/10.3390/bioengineering7030070
24. Nakyai T, Saebea D (2019) Exergoeconomic comparison of syngas production from biomass, coal, and natural gas for dimethyl ether synthesis in single-step and two-step processes. J Clean Prod 241:118334. https://doi.org/10.1016/j.jclepro.2019.118334
25. Franco C, Pinto F, Gulyurtlu I, Cabrita I (2003) The study of reactions influencing the biomass steam gasification process. Fuel 82:835–842. https://doi.org/10.1016/S0016-2361(02)00313-7
26. Gao N, Li A, Quan C, Gao F (2008) Hydrogen-rich gas production from biomass steam gasification in an updraft fixed-bed gasifier combined with a porous ceramic reformer. Int J Hydrogen Energy 33:5430–5438. https://doi.org/10.1016/j.ijhydene.2008.07.033
27. Florin NH, Harris AT (2008) Enhanced hydrogen production from biomass with in situ carbon dioxide capture using calcium oxide sorbents
28. Li B, Yang H, Wei L, Shao J, Wang X, Chen H (2017) Hydrogen production from agricultural biomass wastes gasification in a fluidized bed with calcium oxide enhancing. Int J Hydrogen Energy 42:4832–4839. https://doi.org/10.1016/j.ijhydene.2017.01.138
29. Shen L, Gao Y, Xiao J (2008) Simulation of hydrogen production from biomass gasification in interconnected fluidized beds. Biomass Bioenerg 32:120–127. https://doi.org/10.1016/j.biombioe.2007.08.002
30. Alvarez D, Peña M, Borrego AG (2007) Behavior of different calcium-based sorbents in a calcination/carbonation cycle for CO_2 capture. Energy Fuels 21:1534–1542. https://doi.org/10.1021/ef060573i
31. Harrison DP (2009) Calcium enhanced hydrogen production with CO_2 capture. In: Energy procedia
32. Acharya B, Dutta A, Basu P (2010) An investigation into steam gasification of biomass for hydrogen enriched gas production in presence of CaO. Int J Hydrogen Energy 35:1582–1589. https://doi.org/10.1016/j.ijhydene.2009.11.109
33. Sisinni M, Carlo AD, Bocci E, Micangeli A, Naso V (2013) Hydrogen-rich gas production by sorption enhanced steam reforming of woodgas containing TAR over a commercial Ni catalyst and calcined dolomite as CO_2 sorbentx. Energies 6:3167–3181. https://doi.org/10.3390/en6073167
34. Feng B, An H, Tan E (2007) Screening of CO_2 adsorbing materials for zero emission power generation systems. In: Energy and fuels
35. Han L, Wang Q, Yang Y, Yu C, Fang M, Luo Z (2011) Hydrogen production via CaO sorption enhanced anaerobic gasification of sawdust in a bubbling fluidized bed. Int J Hydrogen Energy 36:4820–4829. https://doi.org/10.1016/j.ijhydene.2010.12.086
36. Han L, Wang Q, Luo Z, Rong N, Deng G (2013) H2 rich gas production via pressurized fluidized bed gasification of sawdust with in situ CO_2 capture. Appl Energy 109:36–43. https://doi.org/10.1016/j.apenergy.2013.03.035
37. Guan J, Wang Q, Li X, Luo Z, Cen K (2007) Thermodynamic analysis of a biomass anaerobic gasification process for hydrogen production with sufficient CaO. Renew Energy 32:2502–2515. https://doi.org/10.1016/j.renene.2007.01.002
38. Fuchs J, Schmid JC, Benedikt F, Müller S, Hofbauer H, Stocker H, Kieberger N, Bürgler T (2018) The impact of bed material cycle rate on in-situ CO_2 removal for sorption enhanced reforming of different fuel types. Energy 162:35–44. https://doi.org/10.1016/j.energy.2018.07.199

39. Di Felice L, Courson C, Jand N, Gallucci K, Foscolo PU, Kiennemann A (2009) Catalytic biomass gasification: simultaneous hydrocarbons steam reforming and CO_2 capture in a fluidised bed reactor. Chem Eng J 154:375–383. https://doi.org/10.1016/j.cej.2009.04.054
40. Abanades JC, Anthony EJ, Wang J, Oakey JE (2005) Fluidized bed combustion systems integrating CO_2 capture with CaO. Environ Sci Technol 39:2861–2866. https://doi.org/10.1021/es0496221
41. Hughes RW, Lu DY, Anthony EJ, MacChi A (2005) Design, process simulation and construction of an atmospheric dual fluidized bed combustion system for in situ CO_2 capture using high-temperature sorbents. In: Fuel processing technology
42. Doranehgard MH, Samadyar H, Mesbah M, Haratipour P, Samiezade S (2017) High-purity hydrogen production with in situ CO_2 capture based on biomass gasification. Fuel 202:29–35. https://doi.org/10.1016/j.fuel.2017.04.014
43. Hawthorne C, Dieter H, Bidwe A, Schuster A, Scheffknechta G, Unterberger S, Käß M (2011) CO_2 capture with CaO in a 200 kWth dual fluidized bed pilot plant. In: Energy procedia
44. Benedikt F, Fuchs J, Schmid JC, Müller S, Hofbauer H (2017) Advanced dual fluidized bed steam gasification of wood and lignite with calcite as bed material. Korean J Chem Eng 34:2548–2558. https://doi.org/10.1007/s11814-017-0141-y
45. Schmid JC, Fuchs J, Benedikt F, Mauerhofer AM, Müller S, Hofbauer H, Stocker H, Kieberger N, Bürgler T (2017) Sorption enhanced reforming with the novel dual fluidized bed test plant at tu wien. In: European biomass conference and exhibition proceedings
46. Rapagnà S, Jand N, Kiennemann A, Foscolo PU (2000) Steam-gasification of biomass in a fluidised-bed of olivine particles. Biomass Bioenerg 19:187–197. https://doi.org/10.1016/S0961-9534(00)00031-3
47. Han L, Wang Q, Ma Q, Yu C, Luo Z, Cen K (2010) Influence of CaO additives on wheat-straw pyrolysis as determined by TG-FTIR analysis. J Anal Appl Pyrolysis 88:199–206. https://doi.org/10.1016/j.jaap.2010.04.007
48. Hanaoka T, Yoshida T, Fujimoto S, Kamei K, Harada M, Suzuki Y, Hatano H, Yokoyama SY, Minowa T (2005) Hydrogen production from woody biomass by steam gasification using a CO_2 sorbent. Biomass Bioenerg 28:63–68. https://doi.org/10.1016/j.biombioe.2004.03.009
49. Udomsirichakorn J, Basu P, Salam PA, Acharya B (2013) Effect of CaO on tar reforming to hydrogen-enriched gas with in-process CO_2 capture in a bubbling fluidized bed biomass steam gasifier. Int J Hydrogen Energy 38:14495–14504. https://doi.org/10.1016/j.ijhydene.2013.09.055

Numerically Analysis of Wave Force on a Moving Thin Plate in the Surging Direction

Deepak Kumar Singh, Surendra Singh Yadav, and Pradip Deb Roy

1 Introduction

The numerical analysis is required to study the wave force and wave behavior in the vicinity of a moving surface-piercing thin rectangular plate to develop a new type of wave energy converter. Nonlinear wave–body interactions are becoming increasingly important in various ocean engineering. Many researchers used multiple methods to study wave motion, including theoretical calculations, computer simulations, and empirical experiments. Various studies were carried out at different times by various researchers regarding the wave–body interaction. Some researchers conducted studies numerically and experimentally on cylinders, rectangular plates, ellipse plates, etc. Nonlinear scattering by a submerged plate has been the subject of recent research. Brossard and Chagdali [1] investigated the creation of higher harmonics by waves traveling over a submerged plate. Probes were utilized to distinguish between harmonic waves and bound based on the Doppler change. For higher harmonic modes, minimal submergence has been found to facilitate energy transfer. Brossard et al. [2] investigated the nonlinear wave's resonant activity around a submerged plate by analyzing nonlinear wave scattering by a submerged plate. In a computational and experimental study, Liu et al. [3] examined the interactions between nonbreaking waves and a submerged plate. Their results, which were predicted using the DBIE technique, match the experimental data well.

Hayatdavoodi and Ertekin [4, 5] explored the correlation between a rigid plate and nonlinear waves using Green-Naghdi equations. On the plate, measured the wave force. There are numerous studies on the effects of periodic waves on plates. Still, none of them examines nonlinear wave conditions that affect coastal structures in shallow water, except for Hayatdavoodi and Ertekin's [5] work. Porter [6] used

D. K. Singh · S. S. Yadav · P. D. Roy (✉)
Department of Mechanical Engineering, NIT, Silchar, Assam 788010, India
e-mail: pdebroy@mech.nits.ac.in

D. Sharma and S. Roy (eds.), *Emerging Trends in Energy Conversion and Thermo-Fluid Systems*, Lecture Notes in Mechanical Engineering,
https://doi.org/10.1007/978-981-19-3410-0_3

linear potential theory to investigate waves scattering by thin plates in 2- and 3-D. He examined that how the waves produced if the plates were forced to move. Rey and Touboul [7] experimentally worked on the impact of currents on wave scattering by a submerged horizontal fixed plate, while Lin et al. [8] looked at it numerically. They found that there was no heaving motion occurred when the waves struck the plate. Miyata et al. [9] and Malavasi and Guadagnini [10] worked on the effect of elevation of the object above the channel floor and found that as the object reached the free surface, the forces acting on it decreased.

The dispersion of waves by a submerged plate has been studied extensively using linear wave theory. Based on the longwave approximation, Siew and Hurley [11] considered a thin plate. They used matched asymptotic expansions to solve the Laplace equation under the assumption of linear condition to calculate the velocity potential and the reflection and transmission coefficients. Patarapanich [12] later gave the final shape of the wave forces. This theory is known as the Longwave Approximation. Patarapanich [12] discovered that the coefficient of reflection oscillates with the plate length and wavelength ratio due to energy flux through various regions around the plate using the Siew and Hurley [11] method. Patarapanich and Cheong [13] numerically as well as experimentally studied the regular/irregular wave transmission and reflection by submerged plate in fluid. They calculated the occurrence conditions for the wave's minimum transmission over a submerged plate.

The present paper numerically investigated the drag force on a moving surface-piercing thin rectangular plate under various wave steepness conditions. Second-order stokes wave theory is used in intermediate water depth to analyze the problem. In this study, numerical investigations were done by ANSYS Fluent commercial software in a 2-D NWT. The Navier–Stokes equations are solved using the finite volume method (FVM) to comprehend free surface flow. The variation of drag force and drag coefficient versus the time has been shown graphically. Besides these, other investigations such as velocity vectors and vortices around the plate are also studied in the paper.

2 Numerical Model

Consider a thin rectangular plate of size 0.15 m height and 0.001 m thickness suspended vertically in a NWT as shown in Fig. 1 along with boundary conditions. The dimensions of the tank are length $l_x = 10$ m and height $l_z = 1$ m. The inflow method is applied for the wave generation at the inlet boundary. The plate moves in the surge direction due to incoming waves. The top boundary is defined as a pressure outlet that is considered open to the atmosphere. No-slip wall conditions are imposed on the bottom and right face of the computational domain. The velocity of fluid near the solid wall is zero due to the no-slip boundary condition. Cartesian coordinates are used in the x–z plane. The x-axis is determined positively in the direction of the wave propagation, and the z-axis is oriented vertically from the still water level

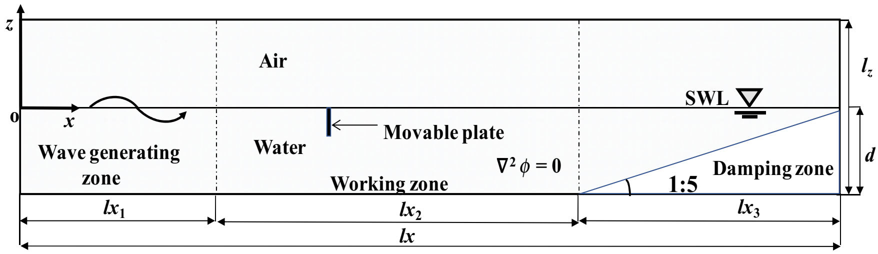

Fig. 1 Definition sketch of a moving surface–piercing thin plate in a numerical wave tank

(SWL) upward, which is measured positive upwards. The influence of *y*-direction is not taken due to consideration of the 2-D domain.

The computational domain has divided into three section: (a) wave generating zone ($l_{x1} = 2$ m), (b) working zone ($l_{x2} = 6$ m), and (c) damping zone ($l_{x3} = 2$ m). The overall size of the NWT is $l_x = 10$ m and $l_z = 1$ m. In this study, the inflow method generates second-order stokes wave of time period $T = 1.1658$ s and wavelength $L = 1.8482$ m. The structure grid has been utilized to discretize the computational domain. Implementing a sloping beach as a damping zone at the end of the NWT was important for preventing the wave reflection from the end wall; otherwise, waves reflect from the end of the tank and the simulation disorders. The beach of 1:5 slope has been formed in the damping zone. Total work has been simulated with a system specification of Intel(R) Xeon(R) W-2155CPU@3.30 GHz 3.31 GHz processor and a 64.0 GB RAM. The simulation time steps, time step size, and the maximum iteration have been selected as 5000, 0.01 s, and 20, respectively. The Courant number is set at 0.25. Wave parameters are used in this investigation, shown in Table 1, and the approximate mesh sizes are shown in Table 2 in a different zone.

Table 1 The parameters of the waves employed in this investigation are as follows

Test	Tank length l_x(m)	Water depth d(m)	Wave length L(m)	Wave height H(m)	Wave steepness (H/L)
1	10	0.4	1.8482	0.05	0.0271
2	10	0.4	1.8482	0.06	0.0325
3	10	0.4	1.8482	0.07	0.0379

Table 2 Different mesh size

Zone	Δx	Δz
Wave generation zone	0.0100	0.0050
Working zone	0.0075	0.0050
Damping zone	0.18441	0.0049

2.1 Governing Equations

The propagation of water waves in a NWT is modeled using commercial ANSYS Fluent software based on the FVM. The flow behavior is assumed to be irrotational, without surface tension, and with atmospheric pressure $p_a = 0$. The governing equations pertaining to 2-D NWT are given as:

Continuity equation:

$$\frac{\partial u}{\partial x} + \frac{\partial w}{\partial z} = 0 \tag{1}$$

x-momentum Equation:

$$\frac{\partial u}{\partial t} + u\frac{\partial u}{\partial x} + w\frac{\partial u}{\partial z} = -\frac{1}{\rho}\frac{\partial p}{\partial x} + v\left[\frac{\partial^2 u}{\partial x^2} + \frac{\partial^2 u}{\partial z^2}\right] \tag{2}$$

z-momentum Equation:

$$\frac{\partial w}{\partial t} + u\frac{\partial w}{\partial x} + w\frac{\partial w}{\partial z} = -\frac{1}{\rho}\frac{\partial p}{\partial z} + v\left[\frac{\partial^2 w}{\partial x^2} + \frac{\partial^2 w}{\partial z^2}\right] \tag{3}$$

where t, p, ρ, and ν are the time (s), pressure (Pa), density (kg m^{-3}), and the kinetic viscosity (m^2 s^{-1}), respectively. u and w are the velocity in x and z directions (m s^{-1}).

In this analysis, the VOF method (Hirt and Nichols [14]) is used to model the interface of two fluids. The following equations are employed to determine α_q:

$$\frac{\partial \alpha_{\mathrm{q}}}{\partial t} + \nabla \cdot \left(\alpha_{\mathrm{q}} \overline{V}\right) = 0 \tag{4}$$

$$\sum_{q=1}^{2} \alpha_{\mathrm{q}} = 1 \tag{5}$$

where $\overline{V}$ denotes the velocity vector. The following formula is used to determine the mixture's density depending on the volume fraction:

$$\rho = \alpha_{\mathrm{q}}\rho_{\mathrm{w}} + \left(1 - \alpha_{\mathrm{q}}\right)\rho_{\mathrm{a}} \tag{6}$$

where $\rho_{\mathrm{a}} = 1.225$ kg/m^3 and $\rho_{\mathrm{w}} = 998.2$ kg/m^3 are the air and water density, respectively.

The drag coefficient calculated as follows:

$$C_d = \frac{F_x}{\frac{1}{2}\rho A u^2} \tag{7}$$

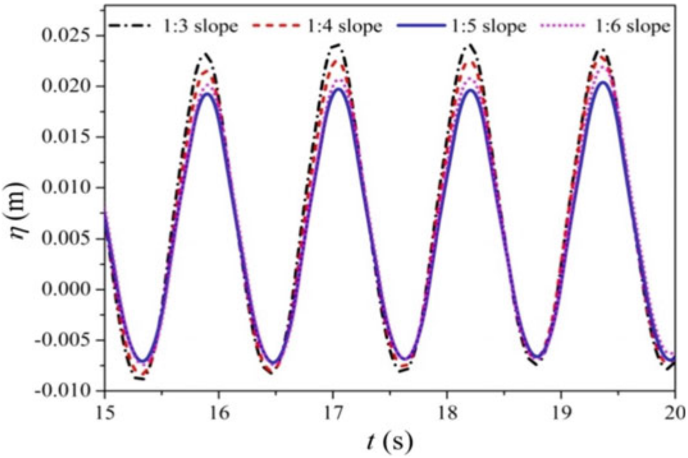

Fig. 2 Various beach slopes have different surface elevations at $x = 7$ m

where C_d is drag coefficient, F_x is the drag force (N), and A is projected area of thin plate (m^2).

3 Geometry of Damping

Damping is required at the NWT's right end to prevent boundary reflection by the wave. Different authors propose different methods in their literature for the absorption of incident waves. Implementing a beach considers by several authors is one of the methods. Maguire [15] recommended beach slope 1:10 gives a better result. Finnegan and Goggins [16] suggested 1:5 is the optimal value after studying the beach slope between 1:3 and 1:6. Lal, and Elangovan [17] and Elangovan [18] recommended beach slope 1:3 gives better damping. However, we have analyze the beach slope for better damping between the range 1:3 to 1:6 and show that 1:5 gives better results. Figure 2 shows that the slope of 1:5 has a lesser wave height, indicating that it is better capable of absorbing waves. So a slope of 1:5 is recommended to limit wave reflection.

4 Validation Study

The present study verifies the accuracy of the flow behavior; a validation test has been conducted with the experimental result described by Gao [19]. The numerical data are assumed the same as that of the experimental data. Figure 3 depicts the surface elevation as a function of time at $x = 0.55$ m in the NWT. It has been observed from

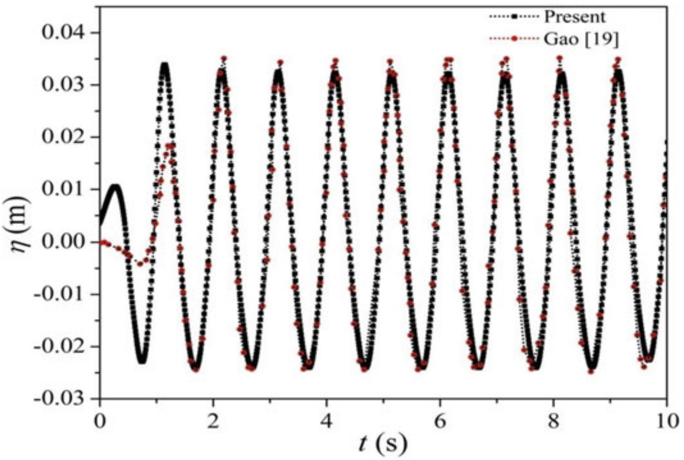

Fig. 3 Time-dependent surface elevation at $x = 0.55$ m

the figure that both results correspond well. The maximum and minimum errors of wave elevation between the numerical model and experimental model are 5.51% and 1.09%, respectively. Hence, based on the above discussion, the present simulation is appropriate for further study.

5 Result and Discussion

The paper presented to investigate the wave–structure interaction for a moving thin plate in intermediate water depth with a sloping beach has been simulated in a 2-D NWT. Velocity vectors and the drag coefficient around the plate are important studies in the flow field. The stokes wave approximation theory was used to complete the study at $d = 0.40$ m and $T = 1.1658$ s. Estimated results have been analyzed under various wave steepness condition, and Table 1 presents the study's wave parameters.

The drag coefficient (C_{d}) is plotted as a time function (t) under three-wave steepness (H/L) conditions, as depicted in Fig. 4. The drag coefficient has been calculated on the free surface using Eq. (7) at a flow time of 15.8–17.5 s to avoid the initial transient effects. The trends of drag coefficients are periodic, but the magnitudes are different. The drag coefficient value has shown a higher value for the $H/L =$ 0.0379, implying that the drag force on the plate at this H/L is maximum. It has also been shown that the solid black curve becomes slightly disorder between the time 16.88–17.25 s due to the effect nonlinearity at a lower value of wave steepness H/L $= 0.0271$.

The drag coefficient (C_{d}) as a function of H/L has been depicted in Fig. 5. The mean values of the C_{d}, 0.0015, 0.0017, and 0.0019, have been derived between the flow time (t) 15–50 s and plotted in Fig. 5 corresponding to each H/L 0.0271, 0.0325,

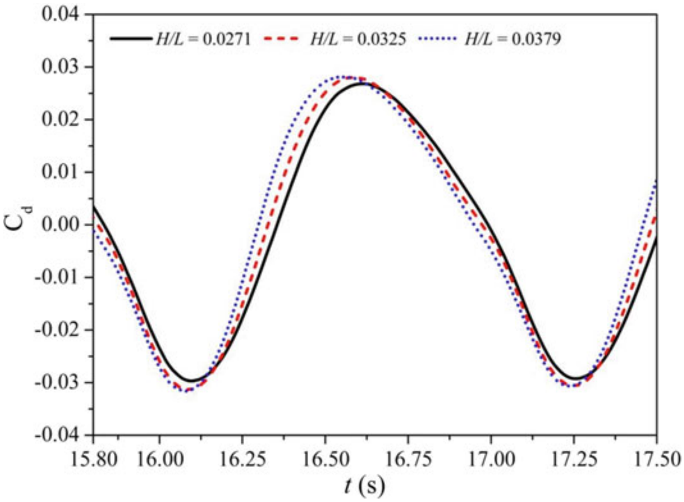

Fig. 4 Drag coefficient (C_d) vs time (t) on the plate for $T = 1.1658$ s and $d = 0.40$ m

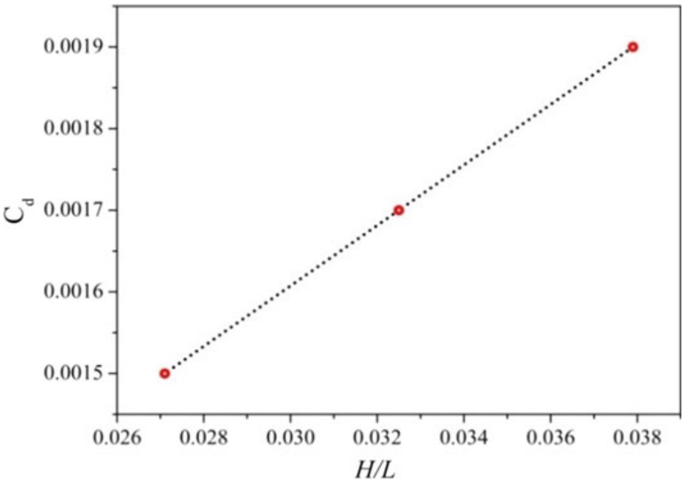

Fig. 5 Drag coefficient (C_d) versus wave steepness (H/L) on the plate for $T = 1.1658$ s and $d = 0.40$ m

and 0.0379. It has been shown from the figure that the C_d increases linearly with the rise of *H/L*.

Figure 6 depicts the plot between the drag force (F_x) on the plate and time (t) at three-wave steepness ($H/L = 0.0271$, 0.0325, and 0.0379) conditions. The graph is showing periodic. Initially, wave force on the plate increases to a maximum value between the time 16.10–16.6 s and then decreases from positive to negative. It has

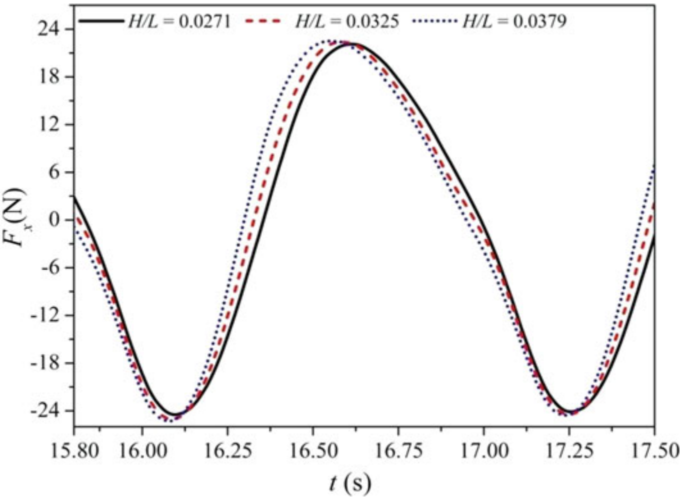

Fig. 6 Wave force (F_x) versus time (t) at $d = 0.40$ m and $T = 1.1658$ s and $z = 0$

been observed from Fig. 6 that wave force on the plate is very high for the *H/L* = 0.0379 compared to the *H/L* = 0.0271 and 0.0325.

Figure 7 shows the plot for one cycle of the velocity vector and vorticity fields around the plate at the surface-piercing position at $d = 0.40$ m and $T = 1.1658$ s. Figure 7 demonstrated the flow field for the wave steepness *H/L* = 0.0271 at different time $t = 16.35$–17.30 s. Figure 7a shows that vortex strength is generated at the left-bottom of the plate and is maximum at time $t = 16.35$ s, and then, vortex strength gradually decreases to zero at $t = 16.60$ s (Fig. 7(b)). This is because the drag force (F_x) on the plate at time $t = 16.35$ s is zero at this location, but the vortex velocity of the water particle is maximum. Due to this, the plate starts to move in the forward direction, and particle vortex velocity decreases gradually to zero. The force (F_x) on the plate reaches a maximum value equal to 20.20 N at $t = 16.60$ s. The loss of energy of the vortex velocity of water particle uses to move the plate in the forward direction with a speed of 0.2 m/s. It has found the maximum displacement of the plate is 4.55 m from its original position of 4.50 m. Further noticed in Fig. 7c, there is no vortex strength behind the plate at time $t = 16.90$ s when drag force (F_x) on the plate is 7.08 N. Figure 7d shows the maximum opposite force $F_x = -23.28$ N generated at time $t = 17.30$ s due to the maximum water particle velocity. And the plate moves in the backward direction with a speed of 0.09 m/s. Here, we have noticed that backward displacement of the plate is 0.047 m from the position of 4.55 m. The process is repeated, and the plate moves in this way forward and backward direction.

Figure 8 and 9 show the plot for one cycle of the velocity vector and vorticity fields around the plate for the wave steepness *H/L* = 0.0325 and 0.0379, respectively. Here, the physics of the motion of the plate is same as Fig. 7. Speed of the plate increases with the increases of wave steepness. The plate moves forward with a velocity of 0.27 m/s and returns with a velocity of 0.07 m/s for the wave steepness *H/L* = 0.0379

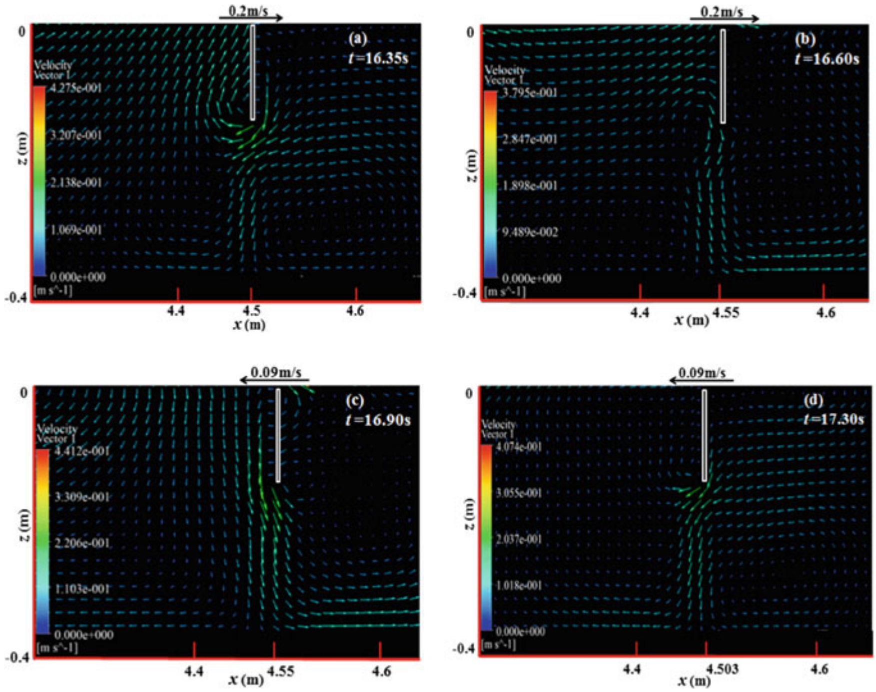

Fig. 7 Velocity vector distribution around the plate at $H/L = 0.0271$

(Fig. 9). Due to this, the plate moves in the forward direction 0.07 m and backward direction 0.038 m. Similarly, for the case of wave steepness $H/L = 0.0325$, the plate moves forward with a velocity of 0.24 m/s and returns with a velocity of 0.08 m/s (Fig. 8). Due to this, the plate moves in the forward direction 0.06 m and backward direction 0.042 m.

6 Conclusions

The present numerical model analyzes the flow behavior around the moving plate in intermediate water with a sloping beach. The plate moves in a surge direction due to incoming waves. Stokes wave theory is used to investigate the problem under three *H/L* conditions. The inflow velocity method and the Dirichlet boundary condition are used to generate the desired nonlinear waves in a viscous NWT. The numerical model is compared with the experimental model Gao [19]. It shows good consistency between numerical and experimental model results. Based on the above numerical modeling, our results support the following conclusions.

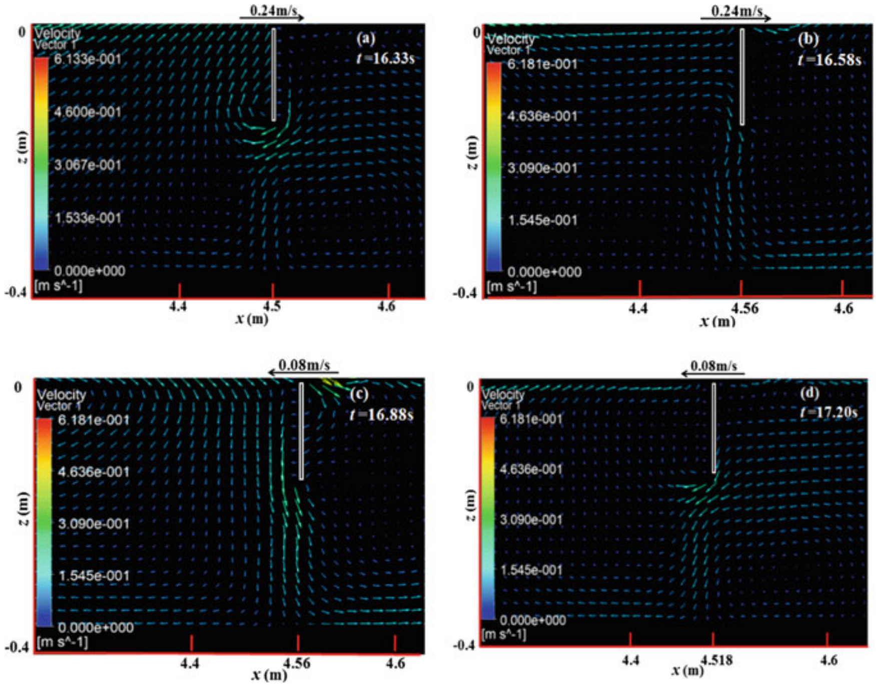

Fig. 8 Velocity vector distribution around the plate at $H/L = 0.0325$

- Drag coefficient (C_d) increases linearly with the H/L. The maximum force of the system is reached at $H/L = 0.0379$.
- Drag coefficient (C_d) is periodic with respect to time (t), and it is higher for the $H/L = 0.0379$, implying that the F_x on the plate is maximum at this wave steepness on the free surface.
- Drag force (F_x) is periodic with respect to time (t), and it is higher for the $H/L = 0.0379$, implying that the F_x on the plate is maximum at this wave steepness.
- Figure. 7a shows that vortex strength is maximum at $t = 16.35$ s when F_x on the plate is zero, but the vortex velocity of the water particle is maximum. At this time, plate does not start to move due to enough capability of wave force (F_x).
- Figure 7b shows that vortex strength is zero at $t = 16.60$ s when drag force (F_x) on the plate reaches a maximum value equal to 20.20 N, but the vortex velocity of the water particle is zero. This energy uses to move the plate in the forward direction with a speed of 0.2 m/s.
- Figure 7c shows no vortex strength behind the plate at time $t = 16.90$ s when drag wave force (F_x) on the plate is 7.08 N.
- Figure 7d shows the maximum opposite force F_x= -23.28 N generated at time $t = 17.30$ s, and the plate moves in the backward direction with a velocity of 0.09 m/s.
- The plate moves maximum distance at a higher wave steepness ($H/L = 0.0379$).

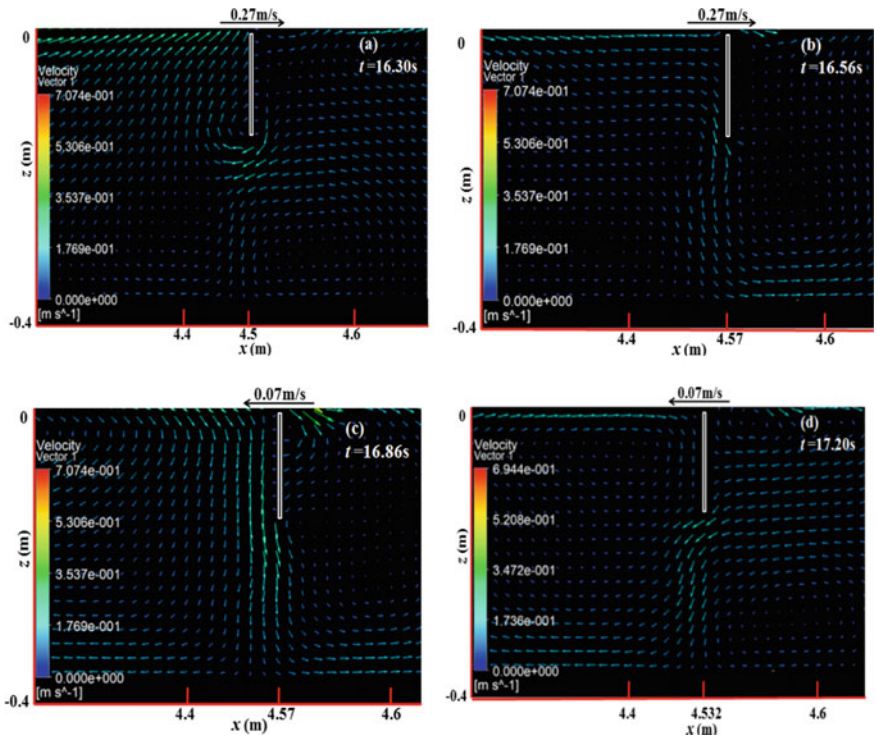

Fig. 9 Velocity vector distribution around the plate at $H/L = 0.0379$

- Vortex generation phenomena are based on wave steepness conditions. Vortex formation is high at the lower wave steepness condition compared to the higher wave steepness.

References

1. Brossard J, Chagdali M (2001) Experimental investigation of the harmonic generation by waves over a submerged plate. Coast Eng 42(4):277–290
2. Brossard J, Perret G, Blonce L, Diedhiou A (2009) Higher harmonics induced by a submerged horizontal plate and a submerged rectangular step in a wave flume. Coast Eng 56(1):11–22
3. Liu C, Huang Z, Tan SK (2009) Nonlinear scattering of non-breaking waves by a submerged horizontal plate: experiments and simulations. Ocean Eng 36(17–18):1332–1345
4. Hayatdavoodi M, Ertekin RC (2015) Wave forces on a submerged horizontal plate-part I: theory and modelling. J Fluids Struct 54:566–579
5. Hayatdavoodi M, Ertekin RC (2015) Wave forces on a submerged horizontal plate–part II: solitary and cnoidal waves. J Fluids Struct 54:580–596
6. Porter R (2015) Linearised water wave problems involving submerged horizontal plates. Appl Ocean Res 50:91–109

7. Rey V, Touboul J (2011) Forces and moment on a horizontal plate due to regular and irregular waves in the presence of current. Appl Ocean Res 33(2):88–99
8. Lin HX, Ning DZ, Zou QP, Teng B, Chen LF (2014) Current effects on nonlinear wave scattering by a submerged plate. J Waterw Port Coast Ocean Eng 140(5):04014016
9. Miyata H, Shikazono N, Kanai M (1990) Forces on a circular cylinder advancing steadily beneath the free-surface. Ocean Eng 17(1–2):81–104
10. Malavasi S, Guadagnini A (2007) Interactions between a rectangular cylinder and a free-surface flow. J Fluids Struct 23(8):1137–1148
11. Siew PF, Hurley DG (1977) Long surface waves incident on a submerged horizontal plate. J Fluid Mech 83(1):141–151
12. Patarapanich M (1984) Maximum and zero reflection from submerged plate. J Waterw Port Coast Ocean Eng 110(2):171–181
13. Patarapanich M, Cheong HF (1989) Reflection and transmission characteristics of regular and random waves from a submerged horizontal plate. Coast Eng 13(2):161–182
14. Hirt CW, Nichols BD (1981) Volume of fluid (VOF) method for the dynamics of free boundaries. J Comput Phys 39(1):201–225
15. Maguire AE (2011) Hydrodynamics, control and numerical modelling of absorbing wave-makers. Doctoral dissertation, University of Edinburgh
16. Finnegan W, Goggins J (2012) Numerical simulation of linear water waves and wave–structure interaction. Ocean Eng 43:23–31
17. Lal A, Elangovan M (2008) CFD simulation and validation of flap type wave-maker. World Acad Sci Eng Technol 46(1):76–82
18. Elangovan M (2011) Simulation of irregular waves by CFD. Int J Mech Mechatron Eng 5(7):1379–1383
19. Gao F (2003) An efficient finite element technique for free surface flow. Doctoral dissertation, University of Brighton

Impact of Soiling on the Performance of Monocrystalline-Si Photovoltaic Modules Under Different Climatic Conditions in East-Central India

Niranjan Singh Baghel and Nikhil Chander

1 Introduction

Environmental effects like soiling and shading reduce the performance of photovoltaic (PV) systems. These effects reduce the transmittance of module glass (soiling) or block the sunlight (shading) falling on solar cells. The reduction in transmittance (incident solar irradiance) reduces the number of photons reaching the solar cells. This leads to a reduction in the photocurrent and hence the output power of the PV module. Losses in performance of PV systems due to soiling and shading are known as soiling losses and shading losses, respectively [1, 2]. Dirt, dust, air pollution, bird droppings, and other particles that cover the surface of modules reduce the irradiance reaching the cell's surface. Soiling losses depend on many things such as installation tilt angle, site geography, weather conditions, composition and physical properties of the soil of a particular site, prevailing wind direction and speed, relative humidity, industrial activity, and other human activities like agriculture, building, and road construction [3–5].

Irradiance is reduced by shading due to any object. The shading reduces the output power of modules. Shading is from structures that are immediately in the neighborhood of the modules [6–8]. Nearby buildings and trees are typical examples. Shading by soiling term is used when accumulation of dirt, dust, plant leaves, and bird droppings occurs on modules with a high density. This accumulation of foreign material blocks the irradiance reaching the solar cells in the module [9, 10]. Thus, soiling and shading can lead to a significant reduction in energy generation by a PV

N. S. Baghel · N. Chander (✉)
Department of Electrical Engineering and Computer Science, Indian Institute of Technology Bhilai, GEC Campus, Sejbahar, Raipur, Chhattisgarh 492015, India
e-mail: nikhil@iitbhilai.ac.in

N. S. Baghel
e-mail: niranjans@iitbhilai.ac.in

D. Sharma and S. Roy (eds.), *Emerging Trends in Energy Conversion and Thermo-Fluid Systems*, Lecture Notes in Mechanical Engineering,
https://doi.org/10.1007/978-981-19-3410-0_4

system. In this article, we do a comparative analysis of photovoltaic parameters of dusty and non-dusty module [11, 12].

We know that the behavior of a PV panel changes with change in climate and location. A location-specific study is required to get a realistic assessment of the energy-producing potential of any SPV installation. By analyzing one place of installation, one cannot say that the same result will be applicable in another places. So, in the present work, the authors have performed a soiling study in the east-central part of India (Chhattisgarh state) which has not been done before by other researchers.

2 Experimental Methods

Figure 1 shows that two monocrystalline-Si PV modules of the same rating (50 Wp) have been installed at a fixed tilt angle of 21° (approximately same as the latitude of the location) facing south direction on the rooftop of IIT Bhilai (21.25° N, 81.63° E). The characteristics of the solar PV (SPV) modules at STC conditions are specified in Table 1. Module parameters like I–V and P–V curves were measured by an I–V tracer (Meco 9009, India). A pyranometer (EKO MS-40) is used to measure irradiance. This is a class C pyranometer. The pyranometer used in the present work was received

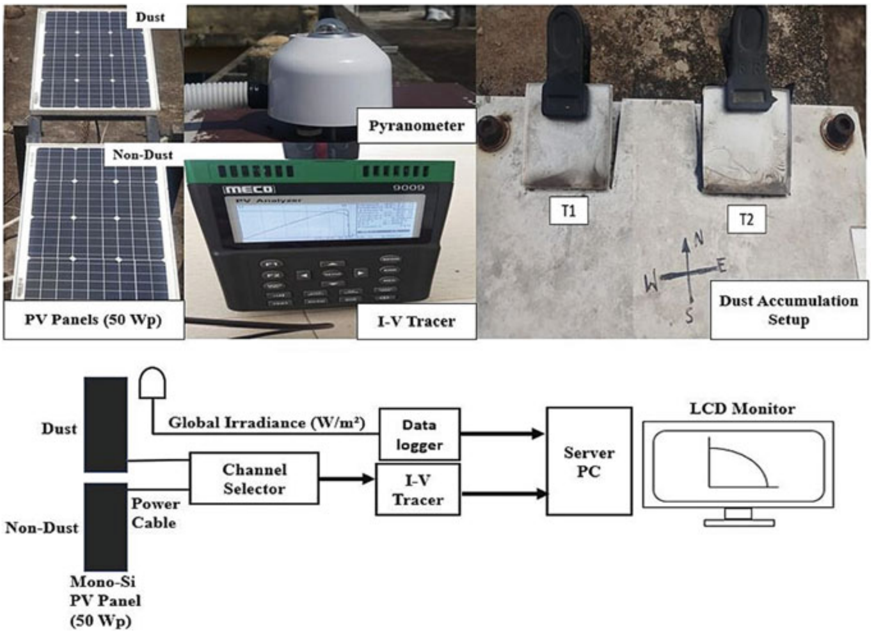

Fig. 1 Outdoor experimental setup and the equipment used for measurements at IIT Bhilai

Table 1 Specifications of the photovoltaic modules used in soiling analysis

Specification	Mono-Si PV module
Power output	50 W
V_{OC}	22.5 V
I_{SC}	2.65 A
V_m	20.0 V
I_m	2.51 A

in early 2020 with a calibration certificate. The manufacturer has certified that re-calibration is not needed before two years of operation. The I–V tracer also has a calibration certificate. The instruments need to be in proper working condition to minimize errors in the measurements.

The I–V and P–V curves can be experimentally measured at a particular set of illumination and temperature conditions. These curves help us to analyze the behavior of PV modules under different conditions. We can analyze soiling losses by taking the transmittance of module glass and correlating it with reduction in photocurrent. But, measuring the transmittance of field-installed PV module top glass is not possible practically. So, we are using small samples of low-iron glass for transmittance studies. SPV modules utilize similar low-iron content glasses as top cover. In this analysis, we have put these glass sample (T_1 and T_2), at a tilt angle equal to the local latitude angle (21°) on the rooftop (Fig. 1). Here, the glass pieces have dimensions of 5 cm × 5 cm × 0.4 cm. We are collecting the transmittance data of T_1 glass on a monthly basis to study the dust effects in different months. At the end of each month, the transmittance data was recorded and the glass was cleaned and again placed back on the dust-study setup. Transmittance of T_2 glass was taken at March end. This glass sample was not cleaned on a monthly basis, and it shows the cumulative effect of dust accumulation on transmittance for the entire experimental period (October 2020–March 2021). The transmittance measurements were performed using a spectrometer (UV2600, Shimadzu) in the wavelength range 300–1100 nm.

3 Results and Discussion

Dust accumulation is one of the important factors that affect the energy generation of the PV module. It is also known as soiling, which reduces the amount of solar irradiance passing through the module glass. We can analyze soiling effects on light transmission by taking the transmittance of PV module glass. We have collected the data on a monthly basis to study the reduction in transmittance. Figure 2 is a microscopic image of dust accumulated on glass coupons which were kept on the dust-study setup as shown in Fig. 1. Different glasses exhibit different amounts and densities of dust particles. The accumulated dust particles reduce the glass trans-mittance according to dust density on the surface of the glass. The reduction in transmittance leads to a reduction in photocurrent as lesser number of photons is

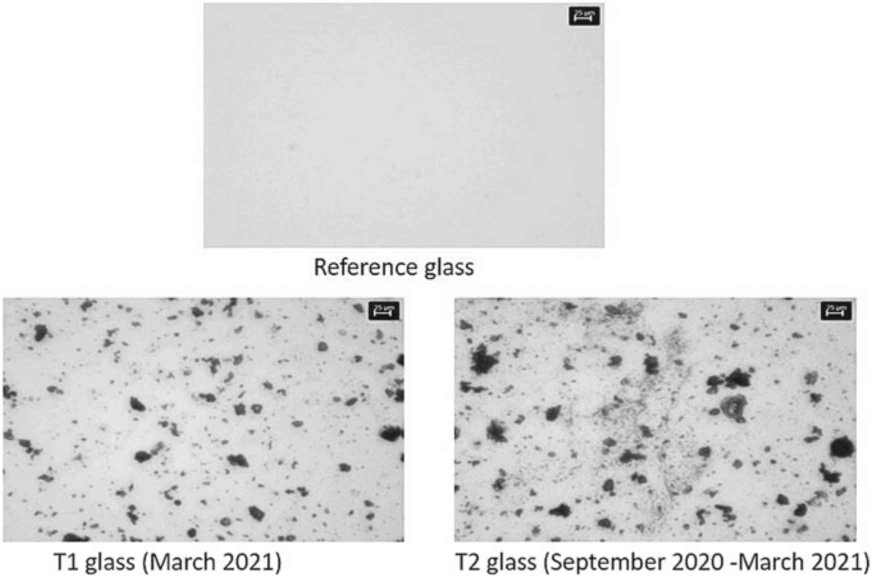

Fig. 2 Microscope images of dust-accumulated setup glasses (scale bar is 25 μm)

incident on the solar cells. In the figure shown below, the glass sample T_2 shows more dust accumulation than the T_1 sample. It is expected because the sample T_2 is showing the cumulative effect of dust deposition over several months, while the sample T_1 is showing the dust accumulated during a single month (March 2021).

Figure 3 shows that the transmittance of glass T_1 has reduced due to the accumulation of dust. During the analysis of Fig. 3, we have observed that the maximum transmittance reduction happened in the month of January 2021, because of low

Fig. 3 Monthly variation in glass (T_1) transmittance at a tilt angle of 21°

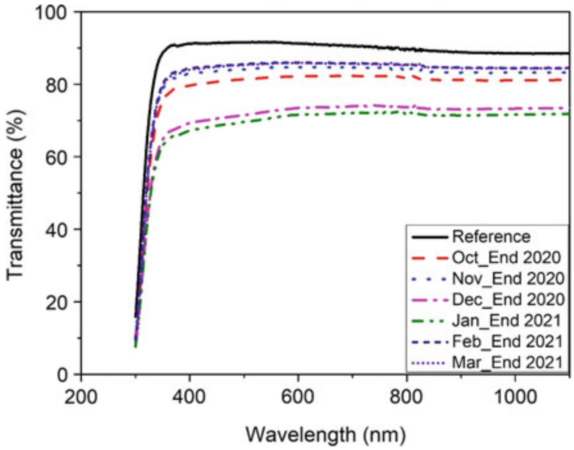

Fig. 4 Glass (T_2) transmittance after 7 months (September 2020 to March 2021)

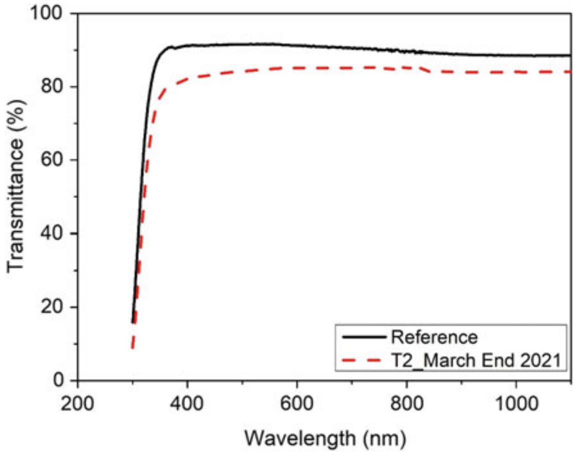

wind speeds and absence of rain. In the months of February and March, there is less reduction in transmittance as compared to other months. Wind speed was high in these months, and there were isolated thundershowers. Transmittance reduction is directly related to the amount and density of dust deposition on the glass surface.

Figure 4 shows the reduction in transmittance after seven months (September 2020–March 2021). After seven months, an average reduction of 6.28% in transmittance was observed for glass T_2 in the wavelength range 400–1100 nm. Due to rainy days and high wind speed, accumulated dust was occasionally removed from the surface of the modules. So, the reduction in transmittance can increase or decrease, depending on the weather conditions.

We know that the dust accumulation on the glass surface reduces the transmittance of glass. Thus, the amount of light entering the module decreases. This reduces the power generation of the PV module, as shown in Fig. 5. The dust accumulation affects the characteristics of SPV modules. Figure 5 shows the I–V and P–V curves of non-dusty and dusty modules in the middle of the month at noontime. The short-circuit current (I_{SC}) and maximum power (P_m) have been reduced due to dust accumulation on the surface of modules. By analyzing Fig. 5 and Table 2, we can clearly observe that the reduction in I_{SC} of the module is the main cause of power reduction. Reduction in current without any changes in the shape of I–V and P–V curves is an indication of uniform shading. And this uniform shading is due to uniform soiling (dust accumulation) on the front surface of modules.

From Figs. 3 and 4, we can observe that the maximum transmittance reduction occurred in January. From Table 2, we can also observe that the maximum reduction in power occurred in the same month. When we compare the power between dusty and non-dusty modules at the end of January (irradiance 805 W/m^2), a reduction of 24.29% in power was observed. This is a very significant reduction. In mid of December 2020, at a low irradiance of 320 W/m^2, 16.16% reduction in power was observed. This is also a very significant reduction in power. In the month of February, there is less reduction in power between dusty and non-dusty modules as compared

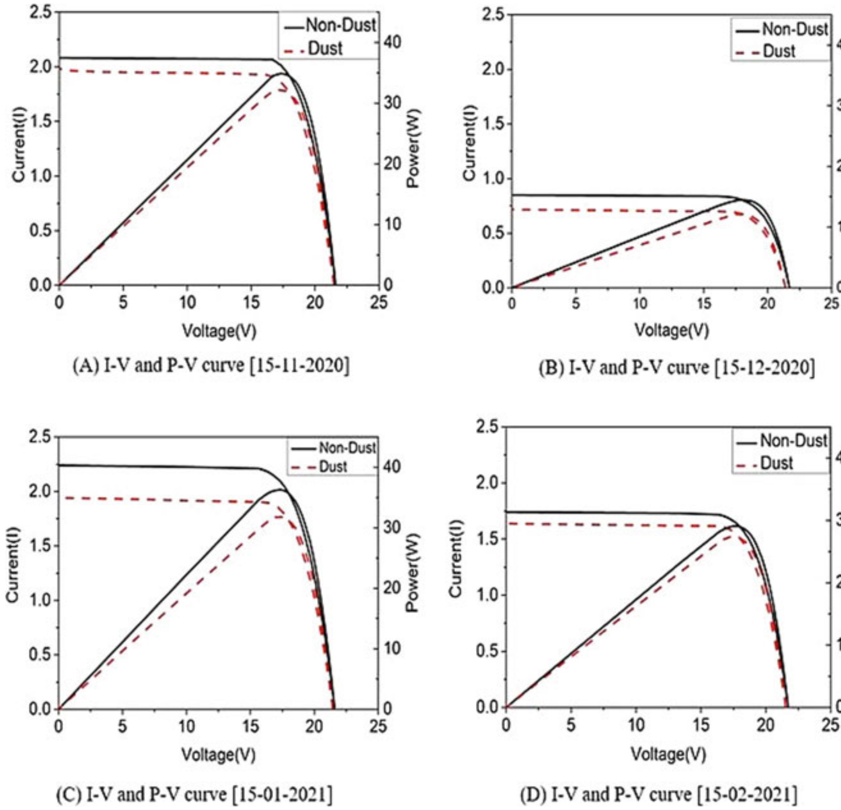

(A) I-V and P-V curve [15-11-2020]
(B) I-V and P-V curve [15-12-2020]
(C) I-V and P-V curve [15-01-2021]
(D) I-V and P-V curve [15-02-2021]

Fig. 5 I–V and P–V curves of dusty and non-dusty mono-Si PV panels on different dates

to other months as shown in Table 2. In this month, the humidity was very less on dry days and there was moderate rain that cleaned the modules. These values of power reduction in different months can be directly correlated to the reduction in transmittance as seen in Figs. 3 and 4.

Figure 6 shows the irradiance and power produced from dusty and non-dusty mono-Si PV panels as a function of time of day. The data for 31 January 2021 are shown. As seen from the figure, the power output of dusty module is consistently less than the clean module from morning till evening. And the difference is especially prominent during noontime (see Table 2; Fig. 6). Figures 3 and 6 also show that dust accumulation reduces the light transmittance with a corresponding decrease in output power of the PV panel.

Efficiency is the most important parameter that shows the energy conversion efficiency of the panel at different irradiance values. It is denoted as the ratio of maximum output power to the input power.

Table 2 Characteristics of dusty and clean mono-Si PV modules recorded in the middle and at the end of month. The data were recorded around noontime on the dates mentioned in the first column

Date (irradiance)	P_{max} (W) (clean)	P_{max} (W) (dusty)	V_m (V) (clean)	V_m (V) (dusty)	I_m (A) (clean)	I_m (A) (dusty)	Percent change in power
15 November 2020 (743 W/m^2)	34.90	32.2	17.31	17.31	2.01	1.86	−7.73
30 November 2020 (720 W/m^2)	32.58	30.01	16.91	16.84	1.93	1.78	−7.61
15 December 2020 (320 W/m^2)	14.48	12.14	18.02	17.87	0.80	0.68	−16.16
31 Dec. 2020 (600 W/m^2)	26.79	22.25	17.31	17.49	1.55	1.27	−16.95
15 Jan. 2021 (760 W/m^2)	36.29	31.85	17.3	17.29	2.10	1.84	−12.23
31 January 2021 (805 W/m^2)	37.96	28.74	17.55	17.87	2.16	1.61	−24.29
15 February 2021 (697 W/m^2)	29.08	27.37	17.63	17.35	1.65	1.58	−5.88
28 February 2021 (867 W/m^2)	35.70	33.37	16.70	16.37	2.14	2.04	−6.53%

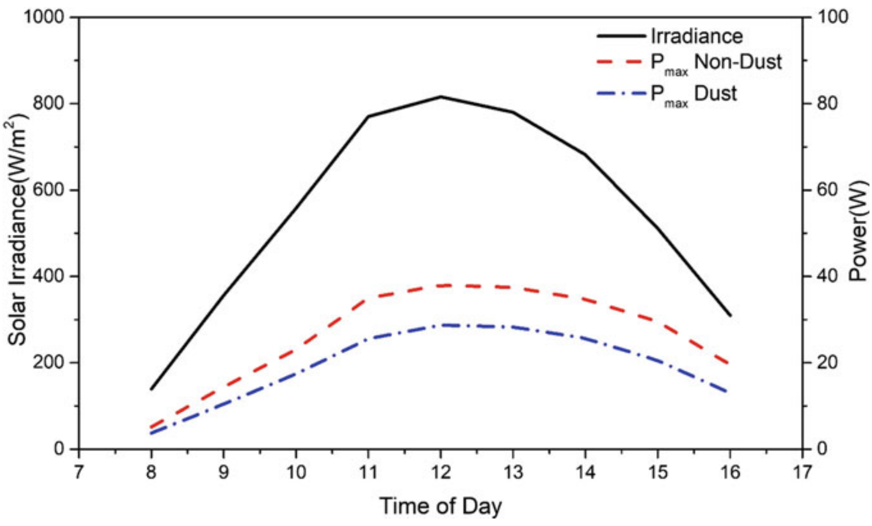

Fig. 6 Irradiance and output power of dusty and non-dusty panels (measured on January 31, 2021)

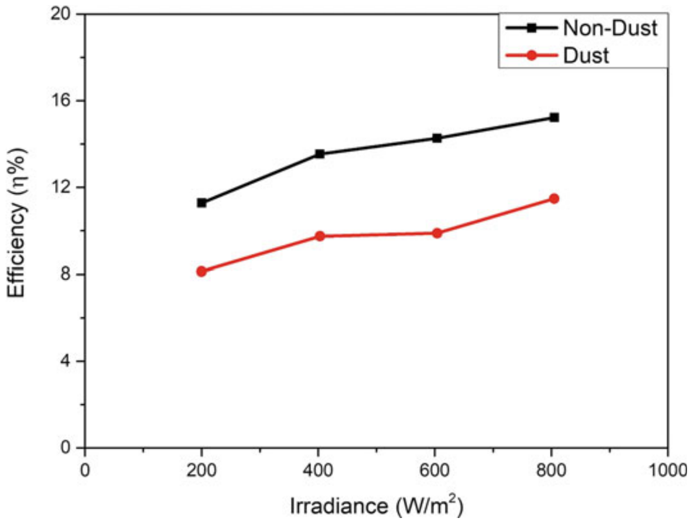

Fig. 7 Efficiency versus irradiance curves for dusty and non-dusty PV panels

$$\eta = \frac{P_{\mathrm{m}}}{\mathrm{POA} * A} \tag{1}$$

Here, P_{m} is the maximum produced output power of a panel at a particular irradiance and temperature, POA is the plane of array irradiance and A is the area of the module.

Figure 7 shows the variation in efficiency of dusty and non-dusty panels as a function of irradiance. We can observe that the non-dusty panel efficiency is higher than the dusty panel for all values of irradiance. Thus, soiling also affects the efficiency of solar panels. Dust accumulation reduces the light transmittance of solar panel glass that reduces the output power and efficiency of solar panels. Thus, a dusty panel generates much lower amount of energy than a clean panel and lead to economic loss as well. Therefore, regular cleaning of PV modules is essential to obtain the desired performance from a PV module or system.

4 Conclusions

The studies of dust accumulation on the module surface show the variation of transmittance with different densities of dust. Dust accumulation is also affected by the tilt angle, climatic conditions, and geographical location. So, frequent cleaning is required to maximize the output of PV modules. For the location studied in the present work, the maximum transmittance reduction occurred in January 2021. A 24.29% reduction in power was observed between dusty and non-dusty modules at an irradiance of 805 W/m^2 in January end. This was the highest reduction observed in the present study. Therefore, cleaning in the winter months should be more frequent. Cleaning two times a week in winter months (December–January) and at least once a week at other times is recommended. This analysis would be very helpful to properly schedule the cleaning of PV modules installed in East-Central India.

Acknowledgements Financial support for the experimental setup, received through Department of Science and Technology, Government of India, grant number DST/INSPIRE/04/2015/003204, is thankfully acknowledged. Authors thank Prof. J. N. Roy of IIT Kharagpur for providing glass samples and mounting arrangement for dust-study experiments. Authors thank Dr. Aritra Ghosh of University of Exeter, Penryn, UK, for providing useful inputs on dust-study setup. I would also like to thank Mr. Arif Khan (Junior Technical Superintendent) and Mr. Shravan Kumar Singh (PhD student) for helping in designing of the experimental setup.

References

1. Costa SCS, Kazmerski LL, DIniz ASAC (2021) Estimate of soiling rates based on soiling monitoring station and PV system data: case study for equatorial-climate Brazil. IEEE J Photovoltaics 11(2):461–468. https://doi.org/10.1109/JPHOTOV.2020.3047187
2. Tripathi AK, Murthy CSN (2017) Effect of shading on PV panel technology. In: 2017 international conference on energy, communication, data analytics and soft computing (ICECDS), pp 2075–2078. https://doi.org/10.1109/ICECDS.2017.8389814
3. Mahnoor B, Noman M, Rehan MS, Khan AD (2021) Power loss due to soiling on photovoltaic module with and without anti-soiling coating at different angle of incidence. https://doi.org/10.1080/15435075.2021.1930002
4. Maghami MR, Hizam H, Gomes C, Radzi MA, Rezadad MI, Hajighorbani S (2016) Power loss due to soiling on solar panel: a review. Renew Sustain Energy Rev 59:1307–1316. https://doi.org/10.1016/j.rser.2016.01.044
5. Chanchangi YN, Ghosh A, Sundaram S, Mallick TK (2020) An analytical indoor experimental study on the effect of soiling on PV, focusing on dust properties and PV surface material. Sol Energy 203:46–68. https://doi.org/10.1016/j.solener.2020.03.089
6. Dhimish M, Holmes V, Mehrdadi B, Dales M, Mather P (2018) Output-power enhancement for hot spotted polycrystalline photovoltaic solar cells. IEEE Trans Device Mater Reliab 18(1):37–45. https://doi.org/10.1109/TDMR.2017.2780224
7. Babu TS, Ram JP, Dragičević T, Miyatake M, Blaabjerg F, Rajasekar N (2018) Particle swarm optimization based solar PV array reconfiguration of the maximum power extraction under partial shading conditions. IEEE Trans Sustain Energy 9(1):74–85. https://doi.org/10.1109/TSTE.2017.2714905
8. Wu Z, Zhou Z, Alkahtani M (2020) Time-effective dust deposition analysis of PV modules based on finite element simulation for candidate site determination. IEEE Access 8:65137–65147. https://doi.org/10.1109/ACCESS.2020.2985158
9. Ziar H, Mishra S, Isabella O, Zeman M (2018) The need for a new parameter on PV modules datasheet: shading tolerability. In: 2018 IEEE 7th world conference on photovoltaic energy conversion (WCPEC) (a joint conference of 45th IEEE PVSC, 28th PVSEC 34th EU PVSEC), 2018, pp 664–667. https://doi.org/10.1109/PVSC.2018.8548194
10. Warade S, Kottantharayil A (2018) Analysis of soiling losses for different cleaning cycles. In: 2018 IEEE 7th world conference on photovoltaic energy conversion (WCPEC) (a joint conference of 45th IEEE PVSC, 28th PVSEC 34th EU PVSEC), 2018, pp 3644–3647. https://doi.org/10.1109/PVSC.2018.8547867
11. Sailor DJ, Anand J, King RR (2021) Photovoltaics in the built environment: a critical review. Energy Build 253:111479. https://doi.org/10.1016/J.ENBUILD.2021.111479

12. Gairola S, Sharma MK, Bhattacharya J (2021) Correlating partial shading and operating conditions to the performance of PV panels, pp 707–716. https://doi.org/10.1007/978-981-15-5955-6_66

Design, Installation, and Performance of a Small Solar Thermal Power Station for Rural Energy Support

Ankit Dev, R. P. Saini, and Ravi Kumar

1 Introduction

The convention energy sources are depleting continuously to fulfill the large increasing demand of energy [1, 2]. The development and adaption of alternate low carbon emission technologies draws attention to renewable energy resources like solar energy, which have vast potential to satisfy a large portion of the current and future energy demand [3–6].

India is the second most populated country in the world, almost 1.38 billion of people [7] with more than 50% below the age of 25 and more than 65% below the age of 35 [8]. The astonishing population growth over the past 20 years can be mainly attributed to a remarkable economic growth, which placed the country among the 10 largest economies in the world by nominal Gross Domestic Product (GDP). Economic progress made significant changes all around this vast nation, both in cities and minor villages, with a remarkable effect on the lifestyle and habits of millions of people.

This rapid change eventually created strong disparities between rural and metropolitan areas. The signs of this important gap can be easily found in many aspects of people's daily life.

While most part of the Indian cities and central villages can base their daily activities on a reliable and stable electric power distribution grid, this is not liable for smaller communities. Rural areas are in fact non-uniformly electrified, depending

A. Dev (✉) · R. Kumar
Department of Mechanical and Industrial Engineering, IIT Roorkee, Roorkee 247667, India
e-mail: adev@me.iitr.ac.in

A. Dev
Department of Mechanical Engineering, MBM Engineering College, Jodhpur 342011, India

R. P. Saini
Department of Hydro and Renewable Energy, IIT Roorkee, Roorkee 247667, India

D. Sharma and S. Roy (eds.), *Emerging Trends in Energy Conversion and Thermo-Fluid Systems*, Lecture Notes in Mechanical Engineering,
https://doi.org/10.1007/978-981-19-3410-0_5

on the financial resources of each single state. Due to this aspect, 400 million Indians are without electricity in rural India, 40% of the whole world's population without access to electricity. Lack of internal resources, economic poverty, and poor planning are some of the most relevant causes which has contributed to leave rural villages in India without electricity, while urban areas have experienced in the last few decades' growth in electricity capacity and consumption. In these circumstances, diesel generators fulfill the basic electric demand, which is normally used to guarantee food preservation (through refrigerators) or essential illumination. Cooking and heating necessities need also to be taken into account. In rural communities, most part of the cooking activities are still accomplished through the use of traditional wood fired stoves or fossil fuels such petrol and kerosene. The dependence of rural households on traditional fuel is mainly due to the poor purchasing capacity of the people to buy commercial fuel and the easy accessibility to traditional sources like cow dung and agricultural wastes [9]. As it is easy to expect, the thermal efficiency of these traditional sources is very low, approximately 15% (energy efficiency). The use of these traditional fuels is estimated to cause around 400,000 premature annual deaths due to various respiratory problems. Furthermore, the vast availability of unemployed and cheap manpower for fuel collection worsens this situation.

The government is increasingly trying to improve these harsh conditions by funding projects and initiatives related to biogas, solar, and wind energy applications. Since the slow process of total electrification will perhaps take many years to provide an extended and reliable grid, alternatives, based on clean and abundant renewable energies, need to be evaluated as viable solution for small and middle size rural applications for India villages. Among the bigger programs, the Jawaharlal Nehru National (JNN) Solar Mission has the ambitious goal of implementing 20,000 MW of solar power by 2022 reducing the cost of solar power generation in the country (Ministry of new and renewable energy, 2013). The Indian government is also trying to sensitize people to clean energies. In a five-year plan, 30,000 million INR (approx. $500 million USD) are budgeted for clean cooking education in more than 500,000 schools [10].

In this context, the India Trento Program for Advanced Research (ITPAR) is running the "Sustainable Technologies for distributed level Applications and energy support to Rural development" (STAR) project. ITPAR is bilateral collaboration supported by the Department of Science and Technology of the Indian Government (DST) and by the Province of Trento with the supervision of the Italian Ministry for Foreign Affairs. It involves some of the main university teams and research institutes of the Province of Trento and India. The STAR project is participated by the research institute Fondazione Bruno Kessler (FBK) from Trento, the Indian Institute of Technology (IIT) Roorkee, IIT Delhi and University South Campus Delhi. The project aims at the integration of a novel energy system in the district of Hardwar, composed of a combined solar thermal plant able to satisfy part of the daily thermal requirements of the Chudiyala Mohanpur village's high school. At the same time, the system is able to store thermal energy and run a hay processer prototype used by the village's farmers to improve the nutritional properties and quality of hay for animal feedstock.

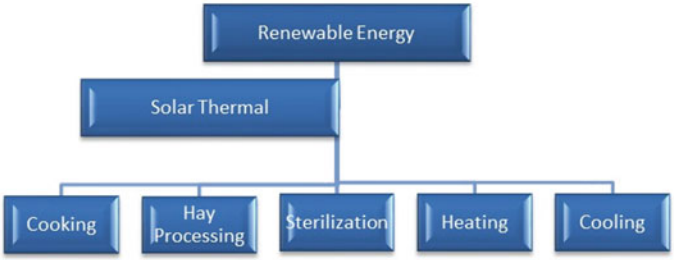

Fig. 1 Application of solar thermal energy

The thermal system integrates two different technologies of solar collectors and a high capacity PCM thermal storage to decouple solar energy and thermal necessities. It is designed as demo system, but it will be able to satisfy part of the energy-related necessities of the school. The hay processing device will be also implemented at a demonstrative size to prove the concept. In parallel, the school will be also supplied with an innovative solar cooler machine to store vegetables for short to midterm periods. The idea of the whole process is depicted in the chart given in Fig. 1.

2 Methodology and System Installation

The main objective of the project work is to improve energy and environmental sustainability of life in rural villages of India. Demonstration of the use of renewable and clean sources of energy and supply to main needs of the local identified community such as sterilized food, clean environment with solar cooking, hot water, and cool environments. The activity chart has been shown in Fig. 1.

2.1 Site Selection

The sites were judged through the available infrastructure and space availability on roof top for the solar systems. Availability of sun light and shading effect on the building and number of initial beneficiaries from the project were considered. In light of the above constrains, the CMD Inter college, Chudiyala, was considered the most suitable site for the implementation of the project. The site was unanimously finalized in the meeting of investigators in IIT Delhi, and it was concluded that the project shall be implemented in CMD Inter College, Chudiyala Village, Bhagwanpur Subdivision, Distt. Haridwar. The site is nearly 25 km away from Roorkee on Roorkee Saharanpur Road.

2.2 System Layout

After finalization of project implementation site, the proposed setup was designed and fabricated. The schematic diagram of setup and site photographic view are shown in Figs. 2 and 3, respectively. The setup consists of solar collectors where the solar thermal radiations are absorbed and the heat is transmitted to the circulating water through the collectors. The solar collectors have dual axis tracking system of sun resulting in very high absorption efficiency (0.8). The hot water in the close loop is stored in a thermal storage tank at 250 kPa pressure. The demineralized water is being used in the loop after mixing with the ethylene glycol 0.5% v/v to prevent any formation of steam. Though this mixture of water and ethylene glycol shall circulate in a close loop provision of makeup water is provided to take care of any leakage of water in circulation. The water will be constantly circulated in the close loop with solar collector till the water temperature of 120 °C is attained at 250 kPa pressure.

For the purpose of cooking and sterilization, this water at 120 °C shall be passed through a plate heat exchanger (PHE) for the transmission of heat to the downside available tap water. In the PHE, the downside water shall be converted into steam at approx. 100 °C. This steam shall be used for the cooking and sterilization purpose. In order to remove condensate in the steam supply line, a steam trap is provided in the supply line.

A standalone R-717 (ammonia)-based adsorption chiller is being used for the cooling purpose. The adsorption chiller has used activated carbon as adsorbent and R-717 as refrigerant. A gasifier is connected with the plant to heat the water. This hot water is circulated inside the chiller to facilitate the initiation of adsorption process and to get the low temperature ammonia at −5 °C temperature after the expansion valve. This low temperature ammonia chills the water to 7–10 °C in a heat exchanger for the purpose of air conditioning. The chilled water is circulated in the fan coil unit, and it produces cooling effect in the room. The gasifier uses fuel wood, bio waste, and cow dung cake for the generation of heat. When there is sunshine, the heating process shall be shifted to the hot water coming from the solar panels through the storage tank.

There are 15 dishes, and each dish can produce 3.4 kW of heating at 1000 W/m^2 DNI. At site, in Chudiyala village, normally DNI is in the range of 600–700 W/m^2. Therefore, 15 dishes are enough to provide 30 kW of heating. The calculations for energy distribution in different components of setup are shown in Fig. 4.

While in operation, the receiver (thermal storage tank) shall provide hot water to the chiller. When there is sunshine deficit, the heating energy shall be taken from gasifier for the cooling purpose. However, for the cooking process the hot water in the tank shall be used for steam generation. The chiller has two tanks filled with adsorbent (activated carbon) which works in cyclic order, i.e., one tank operating at a time. Meanwhile, another tank gets cooled by water, which subsequently discharges heat in the cooling tower.

Steam cooking has been proposed for the schoolchildren to cook the mid-day meal in the school. A steam cooking system, with customized design, will be used for this

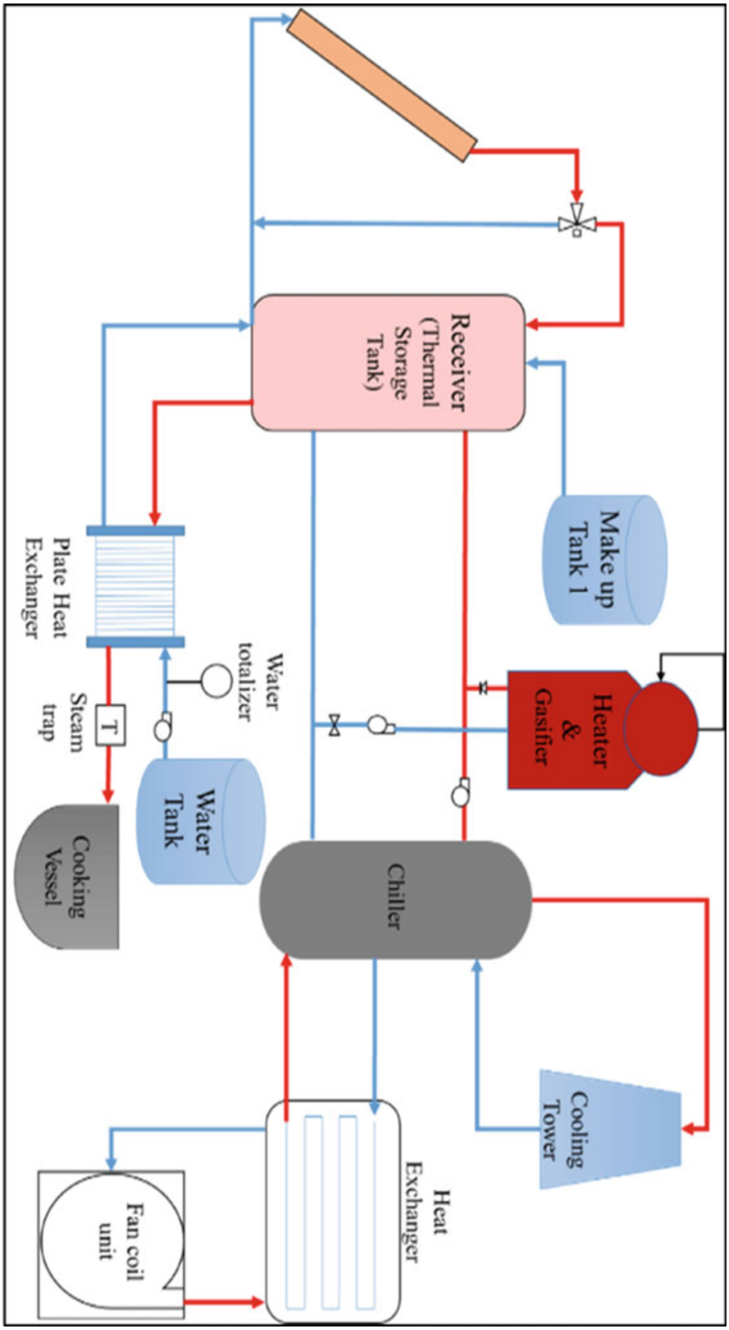

Fig. 2 Schematic of setup

Fig. 3 Site photograph of solar thermal system

purpose. The steam cooker is a direct steam injection type vessel, in which the steam is supplied from the bottom of the vessel and the food is cooked by using the latent heat of steam. Steam will be generated using pressurized hot water stored in thermal storage tank. As shown in schematic of setup, the vessel and thermal storage tank are connected to each other via a plate heat exchanger (PHE). The PHE generates steam after taking heat from the pressurized hot water from receiver (Thermal storage tank).

This complete system has been installed in the kitchen of the school. The cooking vessel and PHE both are placed inside the kitchen, and the thermal storage tank has been placed just outside the kitchen. The schematic diagram for steam cooking system is shown in Fig. 5. One hot water circulation pump is also installed in between receiver and PHE to circulate the pressurized hot water at a higher flow rate. By circulating the hot water at a higher will minimize the heat loss and more quantity of steam will be produced. One make up tank is installed at the other end of the PHE that contains the RO water.

This water will get heat from pressurized hot water while passing through PHE and generate steam that is supplied directly to the cooking vessel.

The hay processing unit will consist of a well-insulated closed vessel in which the steam will be supplied at 100 °C for at least 60 min to sterilize a certain amount of hay. This process is done to kill the harmful bacteria and other microorganism from the hay so that beneficial microorganisms can be grown in the hay. The feeding of this hay to domestic animals the productivity can be increased significantly.

The cooling unit consists of an adsorption chiller which has provision for the operation through the heat from fuel wood, bio waste, or cow dung cake. The system can also be integrated with the heat stored with solar heaters. A market survey was done for the purpose of finalizing the technology for the chiller plant. The integration of chiller plant with the solar system is yet to be done.

After analyzing the primary solar collection technologies at FBK, Trento, Italy, some other latest technologies, i.e., CPC (Compound Parabolic Collectors) also have analyzed. The CPC collectors from two different manufacturers were considered in

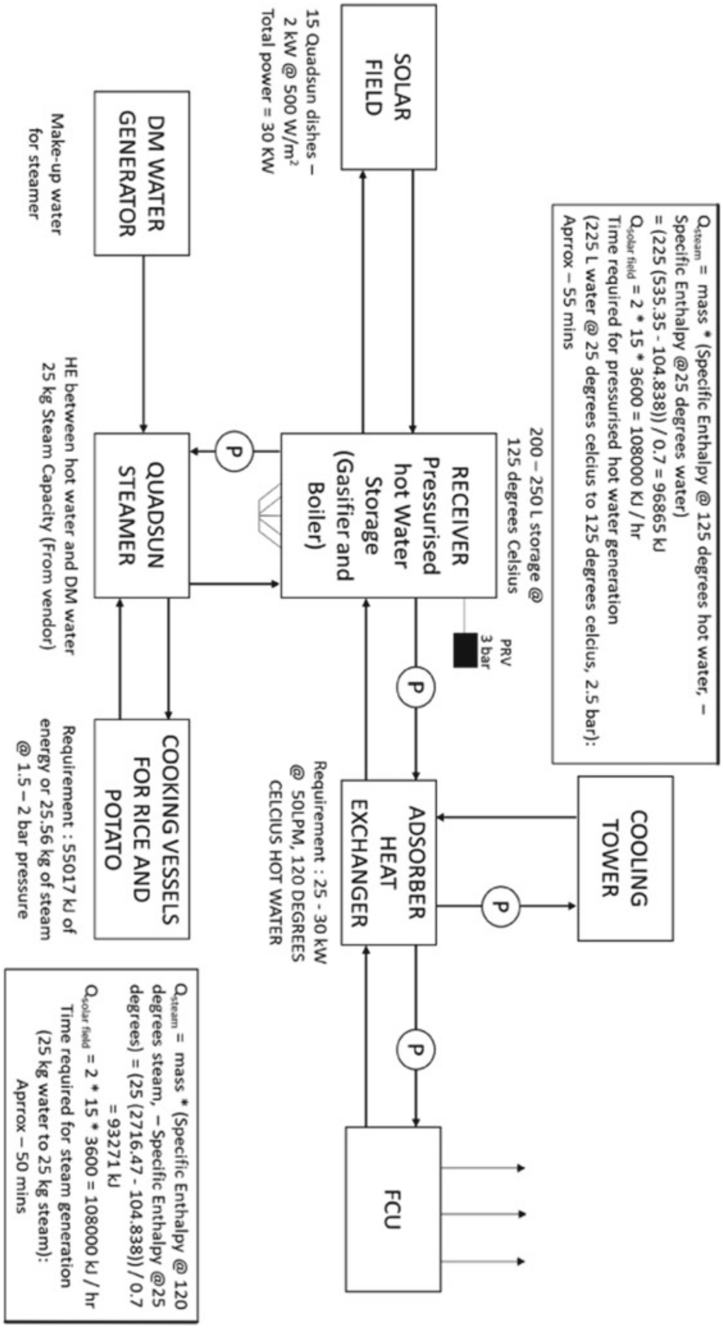

Fig. 4 Energy calculations in different component of setup

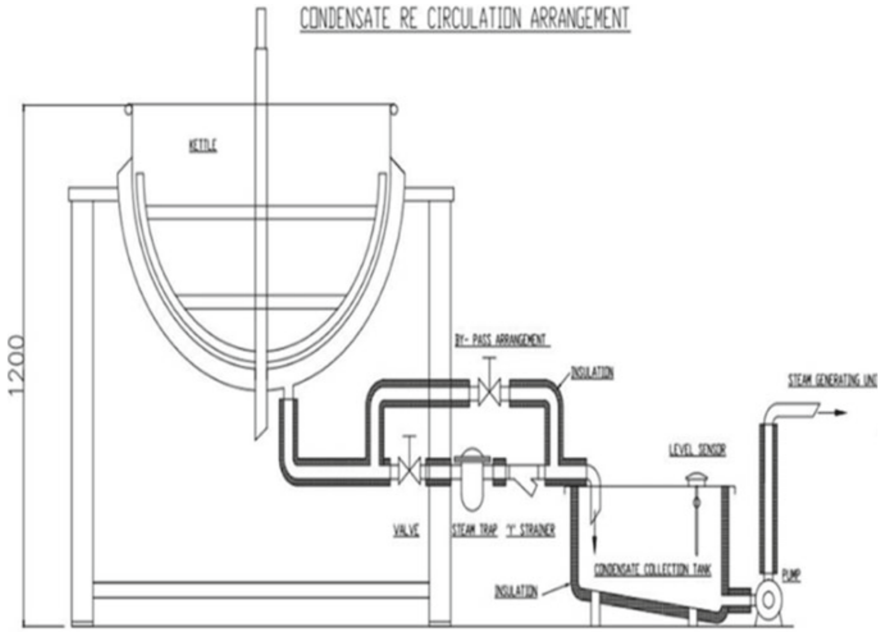

Fig. 5 The schematic diagram for the steam cooking system. All dimensions in mm

the analysis, one of them is a European manufacturer (PARADIGMA) and other one is an Indian (SUNBEST). After analyzing all the technical specification of both the technologies, it was found that the Indian collectors are much cheaper and quite efficient in comparison with European collectors. Finally, the CST panel with paraboloid dish was selected for the project.

The specifications of the CST collector are as follows:

Lightweight Concentrated Solar Thermal (CST) panels are required to generate steam for distributed rural applications. The specifications of each panel are as follows:

Thermal power rating:	$\geq$ 3.5 kW @ 1000 W/m^2 DNI and 25 °C
Optical efficiency:	$\geq$ 75%
Mirror surface area:	$\leq$ 4.5 m^2
Receiver diameter:	$\leq$ 100 mm
Tracking:	Dual axis tracking (optical based accuracy up to 0.001°)
Flow switch:	4 lpm rating (with off Sun setting if flow is less) and provision of adjusting the set point
Sun tracking algorithm:	NREL based
Wake up and sleep:	Fully automatic along with provision of manual setting
Wind speed (tracking):	$\leq$ 15 m/s (programmable)

Wind speed endurance:	40 m/s
Ambient temperature:	$\leq$ 60 °C
Humidity:	Up to 100% rh
Terrain:	Rooftop (RCC/RBC roof)
Max working fluid pressure:	10 bar
Max working fluid temperature:	180 °C
$L \times B \times H$:	$L \times$ B 2.5 m, H 2.0 m
Weight	90 kg
Controller (Microprocessor-based field controller):	As required for monitoring of individual system, logging of field data, grid sensing, and power availability.

After setting up all the fundamentals, installation of all the components has been done. All the solar collectors have been installed on the rooftop. All the pipelines of solar collectors have been insulated well to avoid energy loss. One expansion tank has also been kept for solar collector line to avoid any loss of water in pipeline. The control room also established in the room situated on the rooftop. The thermal storage tank is installed down the roof and just aside the kitchen room and then connected to the solar collector pipeline through the water pump.

The final installation of complete setup at site is shown in Fig. 3.

3 Results and Discussion

The main objective of the project was on the development of an appropriate solution for the rural community of India to fulfill their basic needs like cooking, cooling, hay processing, and hot water requirements, in addition, demonstration of technology for distributed applications. As two temperature sensors have been installed, one is in the thermal storage tank (T_1) and the other one is in the solar collector line (T_2). One wind sensor has been installed on the rooftop, and the max wind speed is set 20 m/s. The flow rate of water in the closed loop is maintained at 70 L/min for about 8 h/day. The pressure in the closed loop is around 1.5 bar. The system has been run for around 8 h with very good solar irradiation. The maximum temperature on a normal day is attained by the system where $T_{1\max}$ is 112 °C and $T_{2\max}$ is 114 °C. When the temperature of thermal storage tank reached 112 °C, the hot pressurized water is circulated through PHE for steam generation. At this temperature, steam is generated at very good rate. And around 5–6 kg rice has been cooked in just 10–15 min and also the temperature drop in thermal storage tank was very less during steam generation process. The temperature variation of complete system on a normal day in summer is shown in Fig. 6.

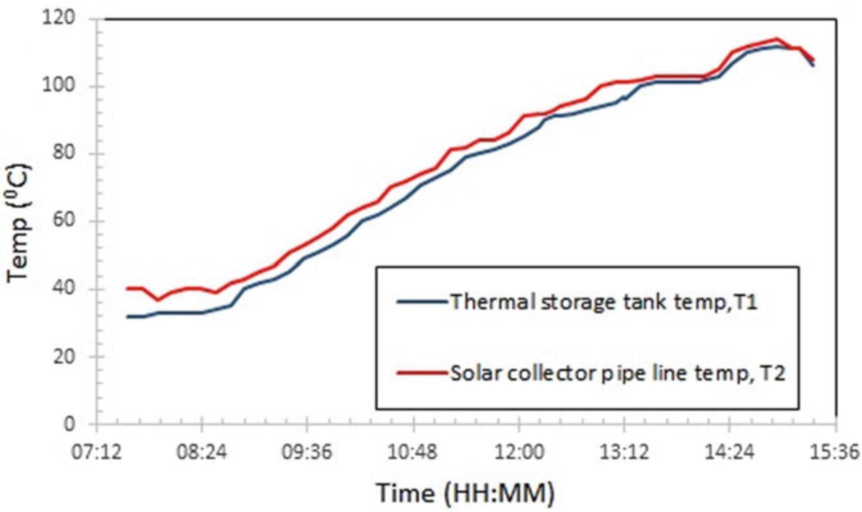

Fig. 6 Thermal performance of system

4 Conclusion

The systems for the distributed applications of solar energy for rural area have been designed and installed at the site in the village Chudiyala, District Haridwar, India. The installed equipment is being used for the demonstration of technology to the rural India. The system is able to satisfy heterogeneous power demands for typical rural applications: hay pasteurization process, refrigerated storage for vegetables, and steam cooking. In a normal summer day, the system generated the steam for cooking at a good rate which is used to cook food.

Acknowledgements Authors acknowledge the support of Department of Science and Technology, India, for the project INT/ITALY/ITPAR-III/RE/2015. The work regarding the chiller is contributed by the IIT Delhi team, which is highly acknowledged by the authors.

References

1. Braun FG, Hooper E, Wand R, Zloczysti P (2010) Innovation in concentrating solar power technologies: a study drawing on patent data. SSRN Electron J. https://doi.org/10.2139/ssrn.1633878
2. Ummadisingu A, Soni MS (2011) Concentrating solar power—technology, potential and policy in India. Renew Sustain Energy Rev 15:5169–5175. https://doi.org/10.1016/j.rser.2011.07.040
3. Gupta PK (1999) Renewable energy sources-a longway to go in India. Renew Energy 16:1216–1219. https://doi.org/10.1016/S0960-1481(98)00486-8

4. Praveen RP (2020) Performance analysis and optimization of central receiver solar thermal power plants for utility scale power generation. Sustainability (Switzerland) 12. https://doi.org/10.3390/SU12010127
5. Bhutka J, Gajjar J, Harinarayana T (2016) Modelling of solar thermal power plant using parabolic trough collector. J Power Energy Eng 04:9–25. https://doi.org/10.4236/jpee.2016.48002
6. Abdelhady S, Borello D, Tortora E (2014) Design of a small scale stand-alone solar thermal co-generation plant for an isolated region in Egypt. Energy Convers Manage 88:872–882. https://doi.org/10.1016/j.enconman.2014.08.066
7. https://www.worldometers.info/world-population/india-population/. Last Accessed 10 Aug 2020
8. http://news.bbc.co.uk/2/hi/south_asia/6911544.stm. Last Accessed 10 Aug 2020
9. Kumar A, Kumar K, Kaushik N, Sharma S, Mishra S (2010) Renewable energy in India: current status and future potentials. Renew Sustain Energy Rev 14:2434–2442. https://doi.org/10.1016/j.rser.2010.04.003
10. https://solarcooking.fandom.com/wiki/India. Last Accessed 10 Aug 2020

Enhanced Heat Transfer

Integration of Perforations in Conventional Heat Sinks for Augmented Heat Dissipation

Mohak Gaur and Amit Arora

Nomenclature

D	Pin diameter (mm)
D_h	Hydraulic diameter of rectangular channel (mm)
D_p	Diameter of perforation (mm)
k_{air}	Thermal conductivity of air (W m^{-1} K^{-1})
ρ	Density of air (kg/m^3)
μ	Viscosity of air (Kg m^{-1}s^{-1})
Nu	Nusselt number
ΔP	Pressure drop across test section (Pa)
η	System performance
η_{ratio}	Performance ratio
Re_h	Reynolds number based on hydraulic diameter
u_o	Inlet velocity (ms^{-1})
T_{in}	Inlet temperature (°C)
T_{out}	Outlet temperature (°C)
T_w	Average base plate temperature (°C)
q_{00}	Heat flux (Wm^{-2})
P_p	Perforation pitch (mm)

M. Gaur (✉) · A. Arora
Department of Mechanical Engineering, Malaviya National Institute of Technology Jaipur, Jaipur, Rajasthan 302017, India
e-mail: mohakgaur108@gmail.com

D. Sharma and S. Roy (eds.), *Emerging Trends in Energy Conversion and Thermo-Fluid Systems*, Lecture Notes in Mechanical Engineering,
https://doi.org/10.1007/978-981-19-3410-0_6

1 Introduction

Rising computational power of electronic chips has resulted in increase in the heat generation rates, and with the current demand of miniaturizing electronic devices, the space available to dissipate the heat generated is limited. Therefore, the need is to incorporate new methods to design a heat sink which can dissipate more heat in the limited space available. For the effective working of processors, the operating temperature should be maintained in 60–80 °C range.

As can be seen in Fig. 1, high operating temperature is the chief cause of electronics failure; hence, effective thermal dissipation is necessary to maintain the reliability of the electronic devices [1]. The utmost conversed tools for dissipating heat are the heat sinks. Heat sink is a device mounted on top of heat generating parts (ICs/CPUs) of electronic device in order to dissipate heat and maintain a low operating temperature of the device. It is the most cost-efficient method available to dissipate heat in electronics. Until recently, numerical analysis was limited to analyze simple heat sink geometries, but with development in technology and the capabilities of computational fluid dynamics simulation (CFD) has made it possible to conduct numerical analysis for thermal and pressure loss characteristics of complex heat sink geometries.

A number of techniques have been employed to increase the heat dissipation rate and reduce the pressure head loss across heat sink. The work methodologies can be of three types, using nanofluids, geometric modification, or adopting non-conventional cooling techniques.

Nazari et al. [2] conducted an experimental study on the cooling of processors using carbon nanotubes (CNTs) and alumina nanofluids. They compared these results with the cooling performance of ethylene glycol which is a commonly used base fluid. The alumina nanoparticles were coupled with water, while the CNTs were suspended in the base solution of ethylene glycol. The volume fraction of CNT in the base fluid was taken to be 0.1 and 0.25 (%w/w), while the volume fraction of the alumina/water nanofluid was considered to be 0.1, 0.25, and 0.5(%w/w). It was reported that an enhancement of 13% was obtained in convective heat transfer coefficient by using CNT/water 0.25 (% wt./wt.) at a flow rate of 21 mL/s. It was reported that a 22% reduction in CPU operating temperature can be obtained by using CNT as

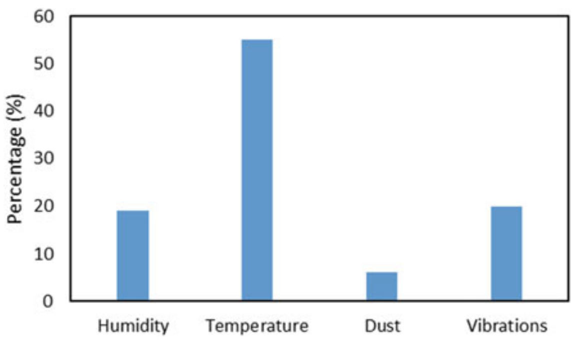

Fig. 1 Chief causes of electronics failure

working fluid, while a reduction of 20% in CPU operating temperature was reported on using alumina nanoparticles as working fluid. Ho et al. [3] investigated the effect of forced convection flow of Al_2O_3/H_2O nanofluid on heat transfer enhancement. It was observed that 1% vol. nanofluid was proved to be more effective than 2% vol. nanofluid for the purpose of heat dissipation. It was accredited to the greater change in dynamic viscosity with temperature. It was reported that a 70% increase in the convective heat transfer coefficient can be obtained using 1% vol. concentrated Al_2O_3/H_2O nanofluids. Thulium and Bayazitaglu [4] investigated the effect of 0.01% vol. concentrated nanoparticles of Al_2O_3/water as a working fluid on silicon-coated MWCNT minichannels and circular pin fin array of MWCNT having 6 rows and 12 columns of fins. A volumetric flow rate of 80 mL/min for the coolant was used to conduct the experiment. It was reported that using both nanofluid and the MWNTs structured surface did not have any noteworthy effect on thermal performance, and the heat dissipation was almost similar to that obtained by using deionized water. Further studies by Vanapali and Breke [5] examined heat transfer capability of nanofluid for forced flow. The geometry, thermal conductivity, and viscosity were varied, and their effect on heat transfer capability was analyzed. It was concluded that there is a high dependency of heat transfer on geometric modifications. Chein and Chuang [6] studied experimentally the performance of microchannel heat sink using nanofluids. A silicon microchannel heat sink was used with CuO-H2O nanofluid. CuO particles' volume fraction in the range of 0.2–0.4% was used to conduct the experiment. It was found that an increase in the heat dissipation capability at a cost of only a slight increase in pressure drop can be obtained when nanoparticles were used as the working fluid. It was found that by increasing the temperature of the walls of heat sink, a reduction in the agglomeration of the nanoparticles can be achieved. Next, Chein and Huang [7] used Cu/H_2O nanofluid in a silicone microchannel and varied the dimensions of heat sink as well as the concentration of nanoparticles. They found that at low particle size and low volume fraction, the increased heat transfer was obtained without any cost of increase in pressure drop.

The use of the agitating motion in order to enhance the heat dissipation of heat sink was studied by Yu et al. [8]. A pin fin array was connected with an agitator plate which gave it periodic motion in transverse direction of air flow. The heat sink and the agitator plate both were placed inside the rectangular channel fluid domain.

Two types of agitator plate movement, namely translation and flapping motion, were considered by them, and the improvement in convective heat transfer coefficient was attributed to the turbulence in the flow created by the agitator plate. They achieved an increase of 61% in heat transfer under certain conditions. It was reported that the heat transfer was 33% more for translational movement of agitator plate compared to the flapping motion of agitator plate. It was observed that there was a linear relationship between amplitude and frequency of the agitating motion with the heat transfer enhancement. Effect of fin spacing on water-cooled minichannel heat sink for microprocessor cooling was analyzed by Jajja et al. [9]. It was found that the base plate temperature and the thermal resistance reduced with the increase in flow rate of water as well as by reducing the fin spacing at 325 W of analog microprocessor power. The lowest base plate temperature of 40.5 °C was achieved using a heat sink with 0.2 mm fin spacing at a flow rate of 1.0 LPM.

Lin et al. [10] conducted an experimental study on the use of wavy channel in order to increase heat transfer in microchannel heat sink. They varied the wavelength and amplitude of the channel walls, and the thermal resistance (R) and bottom wall temperature difference (ΔT) were compared for wavy channel and standard straight channel heat sink under a constant pumping power. It was shown that on decreasing the wavelength or on increasing the amplitude of the wavy channel, the heat dissipation capability was improved and lower thermal resistance was achieved. The increase in heat transfer coefficient was attributed to the formation of eddies in the cross sections of the channel by the curved walls, which resulted in increased intermixing of the fluid and hence improved the convective heat transfer between the coolant and the channel walls. Similarly, Sikka et al. [11] conducted experiment on fluted and wavy plate fin configuration subjected to free and forced convection having lower flow velocities. It was concluded that the novel heat sink designs do not yield any significant increase in thermal performance than an optimized conventional longitudinal-plate heat sink.

Junaidi et al. [12] conducted thermal analysis of splayed pin fin heat sink through computational fluid dynamics simulation techniques. It was observed that the cooling premium of splayed pin fin heat sink was 20–30% better than that of standard pin fin heat sink in a low air velocities environment subjected to natural convection. It was concluded that splayed pin fins are suitable for boards with high density of pin fins.

2 Computational Modeling

2.1 Computational Domain and Boundary Conditions

The staggered perforated pin fin heat sink has been simulated using Ansys 15.0 Fluent software. The flow was considered to be three dimensional, incompressible and had achieved steady state. Dimensions of the fluid region of computational domain as well as the boundary conditions were based on the experimental setup of the experiment performed by Chin et al. [13]. SIMPLEC algorithm was employed to couple velocity and pressure. Finite volume method was employed. The equations that were solved to get solution are namely the energy equation, Navier–Stokes equations, and continuity equation. k-epsilon realizable model with the standard wall function was used to simulate the turbulent flow in channel. The equations can be referred to from Ansys Fluent theory guide [14]. The boundary conditions at inlet were taken to be velocity inlet with uniform velocity, temperature of 300 K, and atmospheric pressure (gage pressure = 0). Turbulence intensity was taken to be 10% as it was in the experiment, and the hydraulic diameter was calculated to be $D_{\mathrm{h}} = 0.067$ m. The fluid domain walls and pin fin walls had no-slip conditions. From downstream of the heat sink

Boundary No.	Name	Type
1	Wall	Adiabatic
2	Outlet	Outflow
3	Inlet	Velocity
4	Base plate	Heat flux

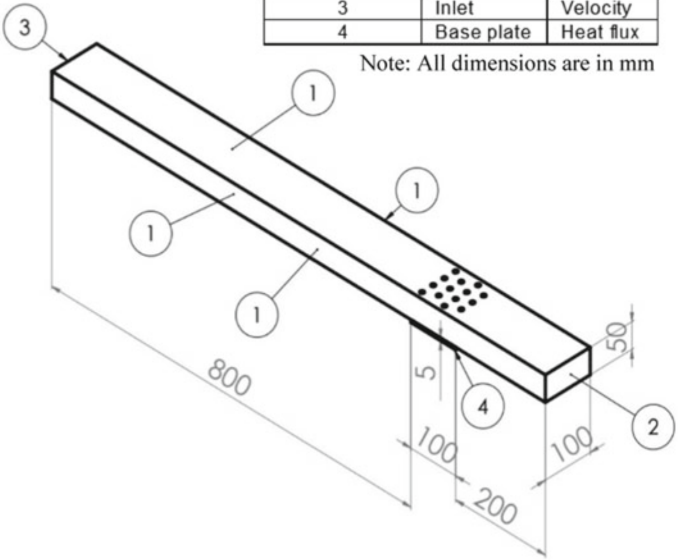

Fig. 2 Fluid region of computational domain

to the outlet, the flow was fully developed. The fluid domain walls were adiabatic excluding the base plate on which a constant heat flux of 5903 W/m^2 was given.

The fluid domain was constructed as shown in Fig. 2. The test section length was 100 mm, while the entrance length was 800 mm, and downstream to exit length was 200 mm. The lengths of sections were taken as such so that the flow was fully developed upstream and downstream the heat sink. The pressure drop was calculated by taking the difference of the average surface value of pressure on a plane 10 mm upstream and 10 mm downstream as was the position of pressure gage in the experiment. All the walls of fluid domain were taken as adiabatic, and a constant uniform heat flux was given to the base plate of heat sink. Velocity inlet boundary condition was taken at inlet, while outflow boundary condition was given to the outlet. The readings were taken at four different Reynolds number 8711.91, 13,199.4, 17,576.2, and 22,063.7, and the corresponding inlet velocities were 1.89 m/s, 2.88 m/s, 3.83 m/s, and 4.81 m/s, respectively.

The computational domain was discretized into grids using cutcell method. The number of control volumes for the solid pin fin array was approximately 1×10^6. Finer mesh structures were located in vicinity of the fins and the perforations as can be seen from Fig. 3.

Grid independence test was conducted for solid pin fin array, and a 30% increase in number of elements changed average Nusselt number by 1.4% and the average pressure drop across the heat sinks by about 0.6%; the formula used to calculate various parameters is given below:

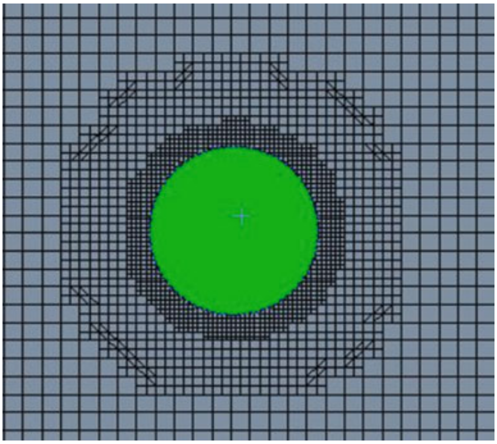

Fig. 3 Meshing in fluid region around the fin

$$\text{Nusselt number (Nu)} = \frac{q_{00} D_\text{h}}{k_\text{air}\left(T_\text{w} - \frac{T_\text{out}+T_\text{in}}{2}\right)} \tag{1}$$

$$\text{Pressure drop } (\Delta P) = P_\text{in} - P_\text{out} \tag{2}$$

$$\text{System performance } (\eta) = \frac{\text{Nu}}{\frac{\Delta P}{0.5\rho u_0^2}} \tag{3}$$

$$\text{Reynolds number } (\text{Re}_\text{h}) = \frac{\rho u_0 D_\text{h}}{\mu} \tag{4}$$

$$\text{Hydraulic diameter}(D_\text{h}) = \frac{4A}{P_\text{c}} \tag{5}$$

2.2 Heat Sink Dimensions

The staggered pin fin arrangement was taken on a rectangular 100 mm*100 mm base plate containing 14 circular pin fins. The diameter of each pin fin was 8 mm. The arrangement of pin fin is as shown in Fig. 4. Four different configurations of pin fins were analyzed including one solid pin fin geometry and three perforated geometries.

Four different perforation pitch (P_p) were considered having values 9 mm, 8 mm, 7 mm, and 6 mm. The diameter of perforation (D_p) was 4 mm for each configuration. The configuration and arrangement of perforations on pin fin are as depicted in Fig. 5.

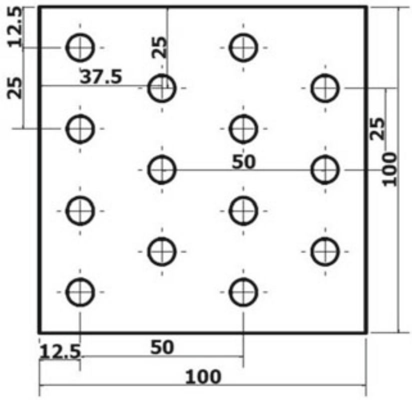

Note: All dimensions are in mm

Fig. 4 Heat sink configuration

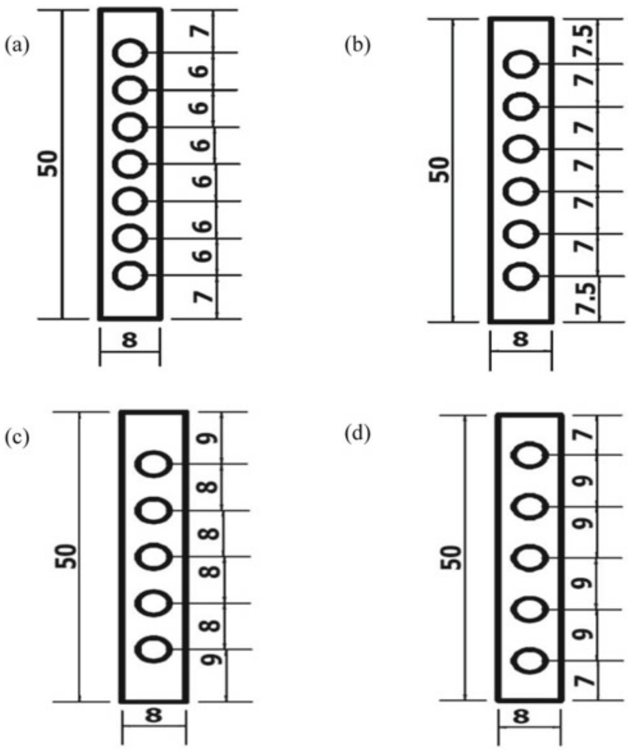

Note: All dimensions are in mm

Fig. 5 Perforated pins **a** $P_p = 6$ mm **b** $P_p = 7$ mm **c** $P_p = 8$ mm **d** $P_p = 9$ mm

2.3 Model Validation

The experimental data was taken from the experiment conducted by Chin et al. [13]. The computational model dimensions as well as upstream and downstream section lengths were taken similar to that of the experimental model. The heat sink material was aluminum, while the working fluid was air. Figure 6 depicts the contrast between the experimentally measured and the simulated Nusselt number and pressure loss across the test section against Reh for heat sink with solid pin fins. As can be seen from the graph, both Nu and ΔP increase with the increase in Reh. The computationally calculated pressure loss across heat sink is slightly overestimated as compared to the experimentally determined pressure drop, and at low value of Reynolds number, pressure drop was 14.64% more than the experimental value, while Nusselt number was 27.34% lower than the experimental value. This could

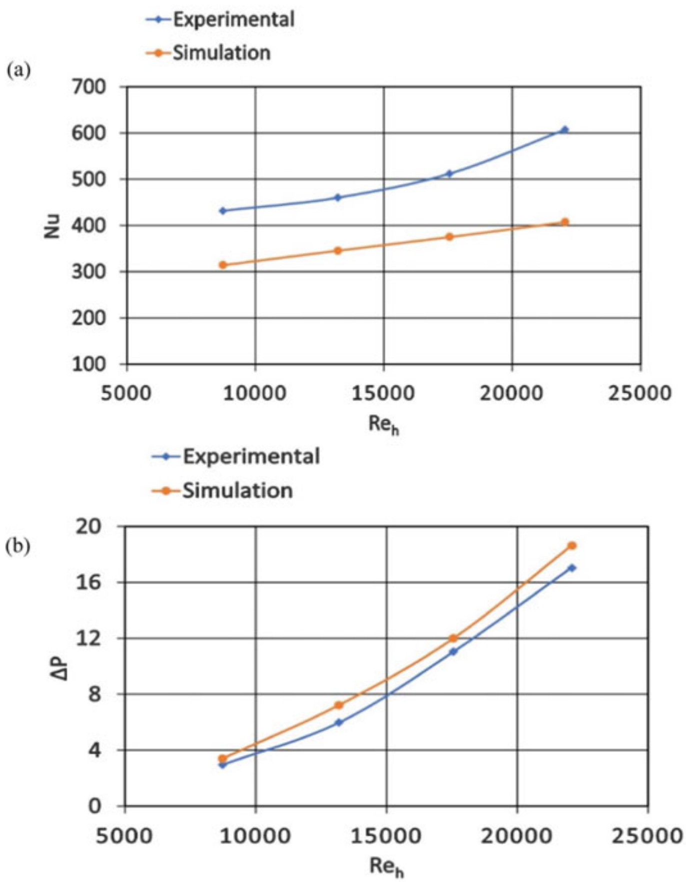

Fig. 6 Model validation **a** Nusselt number **b** pressure drop [13]

be because no clearance is given between fin top and the top wall of computational domain, while such perfect contact is possible in simulation, and there might be imperfect contact between pin fins top and top wall of fluid domain causing gaps between them in the experimental setup which may allow bypass flow leading to reduced pressure drop. The limitations of k-epsilon realizable turbulence model are also a contributory factor in the divergence of Nusselt number from experimental data at higher Reynolds number (Reh).

3 Results and Discussion

In order to appreciate the changes in flow characteristics, streamlines need to be analyzed. For that purpose, fins with least perforation pitch (i.e., 6 mm) and highest perforation diameter (i.e., 4 mm) are considered, as shown in Fig. 7. The comparative study is conducted at $Re_h = 22{,}063.7$. As evident, the perforated fins show better flow characteristics compared to solid fins because perforated pin fins give clear path to the approaching flow, and thus, the approaching fluid experiences lesser obstruction and also the contact area between fluid and the pin fins increases which is the reason for the enhanced thermal performance. Due to such geometric modifications, streamlines are changed around the pin fin array as depicted in Fig. 7. Further, it can be seen for that the streamlines bend around the solid fins, while they pass through

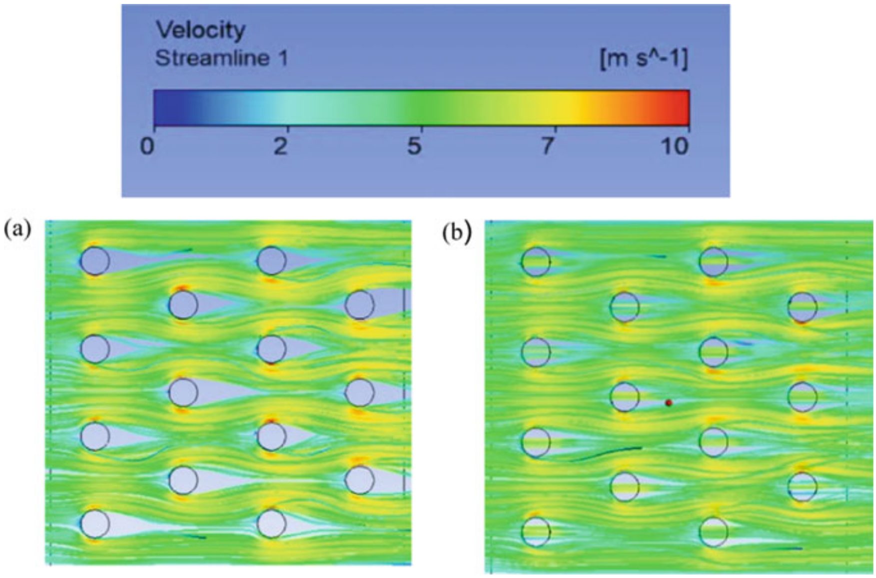

Fig. 7 Streamlines **a** solid pin fin **b** perforated pin fins with $P_p = 6$ mm and $D_p = 4$ mm

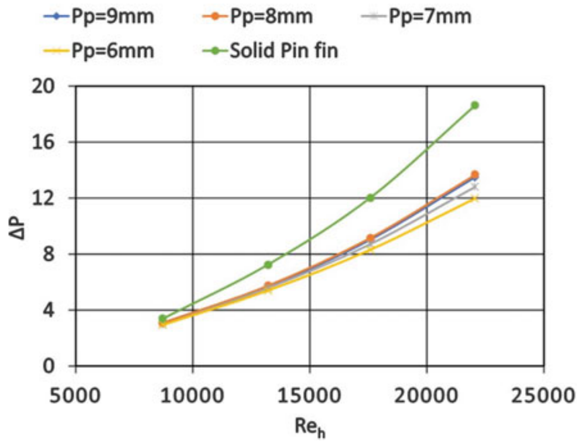

Fig. 8 Change in flow losses

the perforations provided in the modified design, and thus, lesser obstruction is experienced by the air which helps in lowering the pressure drop. Additionally, narrower and smaller recirculation region behind the perforated fins facilitates greater heat transfer augmentation. Various local flow modifications are going to manifest as rise in average Nusselt number as well as pressure loss. The discussion on change in various average performance parameters is discussed in the subsequent subsections.

3.1 Change in Hydraulic Performance

A graph between the pressure loss/drop across the heat sink against the Reynolds number for different perforation pitch P_p for a defined perforation diameter $D_p = 4$ mm has been plotted (Fig. 8), and it can be clearly seen that on increasing the perforation density or reducing the perforation pitch reduces the pressure drop across heat sink. At a high value of Reynolds number, the pressure drop for $P_p = 6$ mm was reduced by 35.63% compared to that of solid pin fins under similar operating conditions. The pressure drop reduced by reducing P_p, and this was predominantly because of increase in the number of perforations on the pin fins which resulted in a lesser obstruction to the flow of air, but for the same number of perforations, the pressure drop at high Reynolds number for $P_p = 9$ mm was 1.22% lower than that of $P_p = 8$ mm.

3.2 Change in Thermal Performance

A graph has been plotted for the Nusselt number against the Reynolds number for different perforation pitch for a preset value of perforation diameter (Fig. 9). It

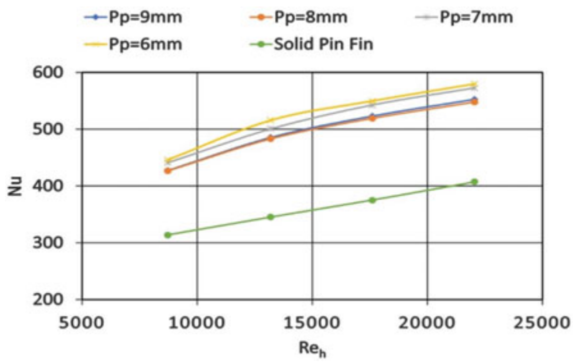

Fig. 9 Change in Nusselt number

has been noted that the Nusselt number increases with the reduction in perforation pitch or increasing the perforation density. This was mainly because of the increase in number of perforations resulting in increased effective convective heat transfer area. At a high value of Reynolds number, the Nusselt number for $P_p = 6$ mm was increased by 42.36% compared to that of solid pin fins under similar operating conditions. If the number of perforations was equal, the perforation pitch did not have any significant effect on Nusselt number as can be seen in Fig. 9. At high Reynolds number, the Nusselt number of $P_p = 8$ mm was lower by 0.85% compared to that of heat sink having $P_p = 9$ mm. Since $P_p = 8$ mm and $P_p = 9$ mm had equal number of perforations ($N = 5$) on single pin fins, the perforation pitch did not have any significant effect on Nusselt number.

3.3 Change in System Performance η

The system performance, η, of a heat sink is a dimensionless number defined as the ratio of Nusselt number to the pressure drop coefficient. This parameter can be used in order to determine the optimum design based on the compromise between most heat dissipation rate and the least pressure loss/drop across heat sink as it determines the relative cost, i.e., pumping loss/pressure drop to attain a definite amount of heat transfer. Figure 10 shows that the system performance increases with the increase in perforation density, but for same number of perforations on pin fins, higher system perforation was observed for configuration having higher perforation pitch. The high flow velocity configuration with $P_p = 6$ mm had system performance 2.21 times to that of solid pin fins under similar operating conditions. The system performance of configuration with $P_p = 9$ mm was reported to be 2.11% greater than configuration with $P_p = 8$ mm at an inlet velocity of 4.81 m/s.

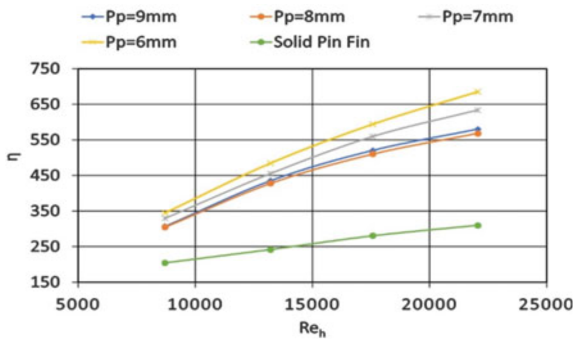

Fig. 10 Change in system performance

4 Conclusion

Steady and incompressible flow of air over staggered perforated pin fin array in a rectangular channel has been analyzed computationally to calculate their convective heat transfer coefficient and pressure drop. Hydraulic and thermal performances of various perforated pin fin geometries have been compared and studied, specifically the effect of perforation density on the system performance of the heat sink is studied. The conclusions of this study are:

Pressure drop across heat sink reduced with the increase in perforation density or by reducing the perforation pitch. This was predominantly because of increase in the number of perforations on the pin fins which resulted in a lesser obstruction to the flow of air, but for the same number of perforations, the pressure drop was lower for configuration having higher perforation pitch.

Nusselt number increased with the reduction in perforation pitch. This was mainly because of the increase in number of perforations resulting in increased effective convective heat transfer area. If the number of perforations was equal, the perforation pitch did not have any significant effect on Nusselt number as there was no change in the convective heat transfer area.

System performance increased with the reduction in perforation pitch for different number of perforations on each pin fin, but for equal number of perforations, the configuration having higher perforation pitch was reported to have a higher value of system performance.

References

1. Khattak Z, Ali HM (2019) Air cooled heat sink geometries subjected to forced flow: A critical review. Int J Heat Mass Transf 130:141–161. https://doi.org/10.1016/j.ijheatmasstransfer.2018.08.048
2. Nazari M, Karami M, Ashouri M (2014) Comparing the thermal performance of water, Ethylene Glycol, Alumina and CNT nanofluids in CPU cooling: Experimental study. Exp. Therm. Fluid Sci. 57:371–377. https://doi.org/10.1016/j.expthermflusci.2014.06.003

3. Ho CJ, Wei LC, Li ZW (2010) An experimental investigation of forced convective cooling performance of a microchannel heat sink with Al2O3/water nanofluid. Appl Therm Eng 30:96–103. https://doi.org/10.1016/j.applthermaleng.2009.07.003
4. Tullius JF, Bayazitoglu Y (2013) Effect of Al2O3/H2O nanofluid on MWNT circular fin structures in a minichannel. Int J Heat Mass Transf 60:523–530. https://doi.org/10.1016/j.ijheatmasstransfer.2013.01.035
5. Vanapalli S, Ter Brake HJM (2013) Assessment of thermal conductivity, viscosity and specific heat of nanofluids in single phase laminar internal forced convection. Int J Heat Mass Transf 64:689–693. https://doi.org/10.1016/j.ijheatmasstransfer.2013.05.033
6. Chein R, Chuang J (2007) Experimental microchannel heat sink performance studies using nanofluids. Int J Therm Sci 46:57–66. https://doi.org/10.1016/j.ijthermalsci.2006.03.009
7. Chein R, Huang G (2005) Analysis of microchannel heat sink performance using nanofluids. Appl Therm Eng 25:3104–3114. https://doi.org/10.1016/j.applthermaleng.2005.03.008
8. Yu Y, Simon T, Cui T (2013) A parametric study of heat transfer in an air-cooled heat sink enhanced by actuated plates. Int J Heat Mass Transf 64:792–801. https://doi.org/10.1016/j.ijheatmasstransfer.2013.04.065
9. Jajja SA, Ali W, Ali HM, Ali AM (2014) Water cooled minichannel heat sinks for microprocessor cooling: Effect of fin spacing. Appl Therm Eng 64:76–82. https://doi.org/10.1016/j.applthermaleng.2013.12.007
10. Lin L, Zhao J, Lu G, Wang XD, Yan WM (2017) Heat transfer enhancement in microchannel heat sink by wavy channel with changing wavelength/amplitude. Int J Therm Sci 118:423–434. https://doi.org/10.1016/j.ijthermalsci.2017.05.013
11. Sikka KK, Torrance KE, Scholler CU, Salanova PI (2002) Heat sinks with fluted and wavy plate fins in natural and low-velocity forced convection. IEEE Trans. Components Packag. Technol. 25:283–292. https://doi.org/10.1109/TCAPT.2002.1010019
12. Junaidi, Md. Abdul Raheem; Rao, Raghavendr; Sadaq, S. Irfan; Ansari, M.M.: Thermal Analysis of Splayed Pin Fin Heat Sink. Int. J. Mod. Commun. Technol. Res. 2, 48–53 (2014). https://www.erpublication.org/ijmctr/published_paper/IJMCTR021417
13. Chin SB, Foo JJ, Lai YL, Yong TKK (2013) Forced convective heat transfer enhancement with perforated pin fins. Heat Mass Transf 49:1447–1458. https://doi.org/10.1007/s00231-013-1186-z
14. ANSYS FLUENT 13 User's Guide: Ansys Fluent Theory Guide. ANSYS Inc., USA. 15317, 724–746 (2013)

Design of Green Building Using Geothermal Cooling Techniques

Helal Ahmad Farhan, Rajbala Purnima Priya, Sukanta Nayak, and Manikant Paswan

Nomenclature

L	Length of GI pipe under the earth
h	Heat transfer coefficient
H	Cooling capacity
m	Mass of air in closed loop
ΔT	Temperature difference between ambient and earth
d	Diameter of pipe
V	Volume of space
K	Thermal conductivity of air
$\mathrm{Nu_d}$	Nusselt number
$\mathrm{Gr_d}$	Grashoffs number
g	Acceleration due to gravity
β	Volume expansion coefficient
ν	Kinematic viscosity of air
T_f	Film temperature
T_w	Ambient air temperature
C_p	Specific heat at constant pressure of air at 25 °C
T_a	Temperature of air in earth tube.

H. A. Farhan · R. P. Priya · S. Nayak · M. Paswan (✉)
National Institute of Technology, Jamshedpur, Jharkhand 831014, India
e-mail: mkpaswan.me@nitjsr.ac.in

D. Sharma and S. Roy (eds.), *Emerging Trends in Energy Conversion and Thermo-Fluid Systems*, Lecture Notes in Mechanical Engineering,
https://doi.org/10.1007/978-981-19-3410-0_7

1 Introduction

Building heating and cooling accounts for major share of energy consumption. Developing as well as developed countries use fossil fuels to generate electricity as they are conventional source to generate electricity, and they face problem in technology installation, high capital cost, and many more things. In this decade, scientists and researchers are more interested in clean and green energy, i.e., renewable sources of energy.

Conventional cooling methods consume significant amount of electricity, and several studies showed that the artificial space cooling causes sick building syndrome. Therefore, passive cooling is an effective way to reduce building load as well as helps to reduce health issue. There are various passive cooling methods which are being used according to their operational feasibility and environmental condition. Greenhouse gas emission is the crucial problem facing everyone which is responsible for global warming. Scientist and environmentalist are now focusing on green and clean sources of energy so that emission of harmful gases such as CO_2, methane, fluorinated gas reduces. Housing and building are second largest area where electricity is consumed directly. Building heating and cooling reported large amount of electricity consumption in building. So, it is important to utilize clean and green source of energy. Natural ventilation technique is one among the various passive cooling techniques which supplies fresh air to the occupants and omits the dust particles from the space. Basically, two mechanisms of natural ventilation have been identified, the first one is wind-driven ventilation, and second one is stack ventilation. Geothermal passive cooling technique is again one among those passive cooling techniques which utilizes the temperature difference of soil and air in heat exchanger to cool the spaces. It has been found in the several studies that the temperature of soil is constant at certain depth for all atmospheric condition, and characteristics of soil can effectively be used by digging a trench and applying effective heat exchanger. By combining these passive cooling techniques may reduce or the building heating and cooling loads. TCs are the material which can be used in order to reduce the cost of ground-source heat pump system [1]. Most of the space cooling methods involve the use of fossil fuel resulting in greenhouse gas (GHG) emissions and harmful effects on the environment [2]. Ground-source heat pipe is one of the strict technologies which functions by exchanging the heat between ground and soil layer at certain depth inside the earth [3, 4]. This can be done by rising ground-loop heat exchanger pipes. Inside the ground-loop heat exchanger pipes, a mixture of water and antifreeze example ethanol flows. One such technology is the ground-source heat pump (GSHP), which operates by exchanging heat with the ground and soil layers at certain depths [5, 6].

2 Literature Review and Objective

The main parameters for wind-driven ventilation are air flow rate through opening and rate of ventilation. Therefore, in order to calculate these parameters, various analytical and computational methods have been investigated and proposed by different groups of researchers. For single-zone simple opening and multiple-zone complex opening, an extensive study for wind-driven ventilation has been done by Kasim et al. [7] for different opening configuration by using computational method and found that the opening located near the upper edge of the wall drives more air through the opening. An empirical relation is developed on the basis of fast Fourier transform by Wang et al. [8] to predict the fluctuating ventilation rate, and this empirical relation correlates the wind speed and rate of ventilation linearly and found that for mean and fluctuating ventilation rate, particle image velocimetry (PIV) does not yield accurate results; therefore, CFD may be used in the PIV. A computational study of CFD in $k - \omega$ domain revealed that overall ventilation best predicted by $k - \omega$ and disagreement of measured value and simulation value depends upon the size of ridge opening. Therefore, it can be concluded that ventilation rate for simple geometry and single zone can be estimated by using simple analytical methods, whereas complex opening and multiple zones required any suitable software, such as CFD. Thermal mass is materials which can store the heat energy and when it is directly or indirectly exposed to the solar radiation. These materials store heat energy in day time and release at night. This mechanism provides better thermal comfort in cold region, but in hot region, thermal mass can be coupled with night ventilation to provide cooling effect in night time, while in day time, proper use of insulation over the walls may reduce the heat leakage in the space. In addition to thermal mass, phase change material can also be incorporated into the construction material as well as make the objects for interior use. Phase change material changes its phase from solid to liquid when temperature increases due to heat absorbed by the material; therefore, this physical reaction is endothermic. And when temperature of environment decreases, heat is released by the material, and material becomes solid; therefore, this reaction is exothermic. Hence, such kind of material may be used for architectural application. Phase change material can be broadly classified into three groups such as organic, inorganic, and eutectic [9]. Edna Shaviv et al. [10] studied the strategy for thermal mass coupled with night ventilation for hot and humid ambient condition and obtained result by using ENERGY simulation model, which showed that the temperature reduced by 3–6 °C when compared with ambient temperature without using any air-conditioning. Moreover, it has also been concluded that the reduction of temperature depends upon the quantity of thermal mass, night ventilation rate, and swing of ambient temperature across day and night. Geothermal passive cooling technique uses temperature gradient of surface of ground and temperature at certain depth underground, which may be used as to cool the spaces directly by using heat exchanger or can be coupled to any other renewable and non-renewable energy systems in order to reduce the cooling load of buildings. As it has been observed through the experiments that the temperature of soil decreases significantly with increase of depth from the ground up to certain level, after that the temperature gradient becomes almost negligible. For this particular technology, several research works have been performed analytically and experimentally. Ralegaonkar et al. [11] performed a case study on geothermal cooling systems for an educational building in tropical climate in India, where evaporative cooler and air-conditioner are generally used to cool the spaces and found that geothermal space cooling systems save approximately 90% of electricity when compared to air-conditioner and saves 100% of water when compared with evaporative cooler. At some particular location, it has been observed that the inner temperature of soil may increase due to soil saturation. Yu et al. [12] experimentally investigated a coupled system of geothermal and solar collector. The collector provides more air flow during day time, since the solar intensity is more; hence, it is completely natural cooling operation without using any external source like electricity. After one year of forced air flow test, the temperature of the soil increased significantly, and hence, cooling effect enormously reduced. The soil took two weeks to overcome the thermal saturation condition after forced air flow test. Moreover, it has also been found that the heat dissipation of underground of soil is more in horizontal direction than in vertical. Therefore, for designing geothermal system for cooling, soil saturation is an important consideration to improve thermal performance of the system. Geothermal cooling application can also be used to increase the performance of photovoltaic (PV) modules which may indirectly reduce the load of the building. Nabil et al. [13] experimentally analyzed the performance of PV module which is coupled with geothermal cooling in hot climate condition in order to improve the performance of PV panel and protect panel from the hot condition. In this study, the ambient air cooled geothermal cooling and then employed to cool the back surface of panels. This mechanism cools the surface from 55 °C to 42 °C; as a result of this, PV module output increased by 18.9% and electrical efficiency increased by 23%. Graffar [14] did an experimental study for air-conditioning based on closed-loop geothermal system. Geothermal conditioner is experimentally observed and found that output temperature of the space is nearly 25 °C irrespective of ambient condition. While the coefficient of performance becomes double when evaporative cooling system coupled with geothermal system to cool, the water and cooling system become more efficient.

The main objective of this paper is to study the geothermal cooling system analytically and experimentally.

3 Methodology

3.1 Geothermal Cooling System

Geothermal cooling system provides an alternative for air-conditioning. The temperature and humidity data shows that from the month of June to October, the humidity is significantly high, so it serves as a good alternative of evaporative cooler too (Fig. 1).

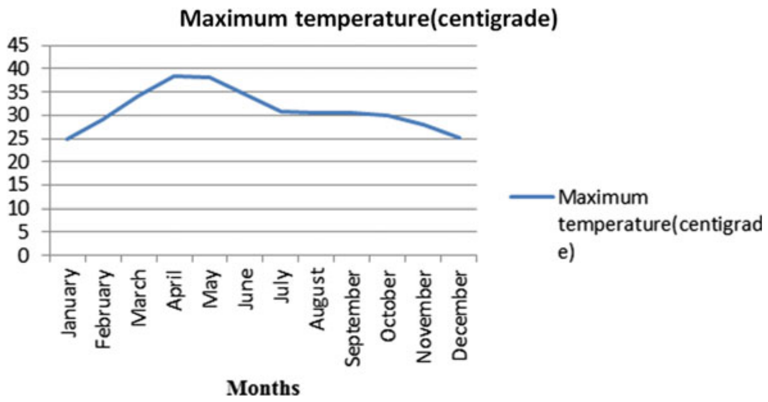

Fig. 1 Maximum temperature data for year 2020 at Jamshedpur

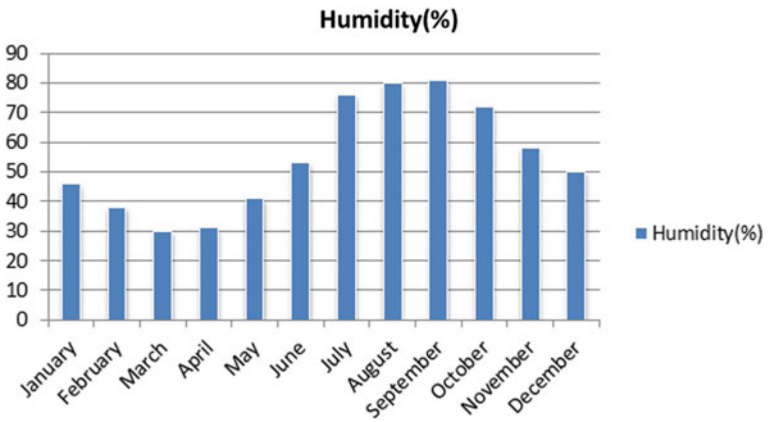

Fig. 2 Average data of humidity for year 2020 at Jamshedpur

The temperature data shows that in this particular location, the cooling load is high in the month of February to June, and particularly in the month of May, the atmospheric temperature is highest; therefore, we selected the month of May for experimental study (Fig. 2).

3.2 Analytical Method

The length of pipe has been calculated theoretically by the basic method available in the books and literatures [11, 15], and performance can be compared with the experimental results.

$$L = \frac{Q}{\pi h d(\Delta T)} \tag{1}$$

$$Q = m C_{\mathrm{p}} \Delta T \tag{2}$$

$$m = \rho V \tag{3}$$

$$h = \frac{K \cdot \mathrm{Nu_d}}{d} \tag{4}$$

$$\mathrm{Nu_d} = 0.53 \cdot (\mathrm{Gr_d})^{0.25} \tag{5}$$

$$\mathrm{Gr_d} = \frac{g\beta d^3 \Delta T}{\upsilon^2} \tag{6}$$

$$\beta = \frac{1}{T_{\mathrm{f}}} \tag{7}$$

$$T_{\mathrm{f}} = \frac{T_{\mathrm{a}} + T_{\mathrm{w}}}{2} \tag{8}$$

The size of the room is 10 * 10 ft and height of the room 12 ft. The GI pipe is to be used with the required length.

3.3 Experimental Method

An experimental setup has been made in a particular location. (Fig. 3)

A well has been dug of 50 ft into the ground to see the variation of underground temperature, and a pipe is used to connect the outlet and inlet of the space. And, 0.5 hp blower is to be used to circulate the air (Table 1).

4 Results and Discussion

According to theoretical procedure by using adequate data and assumption, the length of the pipe has been found as 70 m. The GI pipe of 1 inch diameter has been used. For cooling the volume of 10 * 10 * 12 ft, the ambient temperature has been taken as 38 °C which is the highest for selected location. And, expected outlet temperature from the earth has been taken as 22 °C.

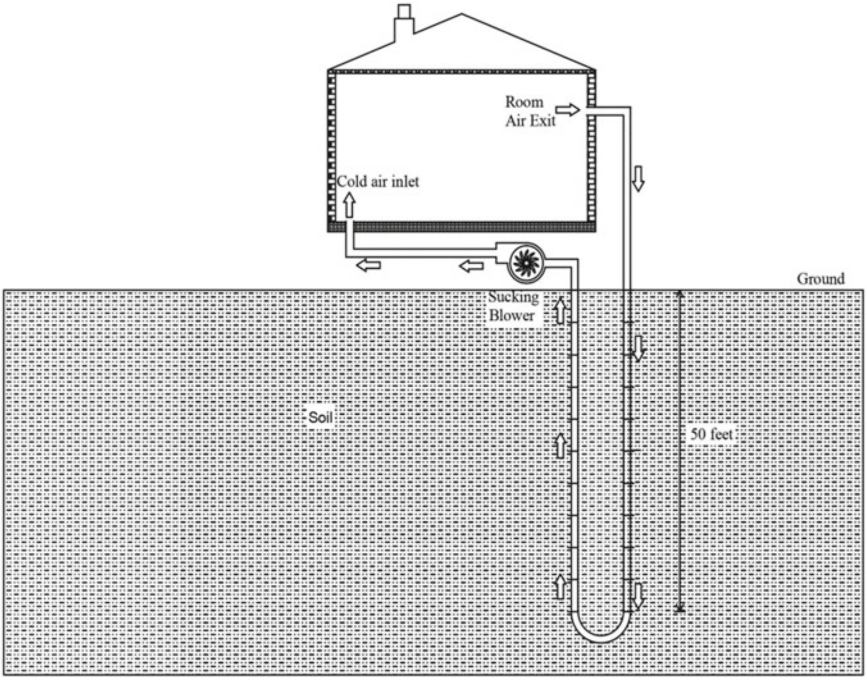

Fig. 3 Experimental setup of geothermal cooling

Table 1 Meteorological data of the weather for May 21, 2021

Sunrise	5:02 AM
Sunset	6:22 PM
Maximum day temperature	38.7 °C
Average wind speed	10.94 km/h
Minimum day temperature	26 °C
Humidity at noon	38%
Average temperature	32 °C

The graph shows that the temperature decreases with increase in depth. Therefore, employing the effective heat exchanger, the temperature of the air may decrease further, and consequently, cooling effect will increase. (Figs. 4 and 5)

The experimental setup consists of copper thermocouples which are used to calculate the temperature of air. And, there are several thermocouples employed to check the temperature of soil at different levels of depth as shown in the graph. The test has been conducted from 11.00AM to 17.00 PM on May 21, 2021.

The average temperature of soil which is a heat sink is 24 °C, and the inlet air temperature at the beginning of the experiment is close to ambient temperature that

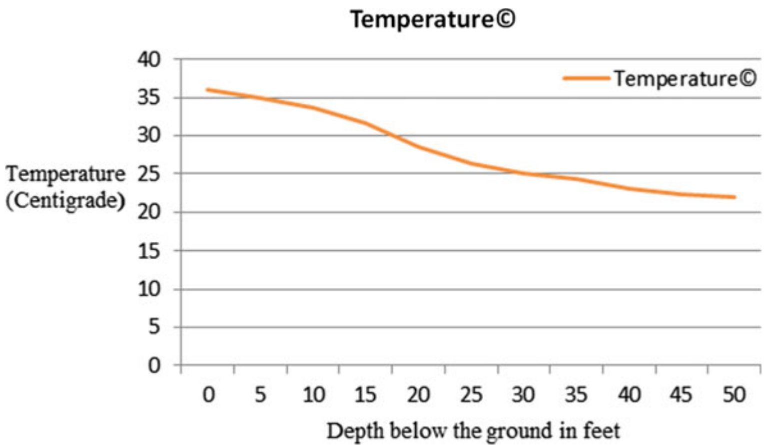

Fig. 4 Variation of temperature with variation of depth in feet

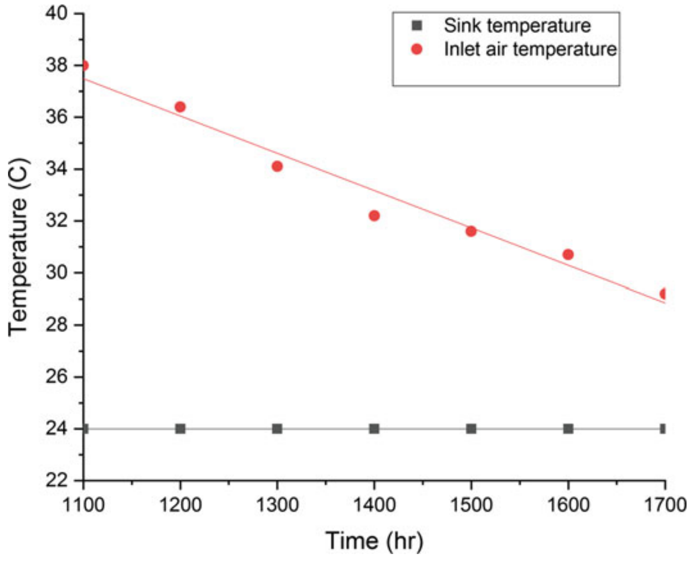

Fig. 5 Variation of soil (sink) temperature and air inlet temperature versus test time

is 38 °C and decreases during the experiment and reaches up to 29.4 °C by operating through a pump of 0.5 hp.

5 Conclusion

Passive cooling techniques can be incorporated into the building to reduce the cooling load. The comparison of theoretical and experimental results for geothermal cooling system shows that the temperature of space reduces by 3–5 °C. And hence, significant amount of cooling may be achieved for the hot climate condition. The performance of geothermal may further increase by improving the design of earth air heat exchangers. The continuous use of geothermal may create problem of thermal saturation of soil; therefore, it is also an important problem which needs to be addressed. Moreover, integrating additional passive cooling systems may help in further reducing the building's load and minimizing the threat of sick building syndrome.

Acknowledgements The authors are highly grateful to the Department of Mechanical Engineering, NIT Jamshedpur, for all the supports for making this research happen.

References

1. Alavy M, Paries M, Wang J, Rosen MA (2021) Assessment of a novel phase change material based—thermal caisson for geothermal heating and cooling. Energy Convers Manage 234:113928
2. Szekeres A, Jeswiet J (2018) Heat pumps in Ontario: Effects of hourly temperature changes and electricity generation on greenhouse gas emissions. Int J Energy Environ Eng 10(2):157–179
3. Koobi-Fayegh S, Rosen MA (2018) Long term study of vertical ground heat exchangers with varying seasonal heat fluxes. Geothermic 75:15–25
4. Rosen MA, Koobi-Fayegh S (2017) Geothermal energy: sustainable heating and cooling using the ground. Wiley, London
5. Sliwa T, Sojczynska A, Rosen MA, Kowalski T (2019) Evaluation of temperature profiling quantity in determining energy efficiencies of borehole heat exchangers. Geothermic
6. Chen F, Mao J, Li C, Hou P, Li Y, Xing Z (2018) Restoration performance and operation characteristics of a vertical U-tube ground source heat pump system with phase change grouts under different running modes. Appl Therm Eng
7. Kasim NFM, Zaki SA, Ali MSM, Ikegaya N, Razak AA (2016) Computational study on the influence of different opening position on wind-induced natural ventilation in urban building of cubical array. In: 4th international conference on countermeasures to urban heat island (UHI). Procedia Eng 169:256–263
8. Warren PR (1978) Ventilation through openings on the one wall only. Energy Conserv Heating Cooling Vent Build 1(1):186–206
9. Pasupathy A, Velraj R, Seeniraj RV (2008) Phase change material-based building architecture for thermal management in residential and commercial establishments. Renew Sustain Energy Rev 12:39–64
10. Shaviv E, Yezioro A, Capeluto IG (2001) Thermal mass and night ventilation as passivecooling design strategy. Renewable Energy 24:445–452
11. Ralegaonkar R, Kamath MV, Dakwale VA (2014) Design and development of geothermal cooling system for composite climatic zone in India. J Inst Eng India Ser A 95(3):179–183. https://doi.org/10.1007/s40030-014-0082-y
12. Yu Y, Li H, Niu F, Yu D (2014) Investigation of a coupled geothermal cooling system with earth tube and solar chimney. Appl Energy 114:209–217

13. Elminshawy NAS, Mohamed AMI, Morada K, Elhenawy Y, Alrobaian AA (2019) Performance of PV panel coupled with geothermal air-cooling system subjected to hot climatic. Appl Therm Eng 148:1–9
14. Momin GG (2013) Experimental investigation of geothermal air conditioning. Am J Eng Res (AJER) 02(12):157–170. e-ISSN: 2320–0847, p-ISSN: 2320–0936
15. Nag PK (2011) Heat and mass transfer, 3rd edn. Tata McGraw Hill Education Private Limited, New Delhi

Three-Dimensional Numerical Simulation of Free Convection Over Parallel Fins Heat Sink

Vikram Meena and Amit Arora

Nomenclature

Nu	Nusselt number
Ra	Rayleigh number
μ	Viscosity of air
C_{p}	Specific heat of air
β	Thermal expansion coefficient
ϑ	Kinematic viscosity
g	Gravity
α	Thermal diffusivity
$T_{\mathrm{avg,s}}$	The average surface temperature of a heat sink
T_{a}	Ambient temperature
Pr	Prandtl number
k	Thermal conductivity of air
L	Fin length
p	Pressure
F	Body force acting on a fluid element

1 Introduction

Thermal management of electronic devices has vast applications in several industries such as the telecommunication industry, aerospace industry, automotive industries,

V. Meena (✉) · A. Arora
Department of Mechanical Engineering, Malaviya National Institute of Technology Jaipur, Jaipur, Rajasthan 302017, India
e-mail: vikrammeena332@gmail.com

D. Sharma and S. Roy (eds.), *Emerging Trends in Energy Conversion and Thermo-Fluid Systems*, Lecture Notes in Mechanical Engineering,
https://doi.org/10.1007/978-981-19-3410-0_8

and renewable energy systems. Efficient thermal management of such devices is essential for their durability and optimum performance. Overheating is the major culprit behind the failures of such devices. Being reliable, cheap, and quiet in operation, passive cooling methods are widely used for the cooling of such devices. Additionally, these methods require no auxiliary power as they rely on natural convection.

Finned heat sinks are being widely used for electronic cooling. They improve the rate of heat transfer to or from the surroundings by adding surface area to increase the convective heat transfer rate. Several orientations of the heat sink like horizontal [1, 2], vertical [3–5], and inclined [6, 7] are studied to find out the optimum performance conditions. Geometrical modifications are also done by some researchers [8]. Micheli et al. [9] experimentally investigated the micro-scaled plate fins and pin fins under natural convection. Their results show that the use of micro-pin fins can reduce the weight of the heat sink along with an increase in thermal performance. Performance investigation of new designs of plate fin heat sinks was experimentally done by Haghighi et al. [10]. Their results revealed that the rate of heat transfer increased and thermal resistance decreased when plate cubic pin fins were used instead of plate fins. The optimum values of fin spacing and the total number of fins were 8.5 mm and 7 mm, respectively. Sathe et al. [11] numerically investigated the impact of slit introduction on the performance of plain heat sinks at vertical orientation. They found that the introduction of slits has reduced the weight of the heat sink along with an enhancement of thermal performance.

Most of the studies are done on the orientation of heat sink, slit introduction, and design modifications of heat sinks under natural convection conditions. A little work is done in the field of plate square pin fins. Accordingly, this article presents a numerical study to investigate the performance of the plate fins and plate square pin fins in a vertical orientation.

2 Mathematical Model

2.1 Heat Sink Model

A total 9 number of plate fins are placed on the base plate with 2 mm thickness, 16.5 mm fin spacing, 200 mm fin length, and 50 mm height. The dimension of the base plate is 150 mm × 200 mm. Heat flux is applied at the bottom of the base plate. The heat input is varied from 25 to 125 W. The dimensions of the fluid domain are 5L, 4L, and 9L for length, width, and height, respectively. The square pin fins are introduced between two plate fins. Three different values of pin fin spacing are taken, namely 8, 10, and 12 mm. The thickness of the pin fin is the same as that of the plate fin.

Radiation losses to the ambient and conduction losses to the surrounding channel are neglected. A 3D steady-state simulation has been done using Ansys Fluent 15.0.

2.2 Governing Equations

Relevant equations of heat and mass transfer are used and then discretization of equations has been done using the finite volume method. The conservation of mass, momentum, and energy in the fluid is applied assuming the fluid with constant properties.

The governing equations and correlations are:

Continuity equation:

$$\nabla \cdot (\rho v) = 0 \tag{1}$$

Momentum equation:

$$\begin{gathered} \rho \frac{Dv}{Dt} = -\nabla p + \mu \nabla^2 v + F \\ (\text{for z} - \text{direction } \; F_Z = -\rho g) \end{gathered} \tag{2}$$

Energy equation:

$$\rho c_{\mathrm{p}} \frac{\mathrm{DT}}{Dt} = \nabla.(k \nabla T) + S_{\mathrm{h}} \tag{3}$$

Mcadam's correlation

$$\mathrm{Nu} = 0.59(\mathrm{Ra})^{1/4} \tag{4}$$

Churchill and Chu's first relation (laminar and turbulent flow)

$$\begin{gathered} \mathrm{Nu} = \left[0.825 + \frac{0.387(\mathrm{Ra})^{\frac{1}{6}}}{\left[1 + (0.492/\mathrm{Pr})^{\frac{9}{16}}\right]^{\frac{8}{27}}} \right]^2 \\ (\text{for } \; 10^{-1} < \mathrm{Ra} < 10^{12}) \end{gathered} \tag{5}$$

Churchill and Chu's second relation (laminar flow)

$$\begin{gathered} \mathrm{Nu} = 0.68 + \frac{0.67(\mathrm{Ra})^{\frac{1}{4}}}{\left[1 + (0.492/\,\mathrm{Pr})^{\frac{9}{16}}\right]^{\frac{4}{9}}} \\ (\text{for } 10^{-1} < \mathrm{Ra} < 10^{9}) \end{gathered} \tag{6}$$

$$\mathrm{Ra} = \frac{g\beta L^3 (T_{\mathrm{s}} - T_{\mathrm{a}})}{\vartheta \alpha} \tag{7}$$

The above equations are applied to solve natural convection heat transfer. All the thermal properties of air are taken as a function of temperature only.

2.3 Materials

Aluminum is used in the design of the heat sink, and the air is taken as the working fluids. The thermo-physical properties of these materials are given in Table 1.

Table 1 Thermo-physical properties of materials

Material	Thermal conductivity (W/m-K)	Density (kg/m^3)	Dynamic viscosity (kg/m-s)
Aluminum	202.4	2719	–
Air	0.0242	1.225	1.7894e−05

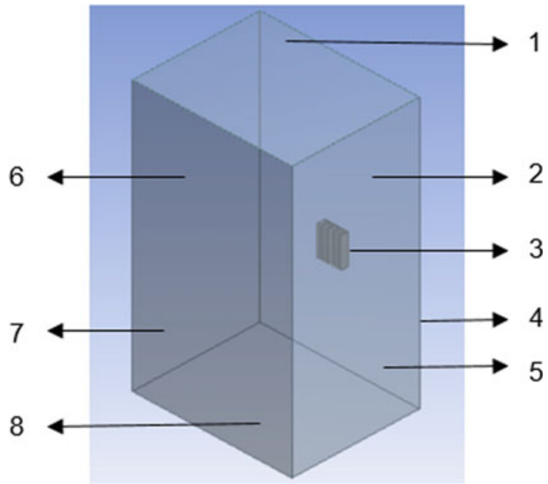

(1-Pressure outlet, 2-Adiabatic Bottom wall, 3-Heat sink, 4-Fluid domain, (5, 6)-Adiabatic side wall, 7-Top wall, 8-Pressure inlet)

Fig. 1 Computational domain

Table 2 Grid independency test

Number of elements	$T_{\text{avg,s}}$
646,000	312.46
1,073,860	312.88
1,359,720	313.31
1,413,082	313.37

2.4 Boundary Conditions and Grid Independency

A 3D fluid domain shown in Fig. 1 is taken for the analysis, and the flow is assumed to be steady and laminar. All the walls of the fluid domain are assumed to be adiabatic. The inlet and outlet section of the channel is imposed with pressure boundary conditions with a null gage pressure. Uniform heat flux is given at the base plate of the heat sink. The temperature of the ambient is taken as 298 K.

Accuracy of results is improved by using a SIMPLE algorithm to upwind the convective terms of second order. The convergence criteria for the momentum and continuity equation are taken as 10–4, while for the energy equation, it is taken as 10–6. To save computational time, a grid independence test has been performed by taking four different mesh sizes to find out the minimum number of elements. Results of the grid independence test are summarized in Table 2. The grid with an element size of 0.0015 m and a total number of elements 1,359,720 were selected for further calculations. Hexahedral meshing is used for higher accuracy. The mesh pattern of a heat sink with plate and plate square pin fin is shown in Figs. 2 and 3, respectively.

2.5 Model Validation

The assumption made in the simulation study is validated based on the average Nusselt number. The experimental data obtained by Sathe et al. [7] for the plate fin is compared with the simulation result. The experimental and simulation results are found to be in good agreement as shown in Fig. 4.

3 Results and Discussions

3.1 Effect of Heat Input

Five different values of input heat loads are taken, namely 25, 50, 75, 100, and 125 W, to analyze the impact of heat load on heat transfer rates. Figure 5 shows the variation in Nusselt number with power input. Nusselt number increases on increasing power input because of the increase in Rayleigh number. Figure 6 shows that the average

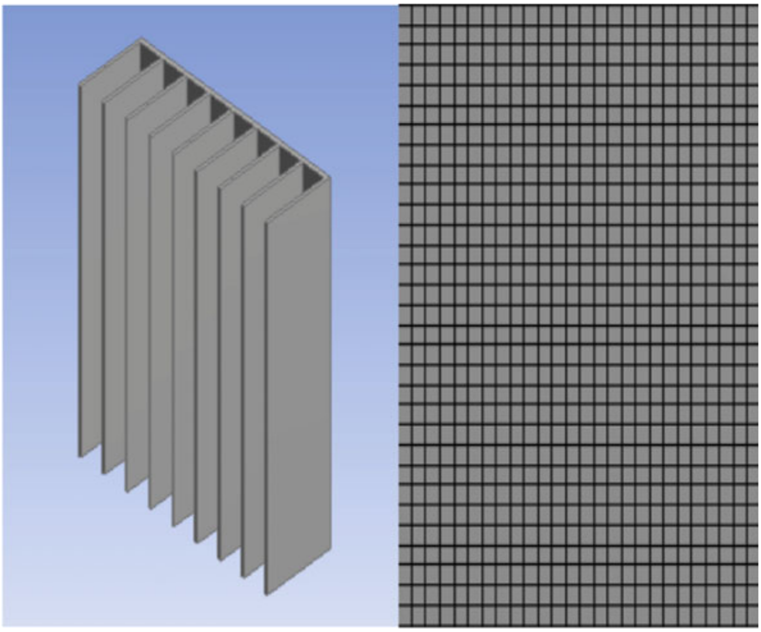

Fig. 2 Mesh pattern of plate fin

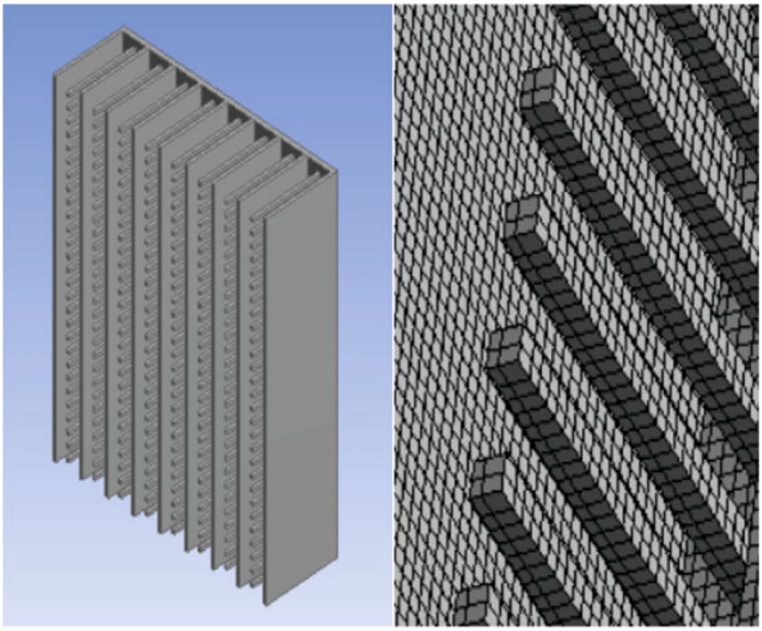

Fig. 3 Mesh pattern of plate square pin fin

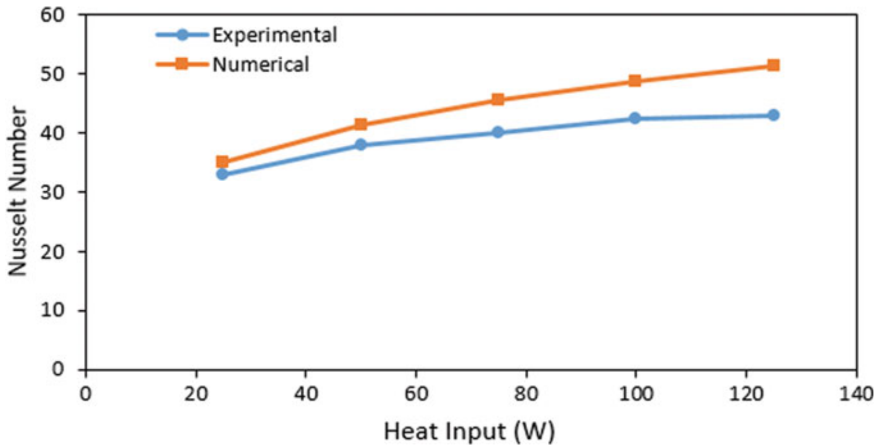

Fig. 4 Model validation

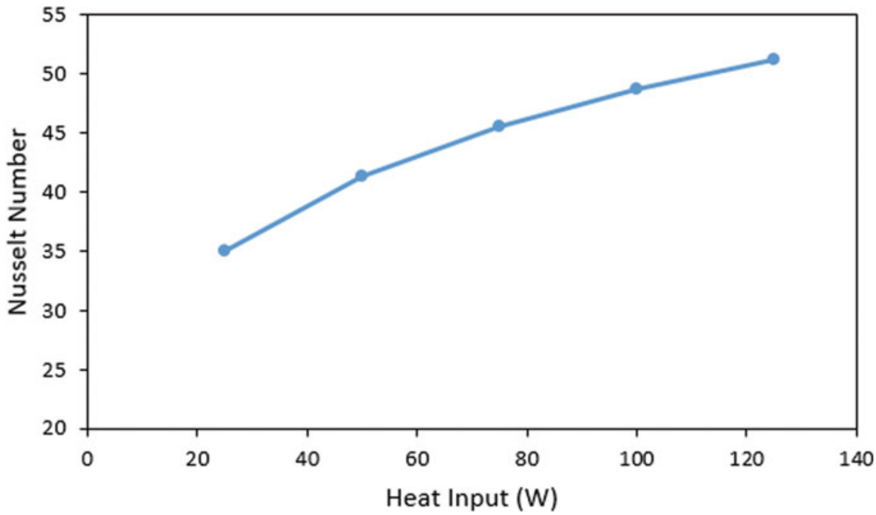

Fig. 5 Effect of heat input on Nusselt number

surface temperature of the heat sink increases with power input which increases the Rayleigh number. The average values of the surface temperature of the heat sink are 313.3 K, 325.8 K, 341.8 K, 355.4 K, and 368.5 K at 25 W, 50 W, 75 W, 100 W, and 125 W, respectively. The temperature and velocity contours at the midplane ($x = 65.75$ mm) are shown in Figs. 7 and 8, respectively. The temperature of the air increases when it comes in contact with the heated surface of the heat sink. This increased temperature accelerates the air from bottom to top due to the buoyancy effect. Thus, chimney flow patterns are developed. Due to the chimney flow pattern, the thermal boundary layer develops along the fin walls and base plate.

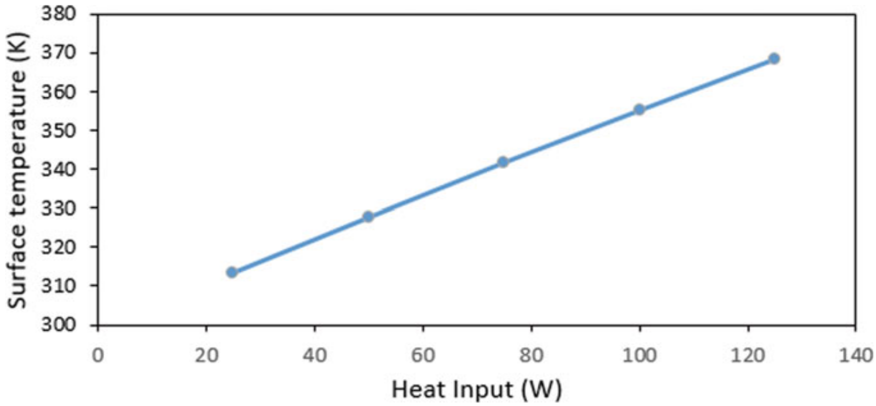

Fig. 6 Surface temperature versus heat input

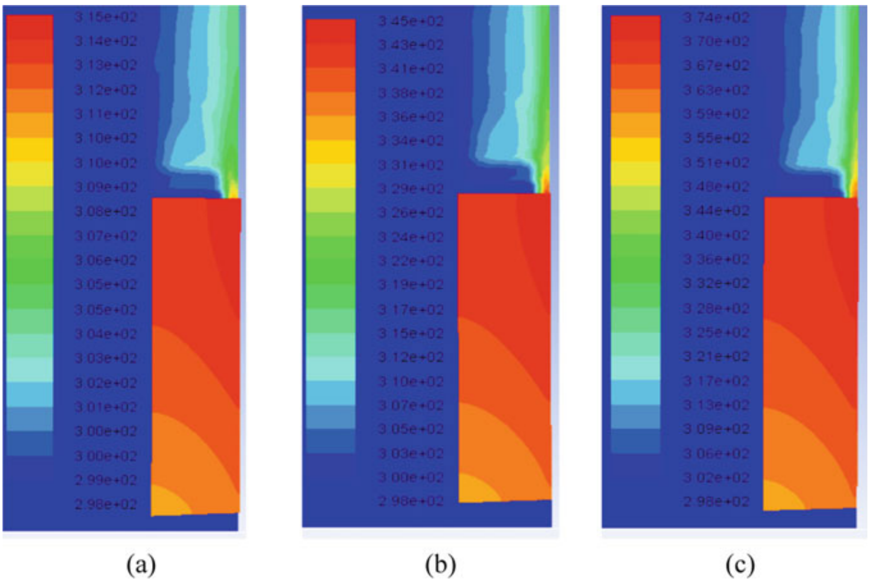

Fig. 7 Temperature contour for plate fin at plane $x = 65.75$ mm **a** 25 W, **b** 75 W, **c** 125 W

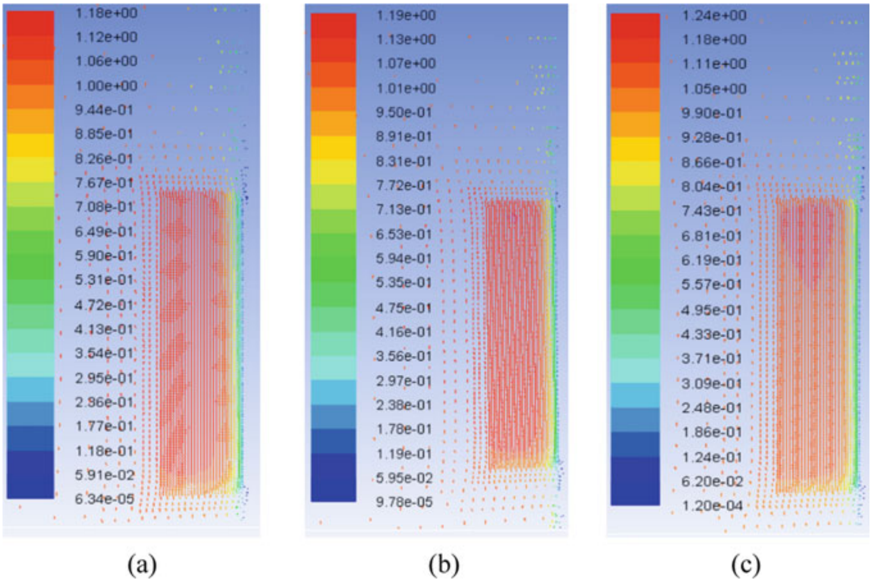

Fig. 8 Velocity contour for plate fin at plane $x = 65.75$ mm **a** 25 W **b** 75 W **c** 125 W

3.2 Effect of Addition of Pin Fin

Eight rows of square pin fins having an area of cross section 2 mm × 2 mm are inserted between 9 plate fins. The height of the square pin fins is kept the same as that of plate fins. Figure 9 shows that the average base plate temperature reduces with the addition of pin fins. The addition of pin fins is found to be more effective at higher values of heat input. Maximum reduction in base temperature is obtained at 125 W.

The average values of base temperature are 307.3 K, 316.7 K, 325.8 K, 334.6 K, and 343.4 K at 25 W, 50 W, 75 W, 100 W, and 125 W, respectively. A reduction of 7.1% is obtained in the average value of base plate temperature at 125 W. The temperature contours of plate square pin fins are shown in Fig. 10 at a plane = 70.375 mm.

4 Conclusions

A numerical simulation study has been done to analyze the impact of heat input and the addition of pin fins on the thermal performance of plate fin heat sink. Based on the study, the following key conclusions are drawn:

- Chimney flow patterns are developed due to the buoyancy effect in the fluid domain.
- Nusselt number and the average surface temperature increase on increasing input power.
- The length of the thermal boundary layer increases with fin length, and higher air velocities are observed at the top of the fins as compared to that at the lower part of fins.
- The addition of pin fins reduces the average baseplate temperature of the heat sink. Reductions in average base plate temperature are more at higher values of input power.
- The maximum amount of reduction in average baseplate temperature is obtained at 125 W by adding pin fins in between plate fins.

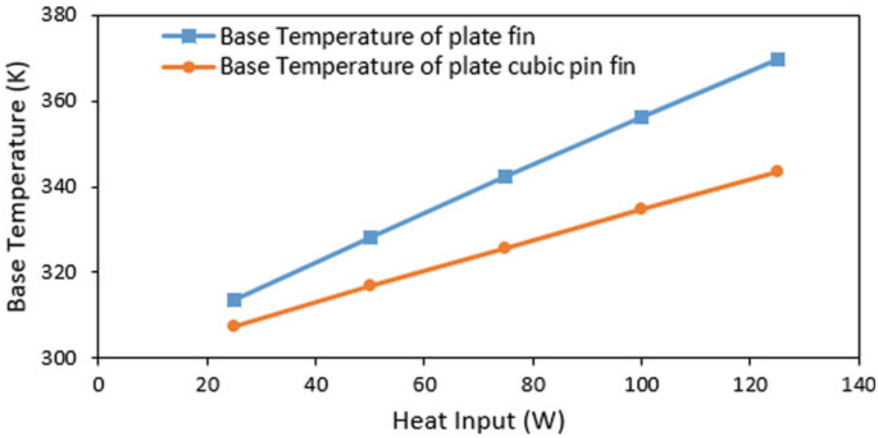

Fig. 9 Base temperature versus heat input

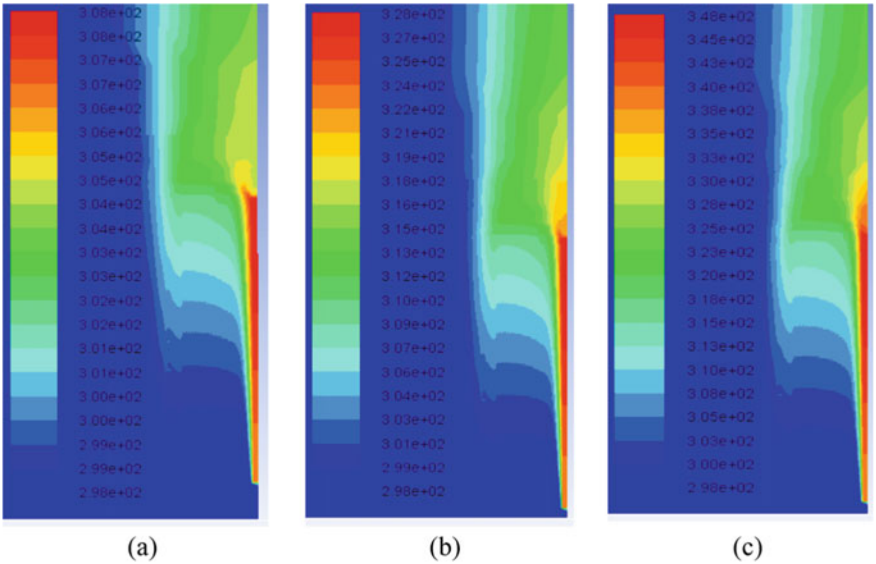

Fig. 10 Temperature contour for plate square pin fin at plane $x = 70.375$ mm **a** 25 W **b** 75 W **c** 125 W

Acknowledgements The corresponding authors are gratefully thankful to the Ministry of Education, Government of India, for providing the facilities and platform for the research work.

References

1. Jeon D, Byon C (2017) Thermal performance of plate fin heat sinks with dual-height fins subject to natural convection. Int J Heat Mass Transf 113:1086–1092. https://doi.org/10.1016/j.ijheatmasstransfer.2017.06.031
2. Sahoo LK, Roul MK, Swain RK (2018) CFD analysis of natural convection heat transfer augmentation from square conductive horizontal and inclined pin fin arrays. Int J Ambient Energy 39:840–851. https://doi.org/10.1080/01430750.2017.1354317
3. Nair DV, Ghoshdastidar PS (2018) A comparative study of 2-D and 3-D conjugate natural convection from a vertical rectangular fin array with multilayered base subjected to distributed high heat flux. Int J Heat Mass Transf 121:1316–1334. https://doi.org/10.1016/j.ijheatmasstransfer.2017.12.037
4. Kim DK (2012) Thermal optimization of plate-fin heat sinks with fins of variable thickness under natural convection. Int J Heat Mass Transf 55:752–761. https://doi.org/10.1016/j.ijheatmasstransfer.2011.10.034
5. Bocu Z, Altac Z (2011) Laminar natural convection heat transfer and air flow in three-dimensional rectangular enclosures with pin arrays attached to hot wall. Appl Therm Eng 31:3189–3195. https://doi.org/10.1016/j.applthermaleng.2011.05.045
6. Yari I, Mehrtash M (2013) Natural convection heat transfer from inclined plate-fin heat sinks. Int J Heat Mass Transf 56:574–593. https://doi.org/10.1016/j.ijheatmasstransfer.2012.08.050

7. Poovanan A, Mageshwaran G, DuraiRaj RB, Dilipan Karthik MK, Hariharan V (2020) Heat sink elimination and optimisation by natural convection method. Int J Ambient Energy 41:84–87. https://doi.org/10.1080/01430750.2017.1392355
8. Ahmadi M, Mostafavi G, Bahrami M (2014) Natural convection from rectangular interrupted fins. Int J Therm Sci 82:62–71. https://doi.org/10.1016/j.ijthermalsci.2014.03.016
9. Micheli L, Reddy KS, Mallick TK (2016) Experimental comparison of micro-scaled plate-fins and pin-fins under natural convection. Int Commun Heat Mass Transf 75:59–66. https://doi.org/10.1016/j.icheatmasstransfer.2016.03.023
10. Haghighi SS, Goshayeshi HR, Safaei MR (2018) Natural convection heat transfer enhancement in new designs of plate-fin based heat sinks. Int J Heat Mass Transf 125:640–647. https://doi.org/10.1016/j.ijheatmasstransfer.2018.04.122
11. Sathe A, Sanap S (202) Free convection heat transfer analysis of slitted fin heat sink of vertical orientation using CFD. Int J Ambient Energy 0:1–11. https://doi.org/10.1080/01430750.2020.1758785

Design of a New Curve-Shaped Fin and Natural Convection Analysis Using CFD

Md Quamar Alam, Amit Kumar, and Md Zishanur Rahman

Nomenclature

h_a	Coefficient of heat transfer for fin array (W/m^2 K)
g	Gravitational acceleration of earth (m/s^2)
T	Fin thickness (mm)
K	Thermal conductivity (Watt/m K)
Nu	Nusselt number
H	Fin height (horizontal) (mm)
S	Fin spacing (mm)
r_{cc}	Inner curve radius
R_{cc}	Outer curve radius
Ra	Rayleigh number
Pr	Prandtl number
W	Heat sink width (mm)
L	Vertical length of fin (mm)
T_∞	Ambient temperature (K)
T_{mean}	Average temperature at the base (K)
Q	Rate of total heat transfer (W).

M. Q. Alam
Department of Mechanical Engineering, Indian Institute of Technology, Patna, India
e-mail: quamar_2221me04@iitp.ac.in

M. Q. Alam · A. Kumar
Department of Mechanical Engineering, Muzaffarpur Institute of Technology, Muzaffarpur, India

M. Z. Rahman (✉)
Department of Mechanical Engineering, Nalanda College of Engineering, Chandi Nalanda, India
e-mail: rzishan10@gmail.com

D. Sharma and S. Roy (eds.), *Emerging Trends in Energy Conversion and Thermo-Fluid Systems*, Lecture Notes in Mechanical Engineering,
https://doi.org/10.1007/978-981-19-3410-0_9

1 Introduction

In today's world, electronic devices are very essential components used in industries. Almost all electrical and digital devices produce heat that must be dissipated to the environment in most of the applications, so that excess heat does not damage the equipment. So, they must be equipped in such a way that effective removal of heat can take place. For such cooling purposes, two approaches are widely embraced: active cooling [1–3] and passive cooling [4, 5]. In active cooling, the fluid is forced through the electronic components for removing the generated heat energy. In passive cooling, heat is dissipated to the surrounding environment by natural convection or radiation mode of heat transfer. Although the cooling method with an active approach can offer a better heat transfer rate, but it requires extra equipment like a fan or cooler with additional consumption of energy and cost. But, natural convection technique is a better choice, and extended surfaces are widely used in industries.

2 Literature Review and Objective

Several papers discuss the effect of the fin in the improvement of free, forced, and mixed convection heat transfer with different shapes and areas of application [6–8]. Hong and Chung [9] conducted a numerical and experimental analysis of the convection heat transfer of an array of the fin with the plate oriented vertically. They came out with optimum fin spacing in the heat sink for maximum heat transfer rate. Chang et al. [10] performed a numerical analysis of the thermal performance of the vertical array of fin with dimples and that without any dimples. It was found that there is a strong functional relationship between the Rayleigh number (Ra) and the average Nusselt number (Nu). Chu et al. [11] proposed a triangular fin shape for the heat sink with an alternating arrangement which appreciably increased the natural convection heat flow. Naserian et al. [12] performed an investigation of the natural convection in laminar type of flow originating from the vertical surface by providing different shapes in the V-type arrangement of the fin. Different parameters like geometry (shape), fin numbers, and spacing between them were considered for investigation. It was found that, on a vertical surface if the number of fin is increased, the thermal performance is also increased as long as the thickness of the boundary layer at its surface is small. In an experimental study by Ahmed, et al. [13], perforations in the square fins and heat flux were the primary varying parameter for investigation. The heat sink with a total of 50 fins and with a base area of 250 mm by 250 mm was considered. They found that the square fin with perforations has thermal performance superior to that of just a solid square fin for the whole range of Rayleigh numbers (Ra) under consideration.

From the review of available works of literature above, it can be said that the attention was drawn to enhance the heat sink's thermal performance. Most of them are limited to cases of vertical heat sinks with studies on vertical heat sinks with simple geometries of fin like square, rectangular, triangular, trapezoidal, staggered, and interrupted fins in free convection. And only a few of them are devoted to cases with wavy and curved geometry. Therefore, this study on heat sink geometry attempts to fill this gap in research up to now. The primary focus of this present work is to present a novel shape of fin that can improve the overall heat transfer rate. The comparison is made between the proposed fins geometry in the present study and the conventional rectangular fin in a free convection mode of heat transfer.

3 Computational Domain and Methods

3.1 Problem Statement

A vertically oriented curve-shaped fin is considered for studying heat transfer by natural convection mode. Base dimensions for heat sink are 101 mm width and 305 mm length (refer to Fig. 1). Aluminum has a high thermal conductivity. So, it was chosen as a heat sink material. Thermo-physical properties for aluminum and

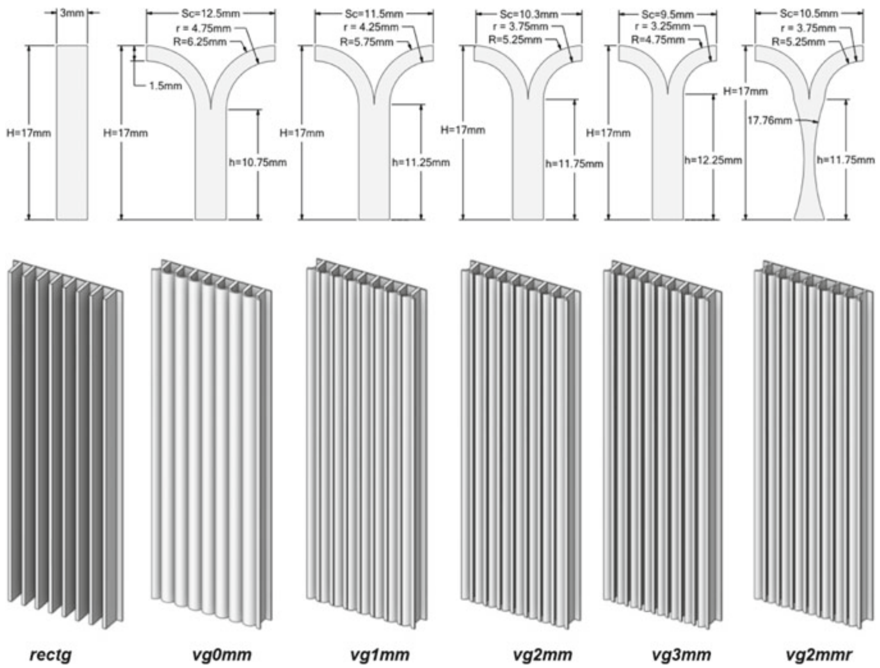

Fig. 1 Schematic diagram showing heat sinks with rectangular-shaped fin and novel curve-shaped fin in top and isometric view

Table 1 Thermo-physical properties of materials

	C_p (J/KgK)	μ (Kg/ms)	k (W/mK)	ρ (Kg/m^3)
Aluminum	871	–	202	2719
Air	1006	1.789×10^{-5}	0.0242	f(T)

air are shown in Table 1. A fluid domain of $1200 \times 300 \times 150$ mm^3 surrounds the heat sink.

The total fin height H is kept fixed, but the height of the rectangular part of fin is differed as 10.75 mm $\leq h \leq$ 17 mm (refer to Fig. 1) so that the effect of the curvature gap on the thermal performance of the heat sink can be studied. And also, the radius of circular curve r_{cc} and R_{cc} on the upper part of the fin is as per Eqs. (1) and (2).

$$r_{cc} = \frac{s}{2} \tag{1}$$

$$R_{cc} = \frac{s+t}{2} \tag{2}$$

3.2 Governing Equations

The governing equations for the fluid flow and heat transfer phenomenon taking place simultaneously were solved to predict the steady-state final temperature at heat sink base and fluid flow pattern.

Continuity equation:

$$\frac{\partial u}{\partial x} + \frac{\partial v}{\partial y} + \frac{\partial \omega}{\partial z} = 0 \tag{3}$$

where $u, v,$ and ω are velocity components along x, y, and z directions, respectively.

Momentum equations:

$$\rho\left(u\frac{\partial u}{\partial x} + v\frac{\partial u}{\partial y} + w\frac{\partial u}{\partial z}\right) = -\frac{\partial P_m}{\partial x} + \mu_{eff}\nabla^2 u \tag{4}$$

$$u\frac{\partial v}{\partial x} + v\frac{\partial v}{\partial y} + w\frac{\partial v}{\partial z} = \upsilon\nabla^2 v + g\beta(T - T_\infty) \tag{5}$$

$$\rho\left(u\frac{\partial w}{\partial x} + v\frac{\partial w}{\partial y} + w\frac{\partial w}{\partial z}\right) = -\frac{\partial P_m}{\partial z} + \mu_{eff}\nabla^2 w \tag{6}$$

where $P_{\mathrm{m}}, \mu_{\mathrm{eff}}, \upsilon$, and β represent the modified pressure, effective viscosity of the flow, kinematic viscosity, and the coefficient of thermal expansion, respectively.

Energy equation:

$$\rho_{C_p}\left(u\frac{\partial T}{\partial x} + v\frac{\partial T}{\partial y} + \omega\frac{\partial T}{\partial z}\right) = k\left(\frac{\partial^2 T}{\partial x^2} + \frac{\partial^2 T}{\partial \gamma^2} + \frac{\partial^2 T}{\partial z^2}\right) \tag{7}$$

where ρ, T, and k are the density, the temperature, and thermal conductivity of the fluid medium, respectively.

In this natural convection problem, the air is supposed to behave like incompressible ideal gas, so the calculation of its density is performed as per equation of state for the ideal gas [14] as given below:

$$\rho = \frac{P}{\overline{R}T} \tag{8}$$

where $\overline{R}$ is the characteristic gas constant.

Transport equations [19]:

$$\frac{\partial(\rho k)}{\partial t} + \frac{\partial(\rho k u_i)}{\partial x_i} = \frac{\partial}{\partial x_j}\left[\mathcal{T}_k\frac{\partial k}{\partial x_j}\right] + G_k + Y_k + S_k \tag{9}$$

$$\frac{\partial(\rho \omega)}{\partial t} + \frac{\partial(\rho \omega u_i)}{\partial x_i} = \frac{\partial}{\partial x_j}\left[\mathcal{T}_\omega\frac{\partial k}{\partial x_j}\right] + G_\omega + Y_\omega + S_\omega \tag{10}$$

where G_k represents the turbulent kinetic energy generation due to the mean velocity gradients. G_ω denotes the specific dissipation generation rate. $_k$ and $_\omega$ denote the effective diffusivity of turbulence kinetic energy (K) and specific dissipation rate (ω), respectively. Y_k and Y_ω denote the dissipation of k and ω, respectively, owing to turbulence.

3.3 Domain Definition and Boundary Conditions

In the present study, six heat sinks are modeled as shown in Fig. 1. For validation of numerical results, a rectangular fin is considered. For each case, two domains are defined: solid fin domain and fluid domain surrounding the fin. Meshing is refined near solid fin and fluid wall contact region, so that boundary layer effects can be captured. Only half of geometry is considered for calculation purposes so that computational effort can be reduced, and it was possible because of the symmetry in the problem considered. The boundary conditions used in CFD simulations are shown in Fig. 2. Starting from the fluid domain, the inlet is set as boundary condition 'pressure-inlet' and at the outlet of the fluid domain as 'pressure-outlet' boundary condition. The boundary condition 'symmetry' is applied to the right and the left

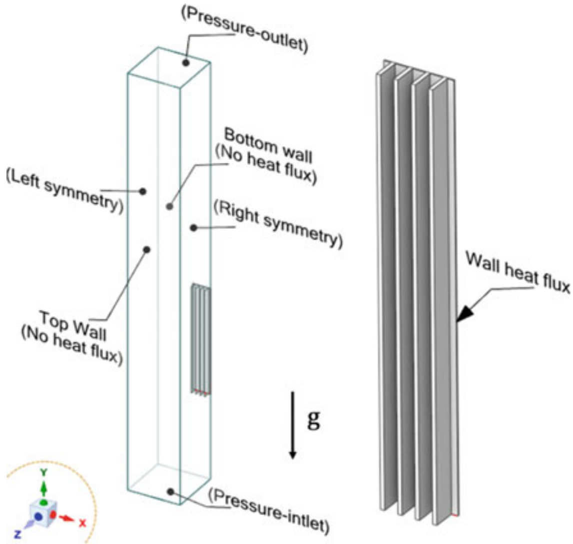

Fig. 2 Boundary conditions

wall of fluid domain, i.e., in X-plane at $X = 0$ mm and $X = 150$ mm. For the top and bottom wall of the fluid domain, the 'no heat flux' condition and 'no slip and no penetration' momentum boundary conditions are applied. And, a constant wall heat flux condition is chosen for the heat sink base, and simulation is repeated for different power supplies of 30 W, 60 W, 90 W, 120 W, and 150 W at the base.

3.4 Numerical Solver Setup

For calculating the solution for fluid flow and heat transfer in our analysis, Ansys Fluent 2021 R1 (Academic research license) is used as a CFD code solver. The solver makes use of the finite volume method (FVM) approach. The COUPLED algorithm is opted for coupling between pressure and velocity. And, the pressure-based solver is chosen as the pressure-based coupling algorithm gets a sturdy and logical single-phase implementation for steady-state flows [14]. For discretizing the convective terms of the energy equation, momentum equation, turbulence equation, and its rate of dissipation equation, 'second-order upwind' scheme is adopted to achieve a more error-free result. The method of the least square cell is used for computing gradient terms. The convergence criteria of 10^{-9} are set for the energy equation, and for the continuity, momentum, and turbulence equation, it is set at 10^{-6}. The relaxation factors 0.7, 0.3, and 1 are put in for the components of velocity, correction of pressure, and thermal energy, respectively.

3.5 Grid Independence Test

A test for grid independency of rectangular fin case is conducted to confirm that the numerical results obtained are accurate. The test was performed with four sets of the grid: 3.4 million, 4.6 million, 5.2 million, and 6.8 million. The meshing with 5.2 and 6.8 elements provided similar results. So, a 5.2 million grid system was selected for the present study. Most of the solutions started converging at 240 numbers of iteration, and each case took about 8–10 h to complete simulation on an intel-based i5 processor with 8 GB of RAM system configuration.

3.6 Model Validation

A rectangular fin (rectg) was chosen for the validation of our CFD study. Results obtained from numerical calculations were compared with that of empirical correlations for vertical plate suggested by the first relation of Churchill and Chu [15], Mc Adam's relation, and Bar-Cohen. Variation of temperature difference with heat input is given in Fig. 3 indicating difference between numerical results obtained from CFD and that obtained from the empirical correlations already available in the literature. There is an acceptable deviation from CFD results, thus validating numerical results in our study.

Churchill-Chu's first relation:

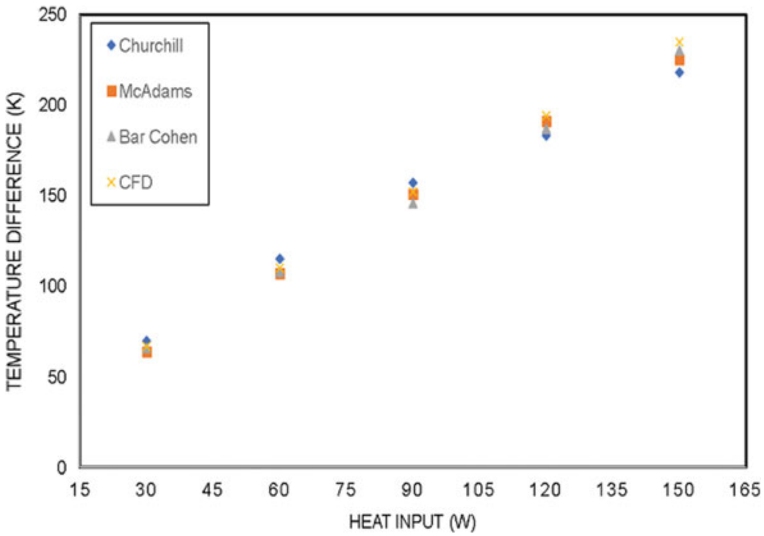

Fig. 3 Validation of numerical results

$$\mathrm{Nu} = \left[0.8251 + \frac{0.387(\mathrm{Ra})^{1/6}}{\left[1 + \left\langle\frac{0.492}{\mathrm{Pr}}\right\rangle\right]^{8/27}}\right]^2 \quad \text{for} \quad 10^{-1} < \mathrm{Ra} < 10^{12} \tag{11}$$

McAdam's correlation:

$$\mathrm{Nu} = (\mathrm{Ra})^{1/4} \quad \text{for } 10^4 < \mathrm{Ra} < 10^9 \tag{12}$$

Bar-Cohen correlation:

$$\mathrm{Nu} = \left[\frac{576}{\left\langle\frac{\mathrm{Ra.S}}{\mathrm{H}}\right\rangle^2} + \frac{2.873}{\left\langle\frac{\mathrm{Ra.S}}{\mathrm{H}}\right\rangle^{0.5}}\right]^{-0.5} \tag{13}$$

4 Results and Discussion

4.1 Temperature Distribution and Flow Pattern

Temperature difference variation with different heat input is shown in Fig. 6. Heat sink with rectangular fin configuration (rectg) is taken as the reference case. Linear variation is observed in all cases with minimal temperature in a case with a 'vg2mmr'-type configuration. An illustration for the cooling enhancement of the proposed fins is shown in Fig. 6, where a difference is taken between the base temperature of configuration (rectg) and that of the rest configurations considered in our study. It is found that the difference of temperature increases (absolute value) by increasing heating power input for different new designs proposed. More specifically, a lower temperature difference is observed in all the new proposed configurations when compared to that of the reference configuration. Also, it is found that the configurations vg2mm and vg2mmr offer the highest cooling enhancement with a base temperature difference of −19 K and −32 K, respectively, for 150 W heating power.

In the present study, heat transfer through radiation is neglected, so only the conduction and convection mode of heat transfer is taking part in the dissipation of heat. So, if the difference of base temperature becomes sufficiently high, the conductive heat transfer is dominating over that of convection. And here, the proposed fin shape (i.e., curvature at the fin tip) is playing a key role in evacuating maximum heat energy and thus improving the overall system performance.

The temperature contours of the heat sink are shown in Fig. 5 for 150 W (4869.34 w/m^2 heat flux). In each of the configurations, the temperature of the lower section of heat sink is less compared to that of the upper part. This difference arose because of the lower part being exposed to the low-temperature ambient air. But, the upper section of the heat sink is in contact with the heated air that is brought up taking

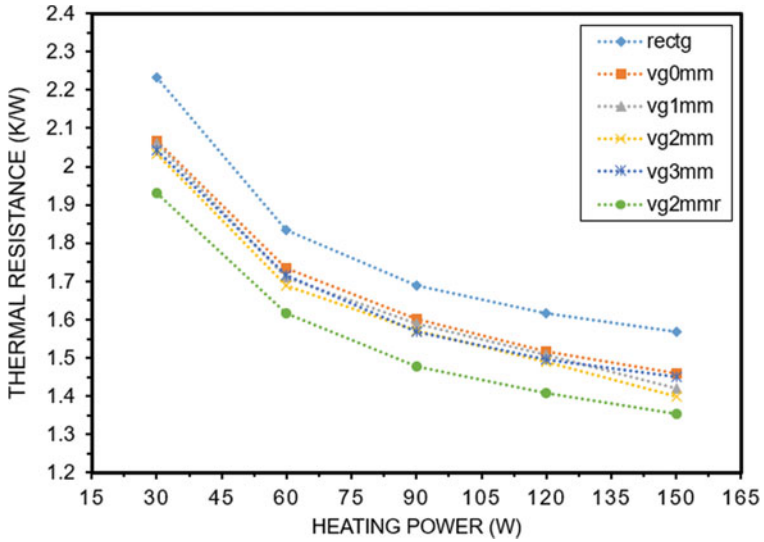

Fig. 4 Variation of thermal resistance with heat input

heat from the bottom part by the buoyancy force which is acting along the positive direction of '*Y*-axis' (opposing gravitational acceleration) as shown in Fig. 5.

4.2 Effect of the Novel Fin Shape on Thermal Performance

The cooling capacity of a fin is characterized by its thermal resistance. For each configuration considered in the present study, the variation of thermal resistance with heat input is shown in Fig. 4. It is quite evident from Fig. 4 that each of the newly proposed configurations (rectg, vg0mm, vg1mm, vg2mm, vg3mm, vg2mmr) has lower thermal resistance than that of the conventional rectangular fin (rectg). The thermal resistance for the new configurations vg0mm, vg1mm, vg2mm, vg3mm, and vg2mmr decreases by 5%, 6.7%, 7.8%, 6.32%, and 11.8%, respectively, when compared with the rectangular fin configuration (rectg) at heating power of 60 W (i.e., 1947.73 W/m^2 heat flux). Also, it is observed that adding vertical gap (refer to Figs. 1 and 5) in the curved portion of the fin subsequently from 1 to 2 mm shows a reduction in the thermal resistance, but at 3 mm gap and onwards, thermal resistance starts increasing again. So, we can say that the newly proposed fin configuration with a 2 mm vertical gap (vg2mm) shows the best cooling performance. Moreover, when this configuration (vg2mm) is further modified by adding internal ripples as suggested by Ihssane [16], (vg2mmr), it results in the best cooling performance with a maximal reduction in thermal resistance by up to 11.8% at 60 W. Also, it can be

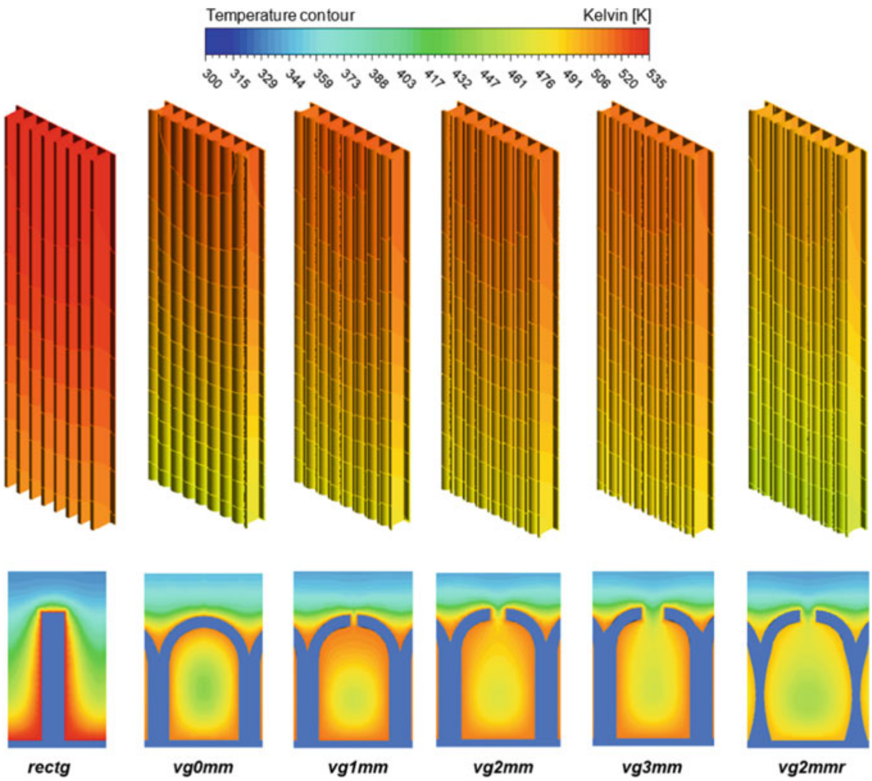

Fig. 5 Temperature contour in isometric view and on plane $y = 152.5$ mm for heating power of 150 W

seen that as the heat input increases from 30 to 150 W, the thermal resistance starts decreasing in each configuration.

And we know that plumes start developing in an environment when there is a temperature gradient along the direction of gravity or we may say there is a variation of temperature with height. Temperature contour with a 3D view and on a plane $y = 152.5$ mm (top view) at 150 w is shown in Fig. 5. When comparing this temperature contour near the fin wall–fluid (air) interface, it is found that the maximal temperature of the hot air is for the conventional rectangular fin configuration and minimum in the heat sink with the curved fin with ripple configuration (vg2mmr) Fig. 7.

5 Conclusion

- Curve-shaped fin offers a higher heat dissipation rate when compared with that of the rectangular fin.

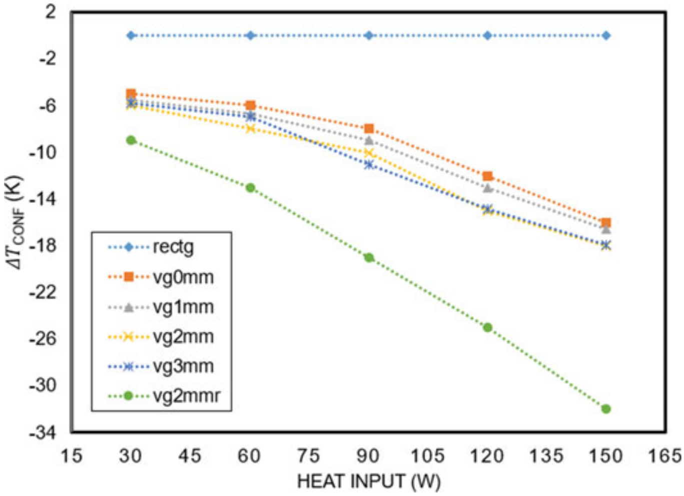

Fig. 6 Temperature difference versus heat input

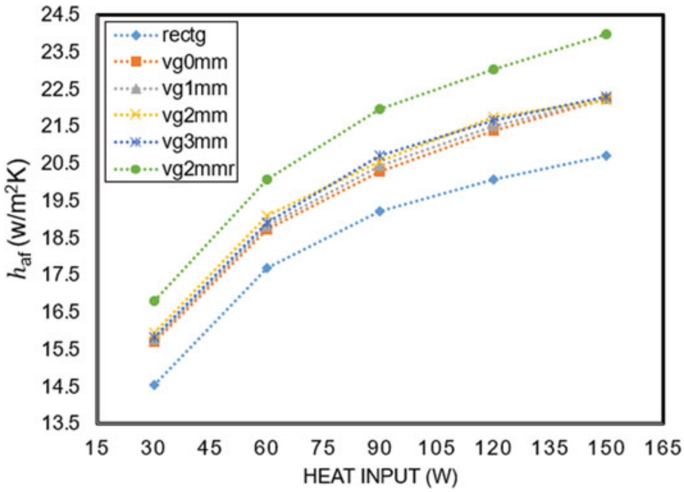

Fig. 7 Variation of array heat transfer coefficient with heating power

- Heat sink having curve-shaped fin has a temperature lower at heat sink's base than that of the rectangular fin by up to 18 K.
- Adding vertical gap increases thermal performance up to 2–3 mm gap, and further increment in gap dimension decreases thermal performance
- Curve-shaped fin with a 2 mm vertical gap offers better performance than that without curvature gap.

- By adding ripples on the curve-shaped fin with a 2 mm vertical gap can reduce the base temperature by up to 32 K.
- The newly proposed fin shape (vg2mmr) gave the best thermal performance with the same compactness as the rectangular fin.

References

1. Choi J, Jeong M, Yoo J, Seo M (2012) A new CPU cooler design based on an active cooling heatsink combined with heat pipes. Appl Therm Eng 44:50–56
2. Shafeie H, Abouali O, Jafarpur K, Ahmadi G (2013) Numerical study of heat transfer performance of single-phase heat sinks with micro pin-fin structures. Appl Therm Eng 58:68–76
3. Bi C, Tang GH, Tao WQ (2013) Heat transfer enhancement in mini-channel with dimples and cylindrical grooves. Appl Therm Eng 55:121–132
4. Huang G-J, Wong S-C, Lin C-P (2014) Enhancement of natural convection heat transfer from horizontal rectangular fin arrays with perforations in fin base. Int J Therm Sci 84:164–174
5. Acharya S, Dash SK (2018) Natural convection heat transfer from a horizontal hollow cylinder with internal longitudinal fins. Int J Therm Sci 134:40–53
6. A. Elatar, M.A. Teamah, M.A. Hassab (2016) Numerical study of laminar natural convection inside a square enclosure with single horizontal. Int J Therm Sci 99:41–51
7. Giri A, Das B (2012) A numerical study of entry region laminar mixed convection over shrouded vertical fin arrays. Int J Therm Sci 60:212–224
8. Li B, Byon C (2015) Experimental and numerical study on the heat sink with radial fins and a concentric ring subject to natural convection. Appl Therm Eng 90:345–351
9. Hong S, Chung B (2016) Int J Therm Sci 101:1–8
10. Chang S, Wu H, Guo D, Shi J, Chen T (2016) Int J Heat Mass Tran
11. Chu W-X, Lin Y-C, Chen C-Y, Wang C-C (2019) Experimental and numerical study on the performance of passive heat sink having alternating layout. Int J Heat Mass Transf 135:822–836
12. Naserian MM et al (2013) Experimental and numerical analysis of natural convection heat transfer coefficient of V-type fin configurations. J Mech Sci Technol 27(7):2191–2197
13. Ahmed M, Abdul Jabbar N. Khalifa (2014) Natural convection heat transfer from a heat sink with fins of different configurations. Int J Innov Appl Stud 9 (3):1043–1047
14. Fluent A (2009) ANSYS Fluent 12.0 user's guide, Ansys Inc. 15317:1–2498
15. Churchill SW, Chu H (1975) Correlating equations for laminar and turbulent free convection from a vertical plate. Int J Heat Mass Transf 18:1323–1329
16. El Ghandouri I, El Maakoul A, SaadeddineS, Meziane M (2020) Design and numerical investigations of natural convection heat transfer of a new rippling fin shape. Appl Thermal Eng 8–11

Electronic Heat Dissipation and Thermal Management by Finned Heat Sinks

Kapil Kalra and Amit Arora

Nomenclature

Nu	Nusselt Number
h	Convective heat transfer coefficient
D_h	Hydraulic diameter
k_f	Thermal conductivity of fluid
ρ	Density of fluid
T_w	Average base plate temperature
T_{in}	Inlet temperature
T_{out}	Outlet temperature
A_s	Total surface area in fluid contact
A	Cross-sectional area of channel
P_c	Perimeter of channel
R_t	Thermal resistance
ΔT	Temperature difference
Q	Heat dissipation power applied on fin base
ΔP	Pressure difference
P_{in}	Inlet pressure
P_{out}	Outlet pressure
Re	Reynolds number
μ	Dynamic viscosity of fluid
V_{in}	Inlet velocity

K. Kalra (✉) · A. Arora
Department of Mechanical Engineering, Malaviya National Institute of Technology Jaipur, Jaipur, Rajasthan 302017, India
e-mail: kapilkalra145@gmail.com

D. Sharma and S. Roy (eds.), *Emerging Trends in Energy Conversion and Thermo-Fluid Systems*, Lecture Notes in Mechanical Engineering,
https://doi.org/10.1007/978-981-19-3410-0_10

f Friction factor
L Length of channel
η Thermal hydraulic index
G Mass velocity.

1 Introduction

Electronic devices integrated with AI have invaded our lives to a large extent. From a small business firm to a large multinational company, devices like computers, laptops, and smartphones have helped to increase the productivity as well as revenue. They are being widely used in the fields of science and research, pharmaceutical industries, education, military, space projects, etc. [1]. The rising computational demands along with the miniaturization of the overall system size lead the researchers to explore new methods of thermal management of such devices, as they are now being exposed to higher heat fluxes [2]. Proper cooling techniques for such devices can increase their functional lives by avoiding a number of failure modes including thermal oxidation of interconnected surfaces and chip cracking [3]. Further, an enhancement in performance is also achieved if these devices are kept within controlled temperature limits.

Generally, the heat dissipated by such devices is delivered to the heat sink via conduction which is then expelled to the ambient by natural or forced convection [4]. Modifying the geometry of heat sink and improving coolant properties are the two commonly practiced techniques to increase the heat transfer through a single-phase coolant [5].

A number of cooling techniques are being used in electronics cooling like jet impingement cooling [6, 7] spray cooling, thermoelectric cooling [5], heat pipes, and finned heat sinks. Among these techniques, finned heat sinks are largely preferred by researchers because of their simple design. Accordingly, this article highlights the impact of various parameters on the thermo-hydraulic performance of finned heat sinks. Finned heat sinks are generally classified on the basis of their shapes, which is shown by Fig. 1.

2 Performance Parameters

Thermal and hydraulic performance are the two objective parameters that are involved in optimizing the performance of any heat sink. The correlations that are used to calculate these parameters are given below:-

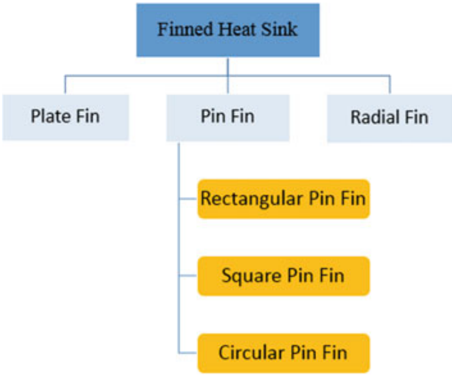

Fig. 1 Classification of finned heat sink

2.1 Thermal Performance

$$\mathrm{Nu} = \frac{h D_\mathrm{h}}{k_\mathrm{f}} \tag{1}$$

$$\Delta p = p_\mathrm{in} - p_\mathrm{out} \tag{2}$$

$$D_\mathrm{h} = \frac{4A}{P_\mathrm{C}} \tag{3}$$

$$R_\mathrm{t} = \frac{\Delta T}{Q} \tag{4}$$

2.2 Hydraulic Performance

$$\Delta p = p_\mathrm{in} - p_\mathrm{out} \tag{5}$$

$$\mathrm{Re} = \frac{\rho v_\mathrm{in} D_\mathrm{h}}{\mu} \tag{6}$$

$$f = \frac{2\rho \Delta P D_\mathrm{h}}{L G^2} \tag{7}$$

3 Effect of Critical Parameters on Performance Parameters

3.1 Perforation

Introducing perforations [8, 9] in solid fins increase the heat transfer coefficient along with a decrease in pressure drop. Tijani and Jaffri [10] numerically investigated the impact of perforations on the thermo-hydraulic performance of pin fins and plate fins under forced convection. Their results revealed that perforations had increased the heat transfer coefficient in both plate fins and pin fins as compared to solid fins because perforations had induced the additional recirculation in $x - y$ plane apart from recirculation in $x - z$ plane [11]. However, perforated pin fins have higher Nu and heat transfer coefficient than the perforated plate fins at corresponding Reynolds number as shown in Fig. 2.

Figure 3 shows the impact of perforations on ΔP for plate fin heat sink and pin fin heat sink. The values of pressure drops were found to be lower for perforated pin fins as compared to that with solid pin fin heat sink which reduced the pumping power.

Another numerical study was done by Chingulpitak et al. [12] to find out the optimum number of perforations and diameter of perforations on laterally perforated plate fin heat sink. They varied the diameter of perforations from 1 to 10 mm by taking three different values of number of perforations, i.e., 14, 27, and 75. They found that the rate of heat transfer increased when the diameter of perforations were increased up to a certain value only beyond which it decreased as shown in Fig. 4. This was mainly because of reduced area available for heat transfer as perforation

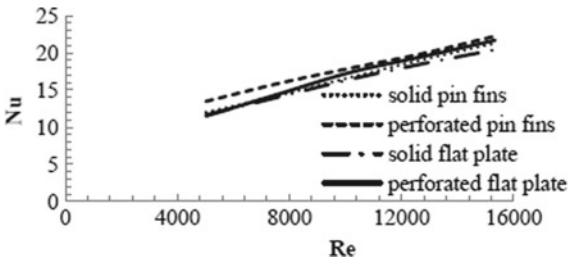

Fig. 2 Effect of perforations on Nusselt number [10]

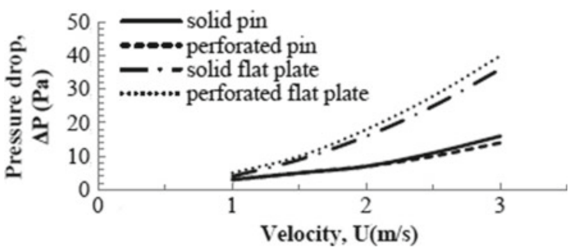

Fig. 3 Effect of perforations on pressure drop [10]

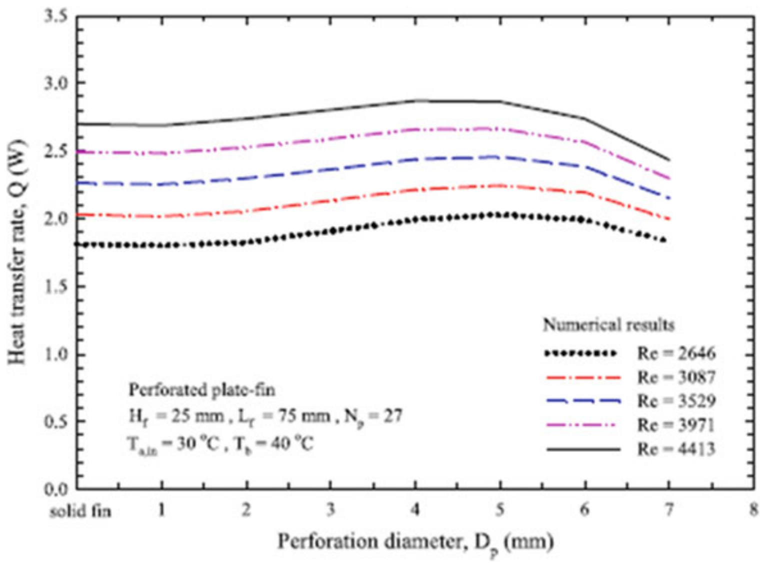

Fig. 4 Effect of perforation diameter on laterally perforated plate fins [12]

diameter is increased. Among all the geometries, the best thermal performance was obtained for the laterally perforated plate fin heat sink with 27 perforations of 5 mm diameter.

Figure 5 shows that ΔP increases on increasing the diameter of perforations if number of perforations and Reynolds number were fixed. However, the value pressure drop was affected by perforations if the diameter of perforations was more than 1 mm because the perforations of 1 mm diameter were so small and their flow pattern resembled that of solid plate fins.

3.2 Fin Shape

Various shapes of fins are available according to the application like plate fins, pin fins, longitudinal fins, annular fins, etc. Some of them are shown in Fig. 6. Heat transfer rate is maximum for pin fins because they provide higher area available for heat transfer but they are not preferred at higher Reynolds number because of higher pressure drops, thus requiring higher pumping power [13].

Aliabadi et al. [14] conducted an experimental and numerical study to find out the impact of shape of pin fin miniature heat sink on its thermo-hydraulic performance. Square, rectangular, circular, trapezoidal, half-circular, rhombic, triangular, and hexagonal were the different shapes considered by them as shown in Fig. 7. Water and Al_2O_3/water nanofluid were the two different fluids used for their study. Their results revealed that at a particular Reynolds number, the highest values of

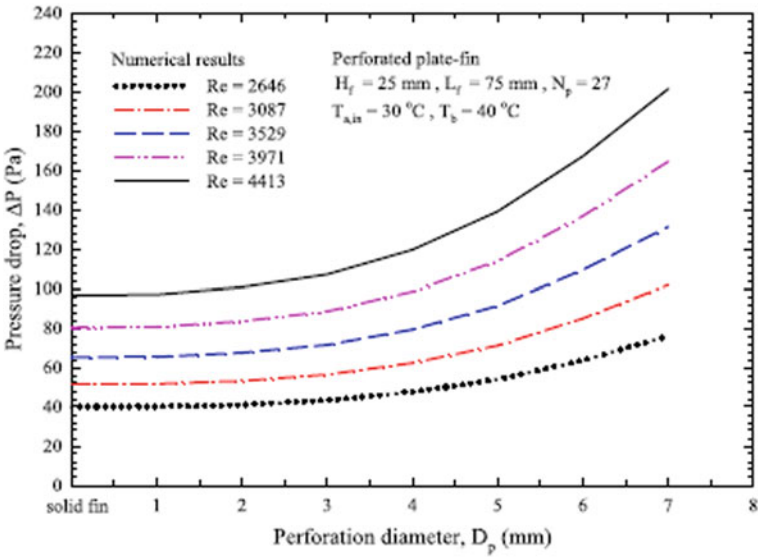

Fig. 5 Effect of perforation diameter on laterally perforated plate fins [12]

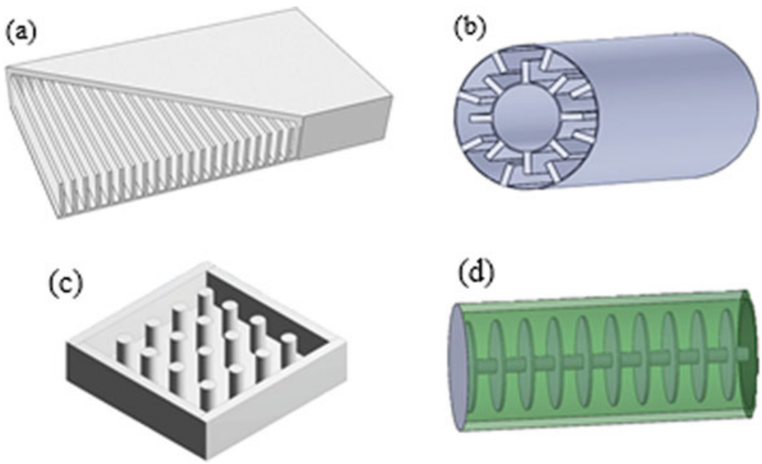

Fig. 6 Different configurations of fins (**a**) Plate fin, (**b**) longitudinal fin, (**c**) pin fin, (**d**) annular fin

heat transfer coefficient were obtained for half-circular pin fin miniature heat sink as shown in Figs. 8 and 9. They used the ratio of heat transfer coefficient to pumping power as an index of overall thermo-hydraulic performance which was found to be maximum for circular and hexagonal pin fin miniature heat sink.

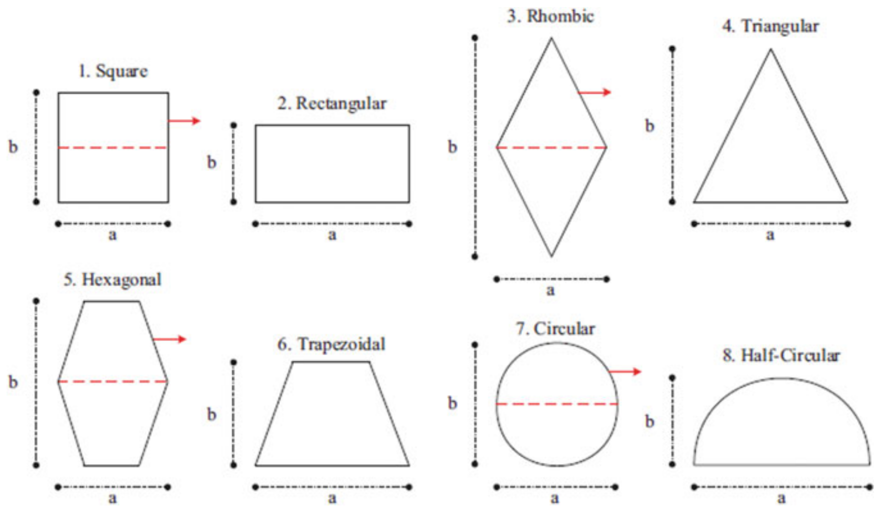

Fig. 7 Different shapes of pin fin miniature heat sink [14]

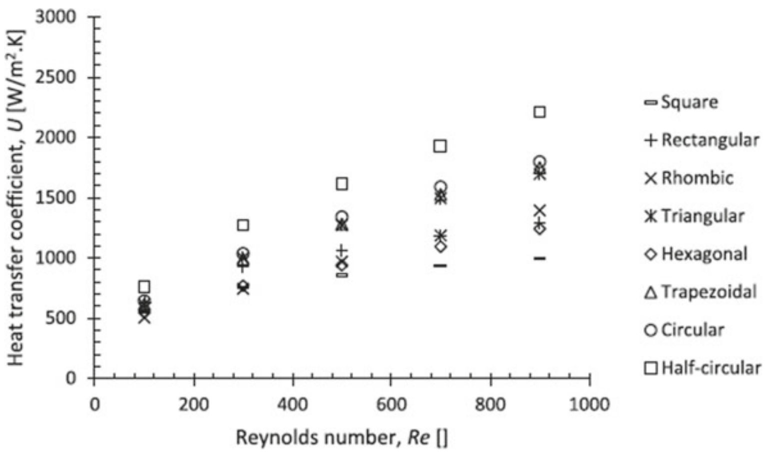

Fig. 8 Thermal behavior of heat sinks [14]

3.3 Splitter

To improve the overall thermo-hydraulic performance of any heat sink, its heat transfer coefficient is increased and pumping power is decreased. Splitters [15–18] are being used by researchers to mitigate the effect of flow separation, thus reducing the pressure drop along the heat sink (Figs. 10 and 11).

In a numerical study, Sajedi et al. [15] investigated the impact of using splitter plates with two different geometries of pin fin, namely square pin fin and circular pin

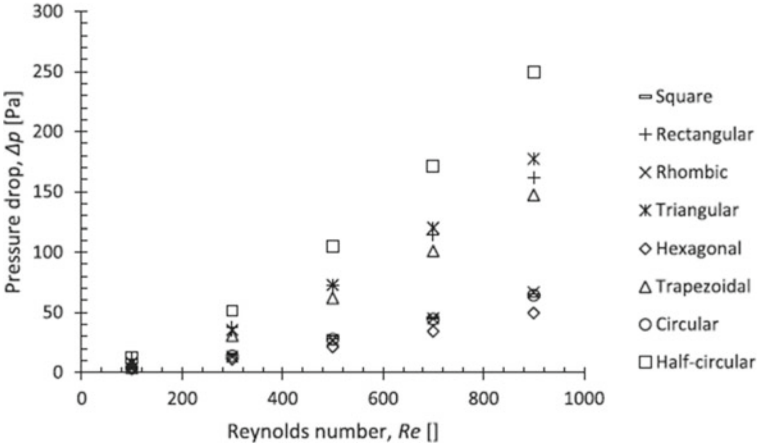

Fig. 9 Hydraulic behavior of heat sinks [14]

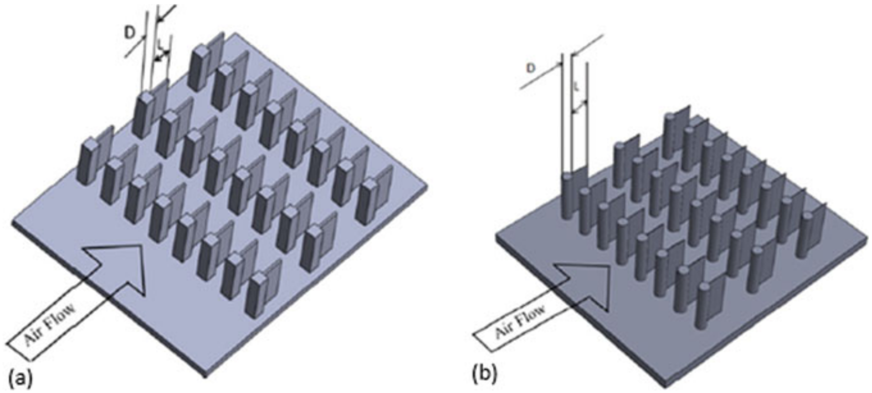

Fig. 10 Schematic diagram of **a** square pin fin heat sink with splitter **b** circular pin fin heat sink with splitter [15]

fin. They varied the length of splitter plate in their study. They found that addition of splitter plates reduce the heat transfer coefficient as well as ΔP as shown in Figs. 12 and 13. The reduction in heat transfer rate was mainly due to the flow stabilization. Also, it was found that the use of splitters was more beneficial with circular pin fins (Fig. 14).

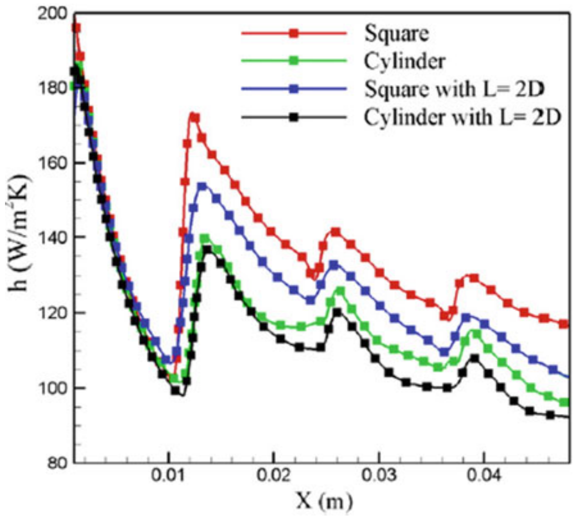

Fig. 11 Effect of splitter on convective heat transfer coefficient [15]

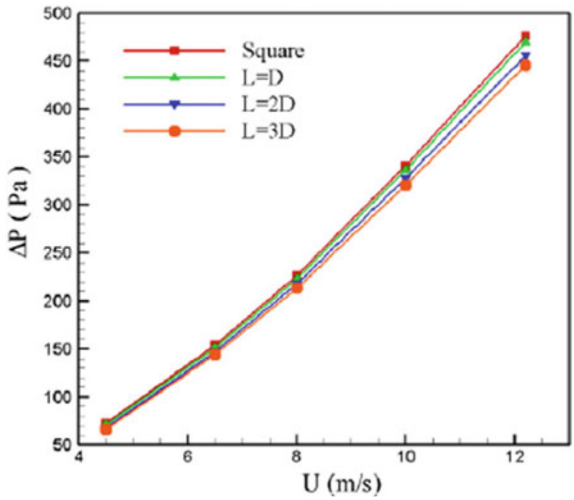

Fig. 12 Impact of splitter on pressure drop in square pin fin heat sink [15]

3.4 Lattice Structure

Lattice structure materials have regularly distributed repeated unit cells. They are now being used to increase the heat transfer efficiency [19–22] by increasing the heat transfer area in electronic devices. In a numerical study, Wang et al. [19] compared the thermo-hydraulic performance of three heat sinks, namely solid pin fin, body-centered-cubic pin fin, and vertex-centered pin fin. Both laminar and turbulent flows were taken into consideration. They observed that pressure drops for both body-centered-cubic pin fin and vertex-centered pin fin were lower than the solid pin fin

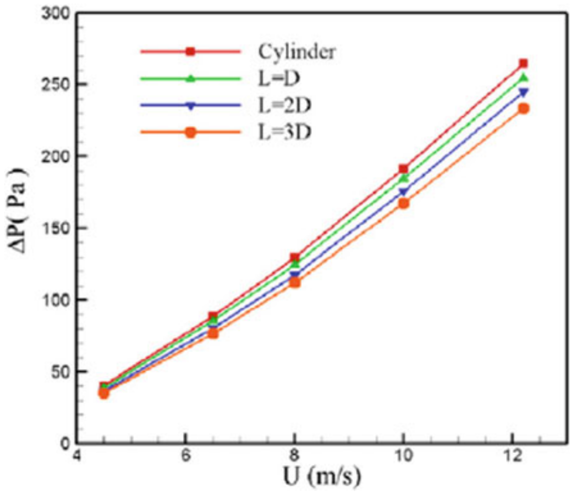

Fig. 13 Impact of splitter on pressure drop in circular pin fin heat sink [15]

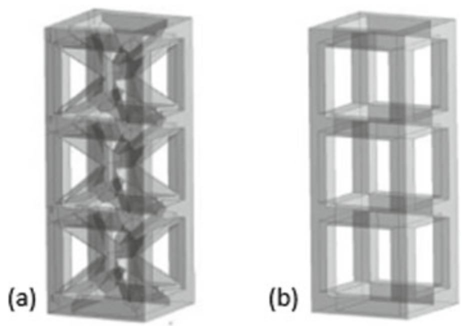

Fig. 14 **a** Vertex-centered pin fin **b** Body-centered-cubic pin fin [19]

heat sinks. However, the thermal resistance for vertex-centered heat sink was quite high that decreased its overall thermal hydraulic index as shown in Figs. 15 and 16.

4 Conclusions

Finned heat sinks are widely used in the thermal management of electronic devices. Their overall performance depends on heat transfer coefficient as well as the pressure drop along the length of the heat sink. Increasing heat transfer coefficient and decreasing pressure drop have always been the interest of researchers. This article highlights the impact of perforations, shape, splitter, and lattice structure on the thermo-hydraulic performance of finned heat sink. Based on various published numerical, experimental, and analytical studies, following conclusions can be drawn:

- Both Nu and ΔP increase on increasing Reynolds number.

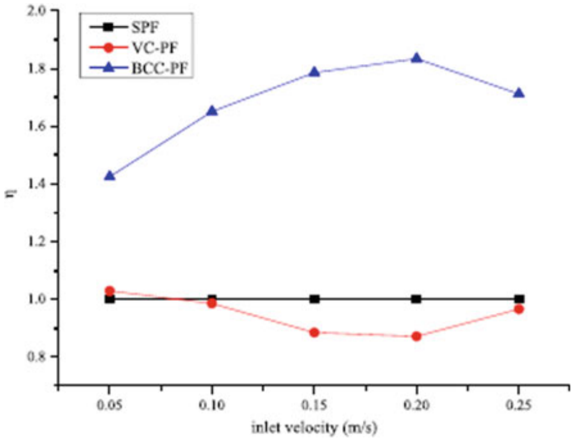

Fig. 15 Thermal hydraulic index for laminar flow versus inlet velocity [19]

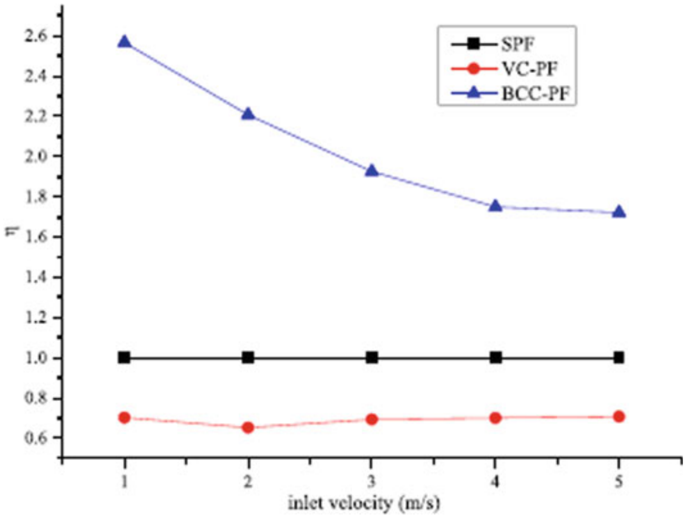

Fig. 16 Thermal hydraulic index for turbulent flow versus inlet velocity [19]

- Introducing perforations in solid fins increase the heat transfer coefficient along with a decrease in pressure drop.
- Perforations have noticeable impact on the thermo-hydraulic performance of laterally perforated plate fin heat sink if diameter of perforation exceeds 1 mm.
- Compared to plate fins, the heat transfer rates are more for pin fins but they offer higher pressure drops at high Reynolds number.

- Among square, rectangular, circular, trapezoidal, half-circular, rhombic, triangular, and hexagonal pin fin miniature heat sinks, and circular and hexagonal pin fin miniature heat sinks have the best thermo-hydraulic performance.
- Both Nu and ΔP are reduced on the addition of splitter plates.
- Adding splitter plates to circular pin fin heat sink is more advantageous than their addition to the square pin fin heat sink.
- Vertex-centered lattice pin fin heat sink has reduced the thermal hydraulic index of the heat sink. However, the thermal hydraulic index of body-centered-cubic pin fin was found to be 140% more than the conventional solid pin fins.

Acknowledgements The corresponding authors are thankful to the Ministry of Education, Government of India, for providing the facilities and platform for the research work.

References

1. Alam MW, Bhattacharyya S, Souayeh B, Dey K Hammami F, Rahimi-Gorji M, Biswas R (2020) CPU heat sink cooling by triangular shape micro-pin-fin: Numerical study. Int Commun Heat Mass Transf 112:104455; Rakopoulos CD, Giakoumis EG (2006) Second-law analyses applied to internal combustion engine operation. Progress Energy Combust Sci 32(1):2–47
2. Akula R, Gopinath A, Rangarajan S, Balaji C (2021) Experimental and numerical studies on heat transfer from a PCM based heat sink with baffles. Int J Thermal Sci 159:106525; Hussain KM (2016) Aerodynamic performance evaluation of a novel turbine, Ph.D. thesis, Department of Mechanical Engineering, IIT Guwahati, India
3. Al-Sallami W, Al-Damook A, Thompson HM (2017) A numerical investigation of the thermal-hydraulic characteristics of perforated plate fin heat sinks. Int J Therm Sci 1(121):266–277
4. Ahmed HE, Salman BH, Kherbeet AS, Ahmed MI (2018) Optimization of thermal design of heat sinks: a review. Int J Heat Mass Transf 1(118):129–153
5. Bhandari P, Prajapati YK (2021) Thermal performance of open microchannel heat sink with variable pin fin height. Int J Therm Sci 159:106609
6. Yang YT, Peng HS (2009) Investigation of planted pin fins for heat transfer enhancement in plate fin heat sink. Microelectron Reliab 49(2):163–169
7. Chung YM, Luo KH (2002) Unsteady heat transfer analysis of an impinging jet. J Heat Transfer 124(6):1039–1048
8. Bakhti FZ, Si-Ameur M (2019) A comparison of mixed convective heat transfer performance of nanofluids cooled heat sink with circular perforated pin fin. Appl Therm Eng 1(159):113819
9. Sundar S, Song G, Zahir MZ, Jayakumar JS, Yook SJ (2019) Performance investigation of radial heat sink with circular base and perforated staggered fins. Int J Heat Mass Transf 1(143):118526
10. Tijani AS, Jaffri NB (2018) Thermal analysis of perforated pin-fins heat sink under forced convection condition. Procedia Manuf 1(24):290–298
11. Huang CH, Liu YC, Ay H (2015) The design of optimum perforation diameters for pin fin array for heat transfer enhancement. Int J Heat Mass Transf 1(84):752–765
12. Chingulpitak S, Ahn HS, Asirvatham LG, Wongwises S (2019) Fluid flow and heat transfer characteristics of heat sinks with laterally perforated plate fins. Int J Heat Mass Transf 1(138):293–303
13. Jonsson H, Moshfegh B (2001) Modeling of the thermal and hydraulic performance of plate fin, strip fin, and pin fin heat sinks-influence of flow bypass. IEEE Trans Compon Packag Technol 24(2):142–149

14. Khoshvaght-Aliabadi M, Deldar S, Hassani SM (2018) Effects of pin-fins geometry and nanofluid on the performance of a pin-fin miniature heat sink (PFMHS). Int J Mech Sci 1(148):442–458
15. Sajedi R, Osanloo B, Talati F, Taghilou M (2016) Splitter plate application on the circular and square pin fin heat sinks. Microelectron Reliab 1(62):91–101
16. Choudhary V, Kumar M, Patil AK (2019) Experimental investigation of enhanced performance of pin fin heat sink with wings. Appl Therm Eng 5(155):546–562
17. Hosseinirad E, Khoshvaght-Aliabadi M, Hormozi F (2019) Effects of splitter shape on thermal-hydraulic characteristics of plate-pin-fin heat sink (PPFHS). Int J Heat Mass Transf 1(143):118586
18. Razavi SE, Osanloo B, Sajedi R (2015) Application of splitter plate on the modification of hydro-thermal behavior of PPFHS. Appl Therm Eng 5(80):97–108
19. Wang X, Chen M, Tate D, Rahimi H, Zhang S (2020) Numerical investigation on hydraulic and thermal characteristics of micro latticed pin fin in the heat sink. Int J Heat Mass Transf 1(149):119157
20. Kim T, Hodson HP, Lu TJ (2004) Fluid-flow and endwall heat-transfer characteristics of an ultralight lattice-frame material. Int J Heat Mass Transf 47(6–7):1129–1140
21. Kim T, Zhao CY, Lu TJ, Hodson HP (2004) Convective heat dissipation with lattice-frame materials. Mech Mater 36(8):767–780
22. Son KN, Weibel JA, Kumaresan V, Garimella SV (2017) Design of multifunctional lattice-frame materials for compact heat exchangers. Int J Heat Mass Transf 1(115):619–629

An Experimental Study of Rewetting on a Horizontal Tube with a Constant Heat Flux

Bhuwanesh Kumar, Ravi Kumar, and Akhilesh Gupta

Nomenclature

Pa	air pressure at Nozzle inlet (bar)
U_{top}	Rewetting velocity in the circumferential direction on the tube upper portion using high-speed camera (mm/s)
U_{bottom}	Rewetting velocity in the circumferential direction on the lower portion using high-speed camera (mm/s)
U	Rewetting velocity in the circumferential direction using high-speed camera (mm/s)
$U_{ext.}$	Rewetting velocity in the circumferential direction using cooling curves (mm/s).

1 Introduction

Liquid–vapor phase change heat dissipation is an essential process in various industrial and engineering applications. The commonly used phase change heat removal methods are pool boiling, thin liquid falling film evaporation, jet impingement, and spray cooling. Heat removable through spray quenching has been commonly used in numerous industrial fields such as nuclear channel cooling when moderators boil off during loss of coolant accident (LOCA), direct and indirect spray cooling of high-power electronics components, refrigeration, glass tempering, and the steel manufacturing processes.

B. Kumar (✉) · R. Kumar · A. Gupta
Department of Mechanical and Industrial Engineering, Indian Institute of Technology Roorkee, Roorkee, Uttarakhand 247667, India
e-mail: 347bhuwanesh@gmail.com; bkumar@me.iitr.ac.in

D. Sharma and S. Roy (eds.), *Emerging Trends in Energy Conversion and Thermo-Fluid Systems*, Lecture Notes in Mechanical Engineering,
https://doi.org/10.1007/978-981-19-3410-0_11

In the spray cooling of a heated horizontal tube, the water sprays with the help of an air-atomizing nozzle onto the tube surface. A fine liquid film is created over the surface of the tube and flows around the tube surface due to gravity. The key advantages of spray quenching are high heat dissipation from a heated surface. High heat dissipation takes place when several liquid drops impact a heated surface and get evaporated. Generally, four different heat transfer regimes are best presented by the transient spray cooling curve.

In the film boiling regime, heat transmission is dominated by conduction, or convection, of heat from the hot wall to vapor, and radiation of heat through the vapour film. Within that region, the body surface temperature is quite high, which causes almost all liquid droplets to get vaporized without touching the heated body. At this temperature of the heated metal surface, the evaporation rate is insufficient. The minimum temperature of the film boiling regime is called Leiden frost or rewetting temperature, after that temperature gradient rises sharply in the unstable film boiling, and significantly in the nucleate boiling zone, before stabilizing the single-phase liquid cooling zone.

2 Literature Review and Objective

According to Lee et al. [1], a "superbly effective cooling method" exists at droplet diameters of 30–80 μm. The evaporation of an "ultrathin" liquid sheet (50–100 μm) may boost convection heat transfer coefficients by up to tenfold. Mohapatra et al. [2] observed that air-atomized spray is an effective cooling technology when compared to other cooling techniques. Additionally, Puschmann and Specht [3] state that the primary benefit of an air-assist quenching is that a large flow rate of air removes partly vaporized droplets from the heated area. This effect precludes the production of a stable vapor sheet at elevated surface temperatures but is only seen at low mass flow. However, Al-Ahmadi and Yao's [4] analysis demonstrates that quenching happens in the transition boiling regime in the case of high bulk density atomized spray quenching as well. As a consequence, while starting from a high surface temperature, the aforementioned case exhibits a rapid cooling rate. Takrouri et al. [5] studied the rewetting on horizontal tubes at different initial temperatures using a rectangular jets system. The mist-cooling curve has been investigated for a cylinder [6]. Celata et al. [7] measured the quenching front velocity of a vertical heated surface. Chitranjan et al. conducted tests to investigate the impact of jet size on the wetting of heated surfaces [8]. Zhang et al. [9] have been investigated the transient cooling of heated stainless-steel substrate with air-assist spray nozzle.

Numerous research on the rewetting of plane surfaces and tubes with different orientations has been published. Only a few researchers have investigated horizontal tube rewetting. Calculating the quenching front velocity on over-temperature nuclear reactor calandria tubes is critical for estimating the rate at which coolant may re-wet the core after a major disaster.

The purpose of this work is to add knowledge of heat dissipation during rewetting of the circular tube by measuring the quench front velocity at which the rewetting front passes through a horizontal circular tube circumference cooled down by a spray jet. The transient heat flux is directly related to the temperature gradient of the body. The current knowledge of rewetting a horizontal tube with constant heat flux using an air-atomizing spray nozzle cooling appears to be insufficient because of many variables such as mass flux, liquid droplets velocity, droplets size, inlet air pressure (in case of the air-assist spray), inlet water pressure, the Sauter Mean Diameter (SMD) of the droplet, and liquid sub-cooling

3 Material and Methods

In this research, the experimental setup consists of three major networks that is the coolant delivery arrangement, temperature and rewetting velocity measuring system, and heating unit as shown in Fig. 1. In the beginning, water was stored in a tank and supplied to the nozzle assembly using a positive displacement water pump. The pressure gauges and needles valve were fixed to control the water and airflow rate.

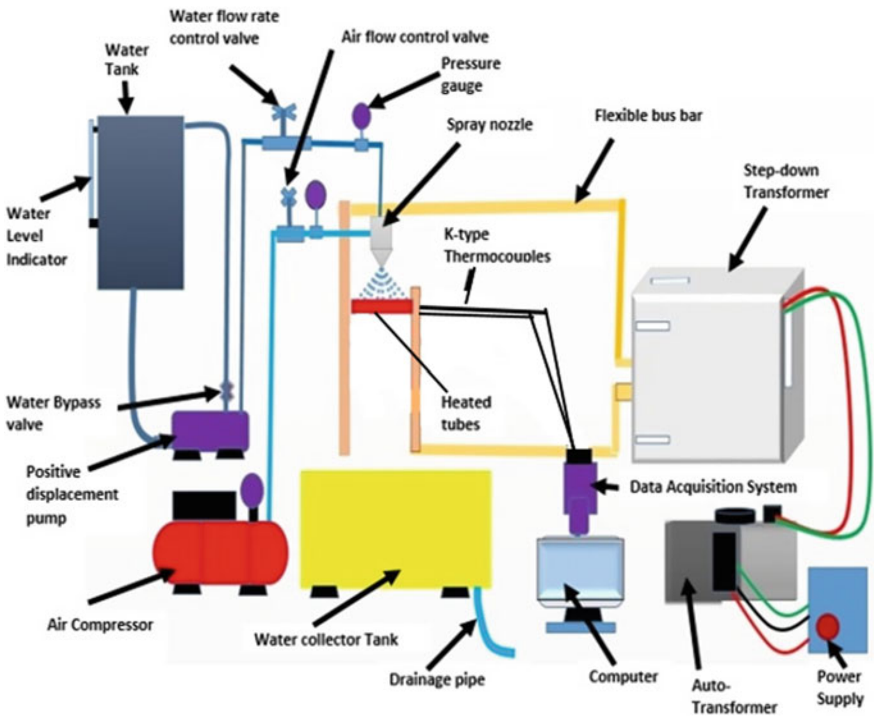

Fig. 1 The schematic diagram of the experimental setup

The spray nozzle was installed on a vertical slide of the worktable, and the test tube was placed beneath the spray nozzle assembly. The spray was injected onto the test-tube surface, with the spray being discharged through an air-atomizing nozzle. The logging system was attached with ungrounded K-type thermocouples, connected to the test-tube surface as shown in Fig. 2. An autotransformer was connected to the step-down transformer and the step-down transformer linked with the test section with the help of two flexible bus bars which are utilized to heat the test tube to the desired temperature. A Fluke Digital multimeter was used to measure the voltage over the measuring section and corresponding current supply. The test-surface stainless-steel tube is shown in Fig. 3. A strip of stainless-steel foil was used to spot weld thermocouples with a diameter of 0.5 mm in the center of the test tube. Temperature measurements were taken using a Data Acquisition System, and the mass flux was measured using a mechanical patternator with the same cross-sectional area as the projected area of the tube (19.05 mm × 100 mm). Using a step-down AC transformer, the test tube's initial constant temperature was set to 800 ± 10 °C, and the related voltage and current were measured. Equation (1) was applied to compute the heat flux provided to the test area.

$$q = \frac{VI\ \cos\theta}{A} \tag{1}$$

where A denotes the tube's outer surface area, V and I denote the voltage and current delivered across the bus bar, respectively, and $\cos\theta$ denotes the power factor, which is equal to 1 in this experiment due to the resistive load.

Each experiment was run at a predetermined liquid flow rate and air pressure. For the collection of experimental data, the rewetting facilities were conceived and developed as part of this investigation. Figure 2 shows a layout of the test facility that

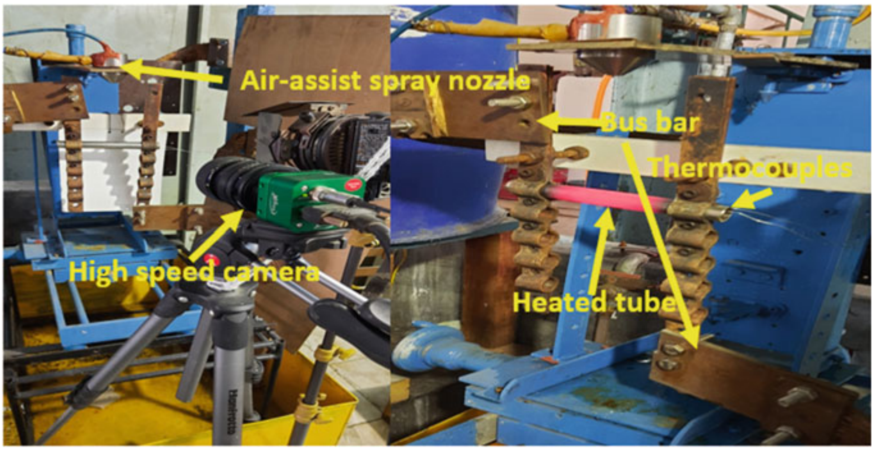

Fig. 2 Photograph of the experimental setup

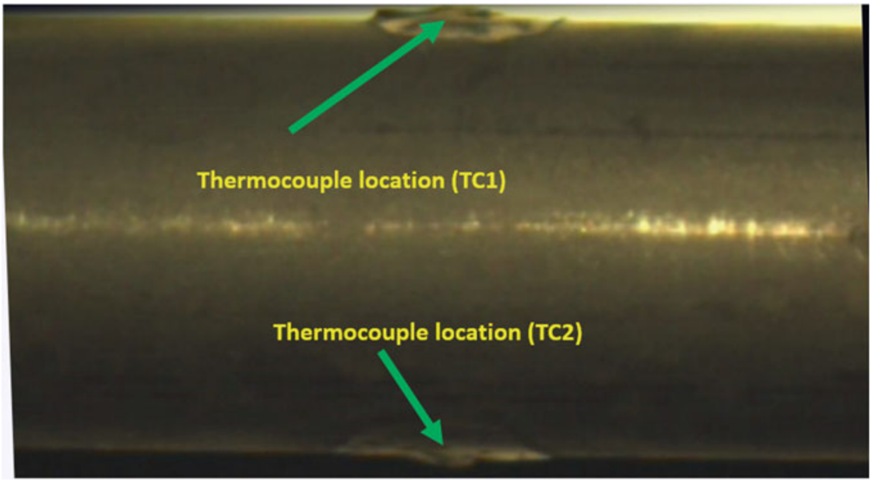

Fig. 3 Test tube with thermocouples

Table 1 Test parameters and ranges

Tube material	Stainless steel 304
Tube OD	19.05 mm
Tube thickness	1 mm
Nozzle to tube distance	140 mm
Constant heat flux	43,310.2 W/ m^2
Constant water flow rate (P_w = 1 bar)	17.5 ml/s
Air pressure range	0–4 bar

highlights the key elements. The test parameters and ranges are shown in Table 1. A video recorder or surface temperature readings can monitor the rewetting event.

3.1 Measurement of Spray Mass Distribution

The water spray impact density plays an extremely important role in spray cooling applications. To determine the spray density, a mechanical patternator was designed and constructed. The local and total water spray density on the tube surface was determined using a simple patternator at fixed liquid and variable air pressure combinations. Figure 4 depicts the patternator's sketch. The patternator comprised five parallel collecting rectangular chambers. Each chamber has a cross-sectional area (A) of 20 mm × 19.05 mm. Each chamber is attached to a unique receiving flask, which is used to collect a water sample. Over a Δt time interval, the chamber gathers the water mass from the spray and the impingement density is computed using Eq. (2).

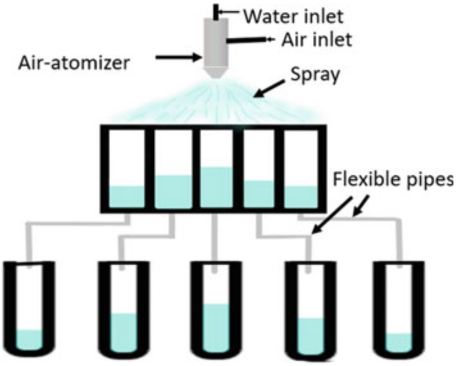

Fig. 4 The schematic diagram of a mechanical patternator

$$I_{\mathrm{d}} = \frac{m}{A \times \Delta t} \tag{2}$$

Figure 5 depicts a plot of spray impact density.

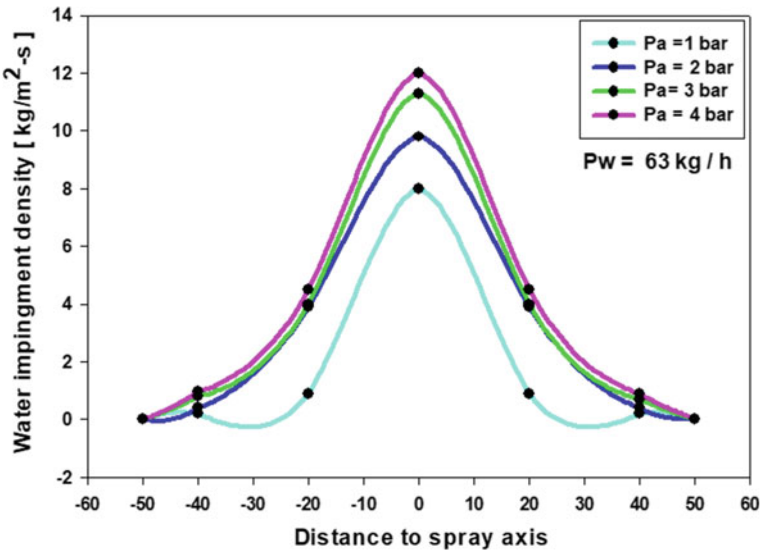

Fig. 5 Water impingement density for various air pressure

3.2 Surface Heat Flux Calculation

The quenching performance of various operational settings may be determined by measuring the surface cooling rate over time using temperature time series. The rate of surface cooling is proportional to the transient surface heat flux and may be calculated using Eq. (3)

$$q = -\rho c_{\mathrm{p}} t \left(\frac{\mathrm{d}T}{\mathrm{d}t} \right) \tag{3}$$

where ρ, c_p are the density and specific heat of the tube material, respectively, which are temperature dependent and t is the tube thickness. The test surface's temperature-dependent density [10] and specific heat [11] were calculated using the following equations.

$$\rho(T) = 7.9841 - 2.6506 \times 10^{-4} \times (T) - 1.1580 \times 10^{-7} \times (T)^2 \ \mathrm{g/cm^3}$$

$$c_{\mathrm{p}}(T) = 450 + 0.280 \times T - 2.91 \times 10^{-4} \times T^2 + 1.34 \times 10^{-7} \times T^3 \ \mathrm{J/kg-K}$$

T is the test section temperature, °C [11].

The temperature gradient ($\mathrm{d}T/\mathrm{d}t$) at any instant "n" is calculated using Eq. (4).

$$\left(\frac{\mathrm{d}T}{\mathrm{d}t} \right)_n = \frac{T_{n-1} - T_{n+1}}{t_{n-1} - t_{n+1}} \tag{4}$$

4 Results and Discussion

4.1 Visual Observation

Figure 6a–j shows typical pictures of rewetting the 19.05 mm OD and 1 mm thickness hot stainless-steel tube in the circumferential direction. The tube's initial temperature was 800 ± 10 °C, and the water temperature was 21 °C. The pictures were shot to 1000 fps with a resolution of 1920 × 1080. These images were used to calculate the position of the rewetting front. From the stagnation point (center of the spray jet point of impact) to the inner border of the wet region, the distance of the quenching front along the circumferential path of the tube was measured. The outer boundary of the rewetting front denotes actual surface-liquid contact occurs. However, the inner

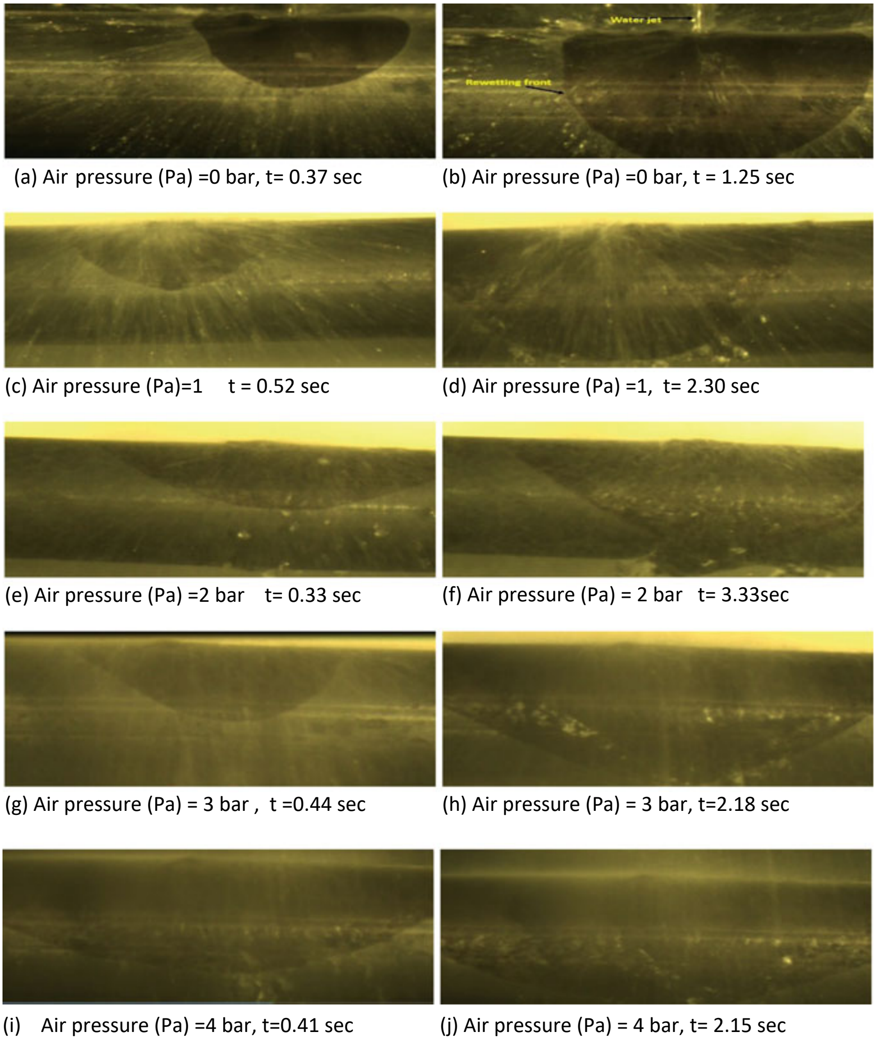

Fig. 6 **a**–**j** Photographs of the rewetting front on the horizontal tube for fixed water pressure and variable air pressure are shown

border was picked for the measurement rather than the outside border since the space between the two borders is very narrow.

Rewetting/quench front velocity $U_{\text{rew}} = \frac{\Delta x}{\Delta t}$, where Δx is the circumferential distance between two thermocouples (TC1, TC2) and Δt is the time taken for the quench front to start at TC1 and reach TC2. The rewetting velocity in the upper half of the test-tube surface was found to be greater than in the lower half. The variation of the rewetting velocity on tube upper half and bottom half portion is tabulated in Table 2. This is due to the strike of the water droplets to the vapor bubbles of the

Table 2 Rewettting velocity measured along circumferential direction using a high-speed camera and thermocouples

Pa(bar)	U_{top} mm/s	U_{bottom} mm/s	U mm/s	U_{ext} ($\Delta x/\Delta t$) mm/s	% error
0	24.259	13.600	17.431	16.351	6.19
1	11.811	6.958	8.759	8.514	2.79
2	12.295	7.480	9.030	8.757	3.02
3	12.466	7.013	8.777	8.372	4.61
4	10.080	8.160	9.033	8.217	9.03

liquid that formed on the tube surface, bubbles burst increases the heat transfer rate. As a result, the rewetting front velocity on the upper portion of the tube is higher than the lower portion. During the test, the rewetting tube surface is shown in Fig. 6a–j as a function of time at various nozzle input conditions. A water layer (supplied by the spray jet) travels across the rewetting front in the top section. More bubbles are created within the liquid on the bottom section, owing to the weaker action of the jet there. As a result, the boiling area grows in size. However, as the water flows down the tube, the temperature rises, increasing the area of the boiling zone. During tube quenching, it was found that the spray jet only impacted the tube's upper surface. The coolant moves in the bottom surface because of gravitational force. This observation is depicted in Fig. 6a–j.

4.2 Estimation of Rewetting Velocity Using the Cooling Curves

Figure 7 shows typical cooling curves of two thermocouples mounted at location TC1 (at the top of the tube) and TC2 (bottom of the tube) of a hot horizontal stainless-steel tube as displayed in Fig. 3. Δx is the circumferential distance between two thermocouples TC1 and TC2, and Δt is the time interval when rewetting on the tube surface start at TC1 and reached TC2.

The most essential variable, rewetting velocity, was determined using the cooling curve method [7]. The rewetting front velocity is estimated by the distance between positions of the thermocouples by a specific period by the rewetting front to shift one thermocouple location to the other thermocouple location [12, 13]. Rewetting velocity $U_{rew} = \frac{\Delta x}{\Delta t}$, where Δx is the distance between two thermocouples (TC1, TC2) and Δt rewetting time between the same thermocouples. The water impingement density has the greatest effect on cooling. Additionally, the air pressure at the nozzle affects cooling. If the water pressure at the nozzle inlet remains constant, the cooling time initially decreases as the air pressure rises. This might be due to a change in the spray's properties. The droplets get smaller and more frequent. Figure 8a–e shows the spray cooling curve estimated during tests. A substantial temperature

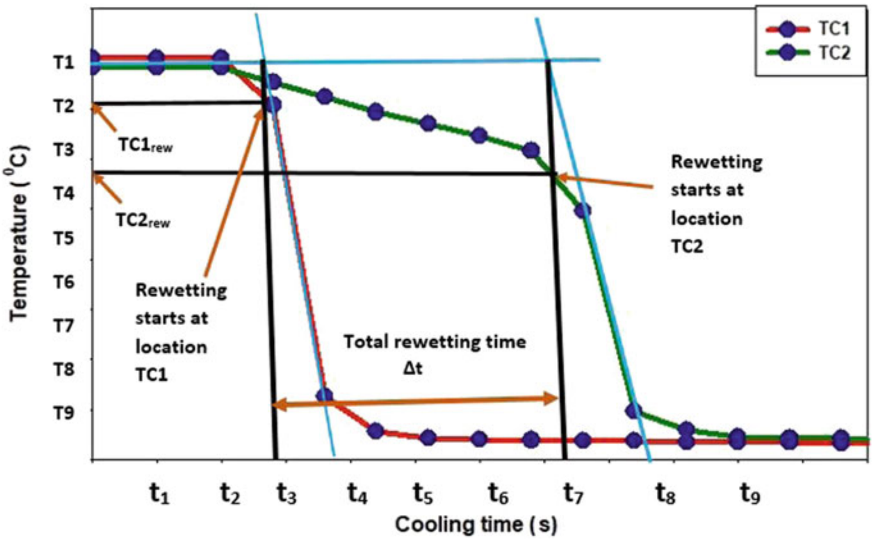

Fig. 7 Transient cooling curves

difference occurred in the circumferential. The validity of the experimental findings is confirmed by high-speed camera observation.

4.3 *The Impact of Nozzle Air Pressure on Transient Surface Heat Flux*

The transient variation in surface heat dissipation as a function of the input air pressure of the atomizer nozzle is seen in Fig. 9. As shown in Fig. 9a–c, the surface heat flux rises at both the locations TC1 and TC2 as the air pressure increases from 2 to 3 bar and then decreases at TC1 and increases at TC2 as the air pressure increases to 4 bar.

5 Conclusions

The rewetting velocity during quenching has been conducted in this investigation. The images, which were captured using a high-speed video camera under a range of operating conditions, showed how the surface rewetting during the spray cooling process. The testing settings included a range of air pressures between 0 and 4 bar, as well as constant water pressure and nozzle to tube surface distance. The rewetting velocity on the top and bottom portions of the horizontal tube was determined using a high-speed camera, whereas the rewetting velocity between the tube top and bottom

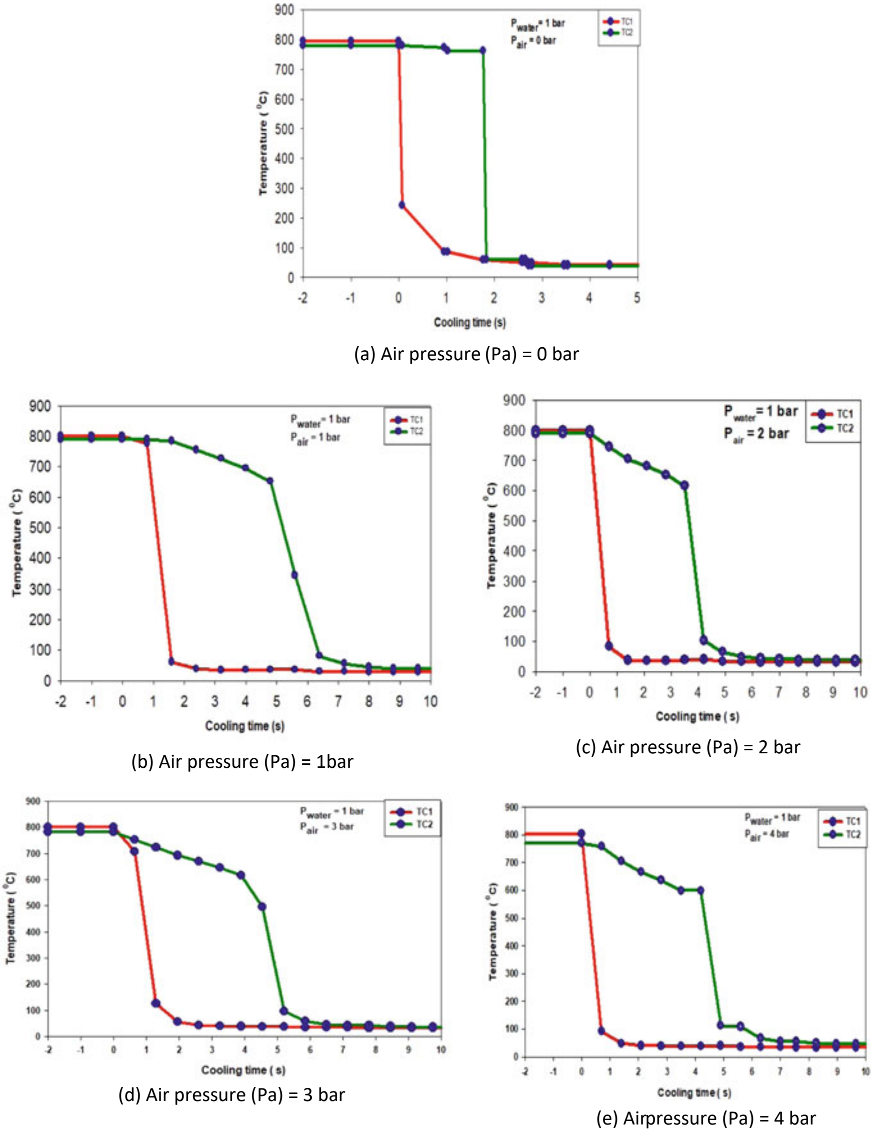

(a) Air pressure (Pa) = 0 bar

(b) Air pressure (Pa) = 1bar

(c) Air pressure (Pa) = 2 bar

(d) Air pressure (Pa) = 3 bar

(e) Airpressure (Pa) = 4 bar

Fig. 8 **a**–**e** Spray cooling curves with constant water pressure and variable air pressure

locations (TC1) and (TC2) was determined using a cooling curve and a high-speed camera for a given nozzle inlet condition. The following findings are drawn by this investigation:

1. The rewetting velocity on the heated horizontal tube upper section was found to be higher than the tube's bottom section.

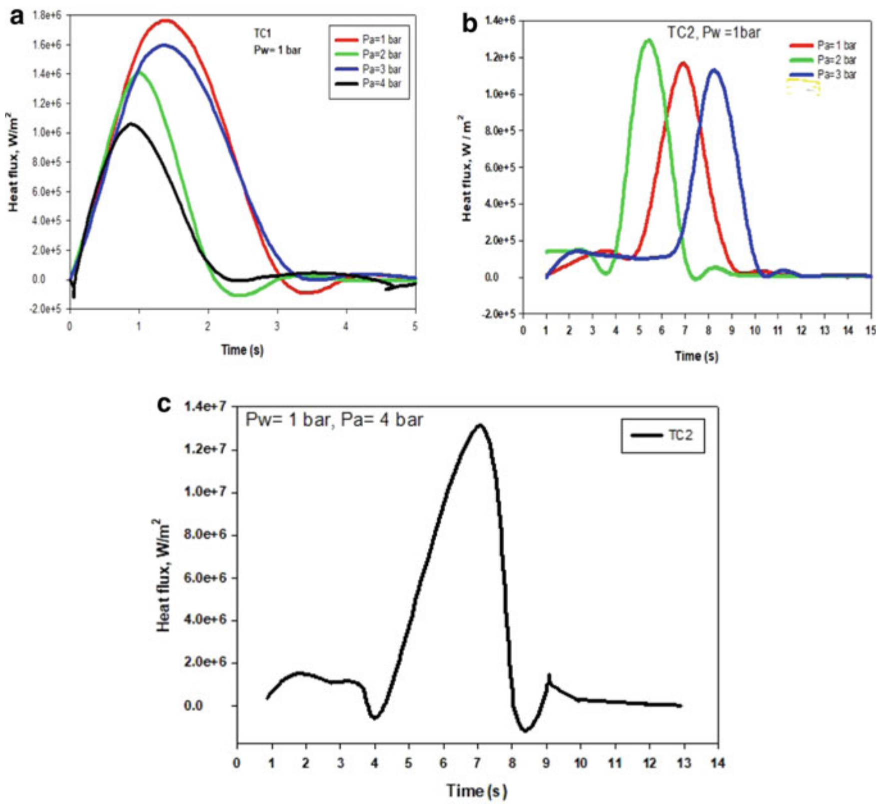

Fig. 9 **a**–**c** Tube surface transient heat flux for fixed water pressure 1 bar and variable air pressure

2. When the inlet air pressure of the nozzle is increased, the rewetting speed of the tube's upper part rises; however, when the inlet air pressure is raised further, the rewetting speed decreases.
3. The rewetting velocity estimated on the tube surface increases initially with increasing air pressure but drops as the air pressure is increased further.
4. With increased air pressure, the tube rewetting time increases.

References

1. Lee S, Yang Z, Hsyua Y (1994) J Heat Transfer 116:167–172
2. Mohapatra SS, Chakraborty S, Pal SK (2012) Experimental studies on different cooling processes to achieve ultra-fast cooling rate for hot steel plate. Exp Heat Transfer 25(2):111–126
3. Puschmann F, Specht E (2004) Transient measurement of heat transfer in metal quenching with atomized sprays. Exp Thermal Fluid Sci 28(6):607–615

4. Al-Ahmadi HM, Yao SC (2008) Spray cooling of high-temperature metals using high mass flux industrial nozzles. Exp Heat Transfer 21(1):38–54
5. Takrouri K, Luxat J, Hamed M (2017) Measurement and analysis of the re-wetting front velocity during quench cooling of hot horizontal tubes. Nucl Eng Des 311:184–198
6. Lee S, Park J, Lee P, Kim M (2005) Heat transfer characteristics during mist cooling on a heated cylinder. Heat Transfer Eng 26(8):24–31
7. Celata GP, Cumo M, Lombardo C, Mariani A, Saraceno L (2005) Experimental result on rewetting of hot surfaces by droplet impingement. Exp Thermal Fluid Sci 29(3):275–285
8. Agrawal C, Kumar R, Gupta A, Chatterjee B (2012) Effect of jet diameter on the rewetting of hot horizontal surfaces during quenching. Exp Thermal Fluid Sci 42:25–37
9. Zhang X, Wen Z, Dou R, Zhou G, Zhang F (2014) Experimental study of the air-atomized spray cooling of high-temperature metal. Appl Therm Eng 71(1):43–55
10. Kim CS (1975) Thermophysical properties of stainless steels. Argonne National Lab., Ill. (USA)
11. Franssen J-M, Real PV (2012) Thermal data for carbon steel and stainless-steel sections. Fire Des Steel Struct 336–338
12. Xu W, Guo J, Liu X, Xiong J, Chai X, Zhang T, Cheng X, Zeng W (2019) Predictions of quench temperature and quench velocity in narrow rectangular channel of novel plate-type reactor. Annal Nucl Energy 131:148–155
13. Tatsuhiro U, Mitsuru I, Yasuhiro I, Yoshiyasu S (1983) Rewetting of a hot surface by a falling liquid film. Int J Heat Mass Transf 26(3):401–410

Energy and Efficiency

Effect of Varying Flowrate of Oxy-hydrogen (HHO) Gas Addition on Combustion and Emission Characteristics of Early Direct Injection Homogenous Charge Compression Ignition Engine

Nikhil Aniruddha Bhave, Mahendra M. Gupta, Sandeep S. Joshi, and Sushant S. Satputaley

1 Introduction

Internal Combustion (IC) engines are being extensively used in transport and stationary applications for a long. Though the IC engine technology is well matured, some of the issues of engines are not adequately addressed. These issues include the use of fossil fuels, limited thermal efficiency, and environmental pollution due to their emissions.

Several attempts are being made to tackle all the abovementioned issues. Among those, the use of a HCCI with oxy-hydrogen gas as a fuel additive was found to be the most effective solution. HCCI overcomes the drawbacks of CI and SI engines and combines their benefits to produce better combustion and emissions characteristics. And the oxy-hydrogen gas improves the combustion performance while reducing the engine emissions.

HCCI refers to the homogenous mixing of air and fuel before combustion. This can be achieved by early injection of fuel during the compression stroke, port fuel injection of fuel, or both at a time. The early direct injection can be achieved by changing the injection time of the Direct Injector by advancing it or retarding it. Some researchers made use of multiple injectors to achieve early injection. Narrow injection angle had also been explored in early injection strategy [1]. The higher

N. A. Bhave (✉) · M. M. Gupta · S. S. Joshi
Department of Mechanical Engineering, Shri Ramdeobaba College of Engineering and Management, Nagpur, Maharashtra 440013, India
e-mail: bhave.nikhil123@gmail.com

S. S. Satputaley
Department of Mechanical Engineering, St. Vincent Pallotti College of Engineering and Tecnology, Nagpur, Maharashtra 441108, India

D. Sharma and S. Roy (eds.), *Emerging Trends in Energy Conversion and Thermo-Fluid Systems*, Lecture Notes in Mechanical Engineering,
https://doi.org/10.1007/978-981-19-3410-0_12

injection pressure was explored in some studies. The early injection strategy was successful in achieving very low NOx and Smoke emissions [2]. However, wall wetting and spray impingement problems arise which produces higher CO and HC emissions [3]. The higher early injection timing leads to lesser pressure and temperature during combustion. This results in lesser Brake Power and Torque and increased fuel consumption compared to conventional diesel combustion. The wall wetting problem got more severe with very high injection pressure producing even higher CO, HC, and NOx emissions also.

Thus, to overcome the above issues of early injection strategies, HHO gas was investigated as diesel fuel additive in CI engine.

2 Literature Review and the Objective

Oxy-hydrogen is a mixture of 70% hydrogen and 29% oxygen and some other active species. The production of HHO gas is done by the electrochemical splitting of water by electricity. In 1977, Yull Brown attempted the electrochemical splitting of water for generation HHO gas production, hence also the name Brown's gas [4]. Oxy-hydrogen, hydroxyl, H_2/O_2, Rhodes gas, and Browns gas are alternative names for HHO gas [5]. HHO gas is produced by electrolysis of water. At normal temperature and atmospheric pressure, the electrolysis process is carried out in an electrolyzer. A DC battery source is generally used for splitting the water into cations and anions [6]. Stainless steel plate electrodes were used as electrode in almost all cases. The gap between the electrodes has considerable effect in HHO gas production. It is recommended that the gap should be minimum. The minimum potential difference between terminals to split water molecule is 1.48 V.

Potassium Hydroxide was used as catalyst in distilled water for HHO gas generation. This part is explained in Sect. 3.

Many researchers have investigated the use of HHO gas as supplementary fuel to diesel in CI engines. It is clear from Table 1 that except NOx all the emissions have improved. This also signifies better combustion. Thus, in the present work, HHO gas is used to energize the diesel fuel in a CI engine with advancing fuel injection timing to reduce exhaust gas emissions. Table 1 describes the significant work carried out by other researchers on the use of HHO gas addition in CI engines.

3 Experimental Setup and Methodology

A mono-cylinder stationary CI engine was used for study presented in Fig. 1. Technical specifications of diesel engine are shown in Table 2. The Kirloskar TV1 engine was modified from conventional direct fuel injection to ECU-controlled CRDI system. The fuel injection pressure, timing, angle, and quantity were controlled by an ECU. The engine was also modified to accommodate piezo-electric sensor, shaft

Table 1 Variation of Emissions parameters according to various studies conducted [9]

References	Oxy-hydrogen gas flowrate	Effect of HHO gas addition on various emission parameters (% Change)				
		CO	CO_2	HC	NOx	Smoke
[10]	Variable	−4.56	−1.3		3.37	
[11]	5 lpm	−16.02	1.66		19.91	
[7]	0.74 lpm	−34.6		−33.5	1.76	−44.83
[12]	3 lpm	−50	6	−40	10	−85
[13]	1 lpm	−12.2			9.47	
[14]	15–35% by vol	−14.4		−6.7		
[15]	12% on energy	−11	−4	+	+	−25
[16]	10 lpm	–			+	
[17]	0.73 lpm	−33.23		−33.23	20.73	
[6]	Variable	−20		−10	25	
[18]	3, 5, 7 lpm				+	

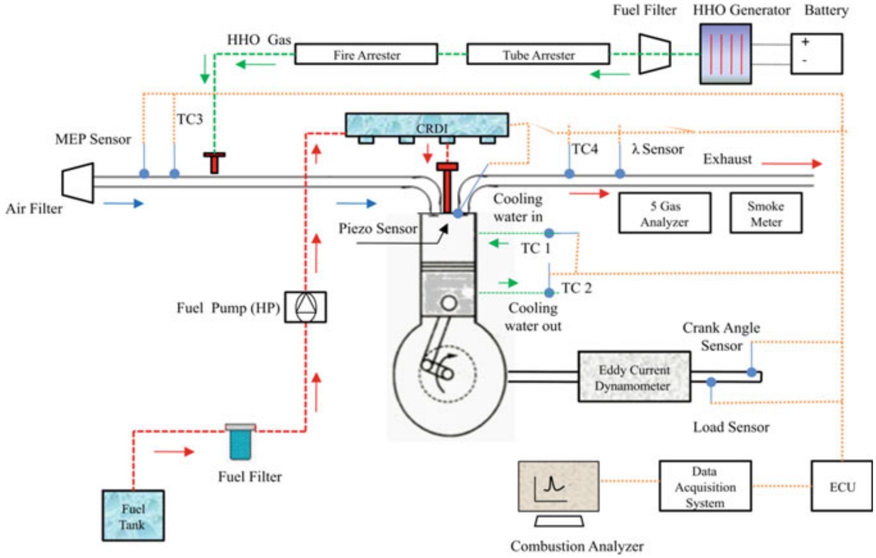

Fig. 1 Experimental setup

encoder, load sensor, MEP sensor, fuel flow sensor, and *K* type thermocouples, to measure in-cylinder pressure, engine speed, dynamometer loading, air flow, fuel flow, and temperature measurement, respectively. During engine operation, data from all the sensors were collected by high-speed data acquisition system. This data was displayed on the computer by Lab view-based combustion analysis software. The combustion parameters were calculated from the cylinder pressure versus crank angle

Table 2 Engine specifications

Make/model	Kirloskar/TV1
Cylinder diameter (cm)	8.75
Length of stroke (cm)	11.0
Total displacement volume (cm^3)	661.5
Rated power and speed (kW/RPM)	3.5/1500
Compression ratio	18
Cylinder	Single inline
The radius of crank (cm)	5.5
Length of connecting rod (cm)	23.4
Engine cylinder cooling (water)	200 LPH

data. The emission measurement was carried out by using AVL Smoke meter and AVL Gas Analyzer.

Electric Current was applied by a 12 V and 5A DC battery with Potassium Hydroxide as the catalyst for the splitting of distilled water. Stainless Steel 316L electrodes were used, and plate effective area was 3.5 × 3.5 $in.^2$. The HHO gas generated was first sent to the flame arrester. This avoids the backflow of flame if the gas catches flame. The gas was sent to a hollow container which is attached to the engine intake manifold for induction. The flow rate was controlled by changing the number of plates taking part in the reaction as shown in Table 3.

During experimental investigation, the engine was allowed to attain steady state condition by running it for 30 min. Baseline reading were taken at fuel injection time and fuel injection pressure of 45bTDC and 250 bar, respectively. The fuel injection pressure was increased to 600 bar keeping the injection timing constant. HHO gas was added from 200 to 800 ml/min flowrate for the next test keeping 45bTDC injection timing and 600 bar injection pressure. The air flow rate, fuel flow rate, temperatures, and emissions were measured during each load condition. The load was varied from 0 to 75%. The loading beyond 75% was not done due to high pressure rise rate of 10 bar/CAD and above. To avoid the cycle-to-cycle variation, 40 cycles were averaged for combustion parameter reading. Each experimental reading was repeated 4 times to minimize human error. The emission reading was taken when the gas analyzer and smoke meter had minimum fluctuation and rise.

Table 3 HHO gas generation volumetric flow rates

S. No	Number of electrode connected	Number of (+ive) electrodes	Number of (−ive) electrodes	Volume flow rate (ml/min)
1	5	1	1	200
2	11	2	1	400
3	13	2	2	600
4	17	3	2	800

4 Results and Discussion

The in-cylinder pressure data variation with crank angle is used to calculate and tabulate various combustion and performance parameters. The Net Heat Release Rate (NHRR) was found out by applying the 1st law of thermodynamics to a control volume. The burnt gas mass fraction was calculated from heat release rate data. The Ignition Delay (ID) period was found out from starting crank angle of injection to starting crank angle of combustion. Combustion Duration (CD) was found in duration of CA90 and CA10. Figure 2 shows Variation Peak Pressure (bar), Maximum NHRR (J/Deg), Ignition ID, CD, and CA50 with Load. Figure 3a–c shows the variation of Peak Pressure and NHRR with crank angle.

Early injection HCCI strategy was adopted for all the tests performed. The peak in-cylinder pressure increased with an increase in fuel injection pressure due to thorough atomization of fuel into fine droplets and better mixing of fuel and air [19]. A similar condition was seen for the increase in load. The peak in-cylinder pressure increased with higher flow rate of HHO gas during each load condition [20]. The in-cylinder pressure varied from 31.52 to 36.59 bar at idling condition, 37.3 to 43.5 bar at 25% loading, and 45.36–53.7 bar at 50% loading.

The NHRR increased when higher fuel injection pressure was adopted [3]. The NHRR also increased as the flow rate of HHO gas was increased to 800 ml/min. The increase in load also enhanced the Heat Release Rates. The NHRR changed from 18.43 to 30.05 J/deg at zero load, 21.91 to 33.92 J/deg at 25% load, and 33.76–45.27 J/deg at 50% load.

Reduction in combustion duration was recorded due to higher burning speed of HHO gas. Combustion duration was also reduced due to higher injection pressure. The HHO gas has rare property to get diffused into wide variety of gases and air. Ignition got longer with HHO gas addition due to better mixing of fuel. The Combustion Phasing CA50 was advanced due to higher fuel injection pressure. HHO addition also resulted in advancing the combustion phasing closer to TDC.

The Mean Gas Temperature also increased due to higher fuel injection pressure and increased flow rate of HHO gas [20]. The variation was from 901 to 1178 at no load, 884 to 1219 at 25% load, and 1080 to 1240 at 50% load. Similarly, the Peak Pressure Rise Rate increased due to an increase in injection pressure and HHO gas addition. The Peak Pressure Rise Rate was more than 10 bar/deg above 50% load conditions.

The HHO gas is a combination of hydrogen, oxygen, and many active species which has very short reaction life. The overall burning speed of HHO gas is above 10 m/s which is faster than hydrogen. This expediates the C–H reaction speed. Oxygen directly supports the combustion process by taking part in burning and oxidation. The active species are strong oxidizing agents which further enhances combustion. The addition of HHO adds energy to existing combustion event which consumes less fuel reducing the brake-specific fuel consumption. Higher peak in-cylinder pressures resulted in enhanced brake power. Both these factors resulted in

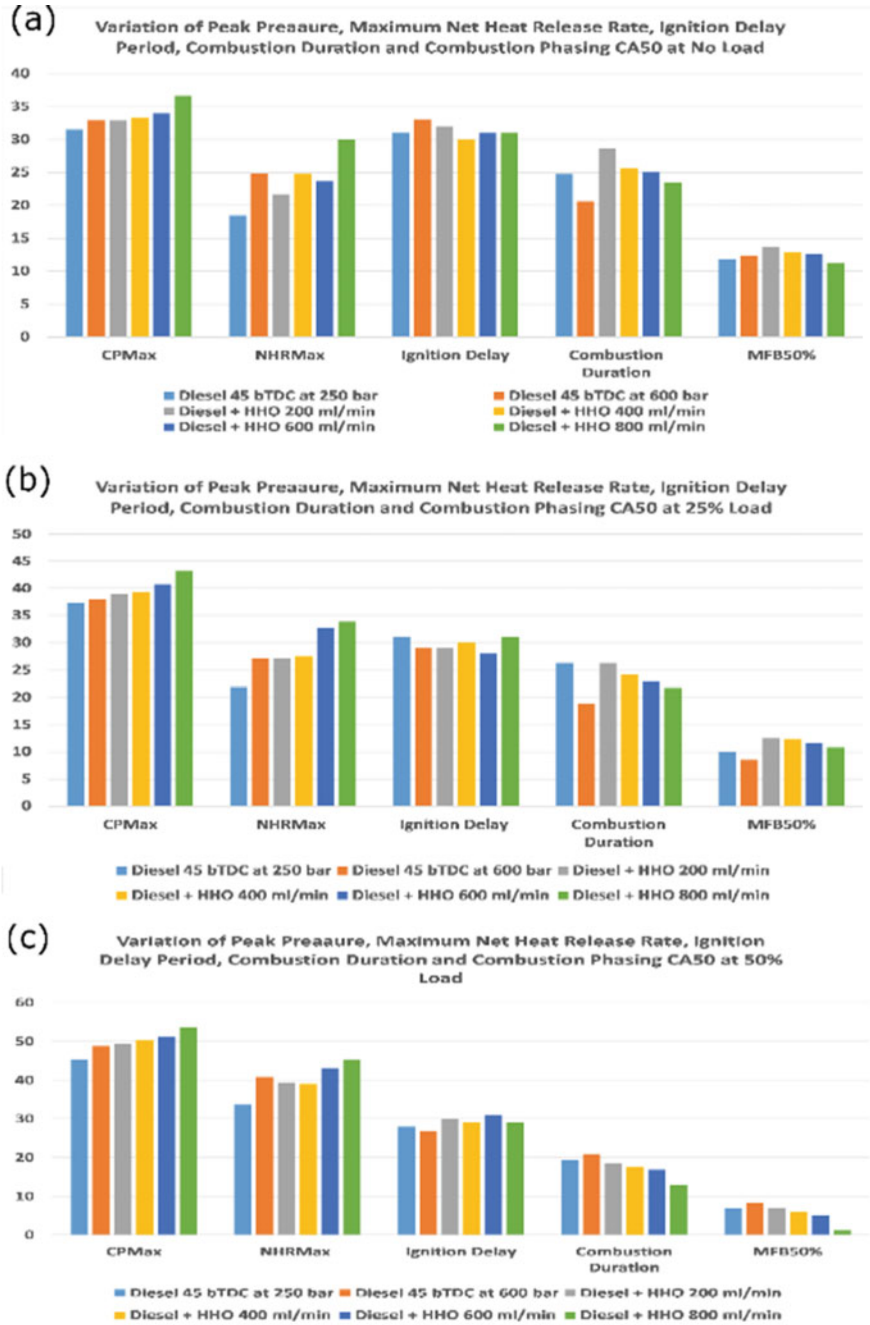

Fig. 2 Variation various combustion parameters with load and HHO flow rates

Fig. 3 Variation peak pressure and NHRR with crank angle

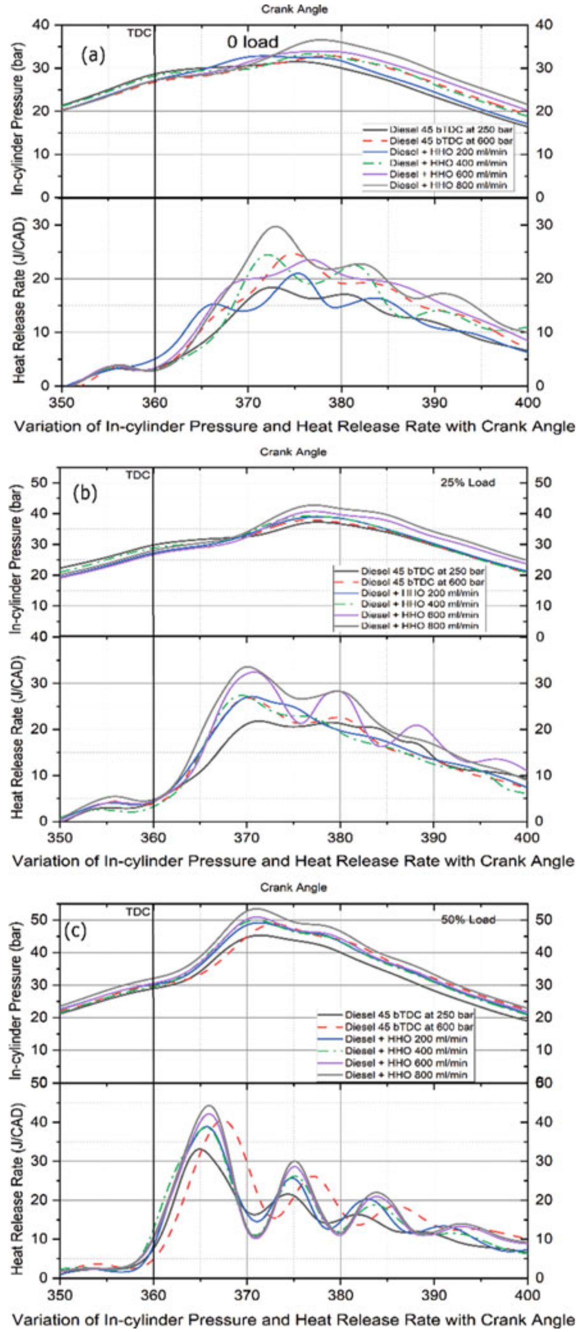

higher brake thermal efficiency. Detailed performance analysis has not been included in this article.

Figure 4a–e represents the variation of regulated emissions with higher flow rate of HHO gas and load. The CO, HC, CO_2, NOx, and smoke were measured by AVL gas Analyzer and Smoke meter.

Figure 4a shows CO emissions decreases when higher injection pressure was adopted [21]. The average reduction was 24.53% due to higher injection pressure. The CO emissions further reduced with higher flow rate of HHO gas. However, higher CO was emitted at 75% load due to higher Peak Pressure Rise Rates. The presence of oxygen in HHO gas promotes the oxidation of CO to CO_2. Thus, the increasing flow rate of HHO gas resulted in reduced CO emissions. CO reduced from 39.28 to 54.83% at 800 ml/min flowrate compared to 45 bTDC and 250 bar injection strategy.

Figure 4b indicates that the HC emissions increased with increasing injection pressure. The average increase in HC emissions was around 12.81%. This is due to fact that wall wetting gets more severe with higher injection pressure. The HC emissions further increased with the increasing flow rate of HHO. Higher HC emissions are caused due to wall wetting, fuel trapping in crevices, and low temperature of combustion. The increase in HHO concentration increases the brake-specific fuel consumption. This may be the reason for the trapping of more fuel in the crevices. The average increase in HC emission was 46.97% for 800 ml/min of HHO gas addition compared to 45bTDC and 250 bar injection strategy.

Figure 4c shows CO_2 emissions increase with an increase in fuel injection pressure. CO_2 further increased for higher flow rates of HHO gas. The higher peak pressure and heat release rates promote better combustion, and most of the CO gets converted into CO_2. The average increase in CO_2 due to higher injection pressure is around 17.02%. While the average increase in CO_2, emission was 42.85% with supply of 800 ml/min of HHO gas compared to 45bTDC and 250 bar injection strategy.

Figure 4d shows the NOx emissions were negligible up to 50% load. It was 12–35 ppm at 50% load condition. The NOx emissions increased drastically for higher injection pressure. There was no steep rise in NOx emissions since the Mean Gas temperatures were fairly low for the NOx formation. Higher NOx emissions were seen due to the high Peak Pressure Rise Rate at 75% Load. The results also show that NOx increased with the increasing concentration of HHO gas at 75% load. NOx is emitted due to the presence of high-temperature concentration regions in the combustion chamber. Hence, NOx emission is an issue for compression ignition engines. However, the early injection HCCI strategy is very useful in reducing NOx emissions [3].

Figure 4e represents the smoke emissions variation with load. The smoke emissions were high for 45bTDC and 250 bar injection strategy. The smoke emissions were reduced with higher injection pressure at 25 and 50% load [2]. The smoke emissions were further reduced with the higher flow rate of HHO gas. Lower smoke emissions were observed due to a reduction in the C/H ratio, and the combustion

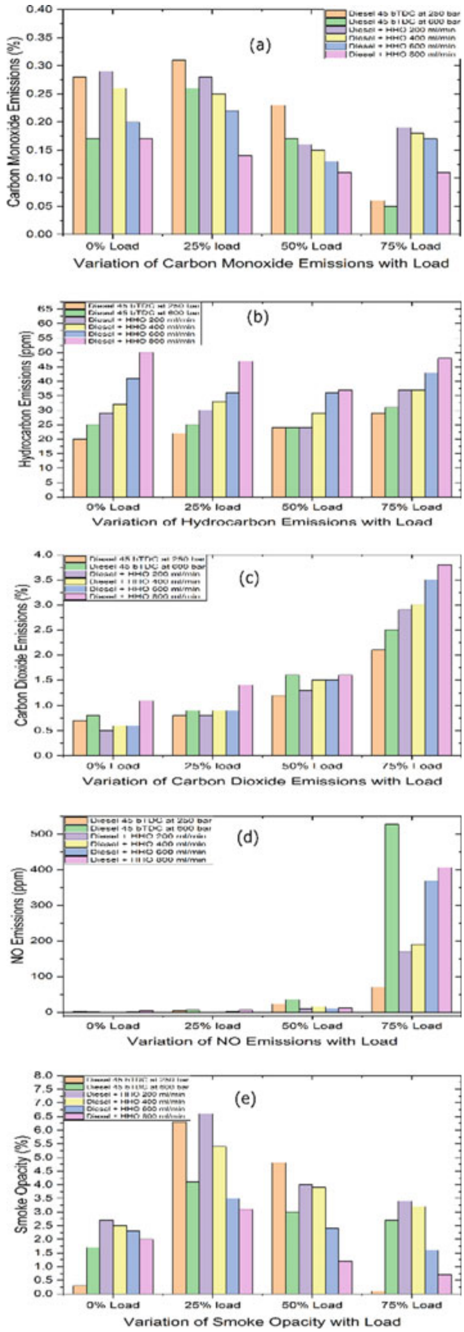

Fig. 4 Variation CO, HC, CO_2, NOx, and smoke with crank angle

was complete. The average decrease in smoke emission was 62.89% for supply of 800 ml/min of HHO gas compared to 45bTDC and 250 bar injection strategy.

5 Conclusions

The experiments were performed on a single cylinder 4 stroke diesel engine. Early direct injection strategy was explored with higher fuel injection pressure and the addition of varying flowrate of HHO gas. Following conclusions were made for this research work.

The Peak Pressure, Heat Release Rate, and Mean Gas Temperature increased due to the adoption of higher injection pressure. The above combustion parameters further increased with an increase in HHO gas concentration. Longer ignition delay periods were recorded with shorter combustion durations.

CO and smoke decreased by an average of 24.53% and 36.21% while HC and CO_2 increased by 12.81 and 17.2% due to higher injection pressure.

Due to the addition of HHO gas, NOx emissions were close to 35 ppm and less up to 50% load, CO emissions were reduced by 47.55% and smoke was reduced by 62.89%. However, HC and CO_2 emissions were higher by 46.97% and 17.02%, respectively.

Acknowledgements The authors are thankful to Shri Ramdeobaba College of Engineering and Management, Nagpur, for providing the experimental facility.

References

1. Kim MY, Lee CS (2007) Effect of a narrow fuel spray angle and a dual injection configuration on the improvement of exhaust emissions in a HCCI diesel engine. Fuel 86(17–18):2871–2880. https://doi.org/10.1016/j.fuel.2007.03.016
2. Kook S, Park S, Bae C (2008) Influence of early fuel injection timings on premixing and combustion in a diesel engine. Energy and Fuels 1077(7):331–337
3. Kiplimo R, Tomita E, Kawahara N, Yokobe S (2012) Effects of spray impingement, injection parameters, and EGR on the combustion and emission characteristics of a PCCI diesel engine. Appl Therm Eng 37:165–175. https://doi.org/10.1016/j.applthermaleng.2011.11.011
4. Al-Rousan AA (2010) Reduction of fuel consumption in gasoline engines by introducing HHO gas into intake manifold. Int J Hydrogen Energy 35(23):12930–12935. https://doi.org/10.1016/j.ijhydene.2010.08.144
5. Nabil T, Khairat Dawood MM (2019) Enabling efficient use of oxy-hydrogen gas (HHO) in selected engineering applications; transportation and sustainable power generation. J Clean Prod 237:117798. https://doi.org/10.1016/j.jclepro.2019.117798
6. Masjuki HH, Ruhul AM, Mustafi NN, Kalam MA, Arbab MI, Rizwanul Fattah IM (2016) Study of production optimization and effect of hydroxyl gas on a CI engine performance and emission fueled with biodiesel blends. Int J Hydrogen Energy 41(33):14519–14528. https://doi.org/10.1016/j.ijhydene.2016.05.273

7. Thangaraj S, Govindan N (2018) Investigating the pros and cons of browns gas and varying EGR on combustion, performance, and emission characteristics of diesel engine. Environ Sci Pollut Res 25(1):422–435. https://doi.org/10.1007/s11356-017-0369-4
8. Subramanian B, Thangavel V (2020) Analysis of onsite HHO gas generation system. Int J Hydrogen Energy 45(28):14218–14231. https://doi.org/10.1016/j.ijhydene.2020.03.159
9. Bhave N, Gupta M, Joshi S (2020) Effect of Brown's gas addition on combustion and emissions of homogeneous charge compression ignition engine. Energy Sources Part A Recover Util Environ Eff. https://doi.org/10.1080/15567036.2020.1817194
10. Uludamar E (2018) Effect of hydroxy and hydrogen gas addition on diesel engine fuelled with microalgae biodiesel. Int J Hydrogen Energy 43(38):18028–18036. https://doi.org/10.1016/j.ijhydene.2018.01.075
11. Tüccar G (2018) Effect of hydroxy gas enrichment on vibration, noise and combustion characteristics of a diesel engine fueled with Foeniculum vulgare oil biodiesel and diesel fuel. Energy Sources Part A Recover Util Environ Eff 40(10):1257–1265. https://doi.org/10.1080/15567036.2018.1476622
12. Rimkus A, Matijošius J, Bogdevičius M, Bereczky Á, Török Á (2018) An investigation of the efficiency of using O_2 and H_2 (hydrooxile gas –HHO) gas additives in a CI engine operating on diesel fuel and biodiesel. Energy 152:640–651. https://doi.org/10.1016/j.energy.2018.03.087
13. Baltacioglu MK, Arat HT, Özcanli M, Aydin K (2016) Experimental comparison of pure hydrogen and HHO (hydroxy) enriched biodiesel (B10) fuel in a commercial diesel engine. Int J Hydrogen Energy 41(19):8347–8353. https://doi.org/10.1016/j.ijhydene.2015.11.185
14. Aydin K, Kenanoğlu R (2018) Effects of hydrogenation of fossil fuels with hydrogen and hydroxy gas on performance and emissions of internal combustion engines. Int J Hydrogen Energy 43(30):14047–14058. https://doi.org/10.1016/j.ijhydene.2018.04.026
15. Birtas A, Voicu I, Petcu C, Chiriac R, Apostolescu N (2011) Effects of air-hydrogen induction on performance and combustion of a diesel engine. SAE Tech Pap. https://doi.org/10.4271/2011-24-0094
16. Ozcanli M, Akar MA, Calik A, Serin H (2017) Using HHO (Hydroxy) and hydrogen enriched castor oil biodiesel in compression ignition engine. Int J Hydrogen Energy 42(36):23366–23372. https://doi.org/10.1016/j.ijhydene.2017.01.091
17. Thangaraj S, Govindan N (2018) Evaluating combustion, performance and emission characteristics of diesel engine using Karanja oil methyl ester biodiesel blends enriched with HHO gas. Int J Hydrogen Energy 43(12):6443–6455. https://doi.org/10.1016/j.ijhydene.2018.02.036
18. Baltacioglu MK, Kenanoglu R, Aydın K (2019) HHO enrichment of bio-diesohol fuel blends in a single cylinder diesel engine. Int J Hydrogen Energy 44(34):18993–19004. https://doi.org/10.1016/j.ijhydene.2019.02.060
19. Monsalve-serrano J, Molina S, Garci A (2019) Effects of fuel injection parameters on premixed charge compression ignition combustion and emission characteristics in a medium-duty compression ignition diesel engine. https://doi.org/10.1177/1468087419867014
20. Sharma PK, Sharma D, Soni SL, Jhalani A, Singh D (2020) Energy, exergy, and emission analysis of a hydroxyl fueled compression ignition engine under dual fuel mode. Fuel 265:116923. https://doi.org/10.1016/j.fuel.2019.116923
21. Siewert RM (2018) Spray angle and rail pressure study for low NOx diesel combustion 2007(724):776–790

Effect of D–DEE–E Blend and Various Operating Parameters on CI Engine Performance: An Experimental Study

Chandan Kumar, K. B. Rana, Mohd. Suhaib Ansari, and Raju Malani

1 Introduction

All over the world, air pollution has become a big threat for the future of the next generation and as such researchers are working relentlessly to find an alternative clean fuel in other green fuel recourses for running CI (compression ignition) engines. India was placed 141 out of 180 nations in the 2016 environmental performance index (EPI). In 2018, India got 9th rank on most polluted (included both air and water pollution) countries in the world [1]. In India, 70% of air pollution comes from automobiles. The automobiles on the road have crossed over 3.7 million, and every year, they are increasing with an average rate of 8% [2]. These vehicles release toxic gases such as carbon monoxide (CO), nitrogen oxides (NOx), hydrocarbon (HC), and others, which create an unhealthy environment. The California Air Quality Board concluded that the small particle from the emission of the diesel engine caused the highest lung cancer. The Asthma and Allergy Foundation of America reported that the main cause of asthma is smoke. But society is very much dependent on these vehicles and cannot eliminate the entire vehicle from society. To overcome the harmful gases from the vehicle, the government of India released the vehicle of BS–IV emission standard in the country on 1 April 2017. Now, the government wants to introduce a BS–VI vehicle by April 1, 2020, escaping the BS–V so that less pollution is generated by the vehicle [3].

Worldwide, the use of diesel engines is increasing compared to SI engines due to their advantageous features. According to the CSO's report, India's economic growth in the year 2018–19 was 7.2%, which was more than 0.5% from the year 2017–18

C. Kumar (✉) · Mohd. S. Ansari · R. Malani
Department of Mechanical Engineering, SKIT, Jaipur 302017, India
e-mail: chandan.kumar@skit.ac.in

K. B. Rana
Department of Mechanical Engineering, RTU, Kota 324010, India

D. Sharma and S. Roy (eds.), *Emerging Trends in Energy Conversion and Thermo-Fluid Systems*, Lecture Notes in Mechanical Engineering,
https://doi.org/10.1007/978-981-19-3410-0_13

[3]. Economic growth increases fuel and gas energy consumption. Improvements to the engine's performance and emissions characteristics can have a significant impact on the economy and human health. Diesel engines are very popular for their high efficiency and lower fuel consumption. But they produce high particulate matter (PM), NOx, CO, smoke, and HC with conventional diesel fuel. Changing numerous engine settings such as injection pressure (IP), compression ratio (CR), and injection timing (IT) can improve engine performance and exhaust emission characteristics [4, 5]. Changing the engine design is difficult and expensive, so it should be appropriate to change some operating parameters. The diesel engine emits more NOx compared to spark ignition (gasoline engine) [6]. The NOx is responsible for acidic rain and photochemical smog. The percentage of NOx produced by a CI engine grows as the pressure and temperature in the combustion chamber rise [7].

The simplest way to remove this problem is fuel additives. The fuel additive is the chemical compounds added with major fuel (pure diesel) in the engine to improve the quality and performance of the vehicle. Oxygenated additives have the potential to improve the combustion process inside the combustion chamber [8]. Oxygenated fuels are a sustainable source of energy, and their oxygen atoms improve the combustion process. Both alcohol and ether have higher densities than diesel, resulting in a more homogenous mixture, as well as a higher oxygen concentration (in their molecular structure) and lower viscosity, making them acceptable for CI engines [9].

The current goal of the research is to better understand the performance characteristics and exhaust emissions of a direct injection diesel engine with a variable compression ratio (VCR) at various CR and IP for a blend of diesel, ethanol, and diethyl ether. The work is carried out at 80% diesel, 10% ethanol, and 10% diethyl ether blend (as suggested by the literature). For this purpose, experiment was performed on direct injection VCR diesel engine without changes of engine design. The findings are also compared to the performance parameters of ternary fuel (diesel–diethyl ether–ethanol) blend with the pure diesel.

By reviewing the various research publications, it was found that there is a need to investigate diesel, diethyl ether, and ethanol blend (D80–DEE10–E10) results at different CR and IP [10].

Diethyl ether is having a high oxygen content, lower auto-ignition temperature, better cetane number (CN), and elevated volatility. It is a very effective fuel in a sub-zero temperature zone for starting the engine in a cold climate. One of the exceptional properties of the DEE is that it burns smoothly in the rich fuel region inside the combustion chamber.

- A high volume of diethyl ether with diesel promotes knocking in the engine [11]
- Smoke, NOx, and PM can reduce by adding DEE with diesel in the CI engine [12]
- BTE enhanced by 7.2% and BSFC reduced by 6.7% when diesel engines were fed with DEE with diesel [13]
- HC and CO can be minimized by DEE and diesel blend.

Ethanol is a good fuel additive among all alcohols for CI engines. It can be obtained from various sources, like sugarcane, sugar beets, corn, and waste biomass materials. Because of its good physicochemical features, such as low flash point, low boiling point, and high oxygen content, ethanol is a good alternative biofuels for CI engines. It is also a safe additive because of its low flashpoint. Ethanol gives us better and complete combustion compare to diesel.

- Ethanol can reduce the PM and NOx of the exhaust emission [14]
- Dissolving ethanol in diesel can reduce the emissions of the vehicle
- The amount of ethanol increased the HC and CO from the engine's emission [15]
- BTE and BSFC both increase with the amount of ethanol [16]
- 10% vol. ethanol addition with diesel did not require any modification and stabilizer in the engine [17].

Several research on the effects of DEE and ethanol on a direct injection diesel engine was conducted. Iranmanesh et al. [18] investigated the possibility of DEE as an additive for improving CI engine combustion characteristics and lowering exhaust emissions. The experiments revealed that BSFC and BTE have improved slightly. The impact of DEE on the exhaust emissions and performance of a four-stroke CI engine was investigated by Mohanan et al. [19]. The most effective emission and performance metrics were found to be a blend of 5% DEE with diesel. Patil et al. [20] experimented on a four-stroke, single-cylinder, direct injection, compression ignition engine, with the results revealing low efficiency and high BSFC at full load conditions. Using a compression ignition engine, Huang et al. [21] investigated the potential of ethanol. At various ethanol blending ratios, fuel consumption increased by 5–31%. HC and CO levels drop during peak loads, while NOx levels drop during low loads. Li et al. [22] looked into the exhaust emissions and performance characteristics of a diesel–ethanol blend fueled in CI engine. The BTE and BSFC increased with the addition of ethanol to the blend. According to their findings with the ethanol–diesel blend, the smoke was reduced by 10% to 15%. In the ethanol–diesel blend, NOx and CO were reduced by 10% and 15%, respectively. Paul et al. [23] concluded that ethanol is not miscible beyond the 10% in diesel, but up to 10% there is no problem of miscibility with ethanol in diesel. Rakopoulos et al. [24] studied the exhaust emission and performance parameters of diesel engines using a diesel–DEE blend. The high proportion of DEE in the blending greatly lowered smoke and NOx emissions. With a larger percentage of DEE in the blend, the number of unburned HC particles rose. The effect of combining ethanol and DEE on the exhaust emission and performance parameters of a CI engine was studied by Paul et al. [10]. The optimum fuel blend was found to be 80% diesel, 10% DEE, and 10% ethanol out of all the blends tested. Because of their better qualities and combustion characteristics, D80–DEE10–E10 blends were utilized at fixed concentrations in this investigation. The engine performance and emission characteristics of the D80–DEE10–E10 blend were examined on a non-road, stationary variable compression ratio, compression ignition engine at different engine operating parameters such as injection pressure and compression ratios, which had not been documented in any research study in the accessible literature.

Table 1 Comparison of various properties [9]

Properties	Diesel	DEE	Ethanol
Molecular formula	$C_{12}H_{23}$	$C_4H_{10}O$	C_2H_5OH
Calorific value (kJ/kg)	44,000	33,900	26,950
Density (kg/m^3)	829	713	792
Viscosity (cST)	2.45	1.20	1.04
Cetane number	52	125	07
Late heat (kJ/kg)	250	350	840
Oxygen content (%)	0	22	34
Self-ign. temp. (°C)	250	380	420

2 Experimental Setup and Methodology

2.1 Preparation of Fuel Blend

The experiments started with the creation of a blend. On a volume basis, a single mixture of diesel, diethyl ether, and ethanol was made (D80, DEE10, and D10). The blend was prepared on a magnetic stirrer with a heating plate. Table 1 summarizes the various physical and combustion characteristics value of pure diesel, DEE, and ethanol.

First, pure diesel (80%) was taken according to the mixing ratio in a glass jar. After that, the DEE (10%) and ethanol (10%) were mixed according to the blend ratio. DEE and ethanol were blended with pure diesel drop by drop. Blend stabilization was checked before experimenting. The blend was kept for 72 h.

2.2 Engine Set up

This experiment was conducted with a 4-s single-cylinder, variable compression ratio compression ignition engine that was water-cooled. With the use of a lever arrangement located on the head (engine top) of the engine, the compression ratio of the engine can be altered by altering the cylinder head position. The injection nozzle is fitted with a calibrated protector, which allows the nozzle pressure to be adjusted. The engine arrangement is depicted in Fig. 1.

Various sensors were fitted to the engine in order to calculate the temperature of various parts of the engine. An eddy current dynamometer, control panel, personal computer, gas analyzer, and smoke meter are also attached to the engine. Table 2 lists the specifications for each piece of equipment.

(a)

(b)

Fig. 1 **a** Engine configuration in pictorial form and **b** pictorial view of a control panel

2.3 *Test Conditions and Procedure*

At a constant speed of 1500 rpm, the experiments were carried out. The load had been varied as 0%, 25, 50, 75%, and 100%. The load calculation had done by the eddy current dynamometer. The experiment was started with ignition switches for

Table 2 Equipment specifications

Equipment	Specification
Engine	TVI Kriloskar, 3750 W, 1500 rpm
Dynamometer	Power 3750 W, eddy current, 1500 rpm, air-cooled
Exhaust gas analyzer	AVL Modal—444 N
Smoke meter	AVL Modal—437C

this battery was connected with their terminals. All the water connections should be open for the cooling of the engine. Check the leak in the gas analyzer also. Adjust the dimmer status on the control panel to gradually vary the load on the engine. The strain gauge load cell measures the engine's applied load. Performance and emission data for various load conditions of the engine were monitored and recorded after 20–25 min.

3 Results and Discussion

3.1 D–DEE–E Blend Performance and Emissions Characteristics

The BTE of the engine for the ternary blend (D80–DEE10–E10) concerning engine load is depicted in Fig. 2. The maximum efficiency of 45% was obtained at full load with 19.5 CR. By changing the IP of the engine, maximum efficiency of 43.4% was obtained at the 210 bar at full load condition as shown in Fig. 3 [25]. If the BTE of the ternary blend is compared with the pure diesel, then the ternary fuels have higher efficiencies at almost all higher compressor ratios and injection pressure.

Break specific fuel consumption has been shown in Fig. 4 concerning load at different CR. The figure indicates that BSFC decreases in almost all cases. The

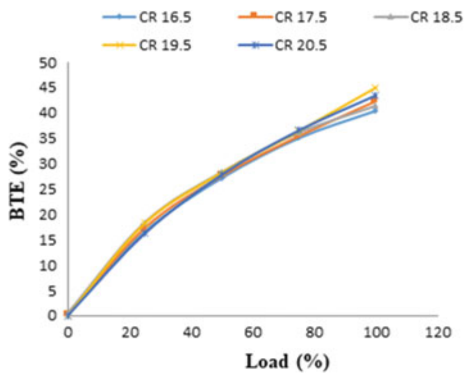

Fig. 2 BTE versus load at different CR

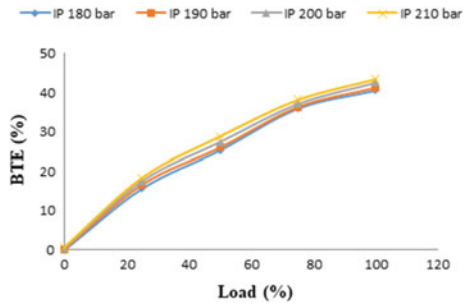

Fig. 3 BTE versus load at different IP

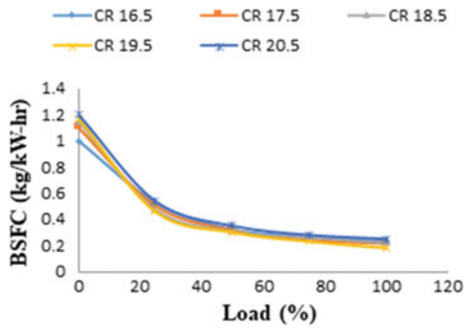

Fig. 4 BSFC versus load at different CR

lowest BSFC 0.18 kg/kW–h at 19.5 CR was obtained under full load conditions. Generally, BSFC decreases with the rise in the CR because of smooth combustion in the combustion chamber [26].

Figure 5 illustrates the effect of IP on BSFC. BSFC improved with higher applied load and injection pressure. At the IP of 210 bar, the ternary blend provides the minimum BSFC that of 0.2 kg/kW-hr.

Figure 6 shows the NOx characteristics concerning the applied load at different CR. The quantity of NOx increased when the load was applied and CR was higher on the engine. The value of NOx decreased when the injection pressure of the fuel is higher as discussed in Fig. 7.

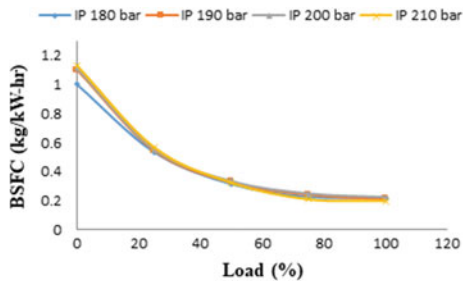

Fig. 5 BSFC versus load at different IP

Fig. 6 NOx versus load at different CR

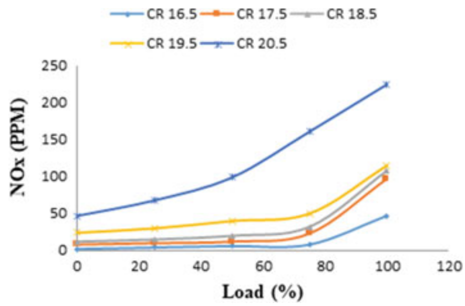

Fig. 7 NOx versus load at different IP

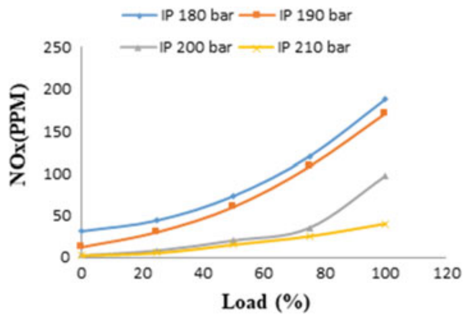

From the above, conclusion is that by reducing the CR and increasing IP in the engine the quantities of NOx reduce significantly at low load conditions [27].

Figure 8 depicts the variance of smoke (HSU) in different CRs with respect to the different applied load. Smoke in HSU decreased when the applied CR is higher. The lowest smoke was obtained at 19.5 CR.

Smoke in HSU (Hartridge Smoke Units) concerning load at different injection pressure has been shown in Fig. 9. Smoke reduces with higher injection pressure. The lowest smoke was obtained at the 210 bar.

Fig. 8 Smoke versus load at different CR

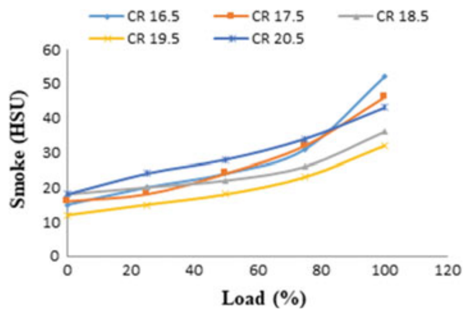

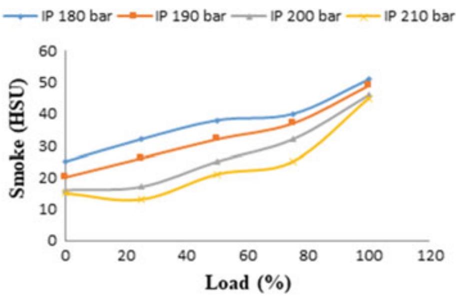

Fig. 9 Smoke versus load at different IP

4 Conclusions

The exhaust emission and performance parameters of the variable compression ratio compression ignition engine with a ternary fuel blend (D80–DEE10–E10) were studied at various CR and IP. The following conclusions can be drawn based on the obtained results and analysis:

The BTE of the blended fuel (D80–DEE10–E10) has been obtained higher than pure diesel. The enhancement in BTE was obtained 4.4% with the blend at 19.5 CR and 200 bar IP as compared to pure diesel (with standard engine parameters) at peak load. Similarly, at 210 bar IP and 17.5 CR, the efficiency of the blend was obtained 2.5% elevated than the pure diesel fuel at peak load.

With an increase in CR, IP, and load, the blended fuel's BSFC was shown to be lower than pure diesel fuel. At a compression ratio of 19.5 and a normal injection pressure of the engine with blended diesel, the lowest BSFC of 0.18 kg/kW-h was obtained.

Oxides of nitrogen for pure diesel were obtained higher than the blended fuel. NOx increases with the higher CR but decreases with higher IP. The lowest NOx of 40 PPM was obtained with 210 bar and 17.5 CR (at peak load condition), which was low (212 PPM) as a comparison to the diesel for the same condition.

Smoke amount of diesel-blended fuel was lower in comparison to the pure diesel with higher IP and CR. The lowest smoke was obtained at 19.5 CR and normal IP with the blended fuel. From the result, it was observed that the engine at 19.5 CR and 210 IP gives the best results for BTE, BSFC, NOx, and smoke.

References

1. The 2016 Environmental Performance Index is a project led by the Yale Center for Environmental Law and Policy (YCELP) and Yale Data–Driven Environmental Solutions Group at Yale University (Data–Driven Yale), the Center for International Earth Science Information Network (CIESIN) at Columbia University, in collaboration with the Samuel Family Foundation, McCall MacBain Foundation, and the World Economic Forum

2. Kumar C, Rana KB, Tripathi B, Nayyar A (2018) Properties and effects of organic additives on performance and emission characteristics of diesel engine: a comprehensive review. Environ Sci Pollut Res 25:22475–22498. https://doi.org/10.1007/s11356-018-2537-6
3. Annual report on energizing and empowering India by the ministry of petroleum and natural gas government of India (2018)
4. Yao C, Hu J, Geng P, Shi J, Zhang D, Ju Y (2017) Effects of injection pressure on ignition and combustion characteristics of diesel in a premixed methanol/air mixture atmosphere in a constant volume combustion chamber. Fuel 206:593–602
5. Khalife E, Tabatabaei B, Demirbas AAM (2017) Impacts of additives on performance and emission characteristics of diesel engines during steady–state operation. Prog Energy Combust Sci 59:32–78
6. Dickey DW, Ryan TW, Matheaus AC (1998) NOx control in heavy–duty diesel engines–what is the limit
7. Kumar C, Rana KB, Tripathi B, Nayyar A (2018) A comparative study of oxygenated additives for diesel in compression ignition engine. Int J Renew Energy Technol 9:16–27
8. Pandian K, Munuswamy DB, Radhakrishana S, Nagappan B, Devarajan Y (2017) Influence of an oxygenated additive on the emission of an engine fueled with neat biodiesel. Pet Sci 14(4):791–797
9. Kumar C, Nayyar A, Bafna M, Agarwal A, Parkash V (2015) Analysis of emission characteristic of NM–diesel blend on VCR diesel engine. IJMECH 4:115–24
10. Paul A, Bose PK, Panua RS, Debroy D (2014) Study of performance and emission characteristics of a single cylinder CI engine using diethyl ether and ethanol blends. J Energy Inst 88:1–10
11. Lee S, Kim TY (2017) Performance and emission characteristics of a DI diesel engine operated with diesel/DEE blended fuel. Appl ThermEng 121:454–461
12. Anand R, Mahalakshmi NV (2007) Simultaneous reduction of NOx and smoke from a direct–injection diesel engine with exhaust gas recirculation and diethyl ether. Proc Mech Part D J Automobile Eng 221(D1):109–116
13. Ibrahim A (2016) Investigating the effect of using diethyl ether as a fuel additive on diesel engine performance and combustion. Appl Therm Eng 107:853–862
14. Kumar C, Rana KB, Tripathi B, Gupta P (2018) Combustion characteristics of methanol blended diesel fuel in CI engine. Int J Pharm Sci Rev Res 50:101–104
15. Xu BY, Qi YL, Zhang WB, Cai SL (2007) Fuel properties and emission characteristics of ethanol–diesel blend on small diesel engine. Int J Automot Technol 8:9–18
16. Kumar C, Bafna M, Nayyar A, Parkash V, Goyal N (2014) Experimental investigation of the performance of VCR diesel engine fuelled by NM–diesel blend. IJETAE 4:122–125
17. Putrasari Y, Nur A, Muharam A (2013) Performance and emission characteristic on a two cylinder DI diesel engine fuelled with ethanoldiesel blends. Phys Procedia 32:21–30
18. Iranmanesh M, Subrahmanyam J P, Babu M KG (2008) Potential of Diethyl ether as supplementary fuel to improve combustion and emission characteristics of diesel engines. SAE paper: 2008–28–0044
19. Mohanan P, Kapilan N, Reddy RP (2003) Effect of diethyl ether on the performance and emission of a 4–S Di diesel engine. SAE paper: 2003–01–0760
20. Patil KR, Thipse SS (2015) Experimental investigation of CI engine combustion, performance and emissions in DEE–kerosene–diesel blends of high DEE concentration. Energy Conserv Manage 89:396–408
21. Huang J, Wanga Y, Li S, Roskilly AP, Yu H, Li H (2009) Experimental investigation on the performance and emissions of a diesel engine fuelled with ethanol–diesel blends. Appl Therm Eng 29:2484–2490
22. Li D, Zhen H, Xingcai L, Wu–gao Z, Jian–guang Y (2005) Physico–chemical properties of ethanol–diesel blend fuel and its effect on performance and emissions of diesel engines. Renew Energy 30:967–976
23. Paul A, Panua R, Bose P K, Banerjee R (2013) An experimental study of performance and emission parameters of a compression ignition engine fueled by different blends of Diesel–Ethanol–biodiesel. IEEE 978–1–4673–6150–7/13

24. Rakopoulos DC, Rakopoulos CD, Giakoumis EG, Dimaratos AM (2012) Characteristics of performance and emissions in high–speed direct injection diesel engine fueled with diethyl ether/diesel fuel blends. Energy 43:214–224
25. Jindal S, Nandwana BP, Rathore NS, Vashistha V (2015) Experimental investigation of the effect of compression ratio and injection pressure in a direct injection diesel engine running on Jatropha methyl ester. https://doi.org/10.1016/j.applthermaleng.2009.10.004
26. My Tech zone (2015) The benefits of high injection pressure on future heavy duty engine performance. SAE–24–2441
27. Kumar C, Rana KB (2019) Tripathi B (2019) Effect of diesel–methanol–nitromethane blends combustion on VCR stationary CI engine performance and exhaust emissions. Environ Sci Pollut Res 26:6517–6531

Three-Dimensional Computational Investigation of Novel Pin Fin Heat Sinks

Kapil Kalra and Amit Arora

Nomenclature

$\overline{\mathrm{Nu}}$	Average Nusselt number
$\overline{h}$	Average convective heat transfer coefficient
D_h	Hydraulic diameter
k_f	Thermal conductivity of fluid
ρ	Density of fluid
$\overline{Tw}$	Average base plate temperature
T_{in}	Inlet temperature
T_{out}	Outlet temperature
A_s	Total surface area in fluid contact
A	Cross section area of channel
P_c	Perimeter of channel
ΔT	Temperature difference
Q''	Heat flux
ΔP	Pressure difference
P_{in}	Inlet pressure
P_{out}	Outlet pressure
Re	Reynolds number
μ	Dynamic viscosity of fluid
μ_t	Eddy viscosity of fluid
v_{in}	Inlet velocity.
k	Turbulent kinetic energy
G_k	Generation of turbulence kinetic energy due to the mean velocity gradients

K. Kalra (✉) · A. Arora
Department of Mechanical Engineering, Malaviya National Institute of Technology Jaipur, Jaipur, Rajasthan 302017, India
e-mail: kapilkalra145@gmail.com

D. Sharma and S. Roy (eds.), *Emerging Trends in Energy Conversion and Thermo-Fluid Systems*, Lecture Notes in Mechanical Engineering,
https://doi.org/10.1007/978-981-19-3410-0_14

G_b	Generation of turbulence kinetic energy due to buoyancy
Y_M	Contribution of the fluctuating dilatation in compressible turbulence to the overall dissipation rate
ϵ	Turbulent dissipation rate
S_k, S_ϵ	User-defined source terms
C_2	Constant = 1.9
$C_{1\varepsilon}$	Constant = 1.44
σ_k	Turbulent Prandtl numbers for k
σ_ϵ	Turbulent Prandtl numbers for ϵ.

1 Introduction

As the computational capacity [1] of the microprocessor is increasing day by day, more advanced cooling systems are required to expel more heat into the surrounding. Microprocessors are made up of semiconductor components, and their performance greatly depends on the operating temperature [2]. Heat sinks are designed to maintain the temperature of these microprocessors below 100 °C to avoid their failure [3]. Also, a large amount of heat gets accumulated near the core area of the microprocessor as they are subjected to higher heat flux. This leads to the formation of hotspots [4] which may increase the local temperature at the hotspots beyond controlled limits. This problem of hotspot formation becomes more severe if a multicore processor is used.

Modifying the geometry of the heat sink and improving coolant properties are the two commonly practiced techniques to increase the heat transfer through a single-phase coolant [5]. Several techniques have been reported for hotspot mitigation like micro-jet impingement [6], micro-gaps [7], micro-channel [8], heat sink cooling, etc. Pin fin heat sinks using water as a cooling fluid has shown promising results in compact electronic device cooling systems [9, 10]. Apart from the abovementioned cooling methods for hotspot mitigation, a little work is done in the field of composite heat sinks. Accordingly, a composite heat sink with two different configurations is proposed in this article.

Difference in thermal conductivities of copper and aluminum is used in the design of composite pin fin heat sinks. The areas with higher heat flux are provided with copper fins while those with lower heat flux are provided with aluminum fins (Fig. 1).

Fig. 1 Base plate of the heat sink to mimic microprocessor surface

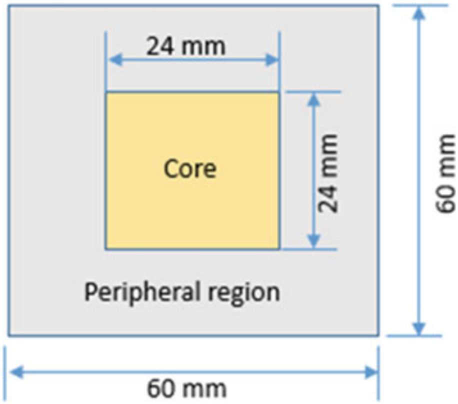

2 Mathematical Model

2.1 Heat Sink Model and Fluid Domain

A total of 100 pin fins of diameter 3 mm are dispersed on the rectangular section of the microprocessor surface which is divided into two regions, namely the core region and the peripheral region as shown in Fig. 1. The heat flux at the peripheral region is taken as 200 KW/m^2, and for the core region, it is taken as 900 KW/m^2. Three different configurations of pin fin heat sinks shown in Fig. 2 are considered with a rectangular base plate of dimensions 60 mm × 60 mm. The fins are equally spaced with longitudinal and transverse pitch of 6 mm. Two different fluids, namely water and air, are used for the simulation study. The height of the pin fins is taken as 25 mm. The entrance length is taken as 745 mm, while the downstream length is taken as 1490 mm as shown in Fig. 3. Downstream length is taken more than the entrance length to mitigate the effects of turbulence created by pin fins as the fluid passes through them.

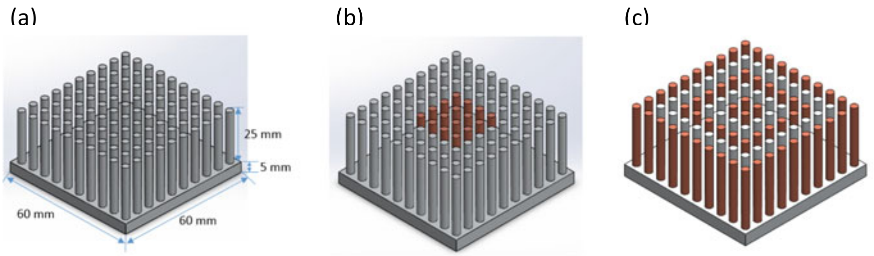

Fig. 2 Schematic diagram of three heat sink configurations **a** All Aluminum fins, **b** Cu–Al composite heat sink with Cu fins in the core, **c** Cu–Al composite heat sink with fins dispersed in alternate rows

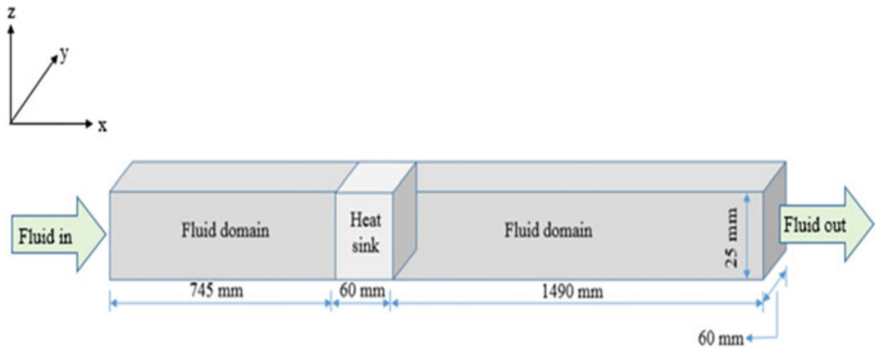

Fig. 3 Fluid domain

Radiation losses to the ambient and conduction losses to the surrounding channel are neglected. A 3D steady-state simulation has been done using Ansys Fluent 15.0. The flow is taken as incompressible.

2.2 Governing Equations

Navier–Stokes equations comprising of the continuity equation, momentum equation, and energy equation are discretized using the finite volume method. The turbulence is modeled using the realizable k-ε model with a standard wall function. Turbulence intensity is taken as 10%, and the hydraulic diameter is taken as 0.03529 m. The pressure–velocity coupling is done by the SIMPLEC algorithm.

Continuity equation

$$\frac{\partial \rho \overline{u}_i}{\partial x_i} = 0 \tag{1}$$

Momentum equation

$$\rho \overline{u}_j \frac{\partial \overline{u}_i}{\partial x_j} = -\frac{\partial \overline{p}}{\partial x_i} + \frac{\partial}{\partial x_j}\left[\mu_t\left(\frac{\partial \overline{u}_i}{\partial x_j} + \frac{\partial \overline{u}_j}{\partial x_i}\right)\right] \tag{2}$$

Energy equation

$$\rho \overline{u}_j \frac{\partial \overline{T}}{\partial x_j} = \frac{\partial}{\partial x_j}\left[\left(\mu + \frac{\mu_t}{\sigma_\epsilon}\right)\frac{\partial \overline{T}}{\partial x_j}\right] \tag{3}$$

$K - \varepsilon$ realizable transport equations

$$\frac{\partial(\rho k)}{\partial t}+\frac{\partial}{\partial x_j}\left(\rho k u_j\right)=\frac{\partial}{\partial x_j}\left[\left(\mu+\frac{\mu_t}{\sigma_k}\right)\frac{\partial k}{\partial x_j}\right]+G_k+G_b-\rho\epsilon+Y_M+S_k \tag{4}$$

$$\frac{\partial(\rho\epsilon)}{\partial t}+\frac{\partial}{\partial x_j}\left(\rho\varepsilon u_j\right)=\frac{\partial}{\partial x_j}\left[\left(\mu+\frac{\mu_t}{\sigma_\epsilon}\right)\frac{\partial\varepsilon}{\partial x_j}\right]$$
$$+\rho C_1 S_\epsilon-\rho C_2\frac{\epsilon^2}{k+\sqrt{v\varepsilon}}+C_{1\varepsilon}\frac{\varepsilon}{k}C_{3\varepsilon}G_b+S_\epsilon \tag{5}$$

Nusselt number

$$\overline{Nu}=\frac{q''}{k_f\left[\overline{T_W}-\frac{T_{in}+T_{out}}{2}\right]} \tag{6}$$

Heat transfer coefficient

$$\overline{h}=\frac{\overline{Nu}D_h}{k_f} \tag{7}$$

Hydraulic diameter

$$D_h=\frac{4A}{P_C} \tag{8}$$

Reynolds number

$$Re=\frac{\rho v_{in}D_h}{\mu} \tag{9}$$

Pressure difference

$$\Delta P = Pin-Pout \tag{10}$$

2.3 Materials

Copper and aluminum are used in the design of the heat sink. Heat sink with all aluminum fins is used as the reference while analyzing the uniformity in the temperature delivered by the composite heat sink. The thermo-physical properties of the fin material and the working fluids are given in Table 1.

Table 1 Thermo-physical properties of materials

Material	Thermal conductivity (W/m–K)	Density (kg/m^3)	Dynamic viscosity (kg/m-s)
Aluminum	202.4	2719	–
Copper	387.6	8978	–
Air	0.0242	1.225	1.7894e−05
Water	0.6	998.2	0.001003

Table 2 Grid independency test

Minimum element size (mm)	Number of elements	Maximum temperature of base plate (K)
0.79	747,809	370.8
0.7	896,024	371.6
0.52	938,404	371.8

2.4 Boundary Conditions and Grid Independency Test

All the walls of the channel are assumed to be adiabatic with the no-slip condition. A uniform flux of 900 KW/m^2 is applied at the core region of the base plate while the peripheral region of the base plate is given a flux of 200 KW/m^2. At the inlet section of the fluid domain, the constant velocity with a temperature of 300 K is provided to the fluid. At the outlet section, the condition of outflow with a flow weighting rate of unity is imposed.

Three different mesh sizes are taken for the grid independency test that are shown in Table 2. The grid independency test is performed on the heat sink model which is shown in Fig. 2b. Water is taken as the fluid, and the Reynolds number is 3512. The mesh size of 0.52 mm with a total number of elements of 938,404 has been selected for the analysis.

2.5 Model Validation

Assumptions made in the simulation study are validated on the basis of the Nusselt number. The experimental data values of the Nusselt number obtained by Chin et al. [11] for the staggered arrangement of pin fins with 14 pin fins are compared with the simulation results. The experimental and simulation results are found to be in good agreement as shown in Fig. 4.

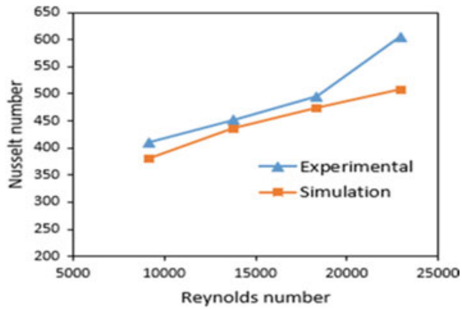

Fig. 4 Model validation

3 Results and Discussions

The temperature contours of the three configurations are compared at three different values of Reynolds number, i.e., $Re_1 = 3512$, $Re_2 = 7024$, and $Re_3 = 10{,}536$ with water and air as cooling fluid. Figures 5 and 6 show the temperature variation of these three configurations at various Reynolds numbers.

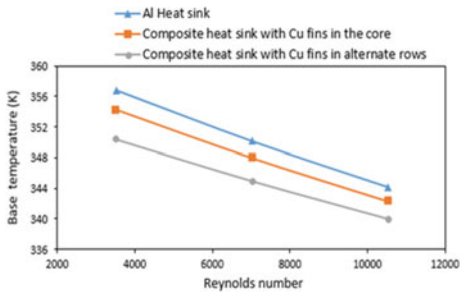

Fig. 5 Average base plate temperature with water as the cooling fluid

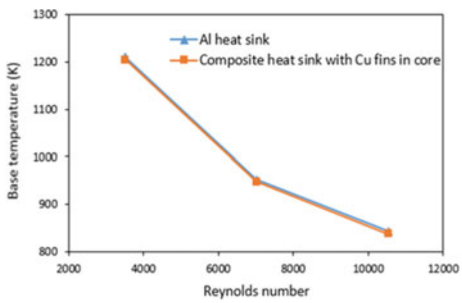

Fig. 6 Average base plate temperature with air as the cooling fluid

3.1 All Aluminum Heat Sink

A heat sink with all aluminum pin fins is analyzed with both water and air to provide reference data for the other two configurations. When air is used as a cooling fluid, the average temperatures of the base plate of the heat sink are found to be 1209.27 K, 952.61 K, and 843.77 K at $Re_1 = 3512$, $Re_2 = 7024$, and $Re_3 = 10{,}536$, respectively. Figure 7a, b shows the temperature contour at $Re_1 = 3512$ and $Re_3 = 10{,}536$, respectively. The center line temperature distribution shown in Fig. 7c reveals that maximum temperature is obtained at the center of the heat sink which acts as a local hotspot area. All these values of temperature are too high for a semiconductor device. Thus, using air for cooling of such microprocessors at the mentioned Reynolds number is not recommended. It is also found that the values of temperature whether average base plate temperature or peak base plate temperature reduce on increasing Reynolds number.

However, when water is used as the cooling fluid, the average values of base plate temperature are found to be 356.82 K, 350.16 K, and 344.19 K which are under the controlled limits but the maximum temperature reached 379.1 K which is greater than the recommended limit of 373.15 K. The temperature contours for this configuration are shown in Fig. 8a, b. Figure 8c shows that the center line temperature distribution is axisymmetric in nature with the peak temperature at the center point. Thus, changes in the material of the heat sinks are done to address this problem of hotspot formation.

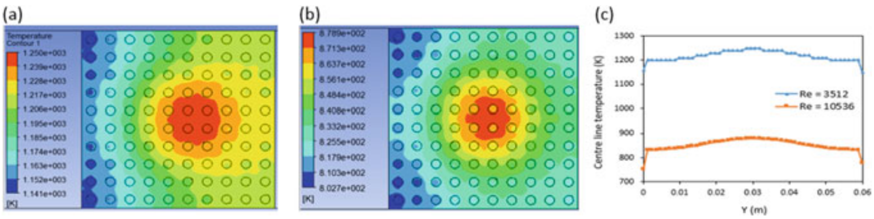

Fig. 7 Base temperature of Al heat sink with air **a** $Re_1 = 3512$, **b** $Re_3 = 10{,}536$, **c** temperature distribution

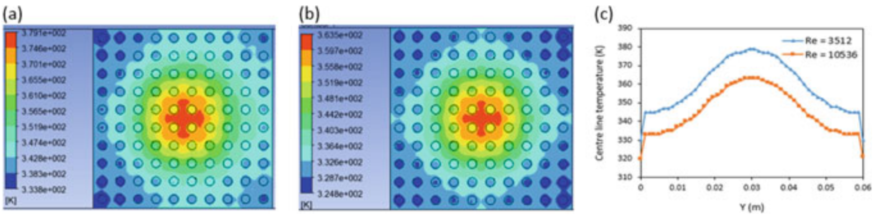

Fig. 8 Base temperature of Al heat sink with water **a** $Re_1 = 3512$, **b** $Re_3 = 10{,}536$, **c** temperature distribution

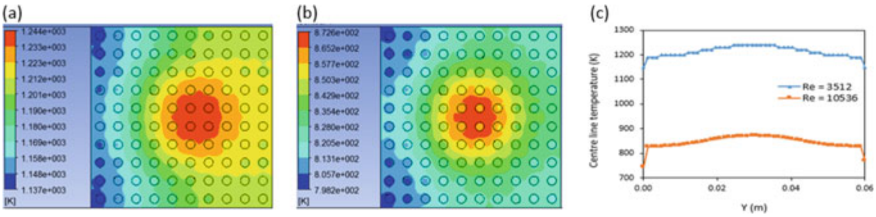

Fig. 9 Base temperature of Cu–Al composite heat sink with Cu fins in the core with air **a** $Re_1 = 3512$, **b** $Re_3 = 10{,}536$, **c** temperature distribution

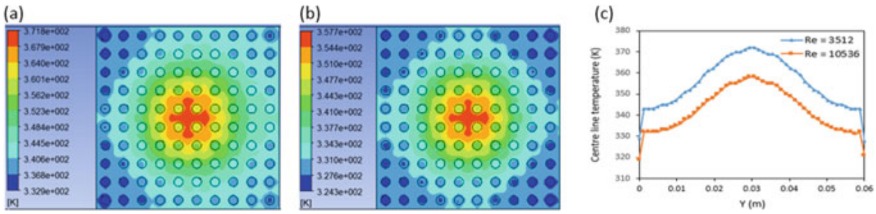

Fig. 10 Base temperature of Cu–Al composite heat sink with Cu fins in the core with water **a** $Re_1 = 3512$, **b** $Re_3 = 10{,}536$, **c** temperature distribution

3.2 Composite Heat Sink with Copper Core

The arrangement of pin fins is shown in Fig. 2b. In this design, the core has copper fins, whereas aluminum fins occupy the outer rows. This arrangement is also found unfeasible to be used with air as a cooling fluid as the average temperatures are quite high but this arrangement has brought down the peak temperature of the base plate within recommended limits with water as a cooling fluid. Also, this arrangement provided reduced average base plate temperatures at the corresponding Reynolds number when compared to the heat sink with all Al fins as shown in Figs. 9 and 10.

3.3 Composite Heat Sink with Fins Dispersed in Alternate Rows

The arrangement of pin fins is shown in Fig. 2c. In this design, the copper and aluminum fins occupy alternate rows. This arrangement is analyzed with only water as the cooling fluid. Air is not taken into consideration due to enormously high temperatures obtained in the previous two arrangements.

Figure 11 shows that the lowest peak temperatures and average base temperatures are obtained for this arrangement at the corresponding Reynolds number when compared to the previous two arrangements. The average values of base plate temperatures are found to be 350.35 K, 344.93 K, and 339.98 K at $Re_1 = 3512$, $Re_2 = 7024$,

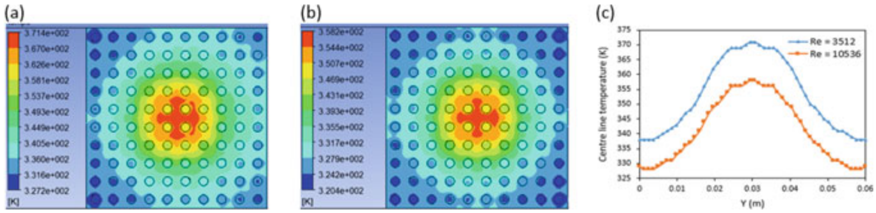

Fig. 11 Base temperature of Cu–Al composite pin fin heat sink with fins dispersed in alternate rows with water **a** $Re_1 = 3512$, **b** $Re_3 = 10{,}536$, **c** temperature distribution

Fig. 12 Center line temperature distribution with water as the cooling fluid at $Re_3 = 10{,}536$

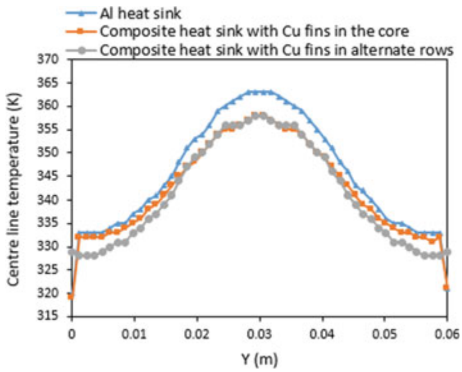

and $Re_3 = 10{,}536$, respectively. This configuration has made the center line temperature distribution flatter along with a slight decrement in the peak temperature when compared with the Al–Cu composite heat sink with Cu fins in core as shown in Fig. 12.

4 Conclusions

A numerical simulation study is performed for different arrangements of pin fin heat sink at various Reynolds numbers to reduce the temperature gradients on the surface of a microprocessor. Based on the study, the following key conclusions are drawn:

- Average base plate temperature decreases on increasing Reynolds number.
- Using air alone with pin fin heat sink for the cooling of a microprocessor is not feasible at the discussed values of Reynolds number as the average base plate temperature is found to be quite high.
- Pin fin heat sink with all Al fins when used with water brought down the average base temperature of the heat sink within recommended limits but the local temperature at some points increased the recommended limit.

- Both arrangements of Al–Cu composite pin fin heat sinks brought down the local as well as the average temperature of the base plate of the heat sink within the recommended limit when used with water.
- Configuration in which Cu–Al fins are dispersed in alternate rows provided the lowest average base plate temperature of 339.98 K at $Re_3 = 10{,}536$ with water among all configurations.

Acknowledgements The corresponding authors are thankful to the Ministry of Education, Government of India for providing the facilities and platform for the research work.

References

1. Huang CH, Liu YC, Ay H (2015) The design of optimum perforation diameters for pin fin array for heat transfer enhancement. Int J Heat Mass Transf 1(84):752–765
2. Hosseinizadeh SF, Tan FL, Moosania SM (2011) Experimental and numerical studies on performance of PCM-based heat sink with different configurations of internal fins. Appl Therm Eng 31(17–18):3827–3838
3. Sauciuc L, Chrysler G, Mahajan R, Szleper M (2003) Air-cooling extension- performance limits for processor cooling applications. In: 19th annual IEEE semiconductor thermal measurement and management symposium, San Jose, CA, USA, IEEE, 2003, pp 74–81. https://doi.org/10.1109/STHERM.2003.1194342K; Hussain M (2016) Aerodynamic performance evaluation of a novel turbine, Ph.D. thesis, Department of Mechanical Engineering, IIT Guwahati, India, 2016
4. Ansari D, Jeong JH (2020) A novel composite pinfin heat sink for hotspot mitigation. Int J Heat Mass Transf 1(156):119843
5. Bhandari P, Prajapati YK (2021) Thermal performance of open microchannel heat sink with variable pin fin height. Int J Therm Sci 159:106609
6. Han Y, Lau BL, Zhang X, Leong YC, Choo KF (2014) Thermal management of hotspots with a microjet-based hybrid heat sink for GaN-on-Si devices. IEEE Trans Compon Packag Manuf Technol 4(9):1441–1450
7. Hu Y, Sarvey T, Bakir M, Joshi Y (2017) Single phase liquid cooling of hotspots in a heterogeneous pin-fin-enhanced microgap with non-uniform fin array. In: 2017 16th IEEE intersociety conference on thermal and thermomechanical phenomena in electronic systems (ITherm) 2017 May 30. IEEE, pp 500–504
8. Hajmohammadi MR, Alipour P, Parsa H (2018) Microfluidic effects on the heat transfer enhancement and optimal design of microchannels heat sinks. Int J Heat Mass Transf 1(126):808–815
9. Lorenzini D, Green C, Sarvey TE, Zhang X, Hu Y, Fedorov AG, Bakir MS, Joshi Y (2016) Embedded single phase microfluidic thermal management for non-uniform heating and hotspots using microgaps with variable pin fin clustering. Int J Heat Mass Transf 1(103):1359–1370
10. Sarvey TE, Hu Y, Green CE, Kottke PA, Woodrum DC, Joshi YK, Fedorov AG, Sitaraman SK, Bakir MS (2017) Integrated circuit cooling using heterogeneous micropin-fin arrays for nonuniform power maps. IEEE Trans Compon Packag Manuf Technol 7(9):1465–1475
11. Chin SB, Foo JJ, Lai YL, Yong TK (2013) Forced convective heat transfer enhancement with perforated pin fins. Heat Mass Transf 49(10):1447–1458

Studies on the Performance and Emission Characteristics of a Diesel Engine Fueled with Honge Pyrolysis Oil Blends

Sharan Shegedar and C. H. Biradar

Nomenclature

$°CA(°)$	Crank angle
bTDC	Before top dead center
DI	Direct injection

1 Introduction

Human population, technological advancement, and industrial growth are all important factors influencing global energy demand. Currently, fossil fuels fulfill the majority of global energy demand. According to the study, overall fossil fuel consumption has increased by nearly 51% in the last two decades, with an additional 18% increase expected in the next 20 years [1]. The main advantages of fossil fuels are their ease of transport and high energy density. However, the drawbacks of fossil fuels include limited reserves, nonrenewable nature, pollution, and price volatility, which have prompted a focus on alternative and renewable fuels to address these issues [2]. Presently, the most pressing issue is climate change caused by automobile emissions. So there is an urgent need to reduce exhaust emissions by using alternative fuels in automobiles (especially in diesel engines).

S. Shegedar (✉)
Department of Mechanical Engineering, Sharnbasva University, Kalaburagi 585103, India
e-mail: sharan.shegedar@gmail.com

C. H. Biradar
Department of Automobile Engineering, PDACE, Kalaburagi 585102, India

D. Sharma and S. Roy (eds.), *Emerging Trends in Energy Conversion and Thermo-Fluid Systems*, Lecture Notes in Mechanical Engineering,
https://doi.org/10.1007/978-981-19-3410-0_15

Bio-fuels are alternative and renewable fuels derived from waste biomass. Bio-fuels are recommended for a variety of issues, such as energy security, environmental issues, foreign exchange, and rural socioeconomic issues [3]. Many developing nations have vast agricultural and forest lands, with the proportion of resources of biomass usage ranging from 40–50%. India has extensive biomass resources, such as non-edible tree-borne oilseeds. Biodiesel can be produced from these plant seeds and used in a diesel engine as an alternate fuel [4]. Pongamia Pinnata (Honge) is a leguminous tree found throughout India. The Honge tree has limited economic importance in India. Hence, the Government of India initiated a Honge tree plantation drive for local bio-fuel production in 2003 [5]. The availability of Honge seeds in India is currently estimated to be around 0.2 million metric tons per year. The oil extracted by the oil expeller is nearly 28–30% of the total weight of the seed, leaving the remaining 70% of the seedcake as a by-product. As a result, 0.145 million metric tons of Honge de-oiled seedcake (HDSC) will be generated per year [6]. This massive amount of HDSC generated each year after oil extraction from the Honge seeds needs to be used effectively and in an eco-friendly manner. However, The HDSC cannot be used directly as a fertilizer or animal feedstock due to toxicity in nature [7]. Furthermore, the HDSC (non-edible seedcake) raises concerns about disposal land availability and GHG emissions [8]. A few studies have reported the successful conversion of non-edible seedcakes into biogas, bio-oil, and bio-ethanol using various processes described in the literature [9–11]. Hence, in the present work, HDSC is used as a feed material for the pyrolysis process to generate pyrolysis oil (bio-oil) rather than simply discarding it as a waste.

Pyrolysis is a thermo-chemical conversion route for converting organic solid waste into valuable products and by-products. It uses heat to decompose the feedstock (biomass) in the anaerobic atmosphere to obtain products such as liquid pyrolysis oil, gaseous product (pyrolytic gas), and solid bio-char [12]. The type and yield of products and by-products obtained from the pyrolysis process depend on the modes of pyrolysis (slow, intermediate, and fast pyrolysis) and various influencing factors such as heating temperature, heating rate, reactor type, residence time of vapor, and particle size [13]. Furthermore, the raw material (biomass feedstock) used and operational parameters influence the quality as well as the yield of bio-oil (pyrolysis oil). The bio-oil acquired via the pyrolysis process contains intricate mix of oxygenated organic compounds like alcohols, aldehydes, alkanes, aromatic, and phenol [13, 14]. The usage of neat bio-oil directly in a diesel engine needs to be avoided because of poor fuel qualities like low calorific value, higher water content, high viscosity, instability issues, and low pH value [14, 15]. However, bio-oil can be improved through upgrading methods to make it appropriate for use as a diesel engine fuel. As bio-oil is not soluble in the base diesel but may be upgraded by emulsifying with diesel fuel using suitable surfactants [14, 16]. When choosing a surfactant, the hydrophilic-lipophilic balance (HLB) value is crucial. An earlier study on emulsification of oil-in-water-in-oil reported that the Span-80 and Tween-80 surfactant mixture having HLB value 13 provides better emulsion stability for oil-in-water-in-oil biodiesel emulsion [17]. Studies on the bio-oil produced from various biomass feedstock and its use as a bio-oil-in-diesel emulsion to power a diesel engine have demonstrated stable engine performance with reduced exhaust emissions [18–20].

According to the study, the biodiesel industry generates a massive amount of seedcake as a by-product each year. These generated seedcakes need to be used to produce bio-oil in an efficient and eco-friendly manner. However, to the best of the author's knowledge, very few studies are available on Honge bio-oil (HBO) derived from Honge de-oiled seedcake via pyrolysis and its use in a diesel engine. These facts motivated the production of HBO through pyrolysis of HDSC and to study the behavior of a diesel engine powered by HBO. The HBO obtained through the pyrolysis process needs to be improved by forming HBO and base diesel emulsions with appropriate surfactants. Therefore, mixed surfactants such as Span-80 and Tween-80 were selected to decrease the surface tension among the HBO and diesel. Four different HBO-diesel emulsions are prepared as test fuels to study the engine behavior, with HBO percentages ranging from 5 to 20% by volume in steps of 5% in the HBO-diesel emulsions. The performance and emission parameters of a diesel engine powered using HBO-diesel emulsions are investigated, compared, and presented in the paper.

2 Materials and Methods

After extracting oil from Honge seeds, the HDSC from the oil expeller was collected in the current study. The HDSC was exposed to sunlight for the removal of excess moisture from it. The physicochemical characteristics of the HDSC were determined and reported in Table1. The calorific value (C_V) of seedcake was determined using ASTM D5865-13. The properties of HDSC were compared to those of other studies and found to be comparable. Hence, the HDSC was considered for producing bio-oil by the pyrolysis process. The procedure outlined below was used for the present work.

- The seedcake was grounded and sieved to uniform particle size ranging from 0 to 0.3 mm, 0.3 to 0.6 mm, and 0.6 to 1 mm. The particle size of 0.3 to 0.6 mm was selected as a feedstock for the pyrolysis process for the present work based on studies, and the Honge bio-oil (HBO) is generated through pyrolysis.
- The stable emulsion was prepared by mixing the emulsifier like Span-80 and Tween-80 in 1:3 volume proportion (Span-80 / Tween-80 = 1/3 by volume). The prepared surfactant (emulsifier) mixture is named ST. 8% of HBO of ST is added to HBO and mechanically stirred at 1000 revolutions per minute (rpm) for 5 min. This prepared mixture was further added to diesel and stirred at 1000 rpm for 5 min. Table 2 lists various HBO and diesel emulsion blends and their proportions by volume. The emulsion blends so prepared were observed to be stable for more than a week for the proportion of HBO in the blends up to 20%. Further increase in the proportion of HBO more than 20% showed unstable emulsion because of stratification of HBO and diesel were observed two hours after preparation of

Table 1 The properties of non-edible seedcakes

Properties	HDSC[a]	Honge Seedcake [4]	Jatropha Seedcake [8]
Density (kg/m^3)	520	489	NA
Proximate analysis (wt. %) (ASTM D3173-75)			
Moisture	9.64	12	5
Volatile matter	71.55	71.21	69
Fixed carbon	13.3	5.08	21
Ash	5.51	11.71	5
Ultimate analysis (wt. %) (ASTM D5291-96)			
Carbon	48.87	47.11	42.3
Hydrogen	7.3	5.63	4.8
Nitrogen	4.33	0.27	5.8
Sulfur	0	–	0.36
Oxygen	39.5	41.91	46.74
C_v (MJ/kg)	18.50	17.65	16.86

[a] Present study

Table 2 Various proportion of HBO-diesel emulsions

Type of emulsified fuel	Proportion of blends by volume
HBO05	05% HBO + 94.6% diesel + 0.4% ST
HBO10	10% HBO + 89.2% diesel + 0.8% ST
HBO15	15% HBO + 83.8% diesel + 1.2% ST
HBO20	20% HBO + 78.4% diesel + 1.6% ST

emulsion. Hence, 20% contribution of HBO by volume in the HBO-diesel was considered for the study.

- These prepared emulsions of HBO-diesel (HBO05, HBO10, HBO15, and HBO20) are used to study the performance as well as emission parameters of an engine.
- In this work, 15 kg of the engine load is considered a full load (100% load) to avoid engine failure due to an increased compression ratio (18:1). The experiments were conducted on an engine with varying loads at a set speed of 1500 rpm.
- Five Gas Analyzer (FGA) is used to analyze an engine's exhaust emissions for all loads, and smoke opacity values were determined by smoke meter. The obtained data are compared with base diesel operations.

2.1 Pyrolysis Reactor

The pyrolysis of HDSC was performed on a laboratory-scale continuous feed pyrolysis reactor to obtain bio-oil. Figure 1 depicts a photographic view of the pyrolysis

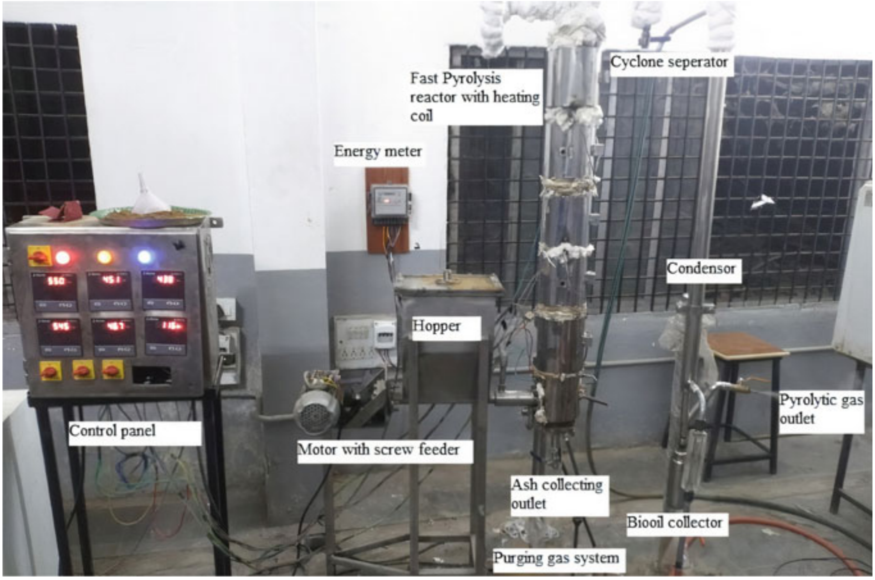

Fig. 1 Pictorial view of pyrolysis reactor

reactor. The HDSC of particle size ranging from 300 to 600 microns was fed in the pyrolysis reactor and then heated to a temperature around 500 °C in a nitrogen atmosphere. The hot volatile gas vapors evolved due to heating of feedstock are then condensed and collected. The obtained liquid phase product is commonly known as pyrolytic oil or bio-oil. Crude bio-oil (HBO) is pungent, dark brown as shown in Fig. 2a. When stored, bio-oil has a distinct phase separation as seen in Fig. 2b. The reason for the phase separation is because of the excessive oxygen content, inherent moisture, and the aging of bio-oil [21]. The obtained bio-oil was characterized (as received basis) using ultimate analysis according to ASTM D5373. The percentage of elemental composition by weight was found to be 43.1% Carbon, 9.7% Hydrogen, 4.3% Nitrogen, and 42.9% Oxygen. There was no evidence of a sulfur composition in the bio-oil. The properties of diesel, HBO, and different emulsion of HBO-diesel are presented in Table 3. The properties of emulsions are nearly identical to those of base diesel and used in a diesel engine.

2.2 *Experimental Setup*

Figure 3 depicts the pictorial representation of the diesel engine setup employed in the current study. The investigation is performed on the computerized, four-stroke (4-S), single cylinder, water-cooled stationary diesel engine equipped with the dynamometer. The setup comprises a panel box, and air-box, a dual fuel tank,

(a) (b)

Fig. 2 **a** Crude Honge bio-oil and **b** phase separation of HBO after storage

Table 3 The properties of diesel, HBO, and HBO-diesel emulsion blends

Property	Test method (ASTM)	Diesel	HBO	HBO05	HBO10	HBO15	HBO20
Density (kg/m^3)	D1298	821	1078	824	827	835	845
Viscosity (mm^2/s)	D445	3.26	28	2.9	3.5	4.2	4.5
Calorific value (kJ/kg)	D4809	43,500	17,200	42,496	41,180	39,800	38,200
Flash point (°C)	D93	57	110	59	61	61	62
Fire point (°C)	D93	62	130	64	65	66	67

smoke meter and FGA. The computerized engine setup has software package "IC Engine Soft 9.0" for the evaluation of performance parameters. The specification details of the diesel engine setup considered for the experiments are listed in Table 4. Figure 4 depicts the diagrammatic view of a diesel engine setup used in the study. The eddy current dynamometer is equipped with a diesel engine for engine loading. The setup helps to study the essential performance attributes. AVL 444 FGA and

Fig. 3 Pictorial view of the engine setup

Table 4 Engine specifications

Particulars	Technical specifications
Model and type	Kirloskar TV1 and 4-S, single cylinder engine
Fuel type	Diesel
Bore dia. and stroke length	87.5 mm, 110 mm
Maximum power	5.2 kW at 1500 rpm
Compression ratio (CR)	18:1
Injection type	Direct injection
Injection pressure	210 bar
Injection timing	23°CA bTDC
Dynamometer	Eddy current, water cooled
Engine speed	1500 rpm
Software	IC engine soft, version 9.0

AVL 437 smoke meters are positioned at the engine exhaust to study the emission characteristics and smoke opacity.

3 Results and Discussion

The characterization of the HBO, HBO-diesel, and base diesel fuel were performed based on density, kinematic viscosity, and calorific value (C_V). The elemental characterization of HBO was performed to find an elemental composition. To determine the

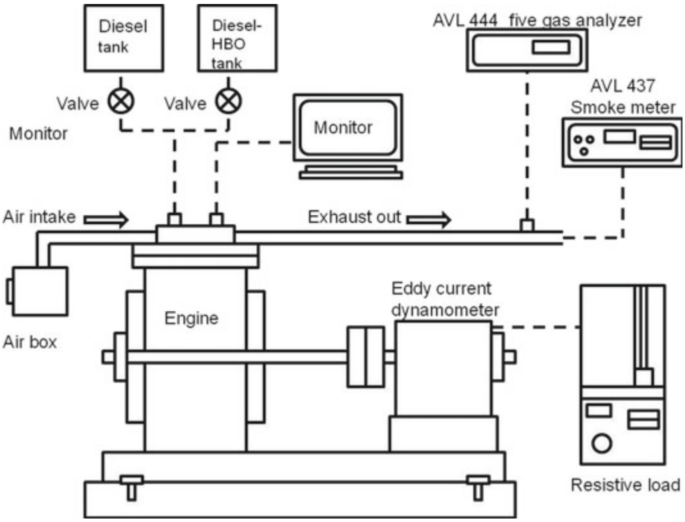

Fig. 4 Schematic diagram of engine setup

suitability of HBO-diesel emulsion as a fuel in the diesel engine, the performance and emission parameters are investigated and explained in the following sections. The properties of HBO-diesel emulsion caused differences in the engine's performance and emissions when compared with the base diesel operation.

3.1 Performance Characteristics

Brake Thermal Efficiency (BTE) and Brake Specific Fuel Consumption (BSFC): Figure 5 shows the variation of BTE for increasing loads. The graph shows that BTE increases with an increasing load for base diesel and all HBO-diesel emulsions. However, HBO20 demonstrated slightly higher BTE (25.45%) at a full load, representing a 2.95% increase over the base diesel operation. Perhaps this is because of greater inherent oxygen content by the HBO20 enabling better combustion and improves thermal efficiency at full loads [22]. Furthermore, the presence of slightly more water in HBO20 may cause a micro-explosion phenomenon during combustion, resulting in increased combustion efficiency and engine power [23]. It is also observed from the graph that HBO05, HBO10, and HBO15 had lower BTE under all load conditions than that of base diesel operation. It could be because of the lower calorific value (C_V) of HBO-diesel emulsion and a higher amount of aromatics in HBO of HBO-diesel emulsion, resulting in more heat loss [24]. These observations lead to certain possible working conditions for using HBO-diesel emulsions in a diesel engine.

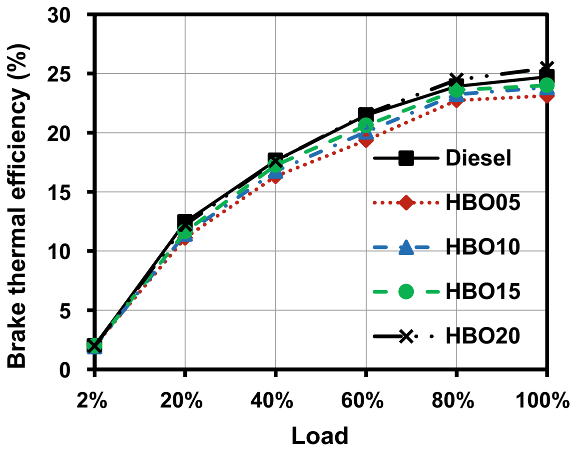

Fig. 5 Variation of BTE with the load

Figure 6 depicts changes in the BSFC with an increasing load. The BSFC of HBO-diesel emulsions are higher than the base diesel with the increasing HBO proportions in the emulsions. This increasing trend of BSFC may be because of the lower C_V of the HBO in the emulsified fuel, which resulted in an increased fuel consumption to get the same power output [24, 25]. The BSFC values of HBO-diesel emulsion blends are nearly identical to the base diesel at the 100% load. The BSFC of HBO20 is raised by 12.1% than the base diesel operation at a full load. This may be because HBO-diesel emulsions have a lower calorific value.

Exhaust Gas Temperature (EGT): Higher EGT in an internal combustion engine cause power loss, resulting in a significant reduction in BTE. Figure 7 depicts the variation in EGT with increasing load. The EGT profile of base diesel and HBO-diesel emulsions are similar. However, the EGT using HBO-diesel emulsions are lower than

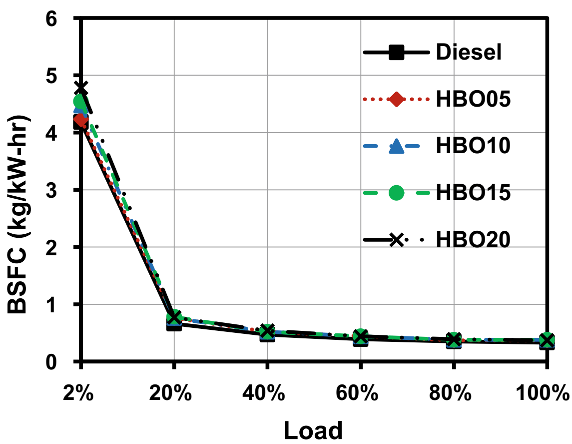

Fig. 6 Variation of BSFC with the load

Fig. 7 Variation of EGT with the load

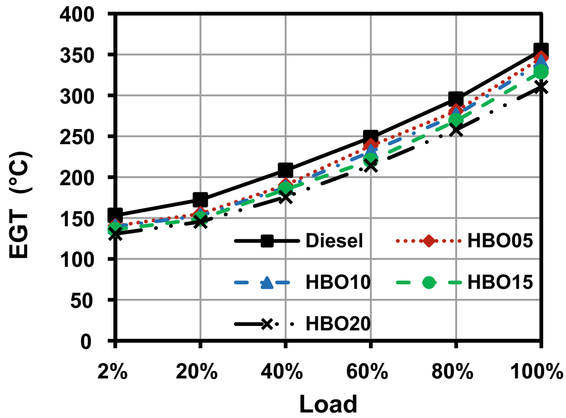

the base diesel throughout all engine load conditions. It could be attributed to the content of moisture in the HOB-diesel emulsion, which vaporize during combustion and absorb part of heat energy generated during the combustion resulting in lower local adiabatic flame temperature [14]. At full load, upon comparing with the base diesel operation, it could be noticed that the percentage reduction in the EGT for HBO05, HBO10, HBO15, and HBO20 were 2.6%, 4.1%, 7.3%, and 12.6%, respectively. This indicates the combustion of fuels at lower temperature lowers NO_X emissions.

3.2 Emission Characteristics

Carbon Monoxide (CO) Emission. Figure 8 depicts a variation in the emission levels of carbon monoxide using base diesel fuel and HBO-diesel blends at varying engine loads. All of the test fuels showed lower CO emissions than base diesel at medium as well as at higher loads. At a full load, the CO emissions of HBO20 dropped by 32% in comparison with base diesel. It is noticeable that the inherent oxygen level of HBOs may result in a lower CO emission [19, 20].

Hydrocarbon (HC) Emission. Figure 9 depicts the HC emission of base diesel and different HBO-diesel blends at varying engine loads. At a full load, HBO20 has a considerable percentage decrease in the HC emission of 38.6% compared to the operation of the engine fueled with base diesel. Hydrocarbon emissions by base diesel fuel are considerably higher than those from HBO-diesel blends, as illustrated in Fig. 9. All the HBO-diesel blends show decreasing trends in HC emissions at the moderate load. The moisture in the fuel decreases viscosity and enhances atomization properties, resulting in lower emissions of HC. Furthermore, because bio-oils are

Fig. 8 Variation of CO emission with the load

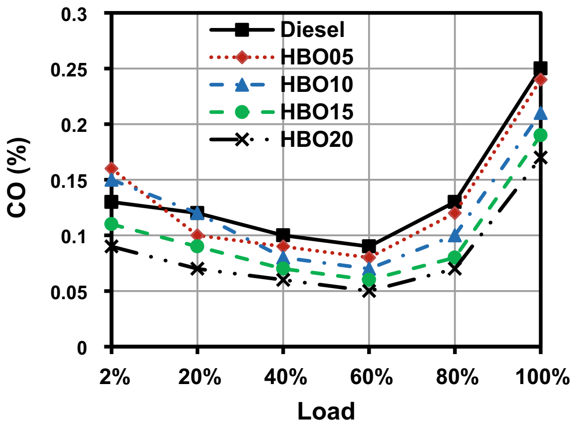

Fig. 9 Variation of HC with the load

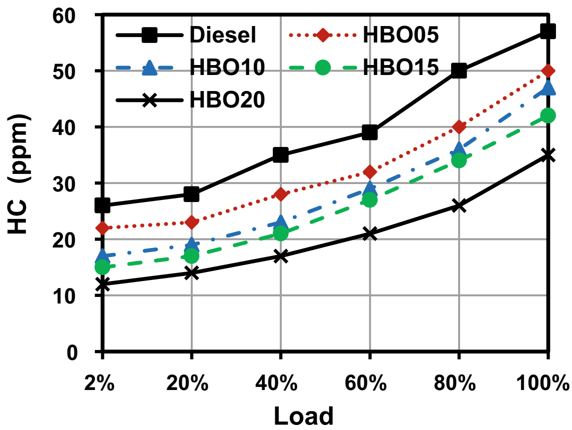

oxygenated liquids, the inherent oxygen leads to lower HC emissions by the complete burning of the fuel [26, 27].

Oxides of Nitrogen (NOX) Emission. Diesel engines emit a considerable quantity of NO_X because of an excess of oxygen and a higher content of nitrogen compounds in the fuel [24]. Figure 10 depicts the change in the emissions of NO_X with varying loads for diesel and HBO-diesel emulsions. The HBO-diesel emulsions exhibit a decreasing trend in NO_X emission. The NO_X emission for the HBO20 blend was reduced by 19.5% than the base diesel run at a full load condition. It is plausible that perhaps the higher moisture and oxygenated organic compound content of HBO in HBO-diesel emulsions resulted in a lower burnt gas temperature, resulting in lower NO_X emissions [20].

Smoke Emission. Figure 11 indicates the changes in the smoke emissions with varying loads. The HBO-diesel blends emit less smoke than the base diesel operation,

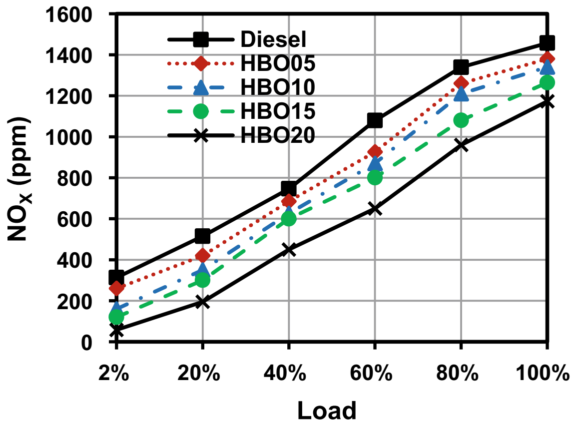

Fig. 10 Variation of NO_X with the load

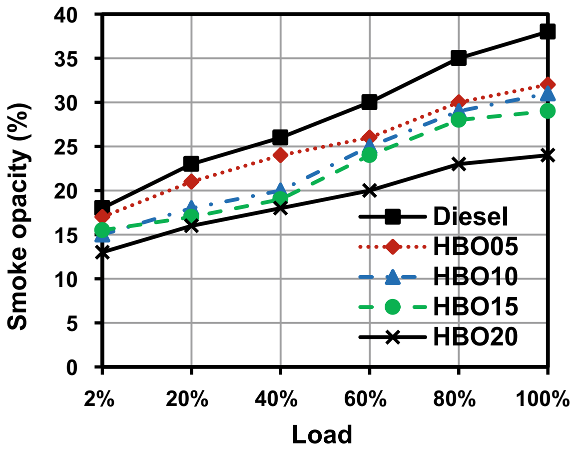

Fig. 11 Variation of NO_X emission with the load

which may be due to HBO's inherent oxygen promotes complete combustion by supplying surplus oxygen to the nearby burning fuel-rich areas of the pyrolytic zone. The use of oxygen-rich HBO with high OH radical content may help to reduce smoke emissions [28, 29]. When a diesel engine was fueled with HBO20, the smoke opacity value was reduced by 28.9% compared to the base diesel operation.

4 Conclusions

Honge bio-oil (HBO) from Honge de-oiled seedcake was obtained by the pyrolysis process with the help of a continuous feed laboratory-scale pyrolysis reactor at the temperature 500 °C. The different proportions of HBO-diesel emulsions were prepared and investigated in a DI diesel engine. The current study leads to the following conclusions:

- All the properties of HBO-diesel blends are comparable with base diesel.
- It is possible to operate a diesel engine using HBO-diesel emulsions up to 20% contribution of HBO without any modifications in the diesel engine.
- HBO20 shown the highest Brake thermal efficiency of 25.45% with a percentage increase of 2.95% compared to base diesel operations.
- All emulsions of HBO with diesel recorded higher BSFC for all loads when compared to the base diesel operations.
- The levels of emissions for all the HBO-diesel were comparatively lower than the base diesel.
- When compared to the base diesel, the percentage decrease in CO, HC, NO_X, and smoke emissions with HBO20 at a full load was about 32%, 38.6%, 19.5%, and 28.9%, respectively.

As a result of the findings, HBO blends can offer lower emissions while maintaining comparable engine performance. Hence, HBO blends may be a viable alternative fuel source for DI diesel engines. Finally, HBO blends can offer lower emissions while maintaining comparable engine performance so it may be concluded that HBO20 can replace the base diesel without any major engine modification.

Acknowledgements The authors acknowledge Sharnbasva University, Kalaburagi, India, for the laboratory support provided to conduct experiments on pyrolysis reactor, and also, the authors are thankful to Apex Innovations Pvt. Ltd. Sangli, India, for providing the diesel and engine testing facilities to conduct experiments.

References

1. Yildiz L (2018) 1.12Fossil fuels. Compr Energy Syst 1:521–567
2. Elshahed MS (2010) Microbiological aspects of biofuel production: current status and future directions. J Adv Res 1(2):103–111
3. Demirbas A (2008) Biofuels sources, biofuel policy, biofuel economy and global biofuel projections. Energy Convers Manage 49(8):2106–2116
4. Prasad L, Subbarao PMV, Subrahmanyam JP (2014) Pyrolysis and gasification characteristics of Pongamia residue (de-oiled cake) using thermogravimetry and downdraft gasifier. Appl Therm Eng 63(1):379–386
5. Muktham R, Ball AS, Bhargava SK, Bankupalli S (2016) Study of thermal behavior of deoiled karanja seed cake biomass: thermogravimetric analysis and pyrolysis kinetics. Energy Sci Eng 4(1):86–95
6. Thiagarajan J, Srividhya PK, Rajasakeran E (2013) A Review of thermo-chemical energy conversion process of non-edible seed cakes. J Energy Biosci 4(2):7–15
7. Rahman MM, Netravali AN (2014) Green resin from forestry waste residue "karanja (Pongamia pinnata) Seed cake" for biobased composite structures. ACS Sustain Chem Eng 2(10):2318–2328
8. Biradar CH, Subramanian KA, Dastidar MG (2014) Production and fuel quality upgradation of pyrolytic bio-oil from Jatropha Curcas de-oiled seed cake. Fuel 119:81–89

9. Barik D, Murugan S (2015) Assessment of sustainable biogas production from de-oiled seed cake of karanja-an organic industrial waste from biodiesel industries. Fuel 148:25–31
10. Chutia RS, Kataki R, Bhaskar T (2014) Characterization of liquid and solid product from pyrolysis of Pongamia glabra deoiled cake. Biores Technol 165:336–342
11. Muktham R, Ball AS, Bhargava SK, Bankupalli S (2016) Bioethanol production from non-edible de-oiled Pongamia pinnata seed residue-optimization of acid hydrolysis followed by fermentation. Ind Crops Prod 94:490–497
12. Bridgwater AV, Peacocke GVC (2000) Fast pyrolysis processes for biomass. Renew Sustain Energy Rev 4(1):1–73
13. Bridgwater AV (2012) Review of fast pyrolysis of biomass and product upgrading. Biomass Bioenerg 38:68–94
14. Yuan X, Ding X, Leng L, Li H, Shao J, Qian Y, Huang H, Chen X, Zeng G (2018) Applications of bio-oil-based emulsions in a DI diesel engine: the effects of bio-oil compositions on engine performance and emissions. Energy 154:110–118
15. Pattiya A (2018) 1—Fast pyrolysis in direct thermochemical liquification for energy applications, 1st edn. Woodhead Publishing, England
16. Chiaramonti D, Bonini M, Fratini E, Tondi G, Gartner K, Bridgwater AV, Grimm HP, Soldaini I, Webster A, Baglioni P (2003) Development of emulsions from biomass pyrolysis liquid and diesel and their use in engines—part 1: emulsion production. Biomass Bioenerg 25(1):85–99
17. Lin CY, Lin SA (2007) Effects of emulsification variables on fuel properties of two- and three-phase biodiesel emulsions. Fuel 86(1–2):210–217
18. Chiaramonti D, Bonini M, Fratini E, Tondi G, Gartner K, Bridgwater AV, Grimm HP, Soldaini I, Webster A, Baglioni P (2003) Development of emulsions from biomass pyrolysis liquid and diesel and their use in engines—part 2: tests in diesel engines. Biomass Bioenerg 25(1):101–111
19. Midhun Prasad K, Murugavelh S (2020) Experimental investigation and kinetics of tomato peel pyrolysis: performance, combustion and emission characteristics of bio-oil blends in diesel engine. J Clean Prod 254:120115
20. Prakash R, Singh RK, Murugan S (2015) Experimental studies on combustion, performance and emission characteristics of diesel engine using different biodiesel bio oil emulsions. J Energy Inst 88(1):64–75
21. Oasmaa A, Sundqvist T, Kuoppala E, Garcia-Perez M, Solantausta Y, Lindfors C, Paasikallio V (2015) Controlling the phase stability of biomass fast pyrolysis bio-oils. Energy Fuels 29(7):4373–4381
22. Ashok B, Nanthagopal K (2019) Eco friendly biofuels for CI engine applications. In: Advances in eco-fuels for a sustainable environment, 1st edn. Woodhead Publishing, Duxford
23. Basha JS, Anand RB (2011) An experimental study in a CI engine using nanoadditive blended water-diesel emulsion. Int J Green Energy 8(3):332–348
24. Kalargaris I, Tian G, Gu S (2017) Combustion, performance and emission analysis of a DI diesel engine using plastic pyrolysis oil. Fuel Process Technol 157:108–115
25. Nanthagopal K, Ashok B, Garnepudi RS, Tarun KR, Dhinesh B (2019) Investigation on diethyl ether as an additive with Calophyllum Inophyllum biodiesel for CI engine application. Energy Convers Manage 179:104–113
26. Kumar S, Prakash R, Murugan S, Singh RK (2013) Performance and emission analysis of blends of waste plastic oil obtained by catalytic pyrolysis of waste HDPE with diesel in a CI engine. Energy Convers Manage 74:323–331
27. Guarieiro LL, de Almeida Guerreiro ET, dos Santos Amparo KK, Manera VB, Regis AC, Santos AG, Ferreira VP, Leão DJ, Torres EA, de Andrade JB (2014) Assessment of the use of oxygenated fuels on emissions and performance of a diesel engine. Microchem J 117:94–99
28. Lu Q, Li WZ, Zhu XF (2009) Overview of fuel properties of biomass fast pyrolysis oils. Energy Convers Manage 50(5):1376–1383
29. Zhu L, Cheung CS, Zhang WG, Huang Z (2011) Combustion, performance and emission characteristics of a di diesel engine fueled with ethanol-biodiesel blends. Fuel 90:1743–1750

Designs of Building Envelopes with Improved Energy Efficiency

Mayank Bhardwaj and Amit Arora

1 Introduction

Environment and energy are two key challenges faced worldwide, and about 40% out of the primary energy consumption is associated with the buildings only. Hence, the building energy conservation became the largest terminal to alleviate the energy crisis and protect the environment. There are two ways to address this issue, i.e. (a) use of energy-efficient building materials and (b) integration of renewable energy resources [1, 2].

The building materials used for constructing the walls are vitally important as they separate as well as protect the interior spaces from the exterior conditions. The thermal interactions around the building are depicted in Fig. 1. Their thermal and mechanical properties also define a building's functioning under various climatic conditions. The building envelope accounted for around 60–80% heat losses; thus, the building envelope should be defined adequately. The use of insulation material is a commonly used method for reducing energy consumption and attaining thermal comfort for the buildings. However, the incorporation of the insulating layer on the building walls increases the building construction cost as well as the construction time [3, 4]. Therefore, the recent trends in the construction industry showed the development of more sustainable and energy-efficient construction materials to minimize the heat transmission from building walls and related building operational costs as well as embodied energy. In India, it has been obligatory to incorporate at least 25% of fly ash in the brick manufacturing as a replacement of clay if the operating factory/industry is located within a range of 100 km from a coal-powered power generation plant [5].

M. Bhardwaj (✉) · A. Arora
Department of Mechanical Engineering, Malaviya National Institute of Technology Jaipur, Jaipur, Rajasthan 302017, India
e-mail: 2020rme9598@mnit.ac.in

D. Sharma and S. Roy (eds.), *Emerging Trends in Energy Conversion and Thermo-Fluid Systems*, Lecture Notes in Mechanical Engineering,
https://doi.org/10.1007/978-981-19-3410-0_16

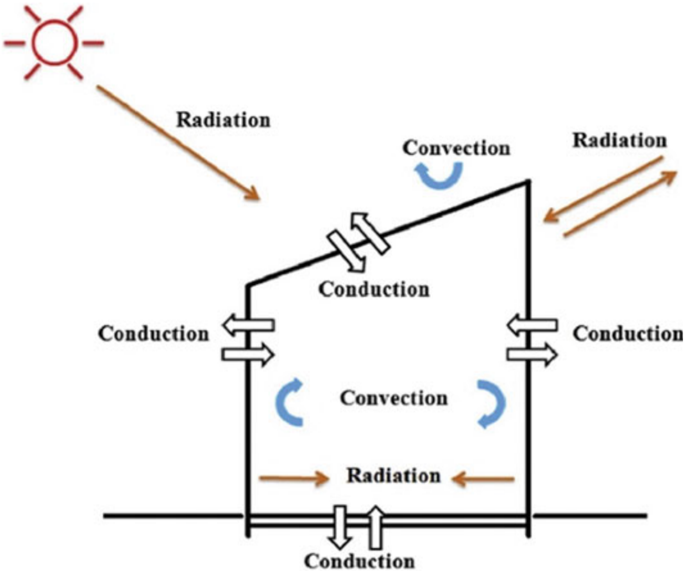

Fig. 1 Heat interactions around the building [4]

2 Evaluation of Brick Performance

Several authors have studied the performance and adaptability of different building blocks based on their thermo-mechanical and physical properties. They used the following equations to compute the required properties.

The bulk density of the developed sample can be calculated as [6]:

$$\text{Bulk density} = \frac{W_{\text{dry}}}{V} \tag{1}$$

where V is volume and W_{dry} is the dry weight of specimen.

The compressive strength (C_s) of sample block computed as follows [7, 8]:

$$C_s = \frac{F_c}{A_p} \tag{2}$$

where, F_c is applied load; A_p is area perpendicular to load direction.

Dry abrasion resistance (C_a) defines the property of a material to resist the material removal due to brushing the specimen [9]:

$$C_a = \frac{S}{(\text{mass}_{\text{before}} - \text{mass}_{\text{after}})} \tag{3}$$

The water absorption rate of the sample is found as [6, 7]:

$$\text{Water absorption rate} = \frac{W_{\text{saturated}} - W_{\text{dry}}}{W_{\text{dry}}} \quad (4)$$

where W is weight of element at dry and saturation conditions.

Open porosity calculation can be done as follows [6]:

$$\text{Open porosity}(\%) = \frac{W_{\text{saturated}} - W_{\text{dry}}}{V\rho_{\text{w}}} \times 100 \quad (5)$$

The measurement of thermal conductivity is commonly performed on guarded hot plate apparatus, which uses the following relation for calculation:

For solid build block sample [6, 9]

$$(\lambda) = \frac{Q \times e}{\Delta T \times A} \quad (6)$$

For hollow building block sample [10]

$$\left(\lambda_{\text{eqv}}\right) = \frac{Q_{\text{ts}} \times e}{\Delta T \times A} \quad (7)$$

where heat flow through test sample (Q_{ts}) is the difference between steady-state power input to heat flow from dummy sample.

In Eqs. (6) and (7), Q is the amount of heat provided to apparatus, e is thickness of the sample, A is cross-sectional area of sample, and ΔT is temperature difference between two plates.

Overall thermal resistance (R) of the building block can be calculated as [8, 11]:

$$R = \frac{1}{h_{\text{inner}}} + \sum_{i=1}^{n} \frac{L_i}{\lambda_i} + \frac{1}{h_{\text{outer}}} \quad (8)$$

where h = convection heat transfer coefficient; L_i = thickness of the material layer; and λ_i = thermal conductivity of material layer.

From the above equations, it is seen that in order to design the sustainable and energy-efficient buildings, the thermal conductivity should be kept as low as possible. Moreover, the mechanical properties like compressive strength, flexural strength, and durability should not be compromised. Thus, the analytical, simulation and experimental studies involving such thermo-mechanical properties are reviewed and summarized in the following sections.

3 State of the Art on Building Blocks

In this section, various types of alternative building bricks, namely hollow bricks, bio-based bricks and municipal and industrial waste, are discussed as either partial or complete replacement of conventional terra-cotta building blocks (clay bricks) to achieve energy-efficient and sustainable building development.

3.1 Hollow Building Blocks

These type of bricks have identical or different cavity shapes and designs depending upon the end usage. Various researchers filled these cavities with mortar, phase change material (PCM), insulating materials, etc., whereas some studies were performed with unfilled cavities, i.e. air-filled cavities. Li et al. [12] performed a thermal optimization study to discover the optimal arrangement of holes for the hollow clay brick (240 mm × 115 mm × 90 mm) by using a 3D simulation model. During their comprehensive study, the brick configuration of L5W4H1 was considered as optimum because it had the lowest values of equivalent thermal conductivity of 0.419 W/m K, i.e. 50% less than reference brick, and also reported the lowest change in the thermal performance even when the temperature difference changes over a wide range. L5W4H1 had a total of 20 holes with the void fraction value of 46.9% as depicted in Fig. 2a. Later, Li et al. [13] studied the seventy-two different configurations of the hollow bricks by varying the number of holes and numerically calculated the equivalent thermal conductivity for the sample size of 290 mm × 140 mm × 90 mm. The optimum brick configuration L8W4H1 (one hole in height, four holes in width and eight holes in length) attained the lowest thermal conductivity of 0.400 W/m K.

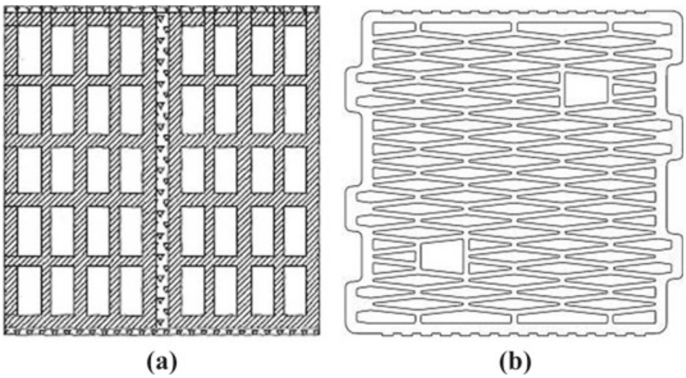

Fig. 2 The geometry of proposed hollow bricks [12, 14]

In the same way, Morales et al. [14] performed a simulation study to improve the thermal performance of a hollow brick by varying the geometrical designs while keeping the brick width constant. Figure 2b showcases one of the proposed hollow brick design. The calculation was in accordance with Spanish UNE, European EU, AENOR and ISO regulations. They concluded that to attain low heat transfer as well as low thermal conductivity, non-rectangular voids were found to be more beneficial. The non-rectangular design also had the advantage of providing more voids in the bricks with the same width. Meanwhile, Sodupe-Ortega et al. [15] studied the hollow bricks prepared with crumb rubber and fine aggregate. From the laboratory experiments, the authors found that the crumb rubber particles were able to improve the compression strength of the composite hollow bricks.

Whereas the authors compared the performance of hollow wood composite fibreboard blocks with and without PCM, the researchers used polyethylene glycol (PCM) with hollow wood composites (poplar wood fibres) and low-dense polystyrene fibreboard to achieve the lightweight building material with higher thermal insulating properties to reduce the thermal load of the building located in China. The results revealed that the value of thermal conductivity of proposed building blocks was found up to 0.07 W/m K as shown in Fig. 3; therefore, it can be used as a significant thermal insulator [16]. Meanwhile, Li et al. [3] proposed the filling of insulating material inside the hollow cavities of the sintered bricks for replacement of the insulation layer. The authors numerically studied the thermal performance of the expanding polystyrene board (EPS)-filled sintered hollow bricks under Chinese climatic conditions. It was concluded that with an 80% EPS filling ratio, the decrement rate had shown an improvement of 10.9% by the externally filled hollow bricks in comparison to the internally filled sintered bricks.

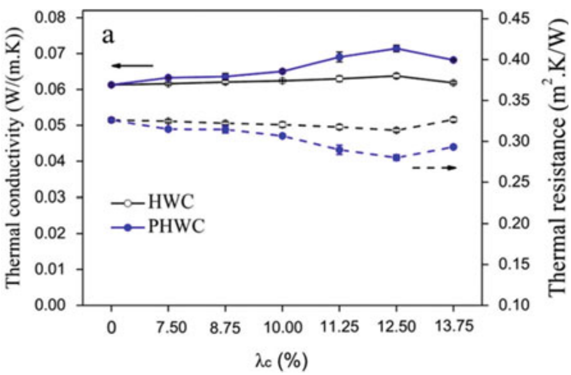

Fig. 3 Thermal resistance and conductivity of PHWC and HWC at different volume ratios (λ_c) [16]

3.2 Bio-aggregate Based Building Blocks

Many researchers are also practising the usage of bio-aggregates as partial or full replacement of conventional (earth or clay) building materials to address the disadvantages of poor ductility, water resistance and shrinkage. Bio-aggregate-based building blocks also add additional value by decreasing the dumping and storing problems of these wastes.

Giroudon et al. [9] mixed lavender and barley straws with an earth matrix. The prepared sample had different sizes, shapes and porosity with 3 and 6% by mass of considered plant aggregates. The authors experimentally investigated the thermal and mechanical properties, resistance in fungal growth and material durability. The lowest thermal conductivity with barley and lavender straws was 0.155 W/m K and 0.289 W/m K, respectively. Moreover, these values are about 70% and 40% lesser than the reference building block.

Marques et al. [17] experimentally assessed the utilization of rice straw bales as building wall material in Portugal and observed that the value of thermal conductivity of rice straw bales varied from 0.039 to 0.048 W/m K under dry and moist conditions. They also stated that the increase in moisture content increased the thermal conductivity of the samples. Subsequently, Olacia et al. [7] prepared bio-based building blocks mixing seagrass and straws with abode bricks. The thermal conductivity of the reference building block (adobe brick) was decreased from 0.82 to 0.66 W/m K with 3% straw (illustrated in Fig. 4). It was also found that the compressive and flexural strength were higher in 3% seagrass-adobe than 3% straw-abode samples. Although the water absorption rate was lesser in seagrass reinforced samples in comparison to straw reinforced brick samples, as depicted in Fig. 5.

In an another study [8], the researchers experimentally studied the locally available bio-based sawdust and palm fibres for making of less thermal conductive

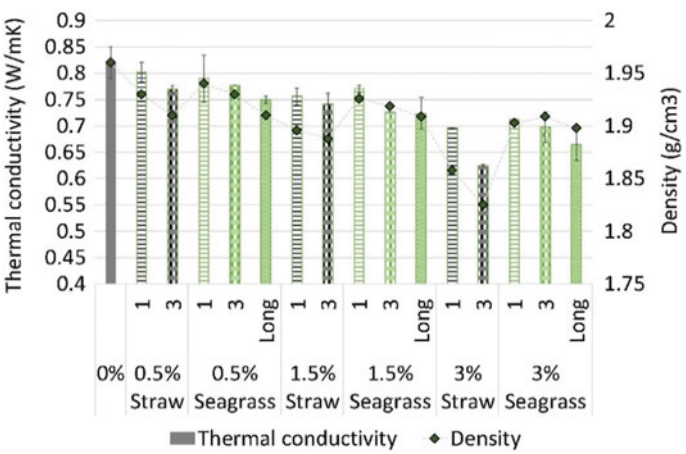

Fig. 4 Density and thermal conductivity of the straw and seagrass-based samples [7]

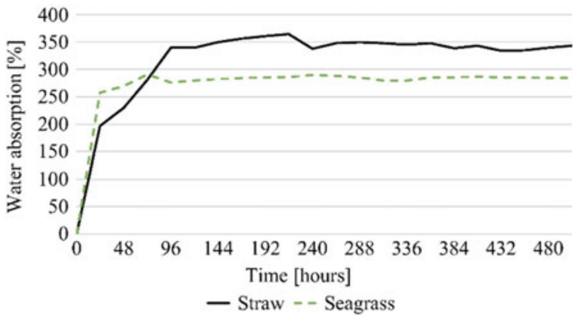

Fig. 5 Water absorption of seagrass and straw fibres [7]

building blocks in Ghana, West Africa. The results revealed that the addition of 30% treated palm fibres with 70% sandcrete for an office building cooling can save up to 453.40 kWh electrical power per year. The same sample also showed a maximum reduction of 38.1% in thermal conductivity in comparison to pure sandcrete building block. Moreover, the building blocks meet compressive strength standards ($\geq$3 MPa), with the sample having 10% of sawdust with sandcrete and 10–30% palm fibres with sandcrete, as displayed in Fig. 6.

Whereas the thermal properties of bricks prepared by adding date palm fibres, straw and olive waste with clay were experimentally evaluated and compared. The authors discovered that the thermal conductivity of the pure clay bricks (0.65 W/m K) got reduced up to 0.26 W/m K by replacing 30% clay with straw. All the samples have shown lesser thermal conductivity than the pure clay blocks. Hence, it can be concluded that the straw outperformed date palm fibres and olive waste as clay

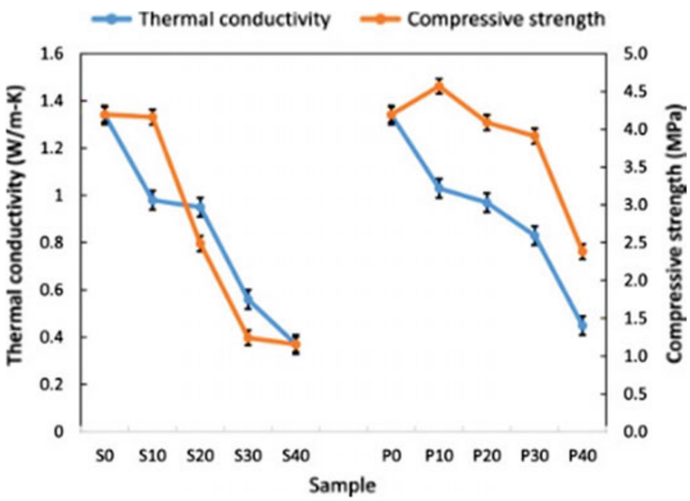

Fig. 6 Compressive strength and thermal conductivity values for different samples of sandcrete (*S*) and palm fibres (*P*) [8]

replacement for the preparation of the building bricks/blocks under Morocco climatic conditions [18].

Rashid et al. [6] compared the thermal conductivity of the various reinforced clay bricks prepared by incorporation of different natural fibres. The results also followed the ASTM guidelines. The studied ecological fibres had shown a reduction in the thermal conductivity with a maximum reduction of about 18% using coconut coir fibres, whereas the bamboo, sisal, jute and polyester fibres displayed the reduction of 11%, 9%, 6% and 16% in comparison to clay bricks, respectively. Moreover, Raut and Gomez [19] developed and tested 16 samples of new types of building blocks by replacing the conventional brick material with the eco-friendly materials such as palm oil fibres and glass powder under the Malaysian climate. The lowest thermal conductivity, i.e. 0.389 W/m K was achieved with M13 brick sample (210 mm $\times$ 100 mm $\times$ 100 mm), whereas this sample shows lowest compressive strength of 7.21 MPa. The additions of palm oil fibres lowered the values of thermal conductivity, while glass powder, palm oil fly ash and lime provided the increment in compressive strength with increment in the percentage content.

3.3 Industrial and Municipal Waste-Based Building Blocks

The management of secondary by-products from various industries became a major concern of many countries as the waste generation has been increased with the technology and civilization development in the past few decades. Hence, these waste by-products have been investigated and studied by a few scientists as building materials to prevent the landfill and negative impact on the environment.

Sakhare et al. [20] developed and performed the performance assessment of the cellular bricks prepared by using bio-briquette ash (BBA). They had done the techno-economic assessment study of the prepared building blocks sample and compared its performance with the fly ash bricks. The developed bio-briquette bricks showed the compressive strength and density of 3.58 MPa and 1000 kg/m^3, which were higher than the FA bricks and in alignment with the Indian standard (IS 2185:2008). It was also seen that the thermal conductivity from the proposed bricks was almost one third, i.e. 0.35 W/m K than the fly ash brick (1.05 W/m K). The cost of brick manufacturing was found to be lower, although the proposed sample size was bigger than the conventional FA bricks. The BBA cellular bricks were able to maintain the inside temperature in the desired comfort range for more than 52% of the year. In another study, the authors performed some laboratory experiments in Spain to find the optimal values of the olive residue to be added in the clay for the preparation of eco-friendly bricks. The study revealed that the optimal clay brick with 10% olive pomace residue had 29% less compressive strength, 0.143 W/m K less thermal conductivity and almost 7% reduction in the bulk density, although the water absorption was increased by 13%. Their environmental study had shown that the proposed brick could be used in the building as the leaching concentrations of the heavy metals inside the building block met the Spanish and USEPA regulations [21]. Later, Eliche-Quesada et al.

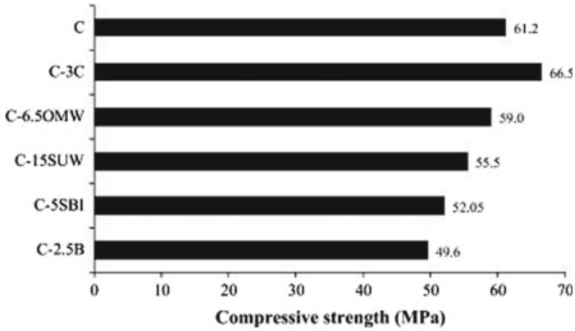

Fig. 7 Values of compressive strength of different brick samples [22]

[22] developed and studied the incorporation of sewage (wastewater) sludge, coffee grounds residue, brewing industry sludge, bagasse and olive mill wastewater as brick material to match the UNE standards (RP3406-REV7 and RP3404). The values of compressive strength are shown in Fig. 7. Also, the mixing of coffee ground waste and olive mill wastewater decreased the thermal conductivity of clay bricks from 0.176 W/m K to 0.142 W/m K and 0.143 W/m K, correspondingly. Moreover, the bulk density of building blocks decreased with an increase in waste amount as the porosity was increased.

In another work, the authors [11] developed a simulation model to study the thermal characteristics of various types of composite wall material (cellular concrete, burnt brick, mud brick, concrete block and fly ash brick) under Indian environmental conditions. It was seen that the brick wall made of fly ash had the lowest decrement factor of 0.401 in comparison to the mud brick, burnt brick, concrete block and cellular concrete, which reported the decrement factor of 0.554, 0.549, 0.559 and 0.497, respectively. In the similar trend, the fly ash outperformed all the other building blocks with a higher time lag of 8.159 h, as depicted in Fig. 8. Hence, the authors

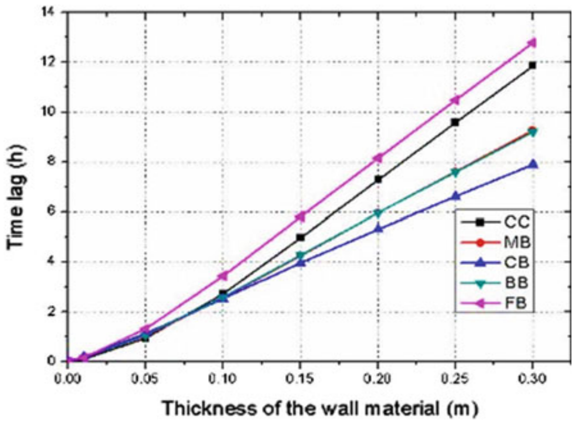

Fig. 8 Time lag achieved with different homogeneous wall materials [11]

had recommended the use of fly ash as a building wall material in replacement of the conventional materials.

The authors experimentally examined the thermal performance of the fly ash when used for the lightweight building blocks production as Turkey produces a lot of fly ash [5]. The average compressive strength of 76.5 kgf/cm^2 was achieved with a sample prepared by mixing 88% of fly ash and 12% of lime as well as the average flexural strength was found as 5.6 kgf/cm^2. Moreover, the average value of thermal conductivity was found as 0.225 W/m K, which definitely enhances the thermal performance of the building envelope with high thermal insulation.

Cheah et al. [23] performed a study to evaluate the use of wood ash and coal plant fly ash for the development of building blocks. In the mixture, the amount of coal ash and wood ash was varied from 0 to 100% with a step size of 10%. They concluded that the building block of having 50% wood ash and 50% fly ash exhibited optimal compressive and flexural strength performance. Subsequently, Dai et al. [24] experimentally studied the feasibility of using electroplating sludge as a building material. In this work, the authors found the mixture of clay (70%) with electroplating (10%) sludge and Na_2SiO_3. $9H_2O$ (20%) as an optimal solution for brick preparation under Chinese climatic conditions.

Munoz et al. [25] developed and examined thermo-mechanical properties of composite adobe bricks using soil and waste from the paper and pulp industry. The compressive strength of the developed samples was significantly influenced by the amount of PPR. For the composition of 90% clay and 10 PPR, the compressive strength was improved by 25% and the thermal conductivity shown a reduction of 50%. The same abode brick sample also kept the toxicity levels within the regulatory range. Hence, the proposed building blocks can be used under the climatic conditions of Chile very effectively and efficiently.

Table 1 summarizes some of the optimum building block compositions found by various researchers, along with their size, compressive strength (C_S) and equivalent thermal conductivity (λ_{eqv}).

4 Conclusions

The building envelope is solely responsible for the maximum heat losses occurring in the building and plays a critical role in augmenting the thermal performance of the building. Thus, eco-friendly and energy-efficient building materials should be explored for the building envelope. Such materials will also enable waste reduction, improved technical performance, less energy consumption and pollution during their life cycle. The present article summarizes various experimental, numerical and simulation studies performed by a number of researchers on the use of hollow bricks, bio-aggregate-based bricks and industrial waste to develop thermally efficient building blocks. The key conclusions derived from this study are as follows:

Table 1 Key findings from some of the reviewed studies

Optimum brick composition	Sample size (mm)	County	C_S (MPa)	λ_{eqv} (W/m K)	References
Sandcrete (70%) + palm fibre (30%)	450 × 125 × 225	Ghana	3.911	0.83	[8]
Lavender straw (3%) + fine aggregate	150 × 150 × 50	France	134	0.325	[9]
Bio-briquette ash (BBA) + clay	300 × 150 × 100	India	3.58	0.35	[20]
Olive pomace bottom ash (10%) + clay (90%)	-	Spain	35	0.85	[21]
Paper and pulp residue (10%) + sand (90%)	160 × 45 × 45	Chile	2.50	0.31	[25]
Glass powder (20%) + palm oil fly ash (35%) + crusher dust (30%) + lime (15%) + oil palm fibres (1%)	210 × 100 × 100	Malaysia	7.21	0.39	[19]

- Earth materials have multiple advantages such as the ability to adjust with local climate, high availability and low environmental impact, though it has disadvantages of poor ductility, water resistance and shrinkage.
- The air conditioning load is found to be more in the buildings that are made with the sandcrete blocks. As these building blocks have higher values of thermal conductivity that results in high heat interaction between the building and ambient environment.
- The reduction in thermal conductivity of construction material is one of the effective methods as it improves thermal insulation to diminish the load on the building air conditioning systems. Thus, it should be kept as low as possible; moreover, the mechanical properties, namely compressive strength, flexural strength and durability, should not be compromised during material selection.
- The hole number has a significant impact on the brick thermal performance as the increase in the number of holes deteriorates the convection heat transfer along with the radiation heat transfer.
- The insulation filled inside the internal holes was found to be less effective than the insulation-filled brick in the external cavities. Also, the incorporation of insulation with higher filling ratio results in improvement in the time lag as well as reduction in decrement factor and inner surface temperature.
- Incorporation of the insulating layer on the building walls increases the building construction cost as well as the construction time

- The use of agricultural by-products as building or construction material can reduce the consumption of natural resources and waste generation. It also supports sustainable development and helps in reducing the carbon footprint.
- The thermal conductivity of the conventional building blocks could be reduced with the introduction of straws. Moreover, the increment in water absorption and porosity can be attained with the incorporation of bio-fibres.
- It is noticed that the compressive strength and thermal conductivity increase with the increase in density values.
- The addition of Na_2SiO_3 diminished the leaching ability of the heavy metals present in electroplating sludge. Also, the mixing of Na_2SiO_3 is an effective method to improve the compression strength and to reduce the water absorption.

References

1. Jain M, Hoppe T, Bressers H (2017) Analyzing sectoral niche formation: the case of net-zero energy buildings in India. Environ Innov Soc Transitions 25:47–63. https://doi.org/10.1016/j.eist.2016.11.004
2. Martins A, Vasconcelos G, Campos Costa A (2017) Brick masonry veneer walls: an overview. J Build Eng 9:29–41. https://doi.org/10.1016/j.jobe.2016.11.005
3. Li J, Meng X, Gao Y, Mao W, Luo T, Zhang L (2018) Effect of the insulation materials filling on the thermal performance of sintered hollow bricks. Case Stud Therm Eng 11:62–70. https://doi.org/10.1016/j.csite.2017.12.007
4. Song M, Niu F, Mao N, Hu Y, Deng S (2018) Review on building energy performance improvement using phase change materials. Energy Build 158:776–793. https://doi.org/10.1016/j.enbuild.2017.10.066
5. Çiçek T, Çinçin Y (2015) Use of fly ash in production of light-weight building bricks. Constr Build Mater 94:521–527. https://doi.org/10.1016/j.conbuildmat.2015.07.029
6. Rashid K, Haq EU, Kamran MS, Munir N, Shahid A, Hanif I (2019) Experimental and finite element analysis on thermal conductivity of burnt clay bricks reinforced with fibers. Constr Build Mater 221:190–199. https://doi.org/10.1016/j.conbuildmat.2019.06.055
7. Olacia E, Pisello AL, Chiodo V, Maisano S, Frazzica A, Cabeza LF (2020) Sustainable adobe bricks with seagrass fibres. Mech Therm Prop Charact Constr Build Mater 239:117669. https://doi.org/10.1016/j.conbuildmat.2019.117669
8. Opoku R, Obeng GY, Darkwa J, Kwofie S (2020) Minimizing heat transmission loads and improving energy efficiency of building envelopes in sub-Saharan Africa using bio-based composite materials. Sci African 8:e00358. https://doi.org/10.1016/j.sciaf.2020.e00358
9. Giroudon M, Laborel-Préneron A, Aubert JE, Magniont C (2019) Comparison of barley and lavender straws as bioaggregates in earth bricks. Constr Build Mater 202:254–265. https://doi.org/10.1016/j.conbuildmat.2018.12.126
10. Al-Hadhrami LM, Ahmad A (2009) Assessment of thermal performance of different types of masonry bricks used in Saudi Arabia. Appl Therm Eng 29:1123–1130. https://doi.org/10.1016/j.applthermaleng.2008.06.003
11. Shaik S, Gorantla KK, Setty ABTP (2016) Investigation of building walls exposed to periodic heat transfer conditions for green and energy efficient building construction. Procedia Technol 23:496–503. https://doi.org/10.1016/j.protcy.2016.03.055
12. Li LP, Wu ZG, Li ZY, He YL, Tao WQ (2008) Numerical thermal optimization of the configuration of multi-holed clay bricks used for constructing building walls by the finite volume method. Int J Heat Mass Transf 51:3669–3682. https://doi.org/10.1016/j.ijheatmasstransfer.2007.06.008

13. Li LP, Wu ZG, He YL, Lauriat G, Tao WQ (2008) Optimization of the configuration of 290 × 140 × 90 hollow clay bricks with 3-D numerical simulation by finite volume method. Energy Build 40:1790–1798. https://doi.org/10.1016/j.enbuild.2008.03.010
14. Morales MP, Juárez MC, Muñoz P, Gómez JA (2011) Study of the geometry of a voided clay brick using non-rectangular perforations to optimise its thermal properties. Energy Build 43:2494–2498. https://doi.org/10.1016/j.enbuild.2011.06.006
15. Sodupe-Ortega E, Fraile-Garcia E, Ferreiro-Cabello J, Sanz-Garcia A (2016) Evaluation of crumb rubber as aggregate for automated manufacturing of rubberized long hollow blocks and bricks. Constr Build Mater 106:305–316. https://doi.org/10.1016/j.conbuildmat.2015.12.131
16. Qi C, Zhang F, Mu J, Zhang Y, Yu Z (2020) Enhanced mechanical and thermal properties of hollow wood composites filled with phase-change material. J Clean Prod 256:120373. https://doi.org/10.1016/j.jclepro.2020.120373
17. Marques B, Tadeu A, Almeida J, António J, de Brito J (2020) Characterisation of sustainable building walls made from rice straw bales. J Build Eng 28. https://doi.org/10.1016/j.jobe.2019.101041
18. Lamrani M, Mansour M, Laaroussi N, Khalfaoui M (2019) Thermal study of clay bricks reinforced by three ecological materials in south of Morocco. Energy Procedia 156:273–277. https://doi.org/10.1016/j.egypro.2018.11.141
19. Raut AN, Gomez CP (2017) Development of thermally efficient fibre-based eco-friendly brick reusing locally available waste materials. Constr Build Mater 133:275–284. https://doi.org/10.1016/j.conbuildmat.2016.12.055
20. Sakhare VV, Ralegaonkar RV (2017) Development and investigation of cellular light weight bio-briquette ash bricks. Clean Technol Environ Policy 19:235–242. https://doi.org/10.1007/s10098-016-1200-5
21. Eliche-Quesada D, Leite-Costa J (2016) Use of bottom ash from olive pomace combustion in the production of eco-friendly fired clay bricks. Waste Manag 48:323–333. https://doi.org/10.1016/j.wasman.2015.11.042
22. Eliche-Quesada D, Martínez-García C, Martínez-Cartas ML, Cotes-Palomino MT, Pérez-Villarejo L, Cruz-Pérez N, Corpas-Iglesias FA (2011) The use of different forms of waste in the manufacture of ceramic bricks. Appl Clay Sci 52:270–276. https://doi.org/10.1016/j.clay.2011.03.003
23. Cheah CB, Part WK, Ramli M (2017) The long term engineering properties of cementless building block work containing large volume of wood ash and coal fly ash. Constr Build Mater 143:522–536. https://doi.org/10.1016/j.conbuildmat.2017.03.162
24. Dai Z, Zhou H, Zhang W, Hu L, Huang Q, Mao L (2019) The improvement in properties and environmental safety of fired clay bricks containing hazardous waste electroplating sludge: The role of Na_2SiO_3. J Clean Prod 228:1455–1463. https://doi.org/10.1016/j.jclepro.2019.04.274
25. Muñoz P, Letelier V, Muñoz L, Bustamante MA (2020) Adobe bricks reinforced with paper & pulp wastes improving thermal and mechanical properties. Constr Build Mater 254. https://doi.org/10.1016/j.conbuildmat.2020.119314

Thermal Studies on Effects of Use of Desiccant Cooling in Cold Storage by Using CFD Analysis

Shalini Singh and B. K. Chourasia

1 Introduction

The process of cooling the food is done for reducing the post-harvesting deteriorations [1]. Post harvesting, the worst occurring issue for vegetables as well as fruits is water loss. This accelerates the deterioration speed [2]. Several types of researches were made about this issue which exhibited that the storage's relative humidity significantly affects the products' quality [3]. The use of desiccant material is made as they are capable of absorbing the moisture content of the air and hence reducing the moisture content. The process of absorption is defined as the contact between the absorbent and absorber molecules through the process of intermolecular interactions [4]. The products of agriculture are precooled and are needed for preserving their qualities and also for extending their availability for fulfilling future demands. When the products are kept at a low temperature, then their enzymatic activity will decrease along with microbial growths, reduce the loss of moisture content, and also decrease the production of ethylene [5].

The development of a transient 3D CFD model was made by [6] for calculating the distribution of moisture, temperature, and velocity within a completely loaded and empty cold storage system.

When the plan for storing onions in the cold storage system under a lower temperature range was made, it was seen that there was a decrease in fresh onion temperature from 0 to 4 °C; it was also seen that there was an increase in the relative humidity which exceeded the desired range of 55–65%. This causes rotting and sprouting of onions which results in reducing the life span of the onions along with increasing the several types of losses in the onions.

S. Singh (✉) · B. K. Chourasia
Department of Mechanical Engineering, Jabalpur Engineering College, Jabalpur, Madhya Pradesh 482011, India
e-mail: er.shalinisingh1996@gmail.com

D. Sharma and S. Roy (eds.), *Emerging Trends in Energy Conversion and Thermo-Fluid Systems*, Lecture Notes in Mechanical Engineering,
https://doi.org/10.1007/978-981-19-3410-0_17

A very significant role is played by the relative humidity when the onions are placed in a cold storage system for a longer period of time. The factor of relative humidity has been considered and observed as a very crucial factor especially for air circulation and temperature. This research paper aimed for conducting an experimental analysis over temperature and relative humidity with varieties of flow rates. Blue silica gel is brought into use as desiccant material which will be used for absorbing the moisture content from the air. Various experimental conditions will be used for accomplishing the objective of this study.

2 Materials and Modeling

The onions are placed inside the crates and are placed above each other. The placement is made in 6 rows and 8 columns.

2.1 Physical Model

The cold storage system brought in use under this research has the capability of storing approximately 3 t of onions at 5 °C of storage temperature. As exhibited in Fig. 1, the rooms are 2.6678 × 2.5654 × 2.8194 m, and other specifications are present in Table 1. The room is availed with a circulation corridor near the walls in between rows. There is an addition of duct within the cold storage room, and inside the duct, a desiccant material named blue silica gel is placed.

This study presents a cold storage system having a capacity of 3 tons, and in accordance with the problem statement mentioned in the study, fans on the wall are implemented over the preexisting cold storage system as shown in Fig. 2, and Table 2 shows the duct fan specification, and a passageway of airflows is created on within which silica gel and air come in contact with each other. In addition, a desiccant material made up of blue silica gel is added to the model which will absorb the moisture content of the air.

2.2 Materials

Onions

The harvesting of fresh onions is made during August, and after that, they are stored in a storage system for one complete year at a temperature of 4 °C. Onion was stored in the fictitious cold storage chamber for testing purposes. Onions that had been preserved for a year had a lower dry matter content than those that had been newly picked [7] (Fig. 3).

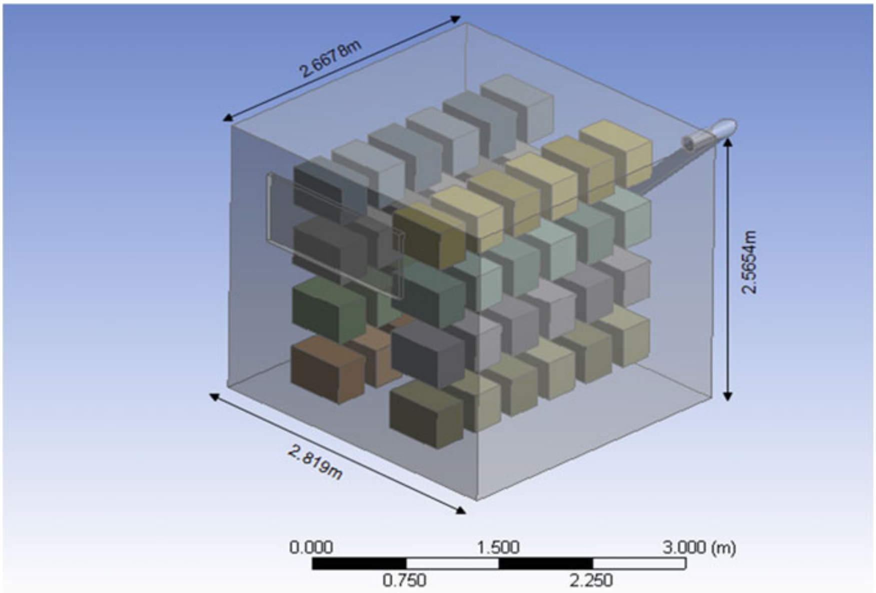

Fig. 1 Major dimensions of cold storage

Table 1 Design parameters of cold storage

S. No.	Particular	Specification
1.	Cold storage length	2.8194 m
2.	Cold storage width	2.6678 m
3.	Cold storage height	2.5654 m
4.	Length	2
5.	Width	4
6.	Height	6
7.	Dimensions of the crates	0.54 m × 0.36m × 0.29 m
8.	Capacity of crates	25 kg/crates
9.	Total capacity	1.2 MT
10.	Airflow velocity	1 m/s

Blue silica gel

With the findings of this research in consideration, 8 percent of its total weight was absorbed by silica gel. When placed in water, the color of the colored crystal will turn pink from blue as shown in Fig. 4a, b. This is a simple indication that can be seen visually to indicate that now gel is completely saturated with the moisture contents of air and should be replaced now. The blue silica gel material property is exhibited in Table 3.

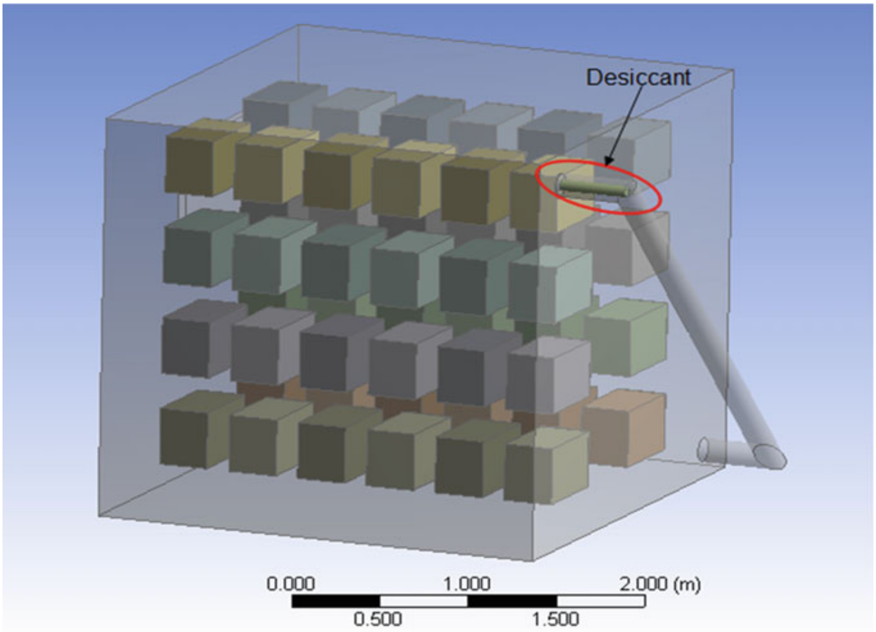

Fig. 2 Placement of desiccant (blue silica gel) into duct pipe attached with cold storage

Table 2 Duct fan specification

S. No.	Particular	Specification
1.	Power rating	48 W
2.	Airflow rate	200 m^3/h
3.	Diameter	150 mm

As exhibited in the above figures, the silica spherical balls were blue at the time when they were placed inside the duct pipe, and they turned pink after absorbing the moisture content from the air.

2.3 Mathematical Model

Fluent Release 19.0 was used for running the CFD analysis for this study. The use of the averaged fluid equation of Reynolds is made for solving the continuous airflow issue. The establishment of this used model is made by utilizing a discretization scheme of second order. Its use is also made for coupling of pressure and velocity. At the interface of air and onion, for determining the convective heat transfer coefficients and airflow fields, the use of transient simulation is made. By the indication made preciously, for refining the simulations and for obtaining better and satisfying

Fig. 3 Onion used in the experiment

(a) (b)

Fig. 4 Silica spherical ball **a** before absorbing moisture **b** after moisture absorbing

outcomes, the definition of convergence criteria is made as for the movement and continuity equation, when there is enough reduction in residuals to make it below 10^{-3}, then the convergence is said to be satisfied. For the energy equation, it is satisfied when the residuals reach a value below 10^{-6}.

The division of the transport phenomenon into water vapors and absorption can be made in the absorber bed. The granules of the silica gel surface the flow rate equation

Table 3 Technical specification of blue silica gel [8]

Technical specification as per IS-3401-1979/1992/2003	
Descriptions	Blue silica gel
Types	Indicating types
pH	6–7
ASSAY (as SiO_2)	97.00–99.00%
Loss on drying %	< 5–6%
Bulk density	0.600–0.700 gm/cc
Chloride (as NaCl)	0.40 ppm
Adsorption capacity at 100% humidity	27.00–40.00%
Loss on attrition %	2.5%
Friability	99.5
Size of the particles (mesh)	1–2, 3–4, 3–8, 5–8, 9–16, 16–30
Ammonium (NH_3)	Nil
Sulfate (as Na_2SO_4)	0.5 ppm
Formula	$SiO_2 + H_2O + CoCl_2$

of Navier–Stokes which is brought in use for solving the flow phases of water vapor [9].

Energy Equation

The principle of energy conversion is followed by the energy equation. Its derivation is made as per the thermodynamics' first law which implies that "a fluid's energy change rate is equivalent to the sum of the rate at which the work is done and the sum of the rate at which the heat is supplied" [10]. The below-mentioned Eq. (1) provides the energy equation's conservative form.

$$\frac{\partial}{\partial t}\left[\rho\left(e+v^2/2\right)\right]+\nabla\cdot\left[\rho\left(e+v^2/2\right)\right] = E_p + E_b + E_{\mathrm{V}} + E_q + E \tag{1}$$

here,

$$E_{\mathrm{p}} = -\left[\frac{\partial}{\partial x}(pu)+\frac{\partial}{\partial y}(pv)+\frac{\partial}{\partial z}(p\omega)\right]$$

$$E_{\mathrm{b}} = \rho\left(f_x u + f_y v + f_z \omega\right)$$

$$E_{\mathrm{V}} = \frac{\partial}{\partial x}(\tau_{xx}u)+\frac{\partial}{\partial y}\left(\tau_{xy}u\right)+\frac{\partial}{\partial z}(\tau_{xz}u)$$

$$+\frac{\partial}{\partial x}\left(\tau_{yx}v\right)+\frac{\partial}{\partial y}\left(\tau_{yy}v\right)+\frac{\partial}{\partial z}\left(\tau_{yz}v\right)$$
$$+\frac{\partial}{\partial x}(\tau_{zx}\omega)+\frac{\partial}{\partial y}\left(\tau_{zy}\omega\right)+\frac{\partial}{\partial z}(\tau_{zz}\omega)$$

$$E_q=-\left[\frac{\partial}{\partial x}\left(k\frac{\partial T}{\partial x}\right)+\frac{\partial}{\partial y}\left(k\frac{\partial T}{\partial y}\right)+\frac{\partial}{\partial z}\left(k\frac{\partial T}{\partial z}\right)\right]$$

$$E=\rho q^{\cdot}$$

The kinetic and internal terms make up the energy growth rate per volume unit, ΔE, whereas the net heat flux goes into the volume control rate per volume unit, q.

Momentum Equation

The equation for calculating the momentum is dependent on "Newton's second law". According to the Newton's second law: "in a specific direction, the change in the rate of momentum is equivalent to the sum of all the forces acting on the fluid in the same direction" [2]. Convection and its reversal suggest the emergence of crawling flow. ρg and $\nabla.\,\sigma ij$ denote body force as well as the sum of applied surface forces, respectively. Therefore, changing coordinate systems, the precise equation will change. The below-mentioned Eq. (2) exhibits the mathematical expression of the momentum equation in an unsteady state:

"Momentum equation in X-direction":

$$\frac{\partial}{\partial t}(\rho u)+\nabla.(\rho uV)=-\frac{\partial p}{\partial x}+\frac{\partial\tau_{xx}}{\partial x}+\frac{\partial\tau_{yx}}{\partial y}+\frac{\partial\tau_{zx}}{\partial z}+\rho f_x \tag{2}$$

"Momentum equation in Y-direction":

$$\frac{\partial}{\partial t}(\rho v)+\nabla.(\rho vV)=-\frac{\partial p}{\partial y}+\frac{\partial\tau_{xy}}{\partial x}+\frac{\partial\tau_{yy}}{\partial y}+\frac{\partial\tau_{zy}}{\partial z}+\rho f_y \tag{3}$$

"Momentum equation in Z-direction":

$$\frac{\partial}{\partial t}(\rho\omega)+\nabla.(\rho\omega V)=-\frac{\partial p}{\partial z}+\frac{\partial\tau_{xz}}{\partial x}+\frac{\partial\tau_{yz}}{\partial y}+\frac{\partial\tau_{zz}}{\partial z}+\rho f_z \tag{4}$$

Continuity Equation

The base of this equation is over the principle of mass conservation. Defining conservation of mass may be done by stating that the rate of change in mass inside a "control volume (CV)" is equal to the net rate of mass flowing into the CV. The mathematical expression of continuity equation is exhibited in Eq. (5):

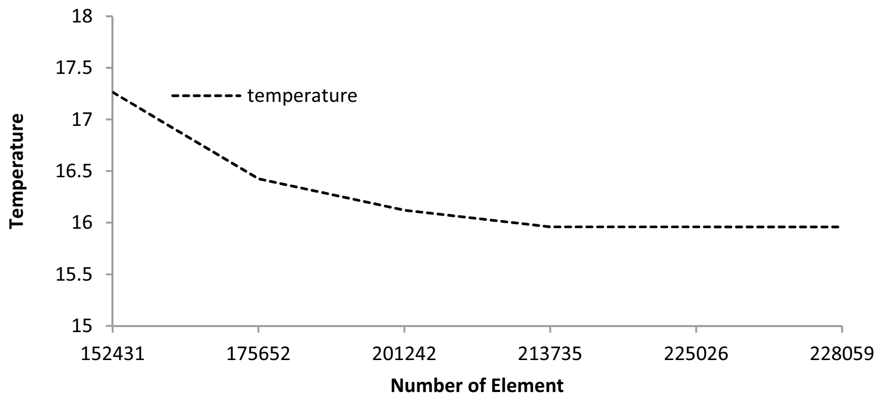

Fig. 5 Grade independent test

$$\frac{\partial \rho}{\partial t} + \frac{\partial}{\partial \mathrm{x}}(\rho \mathrm{u}) + \frac{\partial}{\partial \mathrm{y}}(\rho \mathrm{v}) + \frac{\partial}{\partial \mathrm{z}}(\rho \omega) = 0 \tag{5}$$

2.4 Meshing

Figure 6 is showing the grade independent test which is done for the selection of element size for the design. Different numbers of elements are selected, and the result is compared in terms of temperature. Variation in temperature after element size of 213,735 is almost constant; that is why 213,735 element size is selected (Fig. 5).

The process of creating meshes is different for each form of geometry [9]. The mesh domain was split into 213,735 elements and 71840 nodes as exhibited in Fig. 6. Tetrahedron-type meshing is used in the cold storage area, and on the onion, quadrilateral meshing is used. The overall element size taken is 5 mm, but 2 mm of element size is used in the evaporating section.

2.5 Boundary Condition

For analyzing CFD, the domain which was brought in use had the same size as that of the cold storage room. It also had a similar fan along with a similar heat exchange system. To solve the sets of governing equations, the relevant boundary condition is used. At the initial stage, the exit of the evaporator is brought into consideration as an air velocity inlet. The initial temperature at the inlet was 5 °C with 1 m/s of velocity.

The implementation of the design conditions was made for the simulations. An assumption for the floor was made at a constant temperature of 300 K. The roof along with the side walls was assumed at a natural convection environment having a

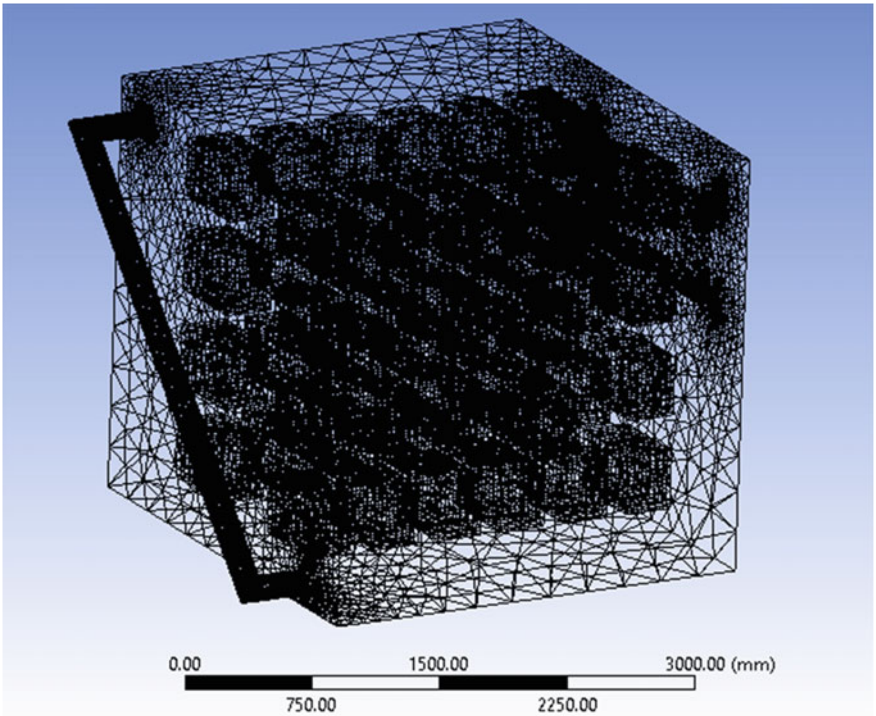

Fig. 6 Wireframe meshing of cold storage

temperature of 300 K. A 1 m/s of inlet velocity was also considered. As this region constitutes of high air velocity and availability of large space is present, it is very much possible that turbulence occurs and the standard $k - \epsilon$ model might not be able to predict accurately.

3 Results and Discussion

3.1 Result Validations

RH is the most significant factor affecting onion moisture content, including moisture loss from fresh crop. The below graph represents the relative humidity to the temperature. Both the results obtained from CFD as well as experimentation are exhibited. The results obtained for very similar and negligible differences can be reported. The maximum difference is when the temperature is 12 °C which showed the value from CFD analysis and experimentation as 68.122% and 66.136%, respectively, as exhibited in Fig. 7. The experimental results were obtained from "Maulana

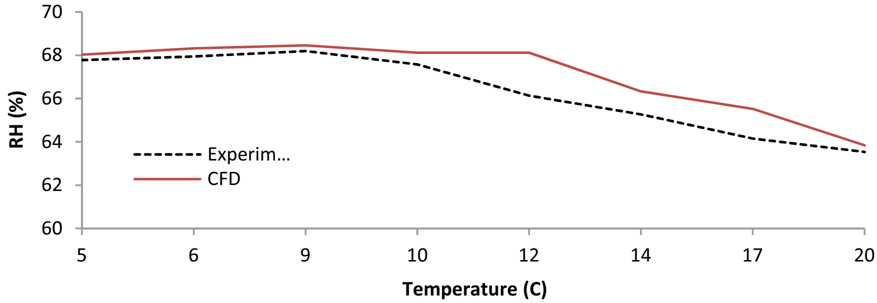

Fig. 7 Validation graph of experimental and CFD study

Azad National Institute of Technology (MANIT), Bhopal, Madhya Pradesh".

3.2 Variation of Relative Humidity

Figure 8 mentioned exhibits the results obtained before integrating the desiccant material in the cold storage system. The value of relative humidity was obtained as 69.04%. As discussed above, if the humidity is above 65%, then the onions will start rotting and sprouting. The results were collected after 40 h from placing the onions in the cold storage.

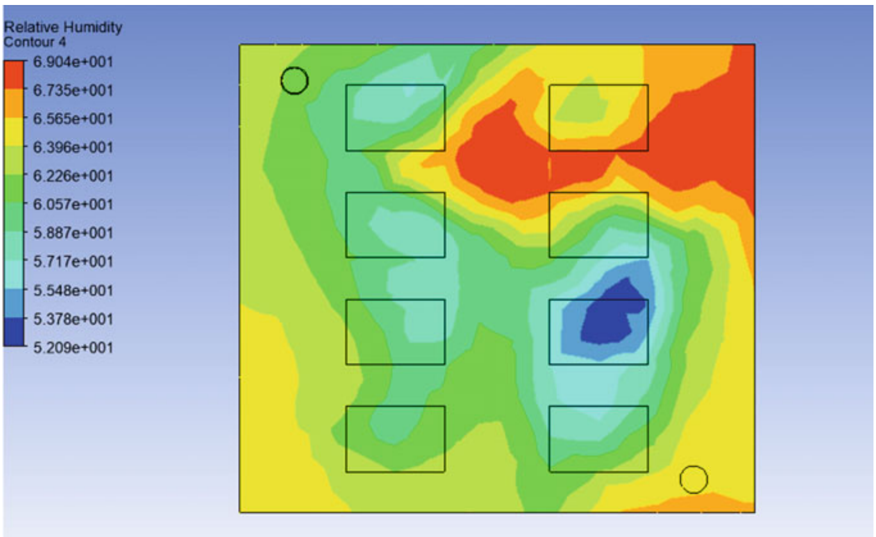

Fig. 8 Relative humidity of cold storage before using desiccant

To remove the issues of rotting and sprouting of the onions, desiccant material made up of blue silica gel is added to remove the moisture content of the air. This reduced the humidity to 58.5% as shown in Fig. 9. The results were collected after 40 h from placing the onions in the cold storage (Fig. 10).

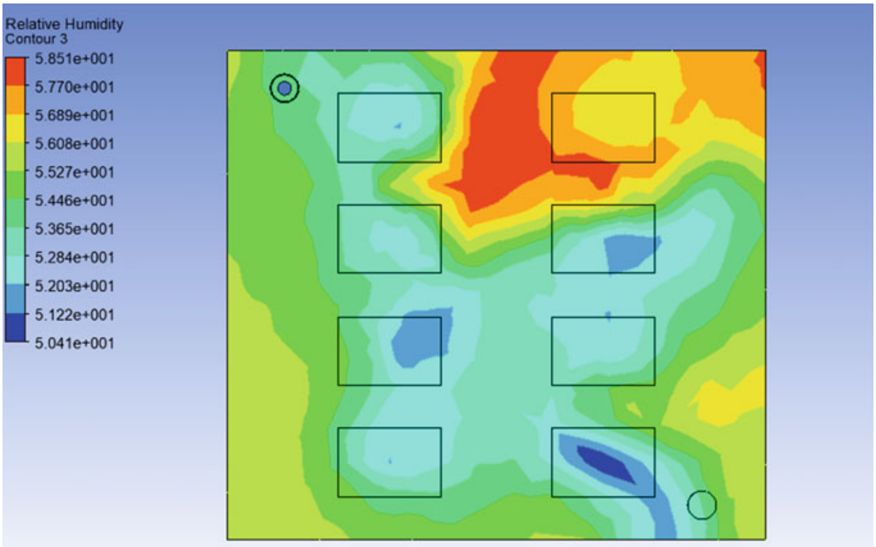

Fig. 9 Relative humidity of cold storage after using desiccant

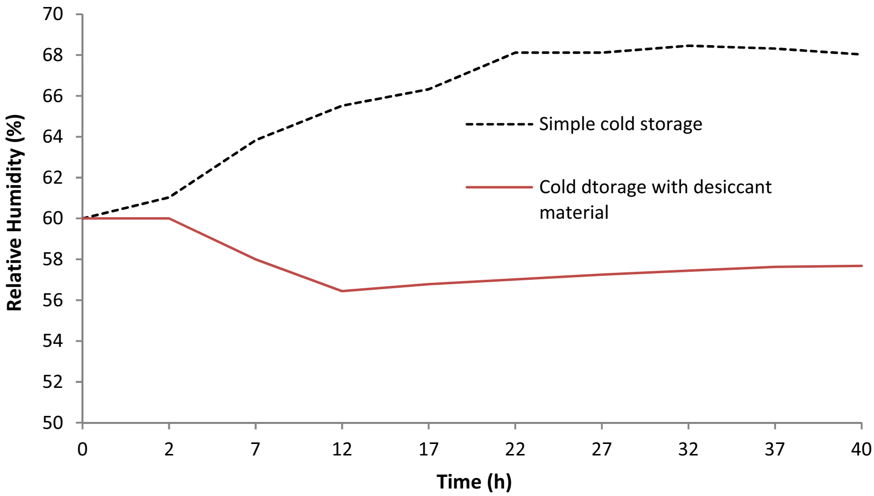

Fig. 10 Comparison of relative humidity of simple and modified cold storage from CFD analysis

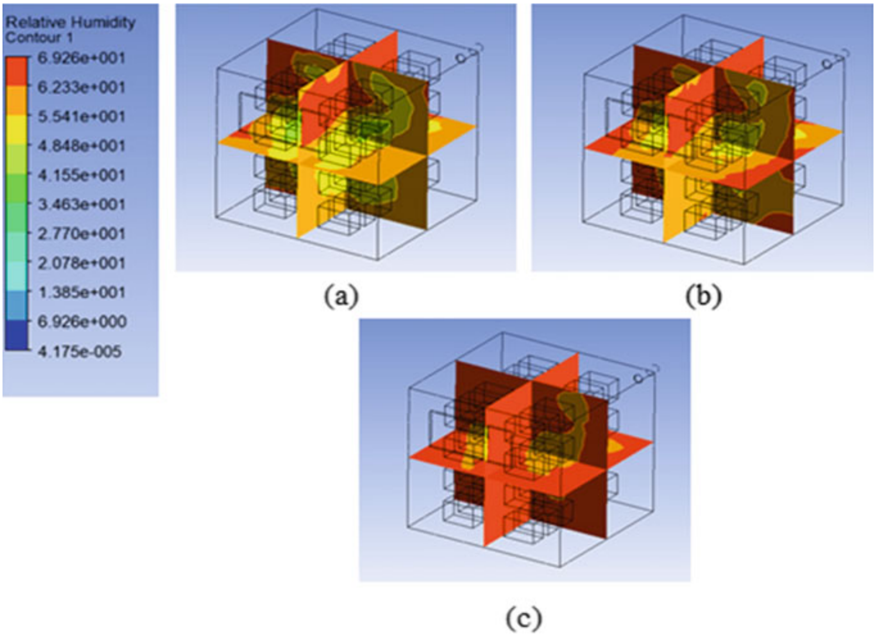

Fig. 11 Relative humidity of cold storage without desiccant **a** after 10 h, **b** after 20 h, and **c** after 40 h

The results were collected through cold storage without desiccant, after 1, 20, and 40 h as shown in Fig. 11. And then, results were collected through cold storage with desiccant, and after 1 h, humidity content had minimum spread which increased after 20 h and was at maximum after 40 h (as shown in Fig. 12).

3.3 Variation of Temperature

The below-mentioned figures exhibit the results obtained before integrating the desiccant material in the cold storage system. The temperature value recorded for onions before using desiccant material was around 25 °C when measured after 10 h, and it drops down to around 19 °C and 14 °C when measured after 20 h and 40 h, respectively, as shown in Fig. 13.

In the duct, a fan of 48 W is mounted for experimental conditions which are helping in proper circulation of air through the duct so that the air of cold storage circulated through the duct and passes through desiccant placed into the duct, and because of this process and fan velocity, temperature also reduces by some little value.

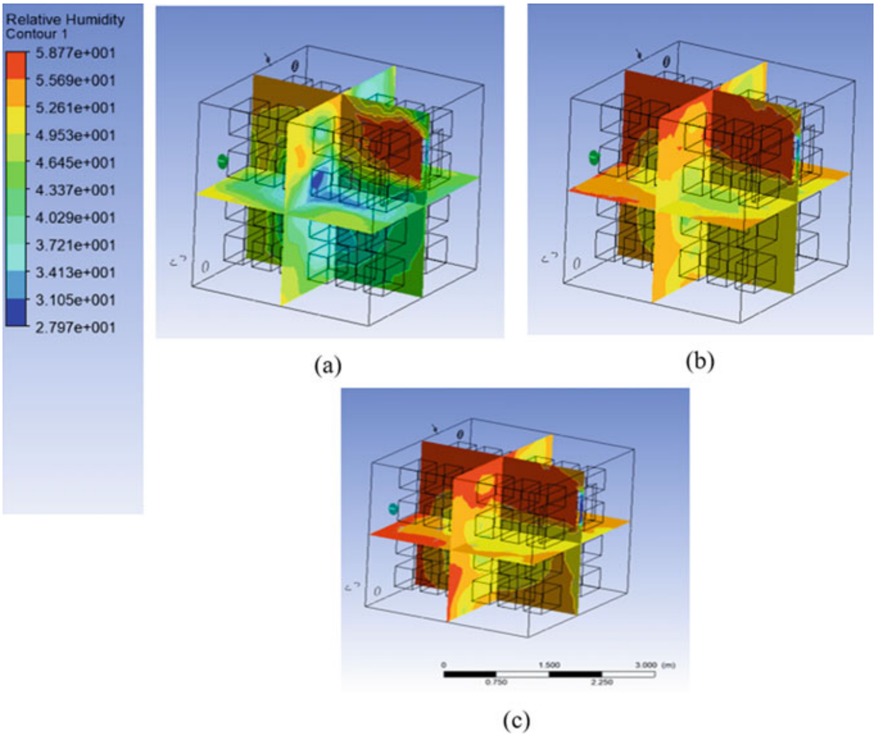

Fig. 12 Relative humidity of cold storage with the use of desiccant material **a** after 10 h, **b** after 20 h, and **c** after 40 h

The results were collected after 1 h, 20 h, and 40 h. After 1 h, it was observed that temperature was at a maximum which decreased after 20 h and was at minimum after 40 h, i.e., around 5 °C, 3 °C, and 2 °C, respectively, (Fig. 14).

The graphical representation of a comparison of the temperature inside the cold storage with desiccant material and cold storage without desiccant material is exhibited in Fig. 15

A total of 40 h of study is presented in above-mentioned graph in Fig. 15. There was a noticeable reduction in the temperature recorded at the initial stage of experimentation and the temperature recorded at the end of the experimentation. The temperature rapidly decreases during the initial 10 h. After that, the decrease in the temperature slows down. The minimum required temperature for storing the onions in the cold storage is attained within 38 h to 40 h which is around in the range of 2–4.6 °C as shown in Fig. 16.

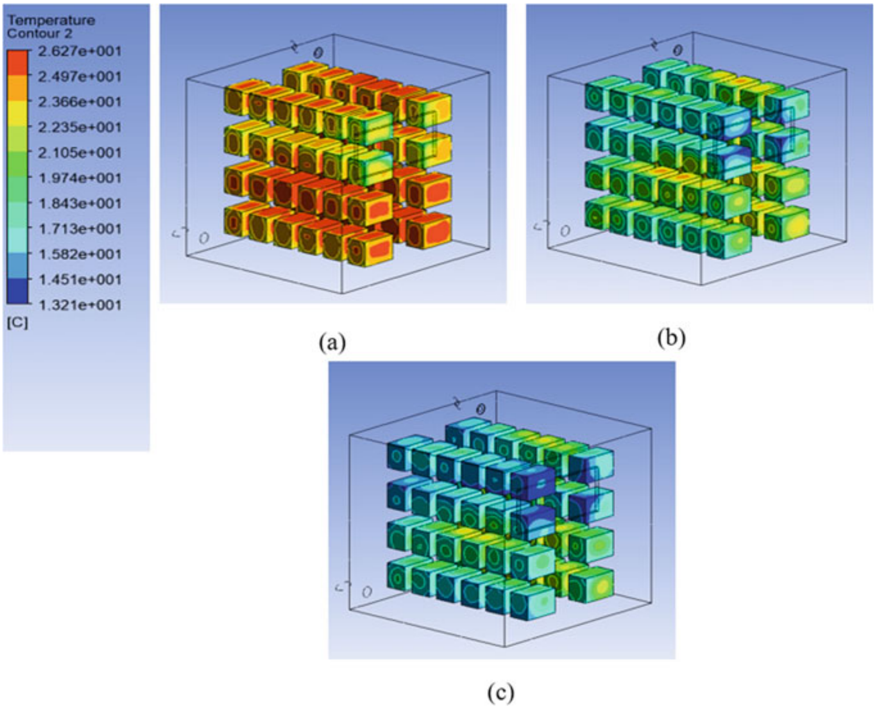

Fig. 13 Onion temperature with the use of desiccant material **a** after 10 h, **b** after 20 h, and **c** after 40 h

4 Conclusions

Experimental and computational fluid dynamics (CFD) methods were used in this investigation. There was a considerable decrease in humidity thanks to the desiccant substance. The maximum humidity required in cold storage for storing onions is within the range of 55–65%. The results in this study showed that after using the desiccant material, the obtained humidity was 58.5% in the CFD analysis. This will help keep the onions fresh for a longer period of time by allowing them to be stored in a more humid environment. Since the humidity content affects the quality of the onions, therefore, this desiccant material can now evidently be used on larger scales. It also reduced the temperature by a significant difference bringing down the temperature under the needed value, i.e., 5 °C. The results showed a temperature of around 4.6 °C which was attained after using the fan in the duct.

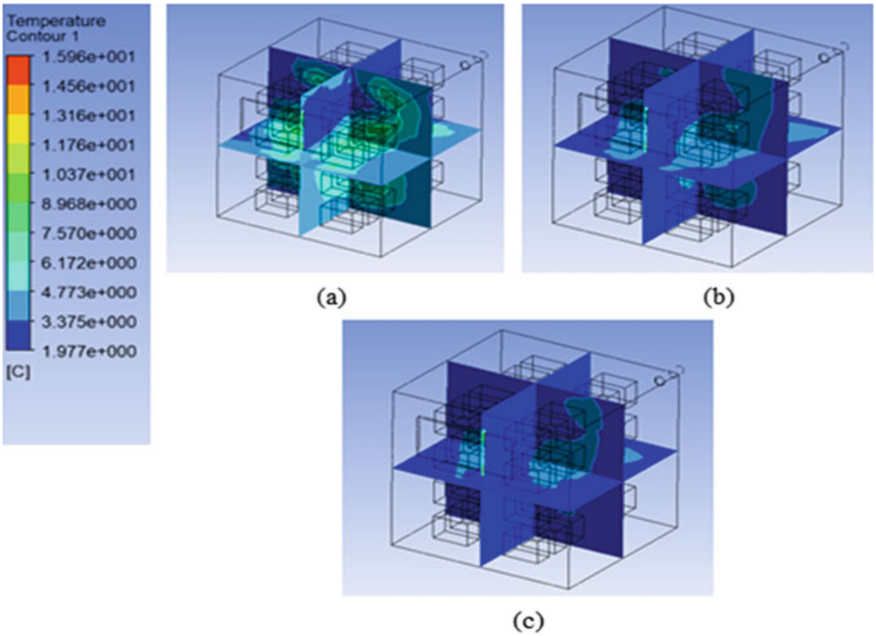

Fig. 14 Cold storage temperature with the use of desiccant material **a** after 10 h, **b** after 20 h, and **c** after 40 h

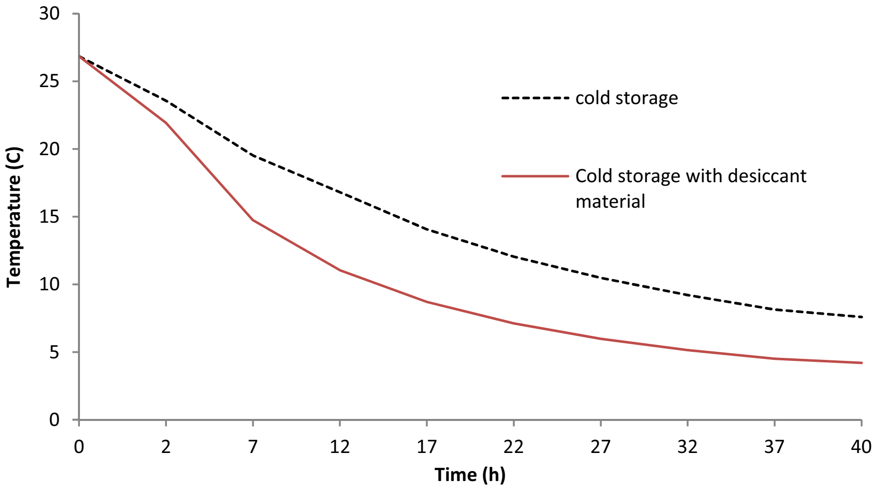

Fig. 15 Comparison of temperature of simple and modified cold storage from CFD analysis

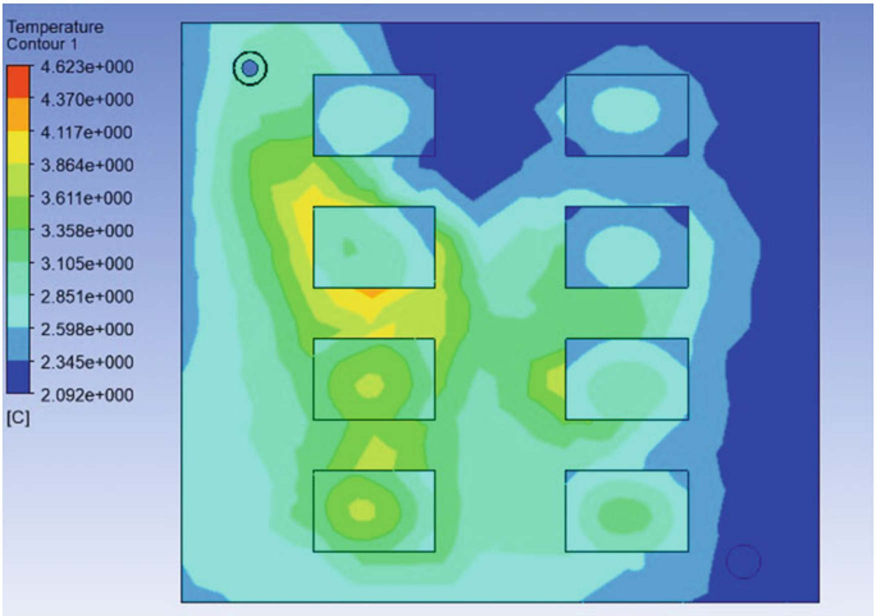

Fig. 16 Final temperature of cold storage with desiccant after 40 h

References

1. Chourasia MK, Goswami TK (2007) Simulation of effect of stack dimensions and stacking arrangement on cool-down characteristics of potato in a cold store by computational fluid dynamics. Biosyst Eng 96(4):503–515. https://doi.org/10.1016/j.biosystemseng.2006.12.010
2. Guo J et al (2020) Characteristic analysis of humidity control in a fresh-keeping container using CFD model. Comput Electron Agric 179:105816. https://doi.org/10.1016/j.compag.2020.105816
3. Jalali A et al (2019) Application of humidity absorbing trays to fresh produce packaging: mathematical modeling and experimental validation. J Food Eng 244:115–125. https://doi.org/10.1016/j.jfoodeng.2018.09.006
4. Khoukhi M (2013) A study of desiccant-based cooling and dehumidifying system in hot-humid climate. Int J Mater Mech Manuf 1(2):191–194. https://doi.org/10.7763/ijmmm.2013.v1.41
5. Ghiloufi Z, Khir T (2019) CFD modeling and optimization of pre-cooling conditions in a cold room located in the South of Tunisia and filled with dates. J Food Sci Technol 56(8):3668–3676. https://doi.org/10.1007/s13197-019-03812-8
6. Akdemir S, Arin S (2006) Spatial variability of ambient temperature, relative humidity and air velocity in a cold store. J Cent Eur Agric 7(1):101–110. https://doi.org/10.5513/jcea.v7i1.360
7. Abhayawick L, Laguerre JC, Tauzin V, Duquenoy A (2002) Physical properties of three onion varieties as affected by the moisture content. J Food Eng 55(3):253–262. https://doi.org/10.1016/S0260-8774(02)00099-7
8. Link T (2003) Silica gel blue. http://www.silicagel.in/silicagel-blue.html
9. White J (2012) A CFD simulation on how the different sizes of silica gel will affect the adsorption performance of silica gel. Model Simul Eng 2012. https://doi.org/10.1155/2012/651434

10. Delele MA, Schenk A, Tijskens E, Ramon H, Nicolaï BM, Verboven P (2009) Optimization of the humidification of cold stores by pressurized water atomizers based on a multiscale CFD model. J Food Eng 91(2):228–239. https://doi.org/10.1016/j.jfoodeng.2008.08.027

Miscellaneous

Comparative Study of Wind Loads on Tall Buildings of Different Shapes

Rahul Kumar Meena, Ritu Raj, and S. Anbukumar

Nomenclature

A	Frontal area of rotor (m^2)
AR	Aspect ratio
Cp	Pressure coefficient
θ	Angle of attack of wind (°)
ρ	Density of air (kg/m^3)
Ω	Omega
ε	Epsilon
α	Roughness coefficient 0.147

1 Introduction

With the advancement of technology and enormous population growth, the need and design of high structures with different configurations have been a growing trend. High-rise structures have always fascinated from the beginning of civilization and are unique in various aspects, such as consideration of lateral deflections. The wind is a complicated phenomenon in which the motion of an individual particle is so unpredictable that one needs to be concerned about the statistical distribution of velocity rather than just simple averages. There are two distinct local influences in determining overall wind power, even if windward pressure and leeward suction add up to one total. When it comes to wind load planning, a structure cannot be considered to have a

R. K. Meena (✉) · R. Raj · S. Anbukumar
Delhi Technological University, Delhi 110042, India
e-mail: rahul.08dtu@gmail.com; rahulkumar_phd2k18@dtu.ac.in

D. Sharma and S. Roy (eds.), *Emerging Trends in Energy Conversion and Thermo-Fluid Systems*, Lecture Notes in Mechanical Engineering,
https://doi.org/10.1007/978-981-19-3410-0_18

regular configuration by default. Designers use wind load standards to compute structural pressure coefficients and force coefficients for other structures that are exposed to wind-induced stresses [1–5]. On the other hand, these standards offer details for plain cross-sectional configurations with a limited number of wind incidence angles. These codes do not provide information on wind loadings for structures with different configurations. As a result, wind tunnel research on models of such forms is popular. Chandan and Kumar [6] simulating wind studies of towering structures was accomplished with the use of CFD (computational fluid dynamics). CFD can yield results that are comparable to those obtained from wind tunnel studies. CFD might examine the entire domain study, provide better visualization of data and be less expensive than wind tunnel tests. Raj and Ahuja [7] The use of a boundary layer wind tunnel was used to conduct experimental study on the wind load on high structures with cross-plan configurations. Bairagi and Dalui [8] as a result of increased turbulence, positive pressure built up in the setback roof, where turbulence is at its most severe, and the largest spectral density frequency was formed at this place. Using CFD simulations for wind incidence angles ranging from 0^0 to 180^0, this article examined the influence of aerodynamics on the setback of tall structures. Hajra and Dalui [9] performed the mathematical-based research of interference effect on octagonal plan configuration high structure using CFX (ANSYS), for 0^0 wind incidence angle using $k - \varepsilon$, SST and $k - \omega$ model, and analysis of these three models shows nearly identical results. Meena et al. [10] research has been carried out to determine how wind affects different types of multi-storey steel structures' bracing mechanisms. Verma et al. [11] for the 0^0, 15^0 and 30^0 wind speeds, the influence of wind load on a high octagonal configuration structure was investigated using computational fluid dynamics (CFD) simulation. This demonstrated that CFD may be utilized to forecast wind-related problems on tall structures with complicated geometries. The conclusions of wind-induced response are dependent on the type of plan in geometry and defining the flow properties. Dalui et al. [12] studied the effects of interference on octagonal plan configuration high structures under the influence effect of wind, windward face and immediate side face to windward face is not affected much by the presence of the interfering structure. Paterka et al. [13] discussed the wind flow pattern around the structures. Wind flow about three-dimensional structures results in separated flow regions fundamentally highly different from those about two-dimensional structures. In three-dimensional, as opposed to two-dimensional modelling, the separation of cavities immediately downwind is not encased by free streamlines. Kawamoto [14] for the assessment of wind load on the structure, a cost-effective turbulence model was created. The mean pressure coefficient improves considerably when employing the $k - \omega$ turbulence model, and the over prediction of turbulence kinetic energy in the k-turbulence model is the source of the error in the $k - \varepsilon$ turbulence model. Pal et al. [15] looked at both square and fish floor layouts. It is the most efficient design in terms of wind-generated pressure and base shear when completely blocked, compared to other designs. Amin and Ahuja [16] suction on side faces and leeward faces is greatly affected by the plan arrangement of the model and wind incidence angle, according to experimental studies of wind-induced pressure on structures of various geometries. Selvem [17] by employing large eddy simulation, the Navier–Stokes equation was numerically solved, resulting in a peak pressure that is substantially greater than that measured in the field. As compared to the three turbulence models, the peak pressure calculated using TTU wind data is substantially closer to the measurements taken in the field. Pirooz and Flay [18] the impacts of a solid tower and an urban environment on collected wind data were explored, as well as numerical and wind tunnel simulations. Some researchers have also explained few important characteristics of wind using wind tunnel test like pal et al. [19] on isolated fish plan shape building, Nagar et al. [20] on plus plan shape building, Pal et al. [21] interference study on same-type building, Kumar and Raj [22] on oval shape building, Gaur and Raj [23] on plus shape, Meena et al. [24] on "*L*" shape, Mahajan et al. [25] on the effect of shear wall on different corner shape structure, Gaur et al. [26] interference study on wind effects and Nagar et al. [27] on different shape of high-rise structure. In this study, the influence of shape of high-rise structure is obtained using the numerical simulation performed using ANSYS CFX on hexagon and octagon shape building model. The entire numerical simulation is performed by utilizing the $k - \varepsilon$ turbulence model. The domain is considered such that no recirculation of flow can occur.

2 Numerical Modelling

The present study is carried out to obtain pressure contour and pressure coefficient for a different types of high structure using the ANSYS CFX package (Version 2020 R-2).

2.1 Model and Boundary Conditions

The purpose of this research is to determine the wind effects on hexagon model A (a) and octagon model B (b) at a 0^0 wind incidence angle. Figure 1 shows the dimensions of the structure as well as the angle of wind incidence.

As shown in Fig. 2, domain is where all the solution of CFD simulation is done and is provided according to Revuz [28]. Domain side wall, inlet and top wall are kept at 5H. The outlet is kept at 15H, where *H* is the height of the structure.

Domain top wall and side wall are kept as free slip wall, and model face and ground are kept as no-slip wall.

2.2 Meshing

Meshing is provided to increase the accuracy of the solution done during simulation. This can be provided by manual and automatic using ANSYS CFX. In the manual

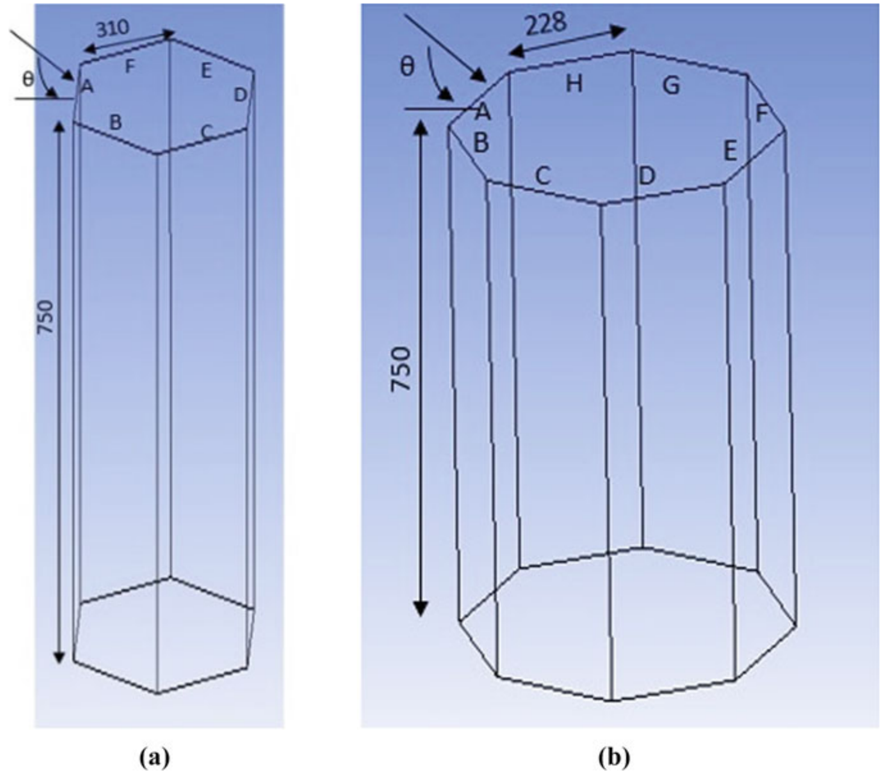

Fig. 1 Model dimension, face name and wind incidence angle **a** model A, **b** model B

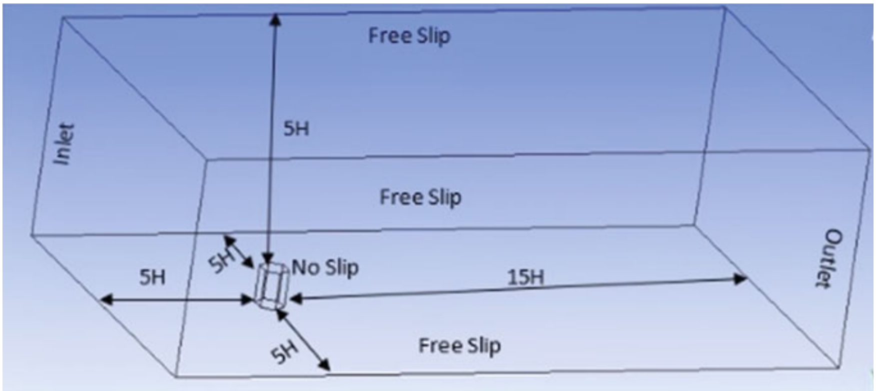

Fig. 2 Domain

method, meshing for different parts can be applied, and depending on the problem, meshing size is selected. The inflation done in CFD simulation for all models is used to reduce the anomalous flow. As shown in Fig. 3, domain provided with tetrahedron meshing, structure and ground meshing is relatively more delicate in size. It increases the solution accuracy. Figure 4a is edge meshing, and Fig. 4b is inflation, used to minimize the unusual flow.

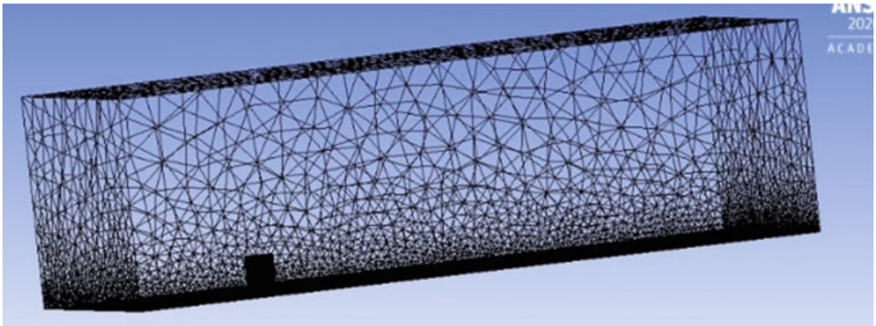

Fig. 3 Domain, ground and structure meshing

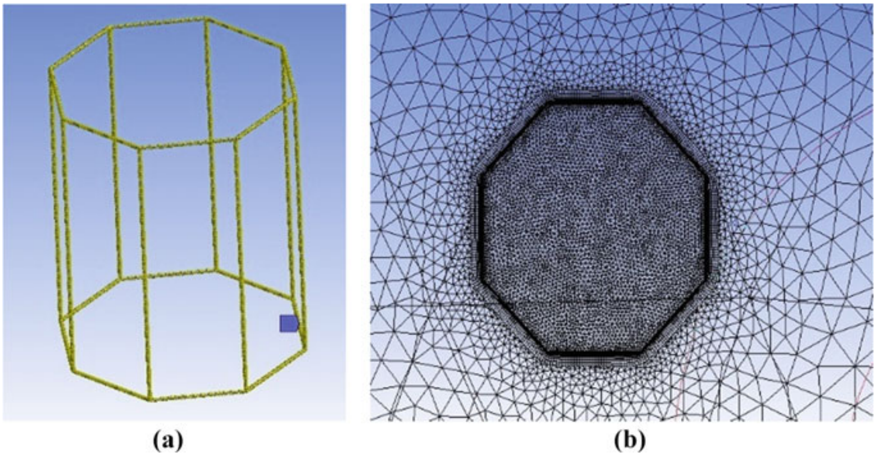

Fig. 4 Meshing **a** edge meshing **b** inflation

3 Result and Discussion

3.1 The Profile of Velocity and Turbulence Intensity

When estimating the vertical profile of wind speed, surface roughness and drag induced by local projections that impede wind flow are important elements. Neither the gradient height nor the gradient velocity causes any drag; these two numbers are referred to as the gradient. The atmospheric boundary layer refers to the layer of air above which topography has an effect on wind speed.

The wind speed profile within the atmospheric boundary layer, as seen in Fig. 5, is determined by equation according to Power Law Eq. (1).

$$\frac{U}{U_H} = \left(\frac{Z}{Z_H}\right)^{\alpha} \tag{1}$$

where U_{H} is the speed at the reference height Z_{H}, which is 10 m/s, α is the ground roughness, that varied as per the terrain conditions, and actual situation in this study is 0.147 for terrain category 2, while Z_{H} is 1.0 m for terrain category 2.

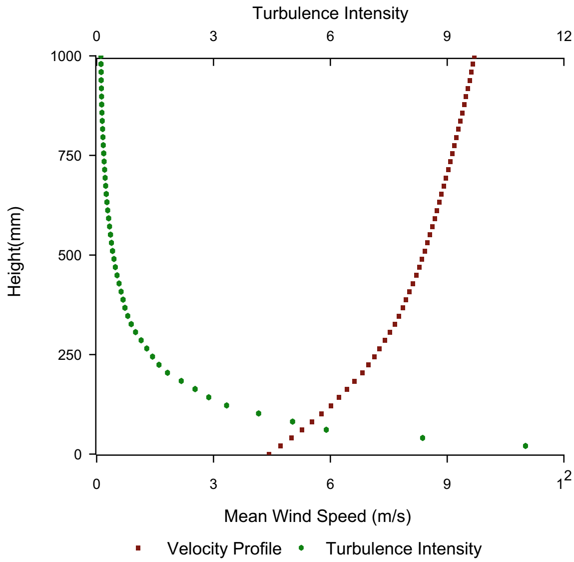

Fig. 5 Height-dependent variations in wind speed and turbulence intensity

3.2 Pressure Contours

Figures 6 and 7 show that the pressure applied to the windward face is positive for the models and that it is negative for the windward and leeward faces. As seen by a bar chart in Figs. 6 and 7, models *A* and *B* are subjected to varying levels of pressure.

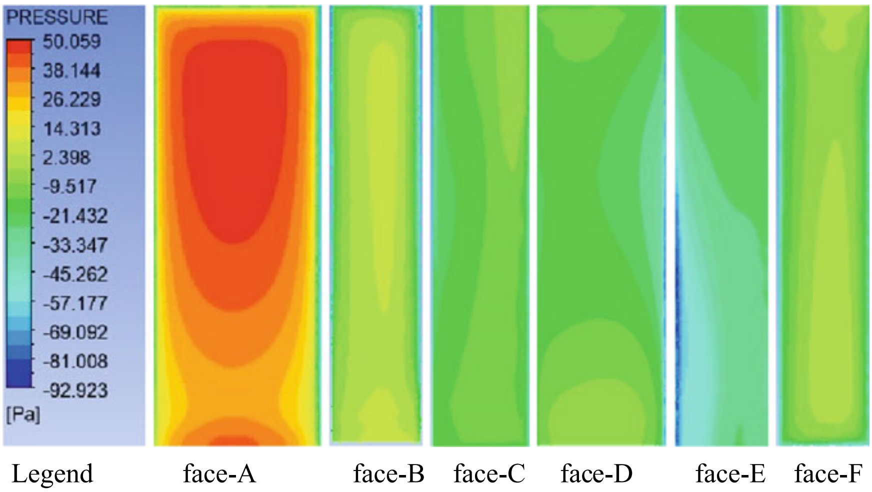

Fig. 6 Pressure contour for model *A* at 0^0 wind incidence angle

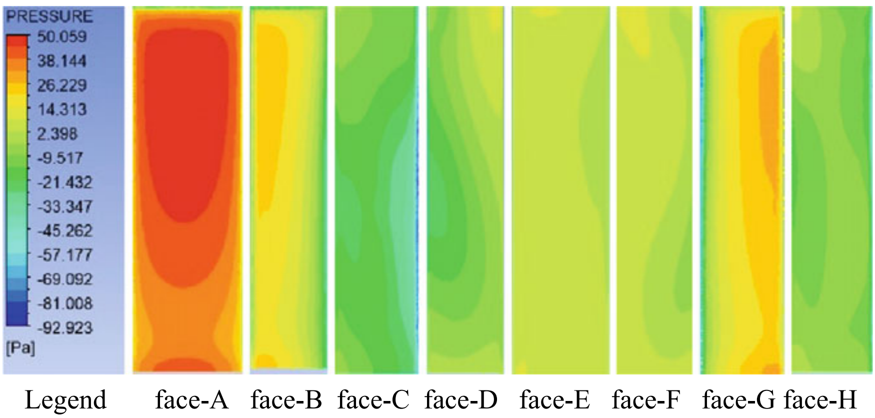

Fig. 7 Pressure contour for model *B* at 0^0 wind incidence angle

3.3 Velocity Streamlines

At each location along the imaginary line, the direction of a fluid particle's velocity is indicated by the tangent. While moving through the air, a fluid particle is called to be on a streamline. For a wind incidence angle of 0^0 degrees, the streamline is symmetric. The model shows how the streamlining will look. Figure 8 shows a structure (a) in plan, (c) in elevation and (e) in three-dimensional view of streamlines at a 0^0 wind incidence angle. With a 0^0 wind incidence angle, Fig. 8 shows the streamlines for the model *B* structure (b) in plan, (d) in elevation and (f) in 3D perspective.

The mean C_p for model *B* is shown in Fig. 7. It can be seen in Fig. 7 that face *A* is the only face of model *B* that is subjected to positive pressure, while the remaining faces of model *B* are subjected to negative pressure. The $k - \varepsilon$, SST and $k - \omega$ models all produce C_p values that are almost equal for each face.

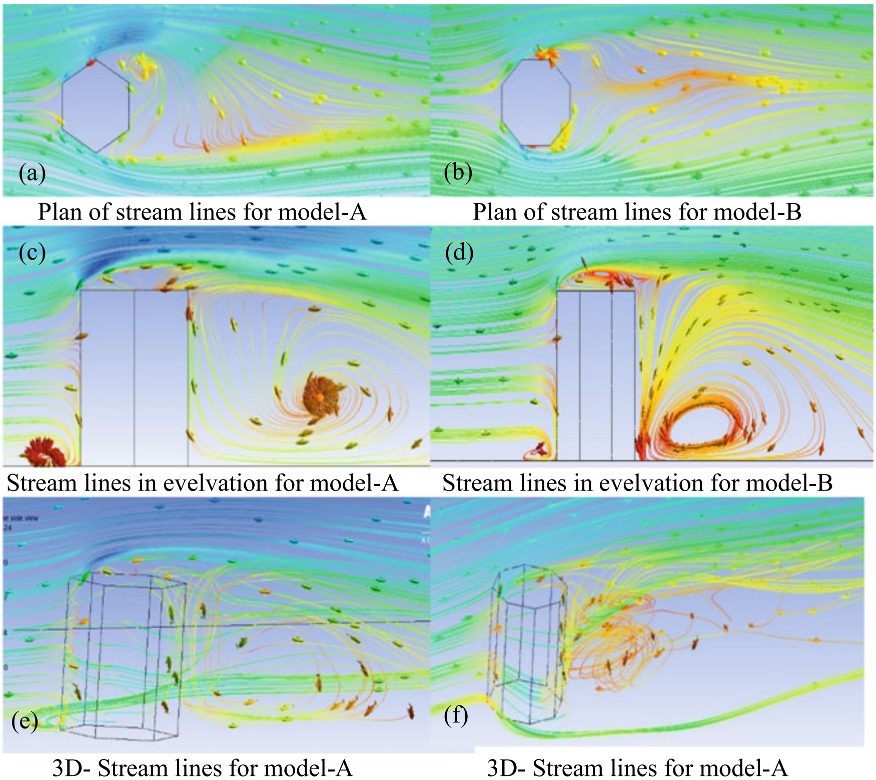

Fig. 8 Streamlines on model *A* and *B*

3.4 Vertical Centre Line Pressure Coefficient

In both Figs. 9 and 10, the structural height and the mean surface pressure coefficient are shown. Because face *A* is a windward face, the wind hits it directly as shown in Figs. 9 and 10. Pressure variation due to 0^0 wind incidence angle is for both the structure models *A* and *B and* is shown in Figs. 9 and 10, respectively, around the centreline of every face.

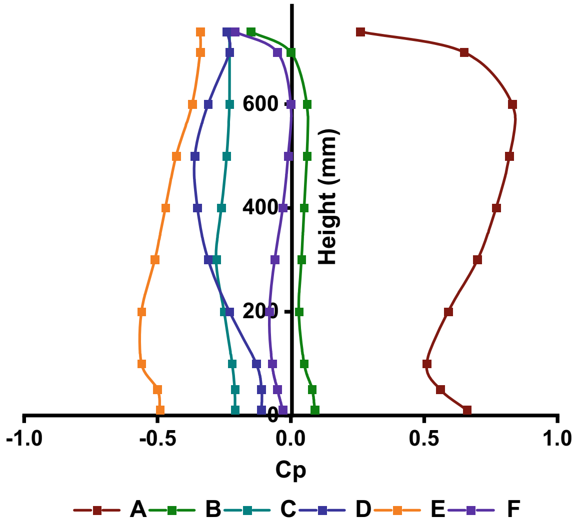

Fig. 9 Variation in pressure along the centreline for all of the faces of model *A*

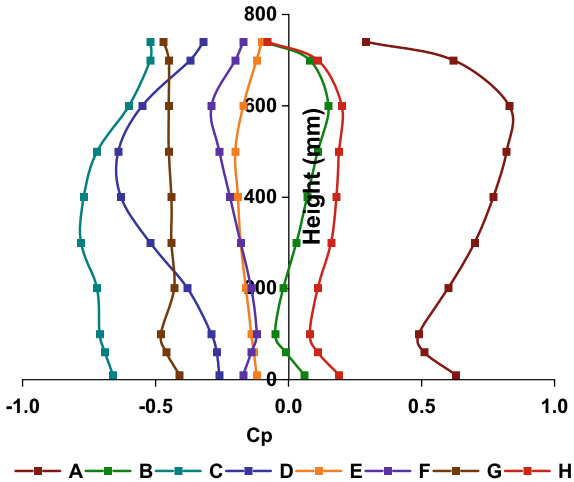

Fig. 10 Variation in pressure along the centreline for all of the faces of model *B*

4 Conclusion

"Hexagon" and "Octagon" design values of the pressure contours, mean pressure coefficients and velocity streamlines are all examined at 0^0 wind incidence angles in this study". $K - \varepsilon$ modelling is utilized to replicate this study. The following are the findings of the study:

- Negative pressure is always applied to face *B*, while positive pressure is always applied to face *A* in both models.
- Octagonal tall structure experiences almost symmetrical pressure distribution.
- The fluctuation of pressure coefficients along the centreline is examined and graphically depicted.
- The octagonal and hexagonal plan cross-sectional shape has more or less the same nature of pressure distribution on the windward surface in the case of symmetrical wind incidence angle.
- The velocity streamlines are depicted in the plan, elevation and 3D views using the figure.
- In the same way that a boundary layer wind tunnel determines the precision of the task, meshing the geometry model and setting the flow physics determine the precision of the task.
- This investigation of the wind pressure distribution on the leeward face illustrates the formation of vorticity, which indicates a significant amount of turbulence, according to the findings.

Acknowledgements The authors are thankful to Delhi Technological University for providing the research facilities and funding to support this study. The authors are grateful to Asha, Aparna and Rythem; they encouraged and supported the author throughout this study.

References

1. IS: 875 (2015) Indian standard design loads (other than earthquake) for buildings and structures-code of practice, part 3(wind loads)
2. ASCE: 7-10 (2013) Minimum design loads for buildings and other structures. Struct Eng Instit Am Soc Civil Eng Reston
3. GB 50009–2001 (2002) National standard of the People's Republic of China
4. Ethiopian Standard, ES ISO 4354 (2012) (English) Wind actions on structures 2012
5. AS/NZS: 1170.2 (2011) Structural design actions—part 2: wind actions. Standards Australia/Standards New Zealand, Sydney
6. Hima Chandan D, Pradeep Kumar R (2014) Numerical simulation of wind analysis of tall buildings computational fluid dynamics approach
7. Raj R, Ahuja AK (2013) Wind loads on cross shape tall buildings. J Acad Indus Res (JAIR) 2(2):111–113
8. Bairagi K, Dalui SK (2018) Aerodynamic effects on setback tall building using CFD simulation. Int J Mech Prod Eng Res Dev 413–420. (Online). Available: www.tjprc.org

9. Hajra S, Dalui SK (2016) Numerical investigation of interference effect on octagonal plan shaped tall buildings. Jordan J Civil Eng 10(4):462–479
10. Meena RK, Awadhiya GP, Paswan AP, Jayant HK (2018) Effects of bracing system on multistoryed steel building. https://doi.org/10.1088/1757-899X/1128/1/012017
11. Verma DSK, Roy A, Lather S, Sood M (2015) CFD Simulation for wind load on octagonal tall buildings. Int J Eng Trends Technol 24(4):211–216. https://doi.org/10.14445/22315381/ijett-v24p239
12. Dalui SK, Kar R, Hajra S (2015) Interference effects on octagonal plan shaped tall building under wind—a case study 9:74–81
13. Peterka JA, Meroney RN, Kothari KM (1985) Wind flow patterns about buildings 21:21–38
14. Kawamoto S (1997) Improved turbulence models for estimation of wind loading. J Wind Eng Ind Aerodyn 67–68:589–599. https://doi.org/10.1016/S0167-6105(97)00102-5
15. Pal S, Raj R, Anbukumar S (2021) Comparative study of wind induced mutual interference effects on square and fish-plan shape tall buildings. Sādhanā 0123456789. https://doi.org/10.1007/s12046-021-01592-6
16. Amin J, Ahuja A (2011) Experimental study of wind-induced pressures on buildings of various geometries. Int J Eng Sci Technol 3(5):1–19. https://doi.org/10.4314/ijest.v3i5.68562
17. Selvam RP (1997) Computation of pressures on Texas Tech University building using large eddy simulation. J Wind Eng Ind Aerodyn 67–68:647–657. https://doi.org/10.1016/s0167-6105(97)00107-4
18. Safaei A, Flay RGJ (2019) Effects of a solid tower and urban area on measured wind data : numerical and wind-tunnel simulations: 6–9
19. Pal S, Meena RK, Raj R, Anbukumar S (2021) Wind tunnel study of a fish—plan shape model under different isolated wind incidences 5:353–366
20. Nagar SK, Raj R, Dev N (2021) Proximity effects between two plus-plan shaped high-rise buildings on mean and RMS pressure coefficients. Sci Iran 0–0. https://doi.org/10.24200/sci.2021.55928.4484
21. Pal S, Raj R, Anbukumar S (2021) Bilateral interference of wind loads induced on duplicate building models of various shapes. Latin Am J Solids Struct 18(5). https://doi.org/10.1590/1679-78256595
22. Kumar A, Raj R (2021) Study of pressure distribution on an irregular octagonal plan oval-shape building using CFD. Civil Eng J 7(10):1787–1805. https://doi.org/10.28991/cej-2021-03091760
23. Gaur N, Raj R (2021) Aerodynamic mitigation by corner modification on square model under wind loads employing CFD and wind tunnel. Ain Shams Eng J. https://doi.org/10.1016/j.asej.2021.06.007
24. Meena RK, Raj R, Anbukumar S (2021) Numerical investigation of wind load on side ratio of high-rise buildings numerical investigation of wind load on side ratio of high-rise buildings. Springer, Singapore
25. Mahajan S, Yadav V, Raj R, Raj R (2022) Effect of shear walls on tall buildings with different corner configuration subjected to wind loads. In: Gupta AK, Shukla SK, Azamathulla H (eds) Advances in Construction Materials and Sustainable Environment. Lecture Notes in Civil Engineering, vol 196. Springer, Singapore. https://doi.org/10.1007/978-981-16-6557-8_59
26. Gaur N, Raj R, Goyal PK (2021) Interference effect on corner—configured structures with variable geometry and blockage configurations under wind loads using CFD. Asian J Civil Eng. https://doi.org/10.1007/s42107-021-00400-0
27. Nagar SK, Raj R, Dev N (2020) Experimental study of wind-induced pressures on tall buildings of different shapes. Wind Struct Int J 31(5):441–453. https://doi.org/10.12989/was.2020.31.5.431
28. Revuz J, Hargreaves DM, Owen JS (2012) On the domain size for the steady-state CFD modelling of a tall building. Wind Struct Int J 15(4):313–329. https://doi.org/10.12989/was.2012.15.4.313

Experimental Studies on the Effect of Liquid Flow Rate on Pressure Drop in Rotating Packed Bed (RPB)

Abhimanyu, Gaurav Kumar, and D. S. Murthy

Nomenclature

G Gas flow rate (m^3/h)
L Liquid flow rate (m^3/h)
ω Rotor rotational speed (r/min)

1 Introduction

Rotating packed bed (RPB) was developed by Ramshaw and Mallinson in 1981. The main aim of the development of RPB was to enhance the efficiency of mass transfer in the gas-liquid multiphase system [1, 2]. The concept of "Higee" (high gravitational) came into existence which eventually led to process intensification (PI). PI can be defined as the progress that can lead to a more clean, safe and efficient technology. It includes optimization of analytical parameters like heat transfer, mass transfer, etc. and using alternative methods or energy sources. RPB uses a strong centrifugal force to produce a gravitational field of a high order, up to 500 g [3]. It consists of packing which is the part where gas-liquid interaction takes place. The liquid distributor is used to inject water inside the packing. It is placed in the rotor eye. From the peripheral edge of the packing, gas is introduced through gas inlet. The liquid and gas interact inside the packing in the counter-current direction. Due to the very high rotational speed of the rotor, a condition of very high centrifugal force is also observed which leads to the difference in hydrodynamic characteristics of the RPB as compared to a conventional tower.

Abhimanyu (✉) · G. Kumar · D. S. Murthy
G. B. Pant University of Agriculture and Technology, Pantnagar, Uttarakhand 263145, India
e-mail: abhimanyubalyan8@gmail.com

D. Sharma and S. Roy (eds.), *Emerging Trends in Energy Conversion and Thermo-Fluid Systems*, Lecture Notes in Mechanical Engineering,
https://doi.org/10.1007/978-981-19-3410-0_19

In traditional columns, the liquid is introduced from the top, and because of gravity, the liquid flows downwards. The vapour (gas) moves counter-currently, up the column. Though operational, these columns have their fair share of problems such as flooding. Due to flooding, these columns require a large diameter to obtain high separation degrees. Since gravity is the only driving force here, achieving a high liquid flow rate is not possible. The gas pressure drop in RPB, which is engaged in packing selection and energy consumption, is not only an important metric for assessing its performance, but also plays a role in fundamental research.

It is now widely used in many industries, where it has replaced the conventional columns, for various processes like absorption, separation, distillation, ozone oxidation, synthesis of nanoparticles, etc. This has been possible due to its small size, less capital cost and environment-friendly nature [4–9]. Though the thermal performance of RPB is less explored, few available records suggest that there is a significant effect of operating parameters on the temperature drop of water inside RPB which is similar to the difference obtained in cooling towers. Hence, more research in this sector could lead to a noteworthy reduction in the volume of cooling towers using RPB [10, 11].

2 Literature Review and Objectives

In conventional packed beds, the liquid flows down due to gravity. Gravity limits the speed in the packed bed, and therefore, sometimes a larger volume is needed to get the work done. Next to this, flooding in the bed may occur when the acceleration of gravity is not big enough. To get rid of this limitation, rotating packed beds were firstly proposed by Ramshaw and Mallinson. The gas-liquid flow characteristics have a great impact on mass transfer efficiency and other parametric behaviours of the RPB. Many research has been conducted to study the extent of the impact of these characteristics on other parameters. Kevyani and Gardner [12] studied the mass transfer and pressure drop characteristics on aluminium foam metal packings having different specific areas ranging from 656 to 2952 m^{-1} with a porosity of 0.92 for all the packings. They observed that for a notable set of observations a larger pressure drop was observed in the case of a dry bed in contrast to irrigated bed. The pressure drop was also increasing with an increase in a specific area in the case of both dry and irrigated bed. The power requirement for the rotor to spin subsequently decreases as the gas velocity increases. Kumar and Rao [13] came out with a model to calculate pressure drop using wire mesh packing. One of the main observation regarding the total pressure drop was that it depends on centrifugal forces, frictional forces and the kinetic energy gain at expense of the pressure head. Singh et al. [14] used two types of packing: (1) metal sponge packing, and (2) wire gauge packing. The metal sponge packing had different packing depths and outer diameters. They observed mass transfer, drop in pressure, energy consumption and fouling of the packing. A semi-empirical interconnection was put forward which predicted that the drop in pressure was within ±30% of the experimental data. Liu et al. [16] studied pressure drop characteristics using two different packings: (1) a rectangular packing and (2) an elliptical cylindrical packing. It was observed that rectangular packing has a higher pressure drop as compared to elliptical cylindrical packing because liquid holdup was high in rectangular packing. Kelleher and Fair [3] evaluated the previous correlation on pressure drop and observed that the pressure drop varies directly with gas kinetic energy and increases with the square of rotational speed. It was observed that the liquid flow rate has the minimal effect on pressure drop. Zheng et al. [15] conducted an experiment using packings with different inner diameters (45, 150 and 280 mm) and observed that pressure drop is increasing along with an inner diameter of packing. Lin et al. [5] used two different packings for their distillation experiment. They observed that the packing with high volume has a higher pressure drop as there was less resistance to gas flow. Liu et al. [17] observed that in the case of cross-flow RPB, the pressure drop of wet bed is affected by rate of liquid flow to some degree as there was less liquid holding inside the packing. Also, the dry bed pressure drop was smaller as compared to the wet bed at the same rotational speed. This was particularly not observed in counter-current flow RPB. Wang et al. [18] observed that the gas pressure drop is largely dependable on the rotor speed and rate of gas flow for both dry bed and wet bed (except on low rotor speed). Due to flooding at low rotor speed, pressure drop increased exceptionally as compared to a dry bed. Hendry et al. [19] studied pressure drop and flooding for counter-current and co-current flow RPB and observed that counter-current flow RPB has higher pressure drop as a centrifugal force acts against the gas flow. They also observed that a free vortex is formed in the eye of RPB creating negative pressure which contributed to the overall pressure drop.

Liquid flow pattern also shows a significant effect on the pressure drop of wet bed. There were mainly three types of liquid flow patterns as observed in previous experimental studies [8, 9]. These liquid flows inside the packing area are as follows: pore flow, droplet flow and film flow. These patterns depend on the rotational speed of the packing. They also observed liquid maldistribution in some cases indicating that the liquid flow inside the packing is not uniform and is complex in nature.

The liquid holdup inside the packing shows the packing resistance to the liquid in RPB, and it is related to the flooding and pressure drop in the RPB. The liquid holdup is affected by the packing structure, rotor speed, gas flow rate, etc. [20–23].

Various experimental studies were conducted to study the pressure drop characteristics of the RPB using various operating parameters, packing materials and configurations. This has garnered popularity to the RPB in the chemical industries. The objective of this experimental study was to observe the effects of the rate of liquid flow on pressure drop characteristics of the RPB.

3 Experimental Setup

The RPB with a counter-current flow has been illustrated in Fig. 1. The counter-current RPB experimental setup used the air-water system which comprised of a stationary housing made up of acrylic sheet and a rotor that was driven by a motor

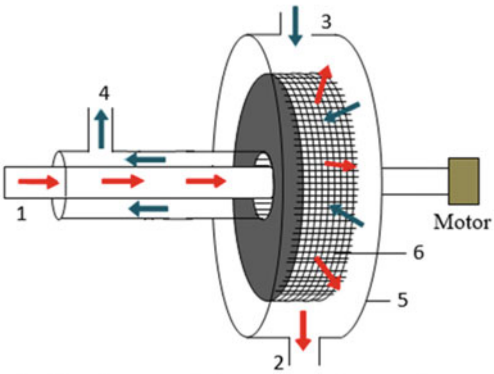

1.Liquid inlet, 2.Liquid outlet, 3.Gas inlet, 4.Gas outlet, 5.Casing, 6.Porous media.

Fig. 1 An illustrative diagram of the RPB unit

(Kirloskar 1 hp power). The rotor speed was controlled using a variable frequency drive. The air swirled from the peripheral edge of the rotor to the inner edge due to pressure driving force. The liquid was injected into the packing through a liquid distributor having 16 holes of 1 mm diameter each, and it moved from the inner edge to the peripheral edge of the packing due to centrifugal force. The air from the blower was introduced to the gas inlet from where it travels inward through the packing radially. The water flow was measured through a rotameter (range: 0–10 LPM), from where it flowed to the liquid distributor and moved outward through the packing and exited through the liquid outlet. During this experiment, the gas pressure drop was measured through a differential pressure transmitter (Aerosense DPT-R8-3W) that was connected to a datalogger (DataTaker DT85 series 4).

The porous medium of RPB was made with stainless steel wire mesh. The packing has an axial length of 45 mm. Other dimensional parameters are given in Table 1.

For the experimental study, the operating conditions were as follows: rotor speed: 400–2000 r/min; rate of air flow: 15 and 30 m^3/h; and rate of water flow: 0.12–0.42 m^3/h. Multiple observations were recorded based on the given operating parameters.

There were uncertainties related to the measurement of pressure. Using the theory given by Moffat [24], uncertainties were calculated. For the present work, uncertainties in the measurement of pressure in the experiment ranged from 0.11 to 0.43% of the measured values.

Table 1 Dimensional parameters of packing

Inner radius	40 mm
Outer radius	120 mm
Specific surface area	2055.5 m^2/m^3
Porosity	0.815

4 Result and Discussion

Figure 2 exhibits the effect of varying rotor speeds on the air side pressure drop at constant rate of air flow at 30 m^3/h and rate of water flow at 0.18 m^3/h. At low rotor speed, there is no considerable effect on drop in pressure. The effect of the centrifugal action is less as compared to the gravitational pull. Therefore, the water was coming out of the packing in form of splashes from all directions. At 400 rpm, water entrainment in the rotor eye was observed. Since the air flow rate was high, it took some portion of the water inside the air outlet pipe. Due to this entrainment, the cross-section area of the air outlet decreased which led to obstruction in the air flow. As a result, an increase of about 50 Pa was observed in the pressure drop in case of wet bed in contrast to dry bed.

But as soon the rotor speed was increased, pressure drop also increased. This is due to the centrifugal force produced by the rotor packing, which increases as the rotor speed increases. The droplet size became very small, and the packing space was available for more air flow without any restriction. The water distributor, placed inside the rotor eye, disrupted the incoming air velocity, and hence, the pressure drop in case of wet bed was less than in case of the dry bed pressure drop because of the Bernoulli effect.

Figure 3 exhibits the effect of varying rates of water flow on the air side pressure drop at constant rate of air flow of 15 m^3/h and 1600 rpm rotor speed. As the results show, there was no noticeable effect of varying rates of water flow across the RPB as it was very marginal, about 40 Pa. It can also be observed from Fig. 3 that as the water flow rate was increasing, the pressure drop was decreasing in the case of a wet bed due to Bernoulli effect. At high rotor speed, air-water interaction was very less as the water turned into mist flow, and due to this reason, the water velocity inside the rotor eye increased. Water velocity depends on water flow rate and the diameter of water distributor. Since there was no obstruction offered by water particles inside the packing, it did not affect the pressure drop.

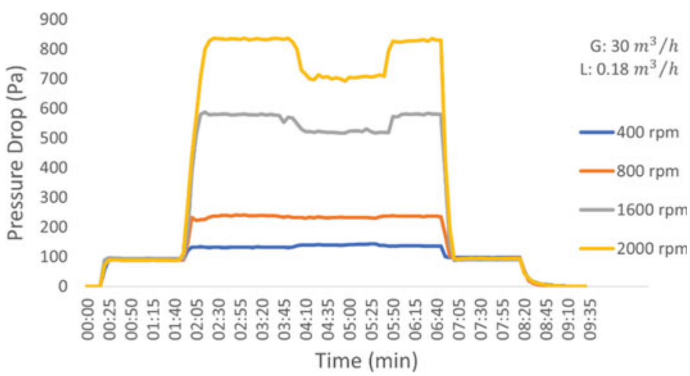

Fig. 2 Difference in air side pressure drop at uniform rate of water and air flow at different rotor speeds

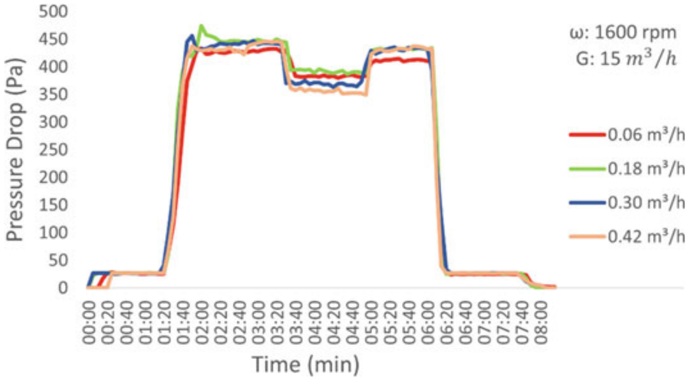

Fig. 3 Difference in air side pressure drop at uniform rate of air flow and rotor speed at different rates of water flow

Figure 4 exhibits the effect of varying rates of air flow on the air side pressure drop at constant rate of water flow at 0.18 m^3/h and 2000 rpm rotor speed. It was observed from Fig. 4 that as rate of air flow was increasing, pressure drop was also increased in case of dry bed. This effect was also observed in many previous studies. As the water flow was turned on, a drop in pressure was observed for both the rates of air flow. The reason behind this observation was that the path length of the air in a wet bed is shorter as compared to a dry bed. Also, at high rotor speed, the water holdup inside the packing reduces suggesting that the pressure drop is highly dependent on the rate of air flow.

Figure 5 showcases the common air side pressure drop behaviour observed at various operating conditions. These conditions are as follows: 1–2: stationary bed (dry); 3–4: rotating bed (dry); 5–6: rotating bed (irrigated); 7–8: rotating bed (wet); and 9–10: stationary bed (wet). The pressure drop at Point 1 was observed when

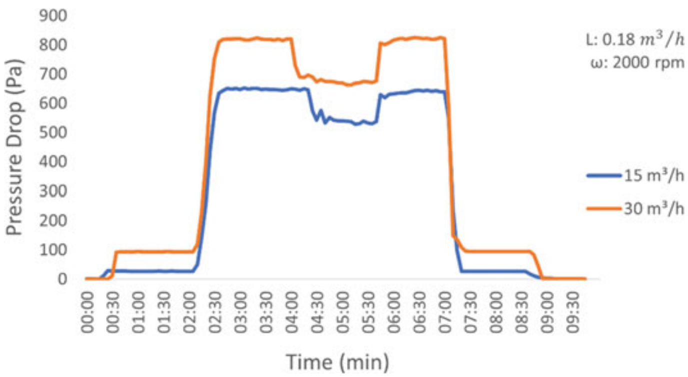

Fig. 4 Difference in air side pressure drop at uniform rate of water flow and rotor speed at different rates of air flow

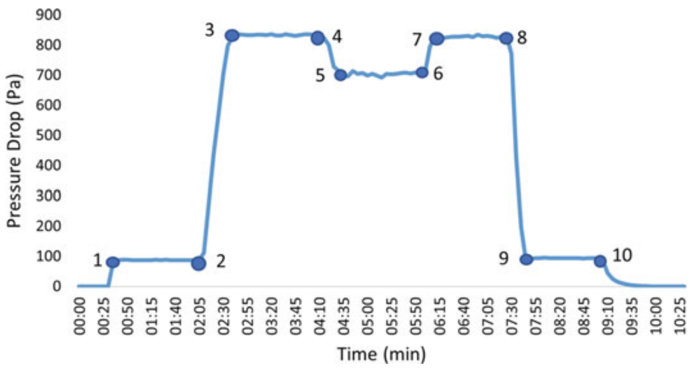

Fig. 5 Air side pressure drop trends at different operating conditions observed in the current experiment

the air flow was turned on. The rotor was turned on at Point 2, and a huge drop in pressure was observed. At Point 4, water flow was turned on and a decrease in pressure drop could be seen as it acts like a lubricant against the drag offered by the air flow. Since the water occupied the space inside the packing, less space was left for the air to occupy. This led to decrease in the drag that the air offered, and there was decrease in pressure drop due to friction, affecting the total pressure drop. The water was coming out of the packing in different flow patterns as reported in previous studies. The flow patterns were dependent on the rotor speed. When the water flow was turned off at Point 6, a rise in pressure drop was again observed. The rotor was turned off at Point 8, and subsequently, the air flow was also turned off at Point 10. All the changes in the operating conditions were done on an average interval of 2 minutes to obtain stable readings.

From all the sets of experiments conducted, the maximum reduction in pressure drop was examined. At the operating condition of 30 m^3/h of air flow rate, 0.42 m^3/h of water flow rate and 2000 rpm rotor speed, about 18.25% of reduction in pressure drop was detected between the irrigated bed and dry bed.

The results obtained from this experimental study can further be used for the optimization of the operating parameters to achieve better performance and application in other industries like thermal power plants.

5 Conclusions

This experimental study investigates the effect of the rate of water flow on the pressure drop characteristics of a counter-current flow RPB. The results showed that the drop in pressure in case of a dry bed is highly dependent on rate of air flow and rotor speed and it increased with rate of air flow and rotor speed.

The results of pressure drop in case of wet bed showed that the air side pressure drop was less than that of dry bed as centrifugal pressure decreases in wet bed. The pressure drop decrease was almost similar for all the rates of water flow.

The operating parameters can be put in following order based on their effect on the air side pressure drop across RPB: rate of gas flow > rotor speed > rate of liquid flow.

In contrast, it was found in the current experimental study that at a particular operating condition where the rate of air flow was 30 m^3/h, rate of water flow was 0.42 m^3/h, and rotor speed was 2000 rpm, as the water flow was turned on, there was a decrease of 18.25% in air side pressure drop of dry bed. It was the maximum reduction in pressure drop that was examined in this experimental study.

References

1. Ramshaw C (1983) HIGEE-an example of process intensification. Chem Eng 389:13
2. Ramshaw C (1983) HIGEE Distillation—an example of process intensification. Chem Eng 13–14
3. Kelleher T, Fair JR (1996) Distillation studies in a high-gravity contactor. Ind Eng Chem Res 35:4646–4655
4. Sun BC, Wang XM, Chen JM, Chu GW, Chen JF, Shao L (2011) Synthesis of nano-$CaCO_3$ by simultaneous absorption of CO_2 and NH_3 into $CaCl_2$ solution in a rotating packed bed. Chem Eng J 168:731
5. Lin CC, Ho TJ, Liu WT (2002) Distillation in a rotating packed bed. Ind Eng Chem 35:1298–1304
6. Lin CC, Su YR (2008) Performance of rotating packed beds in removing ozone from gaseous streams. Sep Purif Technol 61:311
7. Shao L, Chen JF (2005) Synthesis and application of nanoparticles by a high gravity method. China Particuol 3:134
8. Burns JR, Ramshaw C (1996) Process intensification: visual study of liquid maldistribution in rotating packed beds. Chem Eng Sci 51:1347
9. Guo F, Zheng C, Guo K, Feng Y, Gardner NC (1997) Hydrodynamics and mass transfer in cross flow rotating packed bed. Chem Eng Sci 52:3853–3859
10. Murthy DS (2020) Analysis and optimization of thermal characteristics in a rotating packed bed. Appl Thermal Eng 165. https://doi.org/10.1016/j.applthermaleng.2019.114533
11. Kumar S, Kumar S, Murthy DS (2021) Insights into thermal transactions of a novel rotating packed bed. J Thermal Sci Eng Appl. https://doi.org/10.1115/1.4050836
12. Kevyani M, Gardener NC (1989) Operating characteristics of rotating beds. Chem Eng Prog 85:48
13. Kumar MP, Rao DP (1990) Studies on a high-gravity gas-liquid contactor. Ind Eng Chem Res 29:917–920
14. Singh SP, Wilson JH, Counce RM, Villiers-Fisher JF, Jenningst HL (1992) Removal of volatile organic compounds from groundwater using a rotary air stripper. Ind Eng Chem Res 31:574–580
15. Zheng C, Guo K, Feng Y, Yang C (2000) Pressure drop of centripetal gas flow through rotating beds. Ind Eng Chem Res 2000(39):829–834
16. Liu HS, Kin CC, Wu SC, Hsu HW (1996) Characteristics of a rotating packed bed. Ind Eng Chem Res 35:1298–1304
17. Liu Y, Gu D, Xu C, Qi G, Jiao W (2015) Mass transfer characteristics in a rotating packed bed with split packing. CN J Chem Eng 23:868–872

18. Wang H, Qi GS, Liu YZ, Zhu ZW, Tian JX, Fu J (2014) Characteristic of gas pressure drop of a countercurrent flow rotating packed bed
19. Hendry JR, Lee JGM, Attidekou PS (2020) Pressure drop and flooding in rotating packed beds. Chem Eng Process 151(2020):107908
20. Munjal S, Dudukovic MP, Ramachandran P (1989) Mass-transfer in rotating packed beds-I. Development of air-liquid and liquid-solid mass-transfer correlations. Chem Eng Sci 44(10):2245–2256
21. Tung HH, Mah RSH (1985) Modeling liquid mass-transfer in higee separation process. Chem Eng Commun 39(1–6):147–153
22. Yang YC, Xiang Y, Chu GW, Zou HK, Luo Y, Arowo M, Chen JF (2015) A noninvasive X-ray technique for determination of liquid holdup in a rotating packed bed. Chem Eng Sci 138:244–255
23. Chen YH, Chang CY, Su WL, Chen CC, Chiu CY, Yu YH, Chiang PC, Chiang SIM (2004) Modeling ozone contacting process in a rotating packed bed. Indus Eng Chem Res 43(1):228–236
24. Moffat RJ (1982) Contributions to the theory of single-sample uncertainty analysis. ASME J Fluids Eng 104(2):250–258

Energy Analysis of Low GWP Refrigerant Replacement to HFC 410A in Split Air Conditioner

Punit Mishra, Shubham Soni, and Govind Maheshwari

1 Introduction

In response to the ever-increasing trend of energy consumption and concerns about environmental protection, researchers all over the world have been working on new refrigerants that can improve refrigeration system performance while also meeting the criteria of zero ozone depletion potential (ODP) and low global warming potential (GWP) [1, 2]. R410A is a frequently utilized refrigerant in air conditioning systems around the world since it has 0% ODP. R410A is a nearly azeotropic combination of R32/R125 (50/50%) with a temperature glide of just 0.1 °C at atmospheric pressure. It is not only chemically stable, but it is also low in toxicity, making it ideal for air conditioning. In response to concerns regarding R22's negative influence on ozone depletion, an environmental and thermodynamic investigation was conducted [3]. R410A was meant to replace R22 because of its greater heat removal capability and lower global warming potential. R410A can dissipate heat more effectively along with higher coefficient of performance (COP) than R22. As a result, it is suitable for refrigeration and air conditioning systems that are not as large [4]. The disadvantage of R410A is that it has a greater operating pressure and a high GWP value of 1924, making it an unfavourable option that does not fit with the objectives of the regulations [5]. Now, researchers are looking for R410A alternatives with low GWP values and great energy efficiency, as well as criteria that are environmentally benign. Devecioğlu [6] theoretically examined different R410A alternatives, and it was discovered that R446A and R452B could be possible R410A substitutes in air conditioning systems. When using R446A in refrigerated mode, the energy usage is decreased. Heredia-Aricapa et al. [7] look at eight different refrigerants to see if they

P. Mishra (✉) · S. Soni · G. Maheshwari
Department of Mechanical Engineering, Institute of Engineering and Technology, Devi Ahilya Vishwavidyalaya, Indore, India
e-mail: enggpunit@gmail.com

D. Sharma and S. Roy (eds.), *Emerging Trends in Energy Conversion and Thermo-Fluid Systems*, Lecture Notes in Mechanical Engineering,
https://doi.org/10.1007/978-981-19-3410-0_20

can discover a replacement for R410A. R32 was found to be a suitable substitute for R410A among the registered mixes.

R452B offers cooling characteristics and coefficient of performance capabilities that are similar to R410A. With nearly comparable operating pressures, no changes to the system's architecture are required [8]. With R452B and R447B, simulations of a home reversible heat pump were conducted under 35 °C environmental conditions. In comparison to R410A, a very comparable trend in cooling efficiency and capacity was observed. In comparison to R410A, a 3 to 4% increase in COP was reported at temperatures over 35 °C [9]. When R452B was operated for a domestic cooling system with CFD modelling, the volume portion of the refrigerant was found to be less than 4%, indicating that there is no risk of flammability [10]. With R452B, the same type of leak investigation was performed on a 4 t cooling unit, and the conclusion was that no plausible source for potentially flammable occurrences was found [11].

Pardo et al. [12] investigated the low GWP refrigerants as HPR2A, R447A, R454B, R459A and R32 as drop-in replacements for R410A. The study indicated that a blend of HFC/HFO had no trouble replacing R410A, with a few exceptions in the range of $\pm$ 10%. R454B and R459A were also the most successful. McLinden et al. [13] conducted extensive research to show that all single-component refrigerants that may replace R410A in terms of performance are combustible. Non-flammable possibilities exist among low-volumetric-capacity fluids; however, their application would necessitate substantial redesign and result in a low COP. Blends, on the other hand, provide more options. As a result, multiple articles have reported R410A replacement mixes, with R32 being a prominent component in most of these studies [14–17]. In a theoretical study, R32 was offered as a replacement for R410A in variable refrigerant flow systems. The COP of the R32 system was found to be 5% and 6% higher in heating and cooling modes, respectively [18].

The present work emphasized on comparative energy analysis of five refrigerants based on vapour compression cycle applied on split air conditioner having capacity of 1 TR, in order to find an appropriate candidate to replace R410A.

2 Characteristic of R32, R447A, R447B, R452B and R454B

Table 1 shows the refrigerant content (in % of mass) of the refrigerants investigated. R32 is a pure fluid that belongs to the HFC refrigerant family. Because of its low GWP, it has been considered a viable alternative to R410A. When compared to R410A, it consumes less energy. R32, R125 and R1234ze are blended in R447A and R447B. According to the ASHRAE safety categorization, both refrigerants are mildly flammable. The R452B blend contains R32, R125 and R1234yf, with R32 being accepted as flammable and the other two being non-flammable, making the blend mildly flammable according to ASHRAE criteria. It has been classified as slightly flammable and performs well in high-temperature environments. It can be utilized with R410A systems with minor modifications. As with R410A, it has an

Table 1 Mixture composition of refrigerants

Refrigerant	Safety classification	Refrigerant composition (mass %)			
		R32	R125	R1234yf	R1234ze
R410	A1	50	50		
R32	A2	100			
R447	A2L	68	3.5		28.5
R447B	A2L	68	8		24
R452B	A2L	67	7	26	
R454B	A2L	68.9		31.1	

Table 2 Thermodynamic properties of studied refrigerants

Properties	R410A	R32	R447A	R447B	R452B	R454B[2]
Boiling point (K)	221.7	221.3	227.4	223.2	222.5	228.4
Critical temperature (K)	344.5	351.1	355.63	356.7	350.2	354.1
Critical pressure (kPa)	4901	5782	5416.8	5644.7	5220.1	5334
Liquid pressure (kPa)	1664.1	1696.4	1524.1	1548.9	1592.2	1591.9
Vapour pressure (kPa)	1658.8	1689.6	1367.1	1412.2	1543.6	1528.1
Liquid density (kg/m^3)	1057.8	960.4	1019.9	1020.23	992.82	979.43
Vapour density (kg/m^3)	66.27	47.55	44.27	46.17	52.63	51.36
Liquid enthalpy (kJ/kg)	241.33	245.9	247.46	246.81	248.07	242.49
Vapour enthalpy (kJ/kg)	427.41	516.5	480.3	477.12	467.44	464.1
Liquid entropy (kJ/kg-K)	1.21	1.16	1.23	1.23	1.23	1.15
Vapour entropy (kJ/kg-K)	1.83	2.06	2.01	2.00	1.97	1.89
GWP	1924	677	572	714	675	667

extremely low temperature glide. In both regular and high ambient settings, R454B performs admirably. It is a combination of R32 and R1234yf. It is non-toxic and mildly flammable, with a low temperature glide, and the system can be topped up after a leak, if any. It can also be utilized with the R410A system with minor modifications to the design. Table 2 lists some additional thermodynamic parameters for the refrigerants under investigation.

3 The Parameters and Method of Analysis

The investigation was performed on a single-stage vapour compression refrigeration system with a capacity of 1 TR that operates between evaporation temperatures (T_{evap}) of 4.5 °C and condenser temperatures (T_{cond}) of 40–60 °C in 4 °C increments. The layout diagram of the system and corresponding *p*–*h* diagram are shown in Figs. 1 and 2, respectively.

For the analysis of the system, the following assumptions were made:

- No pressure drop has been considered in the evaporator and condenser,
- Heat transfer to or from the compressor, expansion device and connecting tubes were ignored,
- Isenthalpic expansion process is considered in expansion valve,
- Kinetic and potential energy changes were ignored,
- The compressor's isentropic and volumetric efficiencies are both estimated to be 75% and 100%, respectively.

Fig. 1 Layout diagram of split air conditioning system

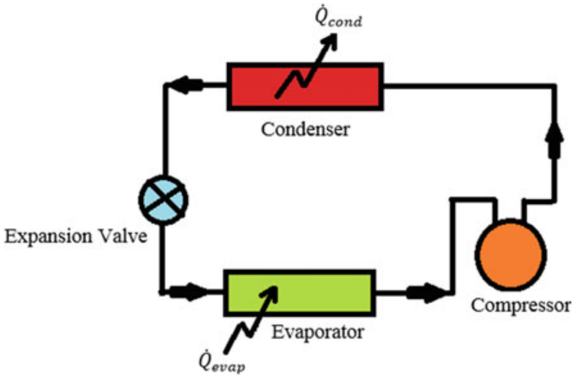

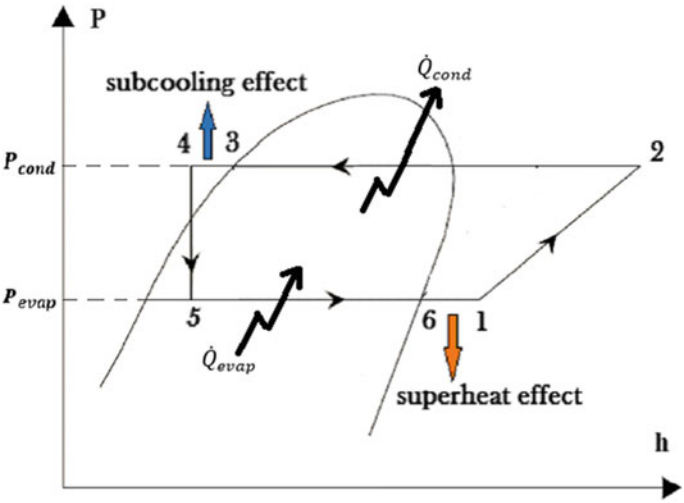

Fig. 2 Pressure versus enthalpy diagram [19]

- 3 °C subcooling in the condenser, 7 °C superheat in the evaporator and 4 °C superheat in the suction line

Heat absorbed by the refrigerant in evaporator $\left(\dot{Q}_{\text{evap}}\right)$ can be calculated using first law of thermodynamics as [6]:

$$\dot{Q}_{\text{evap}} = \dot{m}_{\text{ref}}\left(h_{\text{evap,out}} - h_{\text{evap,in}}\right) \tag{1}$$

where $\dot{m}_{\text{ref}}$ represents refrigerant mass flow rate in the system and $h_{\text{evap,out}}$ and $h_{\text{evap,in}}$ are the specific enthalpy of refrigerant (kJ kg^{-1}) at evaporator outlet and inlet, respectively.

The compressor's energy consumption ($\dot{W}_{\text{el}}$) to compress the refrigerant at condenser pressure can be calculated as follows:

$$\dot{W}_{\text{el}} = \dot{m}_{\text{ref}}\left(h_{\text{comp,out}} - h_{\text{comp,in}}\right) \tag{2}$$

Here, $h_{\text{comp,out}}$ and $h_{\text{comp,in}}$ are the specific enthalpy of refrigerant at compressor outlet and inlet, respectively.

The following expression can be used to compute the heat rejected by the refrigerant in the condenser ($\dot{Q}_{\text{cond}}$):

$$\dot{Q}_{\text{cond}} = \dot{m}_{\text{ref}}\left(h_{\text{cond,out}} - h_{\text{cond,in}}\right) \tag{3}$$

Here, $h_{\text{cond,out}}$ and $h_{\text{cond,in}}$ are the specific enthalpy of refrigerant at condenser outlet and inlet, respectively.

The COP of any refrigerator or air conditioner is the ratio of heat absorbed in the evaporator to work consumed in the compressor. Using Eqs. (1) and (2), we arrive at the following:

$$\text{COP} = \frac{\dot{Q}_{\text{evap}}}{\dot{W}_{\text{el}}} = \frac{\dot{m}_{\text{ref}}\left(h_{\text{evap,out}} - h_{\text{evap,in}}\right)}{\dot{m}_{\text{ref}}\left(h_{\text{comp,out}} - h_{\text{comp,in}}\right)}$$

$$\text{COP} = \frac{\left(h_{\text{evap,out}} - h_{\text{evap,in}}\right)}{\left(h_{\text{comp,out}} - h_{\text{comp,in}}\right)} \tag{4}$$

Equation (1) can be used to compute the mass flow rate of refrigerant ($\dot{m}_{\text{ref}}$) as:

$$\dot{m}_{\text{ref}} = \frac{\dot{Q}_{\text{evap}}}{\left(h_{\text{evap,out}} - h_{\text{evap,in}}\right)} \tag{5}$$

Theoretical piston displacement ($\dot{V}_{\text{P}}$) can be calculated as [6]:

$$\dot{V}_{\text{P}} = \dot{m}_{\text{ref}} \times v_{\text{comp,in}} \tag{6}$$

where $v_{\text{comp,in}}$ is the specific volume ($m^3\ kg^{-1}$) of the refrigerant entering in the compressor.

Volumetric capacity (kJ/m^3) can be calculated as:

$$\text{Volumertic Capacity} = \frac{\left(h_{\text{evap,out}} - h_{\text{evap,in}}\right)}{v_{\text{comp,in}}} \tag{7}$$

4 Result and Discussion

In this theoretical analysis of air conditioner having capacity of 1 TR using several low GWP refrigerants alternative to R410A with evaporator, temperature was taken as 4.5 °C whereas the condenser temperature is taken in the range of 40–60 °C in interval of 4 °C. Based upon the calculations using Genetron Properties 1.4 software and CRE 1.0 software, COP, power consumption, refrigerant mass flow rate, volumetric cooling capacity, compressor displacement, mean discharge temperature and pressure ratios are calculated and plotted against compressor temperature.

4.1 Electrical Energy Consumption Against Different Condensing Temperature

The electrical energy consumed by the refrigerants at different condensing temperature is shown in Fig. 3. It can be seen that all the studied refrigerants consume less power as compared to R410A but R447A consumes least power for producing given cooling capacity of 1TR. At 40 °C condensing temperature, the power consumed by R447A and R447B consumes 3.1 and 2.8% less power than the system using R410A. At higher condenser temperature, more saving in compressor work can be obtained, and at 60 °C, 8.5% less power is consumed. Air conditioners with refrigerant R447B and R454B are the other alternatives that consume 7.78 and 5.67% less power than R410A at 60 °C. R447A. At higher condensing temperature, more saving was obtained.

4.2 Variation in COP Against Different Condensing Temperature

Every researcher aspires to increase the system's COP as much as possible. Figure 4 shows that all of the selected refrigerants have a greater COP than R410A, which is thought to be replaced by the researched refrigerants, and here, R447A has highest

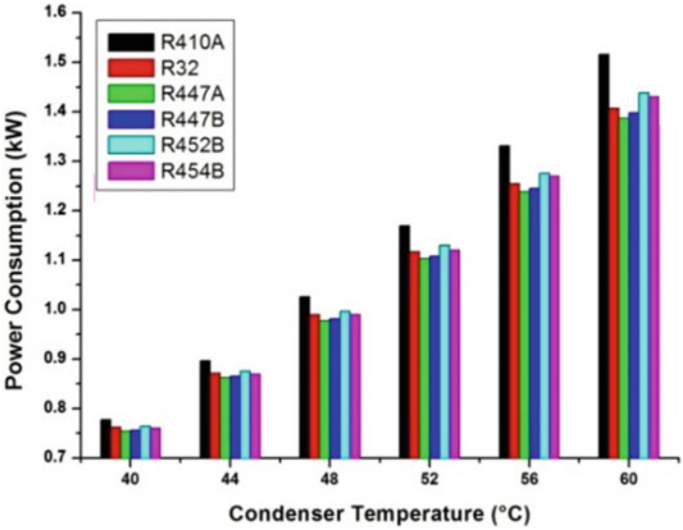

Fig. 3 Variation of power consumption with condenser temperature

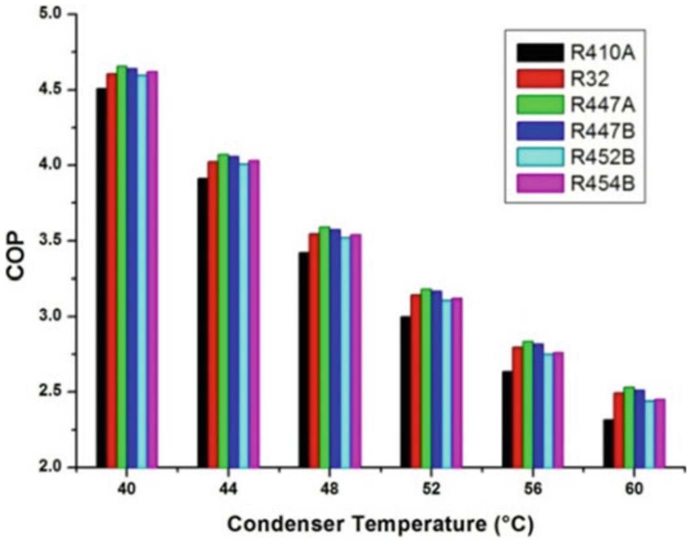

Fig. 4 Variation of COP with condenser temperature

COP. At 40 °C condensing temperature, R447A has a 3.24% higher COP than R410A and it increases to 9.24% at 60 °C of condenser temperature. At 60 °C, the percentage increase in COP for refrigerants R447B and R454B is 8.2% and 5.78%, respectively.

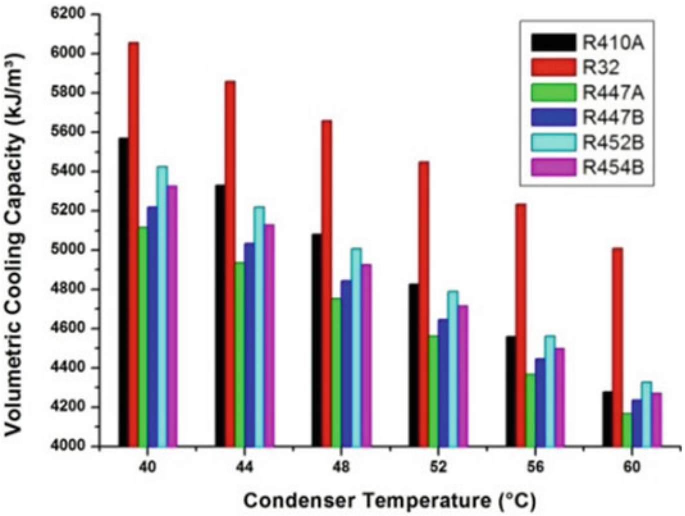

Fig. 5 Volumetric cooling capacity at different condenser temperature

4.3 Cooling Capacity of Different Refrigerants Against Condensing Temperature

The cooling capacity of R32 is found to be the highest of all the replacement options for R410A. Other refrigerants have lower cooling capacity than R410A at lower condensing temperatures, but when the condensing temperature rises, the cooling capacity of the system equipped with R454B and R452B approaches R410A. Figure 5 shows how this works.

4.4 Mass Flow Rate of Refrigerant Required Against Different Condensing Temperature

The volume of refrigerant that circulates in the evaporator has a significant impact on the cooling capacity. As the liquid density of refrigerating fluid falls, a significant decline in refrigerant quantity charged into the system has been noted. Figure 6 shows how varied refrigerant mass flow rates correspond to different condenser temperatures. When using R32 and operating at 40 °C condenser temperature, the refrigerant mass flow rate is reduced by 33.46%, resulting in the same cooling effect of 1 TR. When compared to an R410A system, a higher condensing temperature (60 °C) requires 38.18% less refrigerant. All of the other refrigerants studied in this study require fewer refrigerants than R410Asystem. The mass flow rates of R447A and

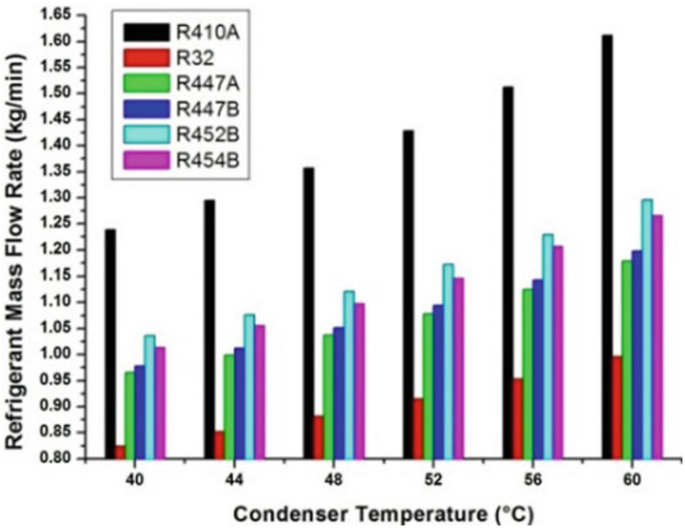

Fig. 6 Variation of refrigerant mass flow rate with different condenser temperature

R447B are relatively similar at low condensing temperatures. At higher condensing temperatures, however, there was an increase in the mass flow rate value.

4.5 Compressor Displacement Against Different Condensing Temperature

Compressor displacement is a key limitation since it represents the system's overall capacity. The volume displaced by the piston inside the cylinder per unit time in a reciprocating compressor is known as piston displacement, and it is the same as the compressor unit's capacity. Figure 7 shows that the R32 system requires 7.94% less compressor displacement than the R410 system. Compressor displacement is higher for all other refrigerants examined. At higher condensing temperature, R452B and R454B system shows significant reduction in compressor displacement and approaches R410A.

4.6 Compressor Discharge Temperature Against Different Condensing Temperature

It is essential to examine the compressor's reliability and longevity before putting a new refrigerant into any system. Lower discharge temperature from compressor is

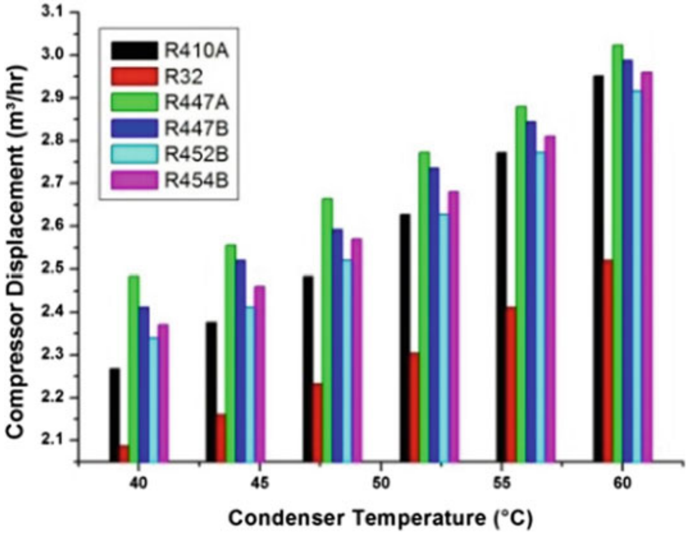

Fig. 7 Variation of compressor displacement with condenser temperature

advantageous as for as compressor durability and life duration are concerned. Figure 8 shows that for all of the proposed refrigerants, the mean discharge temperature at compressor discharge is higher. In comparison to R410, the refrigerants R452B and R454B have a 5–7% higher discharge temperature.

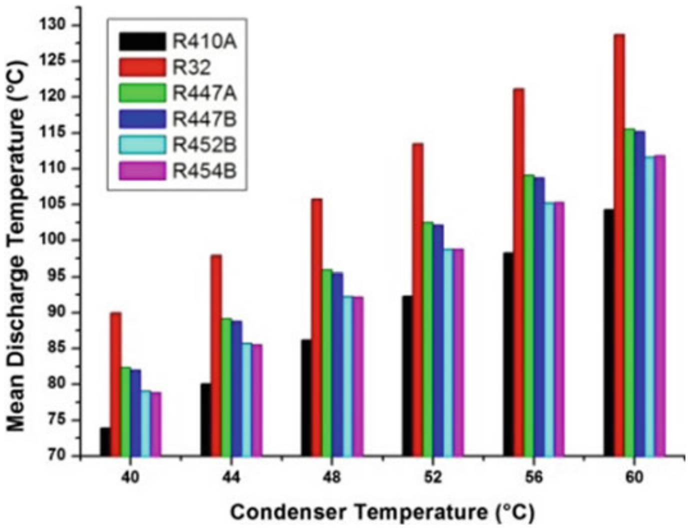

Fig. 8 Mean discharge temperature with different condenser temperature

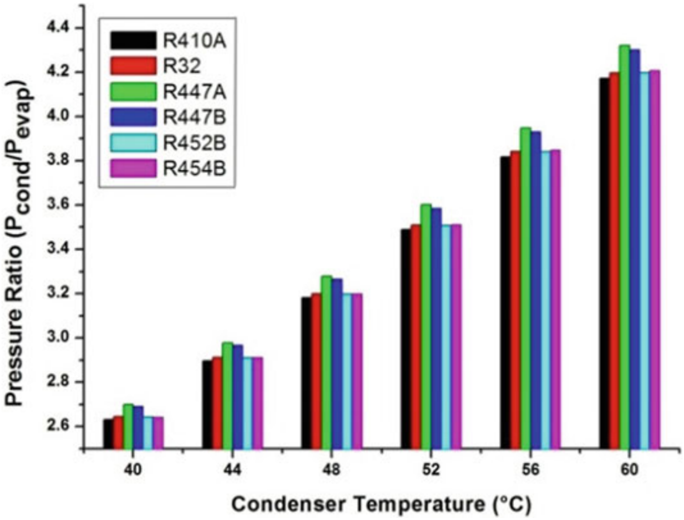

Fig. 9 Mean pressure ratio for different refrigerant systems with condenser temperature

4.7 Pressure Ratio Against Different Condensing Temperature

The pressure ratio is one of the most important factors that determines the volumetric efficiency of a compressor. Figure 9 shows that systems using R452B and R454B have nearly the same pressure ratio as systems using R410A; however, other refrigerants have a greater pressure ratio, which affects the compressor's volumetric efficiency. It is also worth noting that the R410A system operates at a pressure of 9.18 bar at a 4.5 °C evaporator temperature, whereas the R454A and R454C systems operate at pressures of 6.24 and 5.2 bar at the same 4.5 °C evaporator temperature, respectively, which are 32 and 43.35% lower than the R410A system's pressure. This large pressure drop results in material savings in the system's construction.

5 Conclusion

The performance of R32, R447A, R447B, R452B and R454B in an air conditioning device was studied theoretically in order to identify an alternative refrigerant to R410A. The GWP values of all the replacement refrigerants are less than 750, which complies with EU regulations [20]. Following results were obtained during the research:

- R447A refrigerant has the highest COP and least energy consumption among all the refrigerants investigated as R410A replacements. R447B and R454B refrigerants could be another set of refrigerants that could be viewed as a viable alternative to R410A due to their greater COP than R410A.
- R32 requires the lowest mass flow rate and has the greatest cooling capacity, although R447A and R447B may be the second choice in terms of refrigerant flow rate in the system.
- R32 has the highest volumetric cooling capacity of all the refrigerants studied. At greater condensing temperatures, R452B has a better cooling capacity than R410A.
- R32 has the smallest compressor displacement, resulting in a small device. R452B and R454B, on the other hand, could be the following options.
- R410A has the lowest mean discharge temperature, while R452B and R454B could be alternate options with temperature rises of roughly 5–7% less than R410A.
- Pressure ratio is almost identical for R454B, R452B and R32.

Performance parameters	Refrigerant				
	R32	R447A	R447B	R452B	R454B
COP					
Power consumption (kW)					
Mass flow rate (kg/min)					
Volumetric cooling capacity (kJ/m³)					
Compressor displacement (m³/h)					
Mean discharge temperature (°C)					
Pressure ratio					

Most preferred for given criteria
Next choice for given criteria

References

1. Bolaji BO, Huan Z (2013) Ozone depletion and global warming: case for the use of natural refrigerant—a review. Renew Sustain Energy Rev 18:49–54
2. Yuan Q, Ma Y, Liu C, Dai B, Yan Q (2011) Thermodynamic perfectibility based analysis of energy-efficiency standards for air conditioning products in China. Energy Build 43(12):3627–3634
3. de Rossi F, Sasso M (1995) An environmental and thermodynamic analysis to select R22 alternative working fluids. Int J Ambient Energy 16(2):76–82

4. Bortolini M, Gamberi M, Gamberini R, Graziani A, Lolli F, Regattieri A (2015) Retrofitting of R404a commercial refrigeration systems using R410a and R407f refrigerants. Int J Refrig 55:142–152
5. Zhang W, Yang Z, Zhang X, Lv D, Jiang N (2016) Experimental research on the explosion characteristics in the indoor and outdoor units of a split air conditioner using the R290 refrigerant. Int J Refrig 67
6. Devecioğlu AG (2017) Seasonal performance assessment of refrigerants with low GWP as substitutes for R410A in heat pump air conditioning devices. Appl Therm Eng 125:401–411
7. Heredia- Y, Belman JM, Mota-Babiloni A, Serrano-Arellano J, García-Pabón JJ (2020) Overview of low GWP mixtures for the replacement of HFC refrigerants: R134a, R404A and R410A. Int J Refrig 111:113–123
8. Azzolin M, Berto A, Bortolin S, Moro L, Del Col D (2019) Condensation of ternary low GWP zeotropic mixtures inside channels. Int J Refrig 103:77–90
9. Sethi A, Yana Motta S (2016) Low GWP refrigerants for air conditioning and chiller applications. In: International refrigeration and air conditioning conference, 2016, p 1821
10. Guernsey M, Bargach Y, Abdelaziz O, Shrestha S, Shen B, Elatar A, Linkous R, Goetzler W, Bargach Y (2016) Alternative refrigerant evaluation for high-ambient-temperature environments: R-22 and R-410A alternatives for rooftop air conditioners. ORNL/TM-2016/513
11. Kujak S, Schultz K (2016) Compositional fractionation studies of R410A alternative R452B or DR55 and their impact on flammability behavior and safety implications. In: International refrigeration and air conditioning conference, 2016, p 1614
12. Pardo P, Mondot M (2018) Experimental evaluation of R410A, R407C and R134a alternative refrigerants in residential heat pumps. In: International refrigeration and air conditioning conference, p 1991
13. McLinden MO, Brown JS, Brignoli R, Kazakov AF, Domanski PA (2017) Limited options for low-global-warming-potential refrigerants. Nat Commun 8(1):14476
14. Xu X, Hwang Y, Radermacher R (2013) Performance comparison of R410A and R32 in vapor injection cycles. Int J Refrig 36:892–903
15. Zhuang X, Liang R (2011) Study of R32 refrigerant for residential air conditioning applications. In: International congress of refrigeration, 2011, pp 1–8
16. In S, Cho K, Lim B, Kim H, Youn B (2014) Performance test of residential heat pump after partial optimization using low GWP refrigerants. Appl Therm Eng 72:315–322
17. Piao CC, Taira S, Moriwaki M, Tanimoto K, Mochizuki K, Nakai A (2012) Alternatives to high GWP HFC refrigerants: residential and small commercial unitary equipment. In: ASHRAE refrigeration conference, pp 1–10
18. Yıldırım C, Özkan DB, Onan C (2018) Theoretical study of R32 to replace R410A in variable refrigerant flow systems. Int J Ambient Energy 39(1):87–92
19. Lateef Tarish A, Talib Hamzah M, Assad Jwad W (2020) Thermal and exergy analysis of optimal performance and refrigerant for an air conditioner split unit under different Iraq climatic conditions. Therm Sci Eng Prog 19:100595
20. Medina AMB (2014) Regulation (EU) No. 517/2014 of the European parliament and of the council April 16, 2014 on fluorinated greenhouse gases and Regulation (EC) No. 842/2006. Actual Jurídica Ambient L 150/195(37):46–46

Integration of Nanofluids in Microchannel Heat Sinks for Heat Transfer Enhancement

Vikram Meena and Amit Arora

Nomenclature

$\mathrm{Nu}_{\mathrm{nf}}$	Nusselt number of nanofluid
m_{nf}	Mass flow rate of nanofluid
T_{s}	Base temperature of the heat sink
T_{nf}	Bulk mean temperature of the nanofluid
A_{ch}	Cross-sectional area of each flow channel
P_{ch}	Perimeter of each flow channel
μ_{nf}	Viscosity of nanofluid
μ_{f}	Viscosity of base fluid
ρ_{nf}	Density of nanofluid
$C_{\mathrm{p,nf}}$	Specific heat of nanofluid
K_{f}	Thermal conductivity of base fluid
K_{np}	Thermal conductivity of nanoparticle
β_{f}	Thermal expansion coefficient of base fluid
β_{np}	Thermal expansion coefficient of nanoparticle
$\in$	Porosity
D_{P}	Equivalent diameter of porous media.

V. Meena (✉) · A. Arora
Department of Mechanical Engineering, Malaviya National Institute of Technology Jaipur, Jaipur, Rajasthan 302017, India
e-mail: vikrammeena332@gmail.com

D. Sharma and S. Roy (eds.), *Emerging Trends in Energy Conversion and Thermo-Fluid Systems*, Lecture Notes in Mechanical Engineering,
https://doi.org/10.1007/978-981-19-3410-0_21

1 Introduction

1.1 Background

Miniaturization in electronic industries is leading the development of more compact and efficient electronic devices. The reduction in size of such devices requires the improved cooling techniques to keep the base temperature within the safe operating range as the compactness in shape, size, and weight resulted in increasing the power density and speed [1, 2]. Heat sinks are the devices used to dissipate the heat and maintain the base temperature under the threshold limit. The removal of heat plays a vital role in improving the thermal performance of electronic device. The conventional technique uses air as the coolant but it was found to be insufficient with compact and high-speed processors, because the air has low amount of heat capacity and thermal conductivity. Therefore, the researchers were attracted to replace the air with liquid-based heat sinks due to their greater thermal properties [3–5].

In the last two decades, the research was divided in two parts. One is designing and modifying the geometry of heat sinks to increase the contact area for heat dissipation. Another is improving the thermal and physical properties of liquids. Back in 1981, Tuckerman and Pease [6] used the single-layer microchannel heat sinks (MCHS) in their study. They observed that the decrease in the hydraulic diameter of microchannel improved the transfer of heat with MCHS. Abdollahi et al. [4] carried out a simulation analyses to study the heat transfer and the flow characteristics of alumina–water nanofluid in an interrupted MCHS using diamond and ellipse ribs inside the transverse micro-chambers. The results revealed that the ellipse ribs perform better than the microchannel with no ribs or diamond ribs. Pourfarzad et al. [7] experimentally examined the thermo-hydraulic characteristic of Al_2O_3–H_2O nanofluid in a porous miniature heat sink. The results revealed that the Nusselt number (Nu) and the coefficient of convective heat transfer (h) enhanced with the increase in Reynolds number (Re).

Various researchers have studied the incorporation of fins [8–11], microchannels [3, 8, 12, 13], surface texturing, and porous structure [7, 14, 15] to improve the geometry of the heat sinks. Moreover, some of them have used the oils, phase-change materials, and nanofluids [16–19]. The use of nanofluids was observed to be way better than simple fluids as it attains higher thermal characteristics. Moreover, the hydrodynamic and thermal properties of the nanofluid also have a significant impact on the system performance as the addition of nanoparticle with base fluids had been practiced by various authors. Therefore, the effect of both heat sink configuration and nanofluid had been reviewed in this study.

1.2 Nanofluids

Nanofluids are a solution of materials having a size of less than 100 nm with some base fluid. The nanomaterials can be metals, ceramics, polymers, or composites. The additions of nanoparticles enhanced the chemical, thermal, physical, and mechanical properties of the compound. The most commonly used base fluids are water, oils, ethylene glycol, silicone liquids, aliphatic liquids, and fluorocarbons to incorporate with nanoparticles [20]. The preparation of nanofluid is a tough task to be performed as the synthesis of the nanoparticles with base fluid is tedious. The researchers had majorly followed two methods for the preparation which are titled as: (a) one-step and (b) two-step. In first method, the nanoparticles are directly prepared and mixed with a base fluid without storing, drying, transporting, and dispersing of the nanoparticles. The drawback with this method is that the prepared nanofluid contains residual reactants due to partial stabilizations. Whereas the two-step method is most commonly used and found to be cost effective. In this process, the nanoparticles are stored and mixed properly with the base fluid using ultra-sonication and stirring methods (Fig. 1).

2 Thermal and Hydraulic Performance of Nanofluid-Based Heat sinks

To calculate the thermo-hydraulic performance of the heat sinks working with nanofluid, the following equation can be used [11]

The amount of heat transferred with the help of nanofluid

$$Q_{\mathrm{nf}} = m_{\mathrm{nf}} C_{\mathrm{P,nf}} (T_{\mathrm{out}} - T_{\mathrm{in}})_{\mathrm{nf}} \tag{1}$$

The Nusselt numbers (Nu) and the heat transfer coefficient (h) of nanofluids can be found as

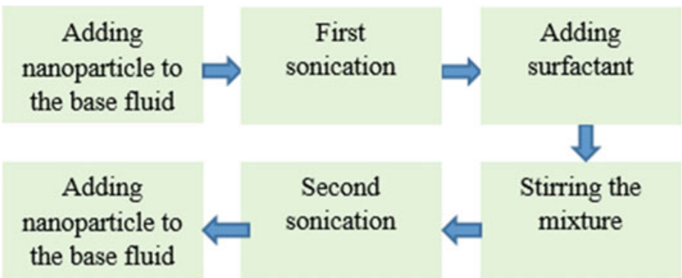

Fig. 1 Two-step method of nanofluid preparation

$$\mathrm{Nu}_{\mathrm{nf}} = \frac{h_{\mathrm{nf}} D_{\mathrm{h}}}{k_{\mathrm{nf}}} \tag{2}$$

$$h_{\mathrm{nf}} = \frac{Q_{\mathrm{nf}}}{A_{\mathrm{s}}(T_{\mathrm{s}} - T_{\mathrm{nf}})} \tag{3}$$

The bulk mean temperature of the nanofluids is calculated by

$$T_{\mathrm{nf}} = \frac{(T_{\mathrm{in}} + T_{\mathrm{out}})_{\mathrm{nf}}}{2} \tag{4}$$

Similarly, the hydraulic diameter (D_{H}) and the Reynolds number $\left(\mathrm{Re}_{D_{\mathrm{h}}}\right)$ can be computed from the following relations,

$$D_{\mathrm{H}} = \frac{4A_{\mathrm{ch}}}{P_{\mathrm{ch}}} \tag{5}$$

$$\mathrm{Re}_{D_{\mathrm{h}}} = \frac{\rho_{\mathrm{nf}} u_{\mathrm{ch}} D_{\mathrm{H}}}{\mu_{\mathrm{nf}}} \tag{6}$$

The friction factor (f) and pumping power (PP) are also used to measure the hydrodynamic performance of the heat sinks, which can be calculated as follows [16, 21]:

$$\text{Pumping Power} = Q(P_{\mathrm{out}} - P_{\mathrm{in}}) \tag{7}$$

$$\text{friction factor } (f) = \frac{2\Delta p D_{\mathrm{h}}}{\rho_{\mathrm{nf}} L_{\mathrm{ch}} u_{\mathrm{m}}^2} \tag{8}$$

The thermo-physical properties of the nanofluid required in Eqs. (1)–(8) can be calculated and defined as per the empirical and mathematical relations provided by various authors.

Density and the specific heat of a nanofluid can be calculated in accordance to the base fluid as,

$$\text{Desnity } (\rho_{\mathrm{nf}}) = (1 - \varphi)\rho_{\mathrm{bf}} + \varphi\rho_{\mathrm{p}} \tag{9}$$

$$\text{Specific Heat}\left(C_{\mathrm{p,nf}}\right) = \frac{(1-\varphi)(\rho c\mathrm{p}\ )\mathrm{bf} + \varphi(\rho \mathrm{cp})\mathrm{np}}{\rho_{\mathrm{nf}}} \tag{10}$$

The values of kinematic viscosity of the nanofluid can be found as,

$$\text{Viscosity } (\mu_{\mathrm{nf}}) = (1 + 2.5\phi)\mu_{\mathrm{bf}} \tag{11}$$

While the effective viscosity for a limited range of volume fraction ($0.001 < \phi < 0.071$) was measured as [4]

$$\mu_{\text{eff}} = \mu_{\text{f}} \times \frac{1}{\left(1 - 34.87\left(d_{\text{np}}/d_{\text{f}}\right)^{-0.3} \times \phi^{1.03}\right)} \tag{12}$$

The values of dynamic viscosity of ethylene glycol–water nanofluid is [9]

$$\mu_{\text{nf}}/\mu_{\text{bf}} = A_1 e^{(A_2\varphi)} \tag{13}$$

The values of thermal conductivity of considered nanofluid can be calculated as,

$$k_{\text{nf}} = k_{\text{bf}}\left[0.981 + 0.00114 \times T(^\circ\text{C}) + 30.661 \times \varphi\right] \tag{14}$$

whereas the effective thermal conductivity for a range of volume fraction can also be calculated by ($0.002 < \phi < 0.09$) [4]

Thermal expansion coefficient (β) of a nanofluid can be calculated by the equation [17]:

$$\beta_{\text{nf}} = (1 - \varphi)\beta_{\text{f}} + \varphi\beta_{\text{np}} \tag{15}$$

3 Effect of Using Different Shape on the Overall Performance of Microchannel Heat Sink

The overall performance of a heat sink depends upon different configurations and shapes of the heat sink along with the type of working fluid used in the application. The following section will discuss about the effect of different configurations which were practiced and studied by various researchers around the world and also present the effect of nanofluids on the heat sink performance.

3.1 Effect of Different Design and Configuration of Heat Sinks

Use of Different Flow Channel Shapes

The effect of using different flow microchannel shapes, viz. triangular, rectangle, trapezoidal sinusoidal, etc. had been studied by many researchers. Ghasemi et al. [12] studied the triangular shape flow channel for the heat sink with water as coolant using FLUENT software package. The results revealed that the system performed efficiently at higher Reynolds number. Shi et al. [3] numerically investigated the effect of Re and geometrical factors on the thermo-hydraulic characteristics of a rectangular microchannel using nanofluid. The results show that the heat transfer coefficient enhanced with the design variable (ratio of microchannel width to wall thickness) and aspect ratio (ratio of the microchannel height to width). The heat transfer coefficient for the aspect ratio of 2, 3, and 4 was increased by 4.49%, 10.03%, and 18.34%, respectively, as depicted in Fig. 2a–b.

Figure 2 shows the design of some commonly studied microchannel heat sinks by various authors. In an another study, Dehghan et al. [22] considered the trapezoidal type heat sink using Al_2O_3–water nanofluid. The authors observed that advancement in geometrical shape (i.e., convergent of the flow passages) provided 2.35 times more heat transfer coefficient (h) in comparison to straight channels. From the above literature, it can be seen that the flow channel had a significant influence on the heat sink performance and cannot be neglected while selecting the MCHS (Fig. 3).

Use of Different Fin Type

The performance of MCHS can also be enhanced by using a pin fin in the flow channel. Many researchers introduced the fin shape inside the channel to improve the thermal characteristics of MCHS by increasing surface contact area. Some of the pin fin shapes have been represented in Fig. 4. Ambreen et al. [9] numerically examined the effect of different pin fins on the thermo-hydraulic performance of nanofluid (TiO_2)-cooled micro pin–fin heat sink. It was concluded that the base temperature using circular fins and hexagons was almost 3 and 1.5 °C higher than the circular fin configuration. In the similar trend, the circular fins had higher hydraulic and thermal performance than the other two configurations.

Duangthongsuk et al. [11] experimentally investigated the thermo-hydraulic characteristics of circular and square fin miniature heat sink. Silica oxide (SiO_2) nanoparticles were dispersed into water with different nanoparticle concentrations. The heat transfer performance was enhanced as the turbulent intensity was high near the pin fins. The miniature circular pin–fin type heat sink performed better with about 6–9% higher heat transfer compared to the miniature square pin–fin (Fig. 5).

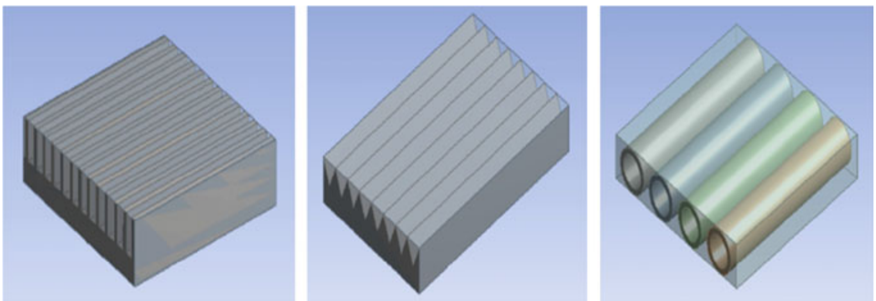

(a) (b) (c)

Fig. 2 Different shapes of microchannel heat sinks **a** rectangular, **b** triangular, **c** circular

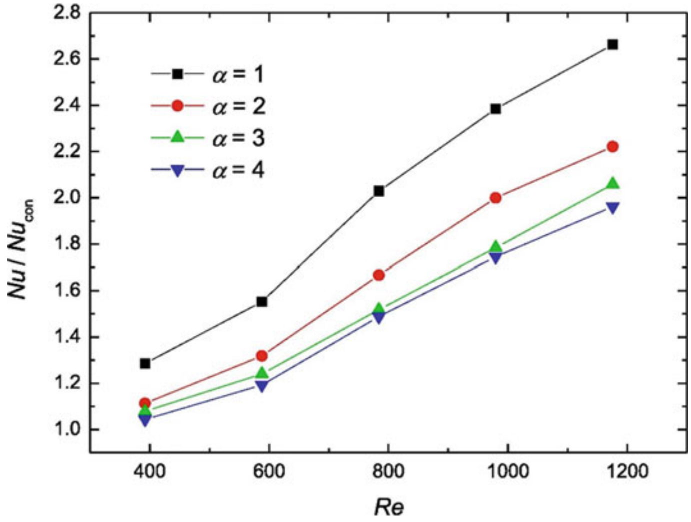

Fig. 3 Effect of Re values on Nu ratio [3]

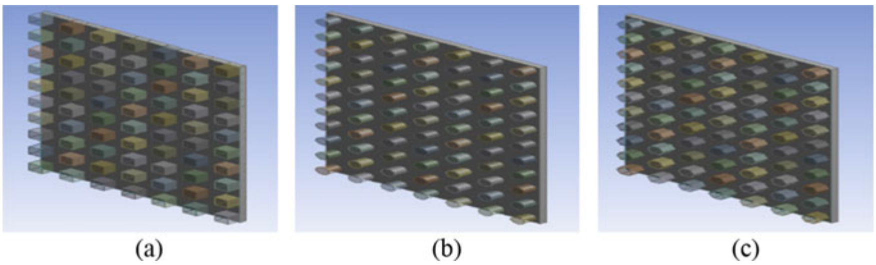

Fig. 4 Different shape of pin fin **a** rectangular; **b** circular; **c** hexagonal fins; **d** solid domain with a fluid domain

Use of Ribs in Microchannel Heat Sink

Various authors introduced ribs inside the passage of microchannel as the incorporation ribs enhance the heat dissipation rate from the device by increasing the contact area and turbulency in flow (Fig. 6).

Abdollahi et al. [4] examined the heat transfer characteristics of an interrupted MCHS. The results show that the ellipse ribs outperform the rectangular and diamond shape ribs as it had higher values of Nusselt number and PEC with lower amount of friction factor. Ghale et al. [23] numerically observed the effect of different rib shape and number inside the microchannel. It was concluded that the introduction of ribs has negative influence on hydraulic performance and positive effect on thermal performance as increasing the number of ribs from 3 to 9 as shown in Fig. 7.

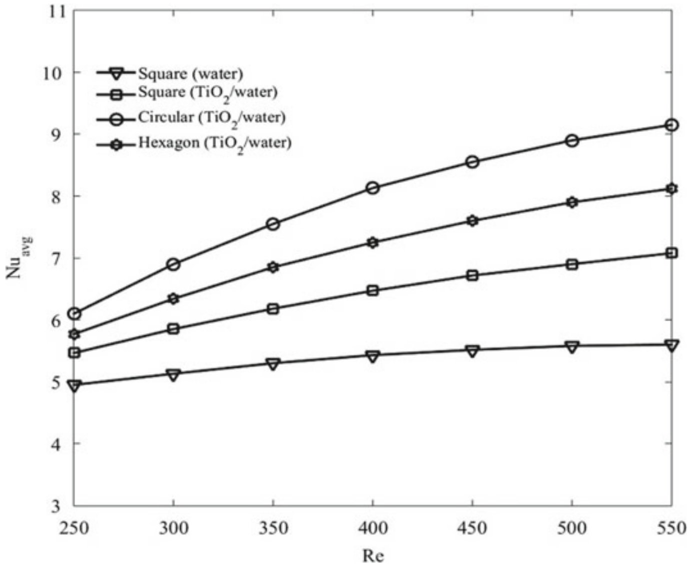

Fig. 5 Change in performance average Nu with Re for various heat sinks [9]

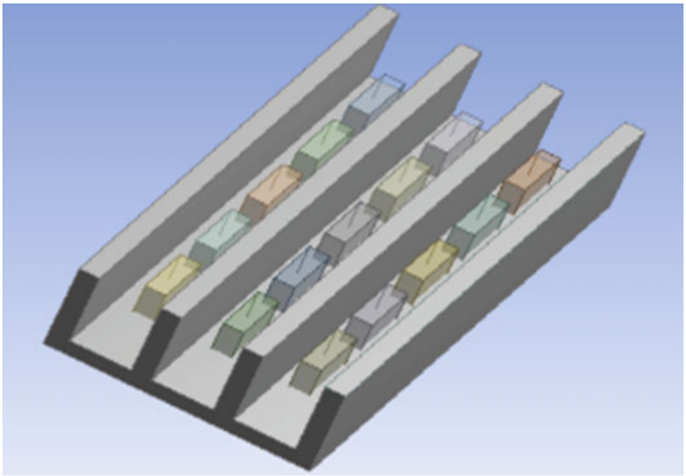

Fig. 6 Schematic and computational domain of ribbed (rectangular) microchannel

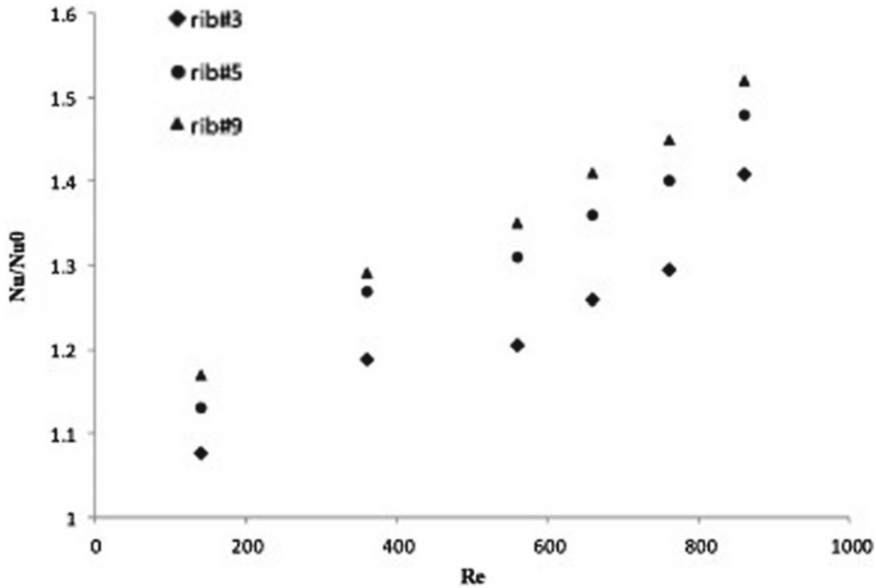

Fig. 7 Change in performance of Nu with Re for various ribs [23]

3.2 *Effect of Nanofluids*

Nanofluids are used to enhance the overall performance of the heat sink by improving the heat dissipation rate and reducing the pumping power as it has better thermo-physical characteristics. The most commonly studied nanomaterials are Al_2O_3, TiO_2, and Cu with water as a base fluid.

The authors observed that the high concentration of nanoparticles increased the Brownian motion in the nanofluid. The researchers compared the thermal performance of alumina–H_2O and diamond–H_2O nanofluid with pure water. They reported that both the nanofluids improved the heat transfer about 21.6% in comparison to the pure water as coolant. It was also concluded that a volume fraction of 2% was optimal as the addition of more nanoparticles in the water increased the thermal resistance and causes lesser thermal performance [18]. In similar way, Saeed et al. [19] concluded that the maximum rise in the coefficient of heat transfer (h) was observed as 33.5% at 2.5% volume fraction for Al_2O_3–water as nanofluid (Fig. 8).

At high values of Re, nanofluids showed lower thermal resistance because of the Brownian motion of nanofluid increases with velocity. The pumping power (PP) of the nanofluid was higher in comparison with the base fluids. Also, the power consumption by pump got increased with the increase in volume fraction of nanoparticle [17] as presented in Fig. 9. Hence, the higher density and viscosity of the nanofluid increase the pumping power (PP) compared with other base fluids [21]. Moreover, Miry et al. [16] reported the increase in power consumption of pump by using Al_2O_3–H_2O and TiO_2–H_2O. The pumping power was increased by 30% and

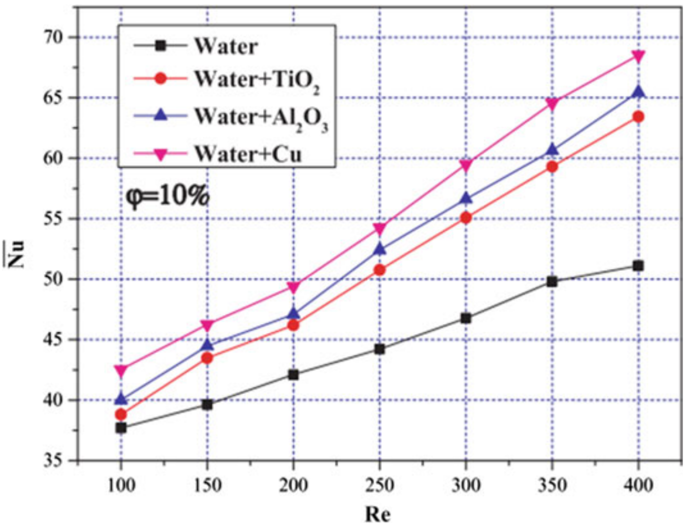

Fig. 8 Performance augmentation of the mean Nu and its enhancement with different Re values and volume fraction [17]

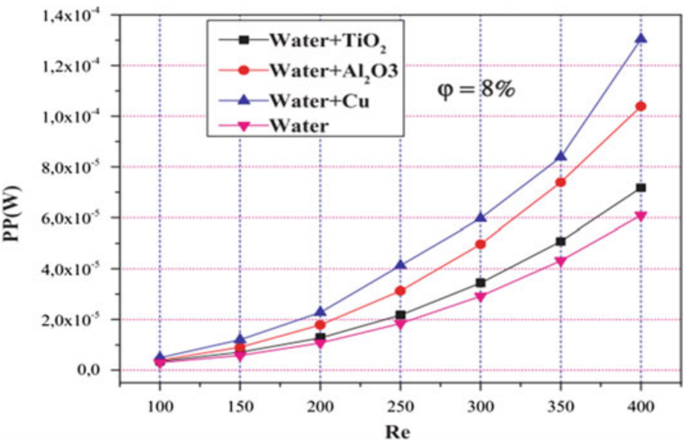

Fig. 9 Performance augmentation in pumping power versus Re at different nanofluids and same volume fraction [17]

45% at 2% volume fraction with alumina/water and titanium oxide/water nanofluid, respectively. In addition to previous study, an increase in the average pumping power for CuO–water was also found by 15.11% at 0.2% volume fraction compared with deionized water [24].

3.3 Effect of Using Porous Structure

In a recent study, the researchers also reported the use of porous structures formed by different arrangements of interconnected voids in a matrix to enhance the heat transfer inside a microchannel heat sink. Pourfarzad et al. [7] experimentally observed the effect of pore density on the thermo-hydraulic characteristics of a miniature heat sink. The coefficient of heat transfer (h) varied from 2.3 to 26.4% and 1 to 22% in lower (15 PPI) and higher (30 PPI) porosity medium, respectively. It was also seen that the heat transfer rate was higher in 30 PPI medium due to lower porosity as well as permeability. Higher permeability of porous medium reduces the effective contact surface area between solid foam and fluid. It was observed that using high porous medium causes higher pressure drops.

The pore density and porosity affect the thermal performance of foam-based heat sinks. Hsieh et al. [14] stated that the values of Nu increase with the porosity and pore density as shown in Fig. 10. A heat sink was also investigated experimentally considering porous stainless steel [15]. The result shows that the heat flux up to 6 MW/m^2 was dissipated by using pore diameter 20 mμ and porous sample with porosity of 32%.

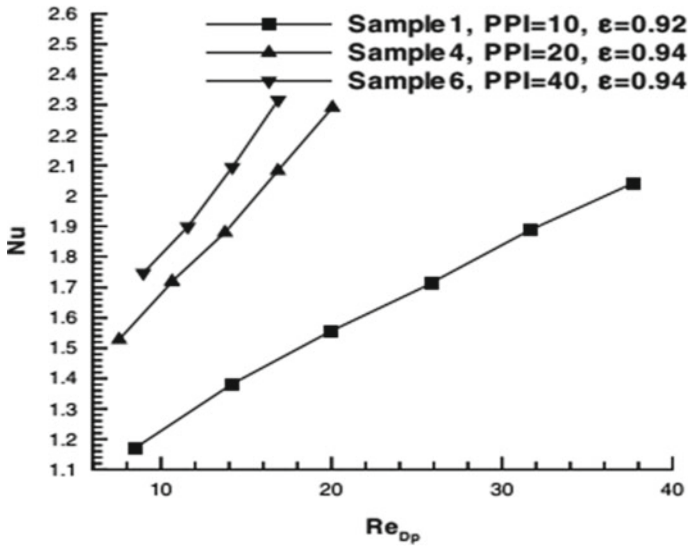

Fig. 10 Performance augmentation of the mean Nu and its enhancement with different Re values and pore densities [14]

4 Conclusion

Technological advancements in the electronic devices in various industries lead to exploration of the more efficient and compact heat sinks for dissipation of the heat at higher rates to keep the devices working effectively under the designed threshold limits. This manuscript recapitulates the studies done by various researchers to design and develop new flow channel configurations of the heat sinks, viz. rectangular, triangular, trapezoidal, sinusoidal, and so on. This review also presented the different types of nanofluids being used with the heat sinks to improve its thermal and hydraulic performance. The conclusions derived from this review study are the following:

- The thermo-hydraulic performance of a heat sink largely depends upon its geometry and thermo-physical properties of the working fluid.
- Trapezoidal type of flow channel outperformed the commonly used rectangular and triangular flow channel heat sinks, as the contact surface area was higher in trapezoidal shape heat sinks. However, the sinusoidal flow channels also performed considerably well under some conditions.
- Utilization of circular pin fins is more beneficial and efficient in comparison to the rectangle and hexagonal type. The geometry and design also depend upon the end-use applications.
- The enhancement in thermo-hydraulic performance of the microchannel mainly depends on the fins diameter, aspect ratio, type of nanoparticle, and their volume fraction.
- Nanoparticles have higher thermal characteristics than the base fluid particles; hence, the incorporation of nanoparticle can increase the thermal performance of the base fluid.
- Mass concentration of nanoparticle increases the pressure drop and friction factor; both result in increase in pumping power.
- The increase in nanofluid concentration results in better performance of the MCHS as the higher particle concentration leads to higher thermal conductivity of the nanofluid. The friction factor (f) is found to be more for a nanofluid in comparison to the pure water.
- An increase in pore density and nanofluid volume fraction delivers better heat transfer that eventually leads to improvement in thermal performance of microchannel heat sinks.

Acknowledgements The corresponding authors are thankful to the Ministry of Education, Government of India for providing the facilities and platform for the research work.

References

1. Yang L, Huang JN, Mao M, Ji W (2020) Numerical assessment of Ag-water nano-fluid flow in two new microchannel heatsinks: thermal performance and thermodynamic considerations. Int Commun Heat Mass Transf 110:104415. https://doi.org/10.1016/j.icheatmasstransfer.2019.104415
2. Ho CJ, Guo YW, Yang TF, Rashidi S, Yan WM (2020) Numerical study on forced convection of water-based suspensions of nanoencapsulated PCM particles/Al_2O_3 nanoparticles in a mini-channel heat sink. Int J Heat Mass Transf 157. https://doi.org/10.1016/j.ijheatmasstransfer.2020.119965
3. Shi XJ, Li S, Agnew B, Zheng ZH (2020) Effects of geometrical parameters and Reynolds number on the heat transfer and flow characteristics of rectangular micro-channel using nano-fluid as working fluid. Therm Sci Eng Prog 15. https://doi.org/10.1016/j.tsep.2019.100456
4. Abdollahi A, Sharma RN, Mohammed HA, Vatani A (2018) Heat transfer and flow analysis of Al_2O_3-Water nanofluids in interrupted microchannel heat sink with ellipse and diamond ribs in the transverse microchambers. Heat Transf Eng 39:1461–1469. https://doi.org/10.1080/01457632.2017.1379344
5. Ali HM, Arshad W (2015) Thermal performance investigation of staggered and inline pin fin heat sinks using water based rutile and anatase TiO_2 nanofluids. Energy Convers Manag 106:793–803. https://doi.org/10.1016/j.enconman.2015.10.015
6. Tuckerman DB, Pease RFW (1981) High-performance heat sinking for VLSI. IEEE Electron Device Lett EDL-2 126–129. https://doi.org/10.1109/EDL.1981.25367
7. Pourfarzad E, Ghadiri K, Behrangzade A, Ashjaee M (2018) Experimental investigation of heat transfer and pressure drop of alumina–water nano-fluid in a porous miniature heat sink. Exp Heat Transf 31:495–512. https://doi.org/10.1080/08916152.2018.1451413
8. Khoshvaght-Aliabadi M, Hassani SM, Mazloumi SH (2017) Comparison of hydrothermal performance between plate fins and plate-pin fins subject to nanofluid-cooled corrugated miniature heat sinks. Microelectron Reliab 70:84–96. https://doi.org/10.1016/j.microrel.2017.01.005
9. Ambreen T, Kim MH (2018) Effect of fin shape on the thermal performance of nanofluid-cooled micro pin fin heat sinks. Int J Heat Mass Transf 126:245–256. https://doi.org/10.1016/j.ijheatmasstransfer.2018.05.164
10. Zargartalebi M, Azaiez J (2019) Effects of nanoparticle adsorption on heat transfer in random pin-based microchannel heat sinks. Int J Heat Mass Transf 130:420–430. https://doi.org/10.1016/j.ijheatmasstransfer.2018.10.109
11. Duangthongsuk W, Wongwises S (2015) A comparison of the heat transfer performance and pressure drop of nanofluid-cooled heat sinks with different miniature pin fin configurations. Exp Therm Fluid Sci 69:111–118. https://doi.org/10.1016/j.expthermflusci.2015.07.019
12. Ghasemi SE, Ranjbar AA, Hosseini MJ (2017) Numerical study on the convective heat transfer of nanofluid in a triangular minichannel heat sink using the Eulerian-Eulerian two-phase model. Numer Heat Transf Part A Appl 72:185–196. https://doi.org/10.1080/10407782.2017.1358990
13. Mohammed HA, Gunnasegaran P, Shuaib NH (2010) Heat transfer in rectangular microchannels heat sink using nanofluids. Int Commun Heat Mass Transf 37:1496–1503. https://doi.org/10.1016/j.icheatmasstransfer.2010.08.020
14. Hsieh WH, Wu JY, Shih WH, Chiu WC (2004) Experimental investigation of heat-transfer characteristics of aluminum-foam heat sinks. Int J Heat Mass Transf 47:5149–5157. https://doi.org/10.1016/j.ijheatmasstransfer.2004.04.037
15. Hetsroni G, Gurevich M, Rozenblit R (2006) Sintered porous medium heat sink for cooling of high-power mini-devices. Int J Heat Fluid Flow 27:259–266. https://doi.org/10.1016/j.ijheatfluidflow.2005.08.005
16. Miry SZ, Roshani M, Hanafizadeh P, Ashjaee M, Amini F (2016) Heat transfer and hydrodynamic performance analysis of a miniature tangential heat sink using Al_2O_3-H_2O and TiO_2–H_2O Nanofluids. Exp Heat Transf 29:536–560. https://doi.org/10.1080/08916152.2015.1046016

17. Bakhti FZ, Si-Ameur M (2019) A comparison of mixed convective heat transfer performance of nanofluids cooled heat sink with circular perforated pin fin. Appl Therm Eng 159:113819. https://doi.org/10.1016/j.applthermaleng.2019.113819
18. Hung TC, Yan WM, Wang XD, Chang CY (2012) Heat transfer enhancement in microchannel heat sinks using nanofluids. Int J Heat Mass Transf 55:2559–2570. https://doi.org/10.1016/j.ijheatmasstransfer.2012.01.004
19. Saeed M, Kim MH (2018) Heat transfer enhancement using nanofluids (Al_2O_3–H_2O) in mini-channel heatsinks. Int J Heat Mass Transf 120:671–682. https://doi.org/10.1016/j.ijheatmasstransfer.2017.12.075
20. Mohammadi M, Taheri A, Passandideh-Fard M, Sardarabadi M (2020) Electronic chipset thermal management using a nanofluid-based mini-channel heat sink: an experimental study. Int Commun Heat Mass Transf 118:104836. https://doi.org/10.1016/j.icheatmasstransfer.2020.104836
21. Zhai YL, Xia GD, Liu XF, Li YF (2015) Heat transfer enhancement of Al_2O_3–H_2O nanofluids flowing through a micro heat sink with complex structure. Int Commun Heat Mass Transf 66:158–166. https://doi.org/10.1016/j.icheatmasstransfer.2015.05.025
22. Dehghan M, Daneshipour M, Valipour MS (2018) Nanofluids and converging flow passages: a synergetic conjugate-heat-transfer enhancement of micro heat sinks. Int Commun Heat Mass Transf 97:72–77. https://doi.org/10.1016/j.icheatmasstransfer.2018.03.022
23. Ghale ZY, Haghshenasfard M, Esfahany MN (2015) Investigation of nanofluids heat transfer in a ribbed microchannel heat sink using single-phase and multiphase CFD models. Int Commun Heat Mass Transf 68:122–129. https://doi.org/10.1016/j.icheatmasstransfer.2015.08.012
24. Selvakumar P, Suresh S (2012) Convective performance of CuO/water nanofluid in an electronic heat sink. Exp Therm Fluid Sci 40:57–63. https://doi.org/10.1016/j.expthermflusci.2012.01.033

Vortex-Induced Vibrations for Energy Harvesting: A Review

G. K. Chhaparwal and Ram Dayal

1 Introduction

The rise of hunger for energy demand is inevitable but the adverse environmental effects of carbon emission by burning of fossils to meet this demand can be avoided. Paris Agreement in 2015 further motivated researchers and investors around the globe to see future in carbon-free renewable energy resources. The rise in worldwide capacity of solar energy and wind energy in last five years also shows that the time when renewable energy will be major source of energy is no more distant. But in this paper, a new type of technique is reviewed that exploits ocean energy in an entirely different way—VIVACE (vortex induced vibration for aquatic clean energy) which is invented by Bernitsas in 2004–05 [1–5]. Before moving to what is VIVACE, let us discuss why do we need VIVACE? The habitat coastal areas have very high real estate property values, and surrounding marine life and environment further make such areas not friendly with other renewable energy options like solar power plant and wind turbines. Many countries have made very strict rules that must be satisfied by the any device that could be installed in these areas. Those are low maintenance, high life, robustness, high energy density, and should not obstruct navigation. There were many other ocean energy harvesting-based devices but all failed to meet the standards required to be installed along the coastal areas like water column, buoy, flap, pendulum [6, 7], turbines, watermills [8, 9], etc.

G. K. Chhaparwal
Rajasthan Institute of Engineering and Technology, Jaipur, Rajasthan 302026, India

R. Dayal (✉)
Department of Mechanical Engineering, Malaviya National Institute of Technology Jaipur, Jaipur, Rajasthan 302017, India
e-mail: ramdayal.mech@mnit.ac.in

D. Sharma and S. Roy (eds.), *Emerging Trends in Energy Conversion and Thermo-Fluid Systems*, Lecture Notes in Mechanical Engineering,
https://doi.org/10.1007/978-981-19-3410-0_22

1.1 Ocean Energy

The ocean is full of different types of energy that can be harnessed to fulfill the ever growing demand of the global energy consumption specially, along the coastal areas where the cost of land and existing flora and fauna are also major concern. For a sustainable energy harvesting, an energy convertor must follow certain criteria as shown in Fig. 1 (Table 1).

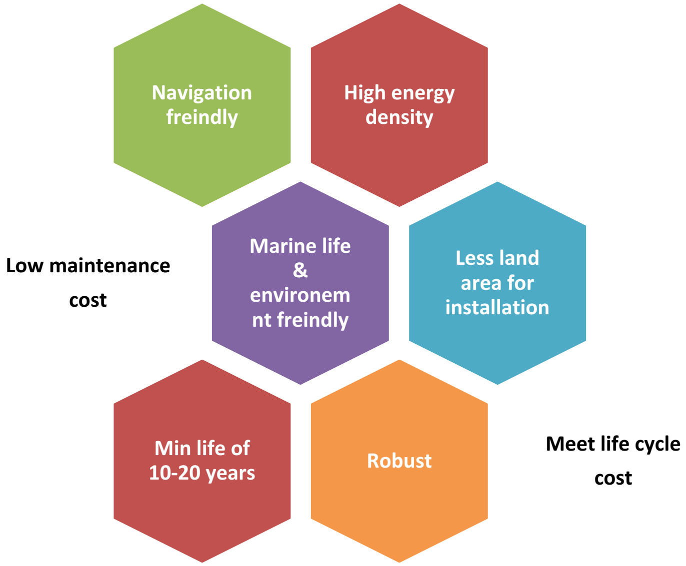

Fig. 1 Minimum criteria required by an ocean energy convertor for a sustainable energy harvesting

Table 1 Various conventional ocean energy convertors and their limitations

Convertor of	Limitations
Surface oscillation (water column, buoy, flap, or pendulum)	High energy output only near resonance, random waves hardly attain optimal performance with often extreme structural loads
Wind and tidal energy (turbines and watermills)	Low efficiency and inefficient function below 2 m/s (~4 knots), disturb marine life and occupy expensive coastal area for operation
Potential energy (water dams)	High water head requirement, large in structure, obtrusive, significant capital cost and construction period, and disturb marine life

1.2 Vortex-Induced Vibrations

In *VIVACE* which is a type of an ocean energy convertor, the suspended circular bars or cylinders are fixed on a vertical column via elastic springs of sufficiently high stiffness. The reciprocating motion (up and down) of the cylinders is synchronized and finally converted into the rotary motion via rack and pinion gear system to get electricity through a generator arm. The fundamental understanding of vortex-induced vibrations (*VIV)* is prerequisite before learning the working of *VIVACE.* The free and forced vibrations of such fixed rigid structures with single or multiple *dof* (degrees of freedom) lay the foundation of principle working of *VIVACE* device. The cylinders oscillate transverse to the velocity of water with weak in-line and strong transverse nonlinear oscillations [10].

The lock-in stage is very important in the vortex-induced vibrations. It is also known as vortex synchronization. At this stage, $f_{\text{form}} \sim f_{\text{n,water}} \sim f_{\text{cyl}}$ or simply the vortex formation and natural frequencies both become almost equal to each other. The unique construction characteristic of the *VIVACE* device allows the synchronization to happen over a larger range of reduced velocity and at high mass ratio as compared to the other convertors. Where reduced velocity factor $U^* = \frac{U}{f_{\text{n, water}} D}$ and mass ratio $m^* = \frac{m_{\text{osc}}}{m_{\text{d}}}$ and $m_{\text{d}} = \frac{\pi}{4} \rho_{\text{w}} D^2 L$ [11–14].

It can be observed that there are many ways to harness energy from ocean, but it was Bernitas and his team who successfully exploited vortex had induced vibration (*VIV*) first time for feasible and sustainable energy harvesting through their invented device called VIVACE in year 2004–05. Unlike other ocean energy-based devices, it is safe for marine life. It is based on the *VIV.* The *VIV* involves several degrees of freedom, and it is self-induced and self-limiting with several mode of responses. Reynolds number (Re) and damping (C) have unusually very high values, which have limited studies in the literature. There are many parameters whose effect can be investigated as briefly discussed in the following points in Table 2.

In a study by [5], the effect of high damping, high Re, and variable R_{L} (for optimization of the electricity generated) is investigated in a Low-Turbulence Free-Surface Water (*LTFSW*) channel with all the necessary mathematical.

2 Experimental Model

2.1 LTFSW *Channel*

The *LTFSW* channel has many advantages over a towing tank which is used to get flow past a cylinder. It provides unlimited number of oscillations per experiment within acceptable turbulence level. However, in *LTFSW,* the width of the channel limits the length of the cylinder and turbulence induced by impeller makes it difficult to achieve very low turbulence level. A two-story high water channel recirculates

Table 2 Table captions should be placed above the tables

Parameter	Explanation
Synchronization or lock-in	It depends on mass ratio which changes the wake pattern properties
Range of synchronization about natural frequency of the cylinder	A broad range of synchronization in VIV makes the device robust against the changes in the flow velocity
Self-limiting amplitude	A suitably high magnitude of the VIV oscillation is managed through energy harnessing resistance which should not suppress VIV oscillation
Initial, upper, and lower branches of amplitude of oscillation	A VIVACE device must work in high damping and high amplitude for wide range of synchronization
Types of wake pattern (2S, 2P, P + S, 2 T)	It depends on the values of mass ratio (m^*) and degree of freedom
Mass ratio (m*):	It is ratio of oscillating mass to the displaced fluid mass which changes types of response and vibrational frequency
Multiple degrees of freedom	A two degree of freedom causes higher amplitudes of the oscillation
Correlation length	It is ratio of the length to the diameter of the cylinder; its larger value is preferred for higher forces on the cylinders
Synchronization under high damping	A less work is reported in literature on this parameter, and higher damping is maintained that can sustain VIV
Reynolds number	The amplitude of oscillation and lift increase with Re, and it is also less investigated in the literature
Proximity to the free surface or solid boundaries	Wake structure and forces on cylinder significantly change with the closeness of the surface of fluid or solid
Product ($m^*\zeta_a$)	A sustainable large *VIV* oscillation amplitude must be maintained to get maximum possible power generation. An optimum trade-off between high damping and generated power obtained so that too much damping should not suppress *VIV*

8000 gallons of treated water via four impeller of diameter 0.787 m connected with 20 hp three-phase electric motor.

2.2 Apparatus

Figure 2 shows the *VIVACE* cylinder placed transverse to the fluid flow as a spring-mass system with all dimensions, stiffness, and damping in the setup. Initially, three setup *VIVACE* models were studied, out of which Model-III works in the desired

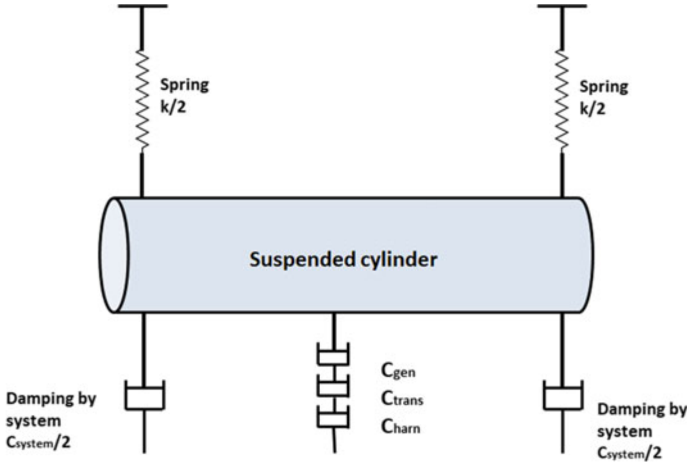

Fig. 2 *VIVACE* cylinder placed transverse to the fluid flow as a spring-mass system

manner. The cylinder in the Model-III is made up of aluminum, and it has diameter $D = 125.7$ mm, length $L = 914.4$ mm, aspect ratio $L/D = 7.274$, and a high blockage ratio $D/H = 0.143$. There are two cylinders with a gap of 10 mm with the walls of the test section, which are suspended by compression coil springs at the ends, with constrained motion in transverse direction via linear bearings and controlled natural frequency of oscillation $f_{\text{n,water}}$ (0.88–1.037 Hz) via changing the active coils.

2.3 Calibration

The velocity measured from the pitot tube placed 30 cm from bottom of the tank and half-width of the tank is calibrated with the velocity of the *VIVACE* cylinder at six water depths with four impeller frequencies within range of velocity 1.2 m/s (above this value, there was non-uniformity in the correlation) for 30 s of time period, and a correlation is developed as given by:

$$\begin{aligned} U(\text{m/s}) = {} & (-0.000034 \times (\text{ Water Depth(cm)}) + 0.061177) \\ & \times \text{ Impeller Frequency} \end{aligned} \tag{1}$$

The input from transducer and generator is fed into the data acquisition system. The amplitude and range of synchronization are significantly reduced as cylinder is placed closer to the free surface.

3 Mathematical Modeling

Equation of motion for the *VIVACE* cylinder,

$$(m_{\text{osc}} + C_{\text{a}})\left[\frac{y^*}{f^2_{\text{n, water}}} + \frac{4\pi\zeta_{\text{total}}y^*}{f_{\text{n, water}}} + 4\pi^2 y^*\right] = \frac{2}{\pi}c_y(t)U^{*2} \tag{2}$$

Fluid power in VIVACE

$$P_{\text{VIVACE, fluid}} = \frac{1}{2}\rho\pi c_y U^2 f_{\text{cyl}} y_{\max} DL\ \sin(\varphi) \tag{3}$$

Mechanical power in VIVACE,

$$P_{\text{VIVACE, fluid}} = 8\pi^3(\text{mosc} + \text{Ca})\zeta_{\text{total}}\left(f_{\text{cyl}} y_{\max}\right)^2 f_{\text{n, water}} \tag{4}$$

Upper limit to the efficiency of the *VIVACE* converter (based on the experimental data):

$$\eta_{\text{UL, VIVACE}} = \frac{P_{\text{VIVACE, fluid}}}{P_{\text{fluid}}} \tag{5}$$

where power in fluid is given by $1/2\rho U^3 DL$; the efficiency of the *VIVACE* device is given by:

$$\eta_{\text{ VIVACE}} = \frac{P_{\text{VIVACE, harn}}}{P_{\text{fluid}}} \tag{6}$$

Generator Model

Torque generated in the generator is given by (Fig. 3):

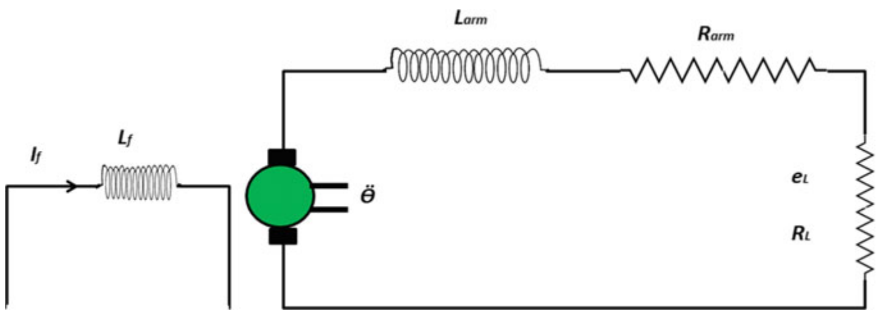

Fig. 3 An equivalent electric circuit diagram of a VIVACE device

$$T_{\text{gen}} = (k_f I_f)\left(\bar{k} I_{\text{arm}}\right) = K I_{\text{arm}} \tag{7}$$

The voltage generator by field induced by the VIV is given by:

$$\frac{\tilde{\theta}}{\tilde{e}_{\text{L}}} = \frac{-K}{\omega^2 \text{JL}_{\text{arm}} + i\omega(L_{\text{arm}}c + R_{\text{arm}}J) + R_{\text{arm}}c - \alpha K} i\omega \tag{8}$$

Transmission Model

The periodic reciprocating (up and down) motion of the cylinder is converted into the periodic rotational oscillatory motion of the shaft of the generator with the help of a rack and pinion gear system, which is shown in Fig. 4. When the gear effect is considered, the expression for the voltage-induced can be written as:

$$\frac{\tilde{\theta}}{\tilde{e}_L} = \frac{-K}{\omega^2 J L_{eq} + i\omega\left(L_{arm} c_1^{eq} + R_{arm} J_1^{eq}\right) + R_{arm} c - \alpha K} i\omega$$

Combined Model

Here, all the components of the *VIV and* energy generation via transmission systems are combined together to get an overall view of the interlinking of the individual system. Due to inertia of the movement of the generator, gear-2 exerts force on the suspended cylinder. There are frictional losses in the gear system as well as damping in the generator due to electric wiring. Both can be managed by the L_{R}(load resistor). All kinds of the damping can be put together to get an interrelationship via following equation:

$$C_{\text{total}} = C_{\text{system}} + C_{\text{trans}} + C_{\text{gen}} + C_{\text{harn}} \tag{10}$$

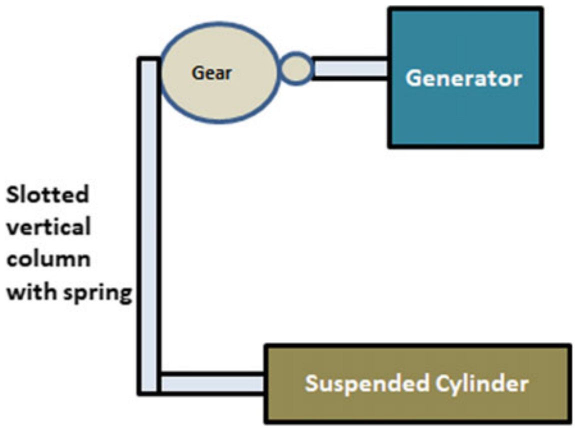

Fig. 4 A schematic diagram showing all the components of a VIVACE device [5]

Table 3 Different types of damping in the *VIVACE* and their causes

Damping	Cause	Measurement
System damping, C_{system}	It is due to structural damping by friction at the component and the material scales and fluid damping which is the result of energy dissipation	In air/water with gear disconnected
Transmission damping, C_{trans}	It is mainly due to friction in the gear system and frictional losses of the generator as frictional bearing losses	In water with transmission connected and generator connected to the transmission (without electrical load)
Generator damping, C_{gen}	It is by the generator armature (internal) resistance R_{arm}	It is due to the generator armature internal resistance R_{arm}, which is a function of the load resistance
Harness damping, C_{harn}	It is due to the load resistance RL used to harness energy	It is obtained by the performing a free decay test of the corresponding system

Analytical estimation of C_{total} is not possible, and hence, it is measured experimentally; there are four sources as summarized in Table 3.

The cylinder is initially displaced to undergo damped up and down movements with y_n and $y_{(n+1)}$ as any two consecutive peaks that are given as:

$$\frac{y_n}{y_{n+1}} = \mathrm{e}^{(\zeta \omega_d T_d)} \tag{11}$$

where $T_d = \frac{2\pi}{\omega_d}$ and damping ratio $= \frac{1}{2\pi} \ln \frac{y_n}{y_{n+1}}$.

The open voltage across the generator is given by:

$$E = \alpha \frac{y(t)}{r_1} \tag{12}$$

The power harnessed by the load resistor R_L:

$$P_L = e_L I_{arm} = I_{arm}^2 R_L = \left[\frac{\frac{\dot{y}(t)}{r_1} \alpha}{R_{arm} + R_L} \right] R_L \tag{13}$$

4 Measurements and Data Analysis

In the measurement and data analysis of the *VIV* phenomenon, cylinder vertical displacement, water velocity, voltage generation at R_L, and the harnessed power

Table 4 Various input parameters that have significant effects on *VIVACE*

Parameter	Effect
Low damping	Enhanced synchronization range and *VIV* amplitude
R_L as infinity	Zero power take-off due to open ends
High damping	*VIV* amplitude and synchronization remains high
High Re values	Supports high oscillation amplitudes

are few important output parameters and those should be recorded during the experimental run. A rigorous evaluation of design, fabrication, and compatibility of various parts must be done via damping tests so that all parts of the *VIVACE* work properly at minimum friction. The role of free surface and bottom effects should be studied. Fourier spectral analysis is not applicable here; *VIV* time series are of nonlinear, non-stationary nature. So, Hilbert-Huang Transform (*HHT*) is used to analyze the resulted time series over large range of velocities and load resistor R_{load}. In the experimental runs, generated voltage and harnessed power can be studied at different velocities and R_{load}. Subsequently, η_{peak}, η_{VIVACE}, and $\eta_{\text{UL-VIVACE}}$ can be calculated for the overall rating of the *VIVACE* device.

A basic parametric analysis to see the effect of various parameters is recorded in terms of dimensionless amplitude of *VIV,* power output, various efficiencies, etc. which suggests many important interrelationships are obtained that are summarized in the Table 4.

5 Conclusions and Future Scopes

Vortex-induced vibrations (*VIV)* have been studied and exploited for low damping only, and it is the first time that an ocean energy convertor has been devised to harness electricity with *VIV* under high damping. The vortex shedding phenomenon is mainly studied in low Reynolds number but in real ocean current flows at high Re. At higher Re, the amplitude of *VIV* increases which supports higher voltage generation. This review paper is aimed to put together the fundamentals of *VIVACE* device via hydrodynamic and mathematical models. The ocean energy convertors like turbines and watermills are unable to work at low water flow speeds, while *VIVACE* has ability to harness energy even in such low velocities at reasonably high efficiencies. In the future scope, the effect of high damping and high *Re* on wake characteristics and energy harvesting can be investigated. The optimum value of cylinder diameter and spring stiffness at given mass ratio can predicted to get a economic *VIVACE* device.

References

1. Bernitsas MM, Raghavan K (2004) Converter of current/tide/wave energy, provisional patent application, US Patent and Trademark Office Serial No. 60/628,252
2. Bernitsas MM, Raghavan K (2005) Supplement to the U.S. provisional patent application titled, converter of current, tide, or wave energy, University of Michigan Ref. No. 2973
3. Bernitsas MM, Raghavan K (2005) Fluid motion energy converter, U.S. Patent Application, United States Patent and Trademark Office, Serial No. 11/272,504
4. Bernitsas MM, Raghavan K (2005) Fluid motion energy converter, international provisional patent application, USA Patent and Trademark Office
5. Bernitsas MM, Ben-Simon Y, Raghavan K, Garcia EMH (2006) The VIVACE converter: model tests at high damping and reynolds number around 10^5. In: 25th international OMAE conference
6. Ogata K (2004) System dynamics, 4th edn. Prentice Hall, New Jersey
7. Szepessy S (1993) On the control of circular, cylinder flow by end plates. Euro J Mech B Fluids 12:217–244
8. Chen SS (1987) Flow-induced vibration of circular cylinder structures. Hemisphere Publishing Corporation, Springer, Washington
9. Khalak A, Williamson CHK (1999) Motions, forces and mode transitions in vortex-induced vibrations at low mass-damping. J Fluids Struct 13:813–851
10. Govardhan R, Williamson CHK (2000) Modes of vortex formation and frequency response of a freely vibrating cylinder. J Fluid Mech 420:85–130
11. Rood EP (1995) Free surface vorticity (Chap. 17). In: Green S (ed) Free-surface vorticity. Kluwer
12. Sarpkaya T (2000) A critical review of the intrinsic nature of vortex induced vibrations. J Fluids Struct 19(4):389–447
13. Walker DT, Lyzenga DR, Ericson EA, Lund DE (1996) Radar backscatter and surface roughness measurements for stationary breaking waves. Proc Roy Soc Lond A 452:1953–1984
14. Huang NE, Shen Z, Long SR, Wu MC, Shih HH, Zheng Q, Yen NC, Tung CC, Liu HH (1998) The empirical mode decomposition and the Hilbert spectrum for nonlinear and nonstationary time series analysis. Proc Roy Soc Lond A 454:903–995